HAL open science

Synaptopathies des cellules ciliées auditives associées à un dysfonctionnement de l'exocytose Ca2+-dépendante

Thibault Peineau

To cite this version:

Thibault Peineau. Synaptopathies des cellules ciliées auditives associées à un dysfonctionnement de l'exocytose Ca2+-dépendante. Neurosciences. Université de Bordeaux, 2021. Français. NNT : 2021BORD0375 . tel-04021463

HAL Id: tel-04021463

https://theses.hal.science/tel-04021463v1

Submitted on 9 Mar 2023

HAL is a multi-disciplinary open access archive for the deposit and dissemination of scientific research documents, whether they are published or not. The documents may come from teaching and research institutions in France or abroad, or from public or private research centers.

L'archive ouverte pluridisciplinaire **HAL**, est destinée au dépôt et à la diffusion de documents scientifiques de niveau recherche, publiés ou non, émanant des établissements d'enseignement et de recherche français ou étrangers, des laboratoires publics ou privés.

THÈSE PRÉSENTÉE

POUR OBTENIR LE GRADE DE

DOCTEUR DE

L'UNIVERSITÉ DE BORDEAUX

ÉCOLE DOCTORALE DES SCIENCES DE LA VIE ET DE LA SANTÉ

SPÉCIALITÉ NEUROSCIENCES

Par **Thibault PEINEAU**

Synaptopathies des Cellules Ciliées Auditives Associées à un Dysfonctionnement de l'Exocytose Calcium-dépendante

Sous la direction du
Dr Didier DULON

Soutenue le 16 décembre 2021

Membres du jury :

Mme FERRARY, Evelyne	Directrice de recherche	Rapporteure
M. PUEL, Jean-Luc	Professeur	Rapporteur
Mme MONTCOUQUIOL, Mireille	Directrice de recherche	Présidente du Jury
M. BONNARD, Damien	MCU - PH	Invité
M. DULON, Didier	Directeur de recherche	Directeur de Thèse

REMERCIEMENTS

Avant d'entamer la lecture de ce travail qui résume 3 ans de thèse « administrativement » mais finalement bien plus humainement, je tenais à dire quelques mots.

Tout d'abord, je tiens à remercier le **Dr Evelyne FERRARY** et le **Professeur Jean-Luc PUEL** d'avoir accepté d'être les rapporteurs de cette thèse et d'expertiser ce travail. Un grand Merci également au **Dr Mireille MONTCOUQUIOL** d'avoir accepté d'être examinatrice de cette thèse et au **Dr Damien BONNARD** d'avoir accepté l'invitation à la soutenance.

Merci infiniment à la coopérative d'audioprothésiste **Entendre** pour le soutien financier tout au long de ces 3 années.

Un **grand Merci bien sûr à Didier** pour sa confiance non pas pendant 3 mais 5 années. Je me souviens encore arriver sur la pointe des pieds dans le laboratoire cherchant désespérément un stage pour ma première année de master. Et finalement d'un claquement de doigt nous voilà 5 ans plus tard avec une équipe qui a bien évoluée. Merci, Didier, pour vos conseils toujours très précieux autant sur le plan professionnel que personnel, pour cet accompagnement durant toutes ces années et surtout pour votre soutien indéfectible malgré les embuches administratives, les échecs expérimentaux et les moments de doute. Sans vous rien de cela n'aurait été possible, et comme vous pouvez l'imaginer 5 ans d'enseignement à vos côtés laissera forcément des traces sur le chercheur que je souhaite devenir et la personne que je suis.

Un **immense Merci également à Yohan**. L'homme à tout faire du laboratoire qui porte à bouts de bras notre équipe et qui mérite bien plus que le statut de technicien. En plus d'être le pilier expérimental et administratif, il est également le pilier social du laboratoire. Je te remercie de m'avoir tant aidé sur nos travaux mais également sur le plan social, nos discussions sur le sport automobile, le cinéma, les séries, la musique et j'en passe, ont été d'un grand soutien également. Ta bienveillance et ta gentillesse ont été indispensable au bonheur qu'ont été ces 5 années au laboratoire. Merci d'être cette personne formidable.

Un Merci à **Margot**, pour m'avoir formé lors de mon arrivée au laboratoire, merci d'avoir pris le temps de me former et m'apprendre toutes les bases de cette fabuleuse cochlée. Merci également à **Séverin** et à **Jean-Christophe** pour leur bonne humeur et leur aide indispensable dans nos travaux.

Un chaleureux Merci à **Charlotte** pour sa gentillesse et le temps que tu as pris pour me former aux injections intra-cochléaires. J'espère que tu t'épanouiras dans tes futurs projets. Merci également à l'ensemble de l'Institut de l'Audition, ce fut un honneur, une fierté de participer à tous ces travaux. Je tiens particulièrement à remercier **Sandrine VITRY**, **Aziz El-AMRAOUI** et **Saaid SAFIEDDINE** pour m'avoir fait confiance dans leur projet.

Merci aux petits nouveaux : **Celeste**, **Manon**, **Léa** et **Steven** qui ont dynamisé le laboratoire. J'espère que vous vous sentez bien accueilli dans notre petite équipe, je vous souhaite de belles réussites dans vos projets respectifs que je suivrai avec grande attention n'en doutez pas !

Comment ne pas remercier également **toute ma famille de m'avoir soutenu tout le long de mon parcours**, pas seulement pendant ces 3 dernières années. **Merci à mes parents de m'avoir offert la plus belle des éducations**, un soutien financier non négligeable également qui m'a permis aujourd'hui d'accomplir un rêve. **J'espère vous rendre fiers avec cette thèse qui n'est autre que le fruit de tout l'amour inconditionnel que vous m'avez porté durant toutes ces années. Merci également à mon frère, Léo,** qui a toujours cru en moi depuis notre plus tendre enfance. J'espère aussi te rendre fier, autant que je le suis de toi. Je te souhaite un immense bonheur dans la nouvelle petite famille que tu construis.

Merci aussi à ma seconde famille, mes amis tourangeaux, qui m'ont apporté un immense soutien moral. Merci de leur bonne humeur, de leur humour, de leur bienveillance. Merci à **Noémie** et **Sébastien** (NTS) pour toutes ces discussions, ces débats depuis tant d'années qui embellissent ma vie. Vous êtes les piliers indispensables qui participent à mon épanouissement personnel. Merci à la team BlackPearl : **Liam, Julio et Nicolas**. Merci de m'avoir supporté toutes ces années dans mes bons comme dans mes mauvais côtés. Merci d'être là pour moi et d'avoir fait partie de ma vie pendant toutes ces années, et bien sûr RDV sur la faille vendredi soir comme d'hab. Merci à **Marine, Elhori, Justine et Thaïs** d'avoir également participé à ce soutien moral avec tous les autres depuis le lycée ! Merci à **Valentin** pour ton amitié indéfectible depuis si longtemps !

Enfin je voudrais remercier toute la team Bordeaux, pour ces soirées jeux de société incroyable mais surtout pour leur gentillesse, leur bienveillance et leur bonne humeur qui m'ont accompagné dans cette aventure bordelaise. Merci particulièrement à **Mélody** de m'avoir accompagné tous ces midis, merci pour ta présence. J'espère que tu t'épanouiras dans tes projets, en tout cas n'en doute pas je serai toujours disponible pour te remonter le moral. Merci également à **Pierre** pour ces parties de tennis de folie et ces séances ciné. Merci à **Juliette** pour ta joie de vivre et ta bonne humeur ainsi que **Jules** pour bien sûr ton humour légendaire. Merci à tous ceux dont je ne cite pas le nom de la team Bordeaux, par soucis de place, mais qui ont grandement participé à mon bonheur et à mon épanouissement.

Merci à tous et bonne lecture,

SOMMAIRE

Publications scientifiques……i
Abréviations……iii
Liste des figures et tableaux……vii

INTRODUCTION……1

Chapitre 1 : Principes de base du son……3
1.L'acoustique du son……3
2.Epidémiologie de la surdité……7
3.Dépistage de la surdité chez l'Homme……7

Chapitre 2 : Le système auditif chez les mammifères……9
1. L'oreille externe……9
2. L'oreille moyenne……10
3. L'oreille interne……11
A. La cochlée……12
B. Les cellules ciliées internes……15
C. Les cellules ciliées externes……16
D. Le vestibule……17
E. Le nerf auditif……18
1.Voie afférente……18
2.Voie efférente……19

Chapitre 3 : La transduction du son……21
A. La mécano-transduction……21
1. Les stéréocils……21
2. Les canaux de mécano-transduction……23
B. Les synapses à ruban……25
1. Le ruban……25
2. Les vésicules glutamatergiques……29
3. Les senseurs calciques……32
4. Les canaux calciques……33
a. Généralités sur les canaux calciques……33
b. Inactivation par le voltage et le Ca^{2+}……35
c. Inactivation par les protons……36
d. Les isoformes des canaux calciques……37
5. Les canaux potassiques activés par le Ca^{2+}……38
a. Les principaux canaux potassiques des cellules ciliées ……38
b. Propriétés et régulation des canaux BK……39

Chapitre 4 : Surdités……41
1. Types de surdités……41
2. Surdités neurosensorielles……41
3. Perte de l'audition liée à l'âge……43
4. Vieillissement cellulaire dû au stress oxydatif……43

a. Le stress oxydatif……43
b. L'inflammation dû au vieillissement cellulaire……45
c. Les voies apoptotiques des cellules ciliées……46
d. L'autophagie……48

Chapitre 5 : Objectifs de la thèse……49
1. Caractériser le rôle de clarine-2……49
2. Etudier le rôle de SNAP-25……49
3.Caractériser les changements fonctionnels et structurels lors du vieillissement……50

RESULTATS……51

Article 1 : Clarin-2 is essential for hearing by maintaining stereocilia integrity and function……53

Article 2 : Functional defect at IHC ribbon synapses of Clrn2 mutant mice……79

Article 3 : Targeted SNAP-25 deletion disrupts the function and structure of inner ear hair cell ribbon synapses……91

Article 4 : Synaptic release potentiation at ageing auditory ribbon synapses……143

DISCUSSION……167

I. Rôle de la clarine-2 dans la maintenance morpho-fonctionnelle des stéréocils……169
II. Rôle de la clarine-2 au niveau des synapses à ruban ……170
III. Perspectives sur le rôle de la clarine- 2……172
IV. La SNAP-25 est essentielle pour la fusion rapide des vésicules synaptiques et la survie des synapses à ruban……173
V. Les changements structurels et fonctionnels des synapses à ruban des CCI lors du vieillissement……174
VI. Stress oxydatif et vieillissement des CCIs……176
VII. Perspectives……178

RÉFÉRENCES BIBLIOGRAPHIQUES……179

PUBLICATIONS SCIENTIFIQUES

Article 1: Lucy A Dunbar, Pranav Patni, …, Thibault Peineau, …, Walter Marcotti, Aziz El-Amraoui, Michael R Bowl (2019). Clarin-2 is essential for hearing by maintaining stereocilia integrity and function. EMBO Mol Med 11(9), e10288. doi: 10.15252/emmm.201910288.

Article 2: Thibault PEINEAU, Sandrine VITRY, Yohan BOULEAU, Aziz EL-AMRAOUI, Didier DULON. Functional defect at IHC ribbon synapses of *Clrn2* mutant mice (Manuscript en préparation).

Article 3: Charlotte Calvet, Thibault Peineau, Andrea Lelli, Baptiste Plion, Ghizlène Lahlou, Julia Fanchette, Sylvie Nouaille, Jacques Boutet de Monvel, Amrit Estivalet, Philippe Jean, Vincent Michel, Martin Sachse, Nicolas Michalski, Paul Avan, Christine Petit, Didier Dulon, Saaid Safieddine. Targeted SNAP-25 deletion disrupts the function and structure of inner ear hair cell ribbon synapses (Manuscrit en préparation).

Article 4: Thibault Peineau, Séverin Belleudy, Susanna Pietropaolo, Yohan Bouleau, and Didier Dulon. (2021). Synaptic Release Potentiation at Aging Auditory Ribbon Synapses. Frontiers in Aging Neuroscience 13(670). doi: 10.3389/fnagi.2021.756449.

Communication 1 (Poster) : Jean-christophe Leclère , Thibault Peineau, Margot Tertrais, , Yohan Bouleau et Didier Dulon : The use of CRISPR-Cas9 genome editing technology in vivo to probe the role of synaptic protein isoforms in mouse auditory hair cells (2019). ARO 42nd Annual MidWinter meeting, le 9-13 février 2019 à Baltimore, Maryland (USA).

Communication 2 (Poster) : Thibault Peineau, Margot Tertrais, Jean-christophe Leclère, Yohan Bouleau et Didier Dulon : The use of CRISPR-Cas9 genome editing technology in vivo to probe the role of synaptic protein isoforms in mouse auditory hair cells (2019). Journée Scientifique de l'Ecole Doctorale du 14 mai 2019 à Haut-Carré, Talence.

Communication 3 (Oral) : Thibault Peineau, Margot Tertrais, Jean-christophe Leclère, Yohan Bouleau et Didier Dulon : Different $Ca_V1.3$ Ca^{2+} channel isoforms control transient and sustained exocytosis at auditory hair cells ribbon synapses (2019) Journée Bordeaux Neurocampus du 15 mai 2019 à Haut-carré, Talence.

Communication 4 : Didier Dulon, Thibault Peineau, Séverin Belleudy et Yohan Bouleau : Age-related structural and functional changes at auditory hair cell ribbon synapses (2019) IEB Padova du 5 septembre 2019, à Padoue (Italie).

Communication 5 (Poster) : Thibault Peineau, Séverin Belleudy, Yohan Bouleau et Didier Dulon : Age-related structural and functional changes at auditory hair cell ribbon synapses (2019) International Inaugural Conference of the Hearing Institute du 16 septembre 2019 au Collège de France à Paris.

Communication 6 (Oral) : Thibault Peineau, Séverin Belleudy, Yohan Bouleau et Didier Dulon : Presynaptic plasticity at ageing auditory ribbon synapses : Enlarged ribbons with Increased Ca^{2+} microdomains and reduced BKCa channel clusters (2020) Neuroscience – Insitut de l'Audition, Departmental days du 5 novembre 2020 en visio-conférence.

ABRÉVIATIONS

a.a : Acides aminés

AAV : Adeno-Associated Virus

ABR : Auditory Brainstem Response (ou PEA pour Potentiels évoqués auditifs)

AHRL: Age related hearing loss (Surdité liée à l'âge)

AMPA: α-Amino-3-hydroxy-5-Methyl-4-isoxazolepropionic acid

ATP: Adénosine triphosphate

ADP: Adénosine diphosphate

AZ : Active zone

BK (canaux) : Canaux potassiques à forte conductance

Ca^{2+}: Calcium ion

CaBP : Calcium Binding Protein

CaM : Calmoduline

$Ca_V1.3L$: Isoforme longue de $Ca_V1.3$

$Ca_V1.3S$: Isoforme courte-*short* du canal Cav1.3

CCEs : Cellules Ciliées Externes (IHC : Inner hair cells)

CCIs : Cellules Ciliées Internes (OHC : Outer hair cells)

CDI : Calcium-dependant inactivation

dB: Décibel

DCRD : Distal Carboxy terminal Regulatory Domain

DISC : Death induced signaling complex

DPOAE : Distortion product otoacoustic emissions

EPSC et EPSP: Excitatory post-synaptic currents and Excitatory post-synaptic potentials

H_20_2 : peroxyde d'hydrogène

K^+: Potassium ion

KO: *knock-out* – Délétion du gène

MET : Mecano-electrical transducer (canaux de mécanotransduction)

mTOR : mammalian Target of rapamycin

Na^+ : Sodium ion

nAChR : Récepteurs nicotinique

NAD(P)H : Nicotinamide adénine dinucléotide (phosphate)

NOX : NAD(P)H-oxydase

OC : Organe de Corti

O_2 et O_2^- : Dioxygène et Superoxyde respectivement

PCRD : Proximal Carboxy terminal Regulatory Domain

PGD : Pore gated domain

RCK : Regulator of potassic conductance

ROS : Reactive oxygen species (dérivés réactifs de l'oxygène)

RRP: Readily releasable pool

RE : Réticulum endoplasmique

SK (canaux) : Canaux potassiques à faible conductance

SNAP-25: Synaptosomal-associated protein 25

SNARE: Soluble N-éthylmaleimide-sensitive-factor attachment protein receptor

SOD: Superoxyde dismutase

SRP: Secondarily releasable pool

TMC1/TMC2 : Transmembrane channel-like protein 1 and 2

TRP : Transient receptor potential channels

UPR : Unfold protein response

VGLUT3 : Vesicular Glutamate Transporter 3

VSD : Voltage sensory domain

LISTE DES FIGURES ET TABLEAU

Figure 1. Seuils auditifs et échelle des pressions acoustiques en dB.

Figure 2. Représentation théorique d'une onde

Figure 3. Propagation de deux ondes de deux fréquences différentes

Figure 4. Décomposition d'un son complexe

Figure 5. Audiogrammes représentant les pertes auditives moyennes (en dB) d'un individu moyen à différentes fréquences chez l'Homme en fonction de l'âge

Figure 6. Dessin anatomique de l'oreille externe

Figure 7. Dessin anatomique de l'oreille moyenne

Figure 8. Dessin anatomique de l'oreille interne

Figure 9. Dessins représentatifs des rampes de la cochlée

Figure 10. Dessin d'une coupe transverse de l'organe de Corti

Figure 11. Représentation schématique de l'innervation de l'organe de Corti

Figure 12. Représentation schématique de l'association mécanique de la partie apicale d'un stéréocil avec son stéréocil adjacent supérieur via le "tip-link"

Figure 13. Représentation schématique de l'hypothèse expliquant l'ouverture des canaux MET (TMC1/TMC2) via l'étirement du "tip-link", entraînant une déformation de la membrane plasmique apicale du stéréocil

Figure 14. Représentation de la relation entre la distance à partir de l'apex de la cochlée et le nombre moyen de synapses par CCI chez les souris P30 de lignée C57BL/6J

Figure 15. Représentation schématique d'un ruban synaptique.

Figure 16. Représentation schématique du mécanisme de remplissage des vésicules synaptiques des CCIs en glutamate.

Figure 17. Représentation schématique du « Docking » et « Priming » des vésicules synaptiques dans les synapses neuronales.

Figure 18. Comparaison de la structure et des domaines C2 des synaptotagmines et de l'otoferline.

Figure 19. Représentation schématique du nuage calcique (nanodomaine er microdomaine) produit par l'activité des canaux calciques CaV1.3 situés au niveau des ZA des CCIs

Figure 20. Représentation schématique des canaux calciques CaV1.3 des CCIs

Figure 21. Représentation schématique des sous-unités composant les canaux BK

Figure 22. Représentation schématique de la voie d'oxydation des NADPH par le complexe NOX

Figure 23. Les voies de signalisation de l'apoptose dans les cellules ciliées

Figure 24. Voie de signalisation de l'autophagie dans les cellules ciliées

Figure 25. La clarine-1 est essentielle à l'organisation morpho-fonctionnelle des zones actives des CCIs

Figure 26. Représentation schématique des différentes protéines impliquées dans la fusion des vésicules glutamatergiques dans les synapses à ruban des cellules ciliées.

Figure 27. Evolution de la synapse à ruban des CCIs des souris C57BL/6J avec l'âge

Tableau 1. Liste des protéines les plus couramment impliquées dans des surdités génétiques chez l'Homme.

INTRODUCTION

Chapitre 1 : Principes de base

1. L'acoustique du son

Le son est une onde mécanique qui se propage par la compression et la distension des molécules du fluide du milieu de propagation qui vibrent autour de leur état d'équilibre. La variation de pression entre la compression et la distension va définir ce que l'on appelle scientifiquement l'intensité du son et plus communément le volume sonore.

On mesure l'intensité du son en newtons / mètre² définit en pascals (Pa= N/m^2). Mais l'échelle que l'on utilise le plus souvent pour parler de l'intensité d'un son est le décibel. C'est une échelle logarithmique basée sur une valeur de pression référence (P_{ref}) qui correspond à la plus petite pression du son détectable par l'oreille humaine. Cette valeur dépend donc du milieu de propagation mais historiquement elle est basée sur celle de l'air qui est de 20 µN/m². On détermine alors l'intensité du son par cette formule :

$$\boxed{\text{dB SPL} = 20 \log_{10} (P_{mesurée}/P_{ref})}$$

SPL = Sound Pressure Level

$P_{mesurée}$= Pression acoustique mesurée

P_{ref}= Pression minimale de référence dans l'air de 20 µPa

On peut parler aussi de Puissance acoustique (W/m²) = (Pa)²

Ainsi une pression d'une onde sonore de 20 µN/m² donnera 20 $\log_{10}$ (1) = 0 dB SPL pour une fréquence 1kHz, correspondant au seuil théorique de l'oreille humaine. La valeur de 120 dB SPL correspond au maximum de détection de l'oreille humaine et se situe dans une zone de douleur et de destruction pour nos oreilles.

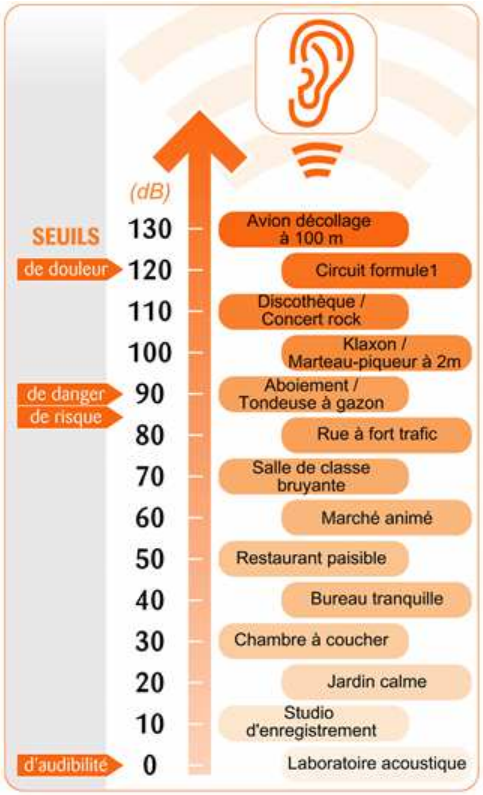

Figure 1. Seuils auditifs et échelle des pressions acoustiques en dB.
d'après Bruitpedia :
https://www.bruitparif.fr/l-echelle-des-decibels/
L'échelle des pressions acoustiques en dB SPL est associée à des environnements représentant approximativement le niveau d'intensité sonore.

Une onde sonore dépend de la compressibilité des molécules du milieu de propagation. En absence de support physique, le son ne se propage pas dans le vide. La célérité d'une onde sonore dépend du milieu de propagation, par exemple elle est de 340 m/s dans l'air et de 1 500 m/s dans l'eau. La célérité dépend aussi d'autres facteurs comme la température, la pression atmosphérique, la densité du support etc.

Les différences de compression des molécules de deux milieux produisent une barrière physique à la propagation de l'onde sonore. L'impédance acoustique d'un milieu se définit par sa résistance à propager une onde sonore et s'exprime en N.sec/m^3. Ainsi l'impédance de l'air est de 400 N.sec/m^3 et celle de l'eau est de 1,5 x10^{6}N.sec/m^3. Une pression d'onde sonore dans l'air aura 3 750 fois moins d'impact à la surface de l'eau, c'est-à-dire que si vous avez la tête sous l'eau vous n'entendrez que très peu les bruits émis très proche de vous

dans l'air, en revanche du fait de la célérité du son dans l'eau vous entendrez des bruits émis de très loin dans l'eau.

L'onde sonore se définit aussi par sa fréquence qui correspond au nombre de périodes de l'onde par unité de temps, définit en Hertz (1 Hz = 1 période/seconde). En musique on parlera de hauteur ou de ton, plus la fréquence est élevée plus la hauteur est grande. Les sons avec des fréquences élevées seront perçues comme des sons plus aigus alors que les sons avec des fréquences basses comme des sons graves.

Le champ auditif humain est compris en 20 Hz et 20 kHz. En dessous de 20 Hz, on appelle cela les infrasons et au-dessus de 20 kHz, des ultrasons. Par comparaison le champ auditif des souris se situe entre 1 kHz et 70 kHz. Pourtant parmi ces fréquences seule une partie est utilisée quotidiennement pour la communication, chez l'Homme cela se situe entre 1 et 3 kHz, on appelle ce champs la zone conversationnelle.

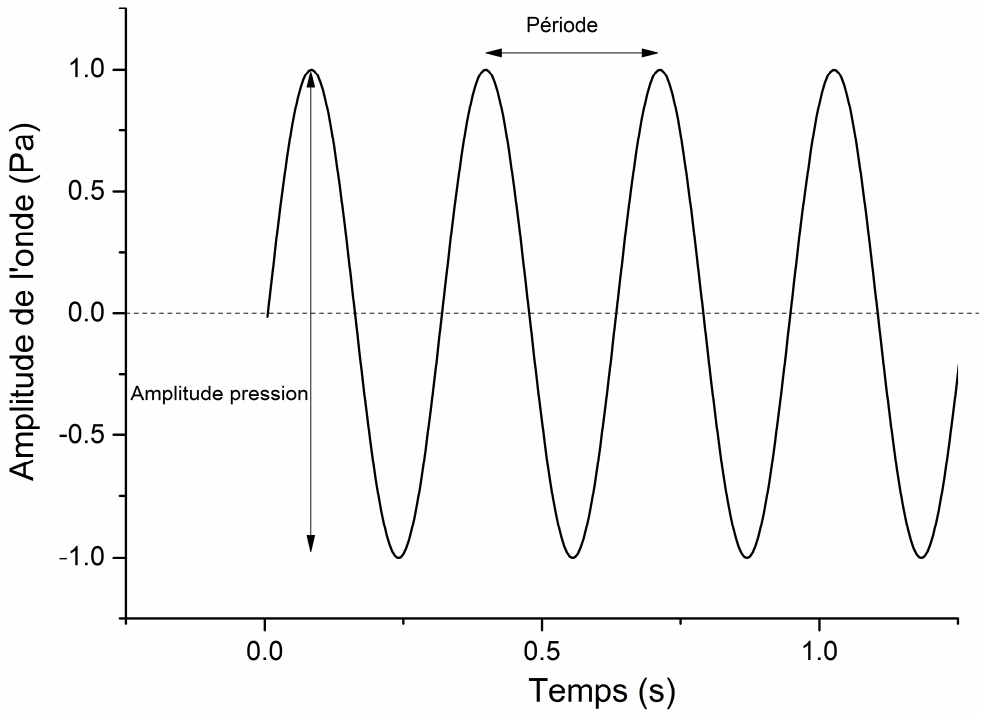

Figure 2. Représentation théorique d'une onde. Une onde se définit par son amplitude, qui correspond à la différence entre le sommet positif de l'onde et le creux négatif, et sa fréquence qui correspond au nombre de périodes T par unité de temps (fréquence par seconde f = 1/T en Hz).

L'intensité sonore est indépendante de sa fréquence au contraire de sa vitesse de propagation. En effet, la vitesse de propagation d'une onde est dépendante de la fréquence vibratoire, on observe que les ondes sonores de basses fréquences se propagent beaucoup plus vite et plus loin que celles de hautes fréquences. Cela s'explique par le fait que les particules se déplacent à une vitesse constante, plus la fréquence augmente plus les particules doivent parcourir de distance pour une même distance parcourue par l'onde.

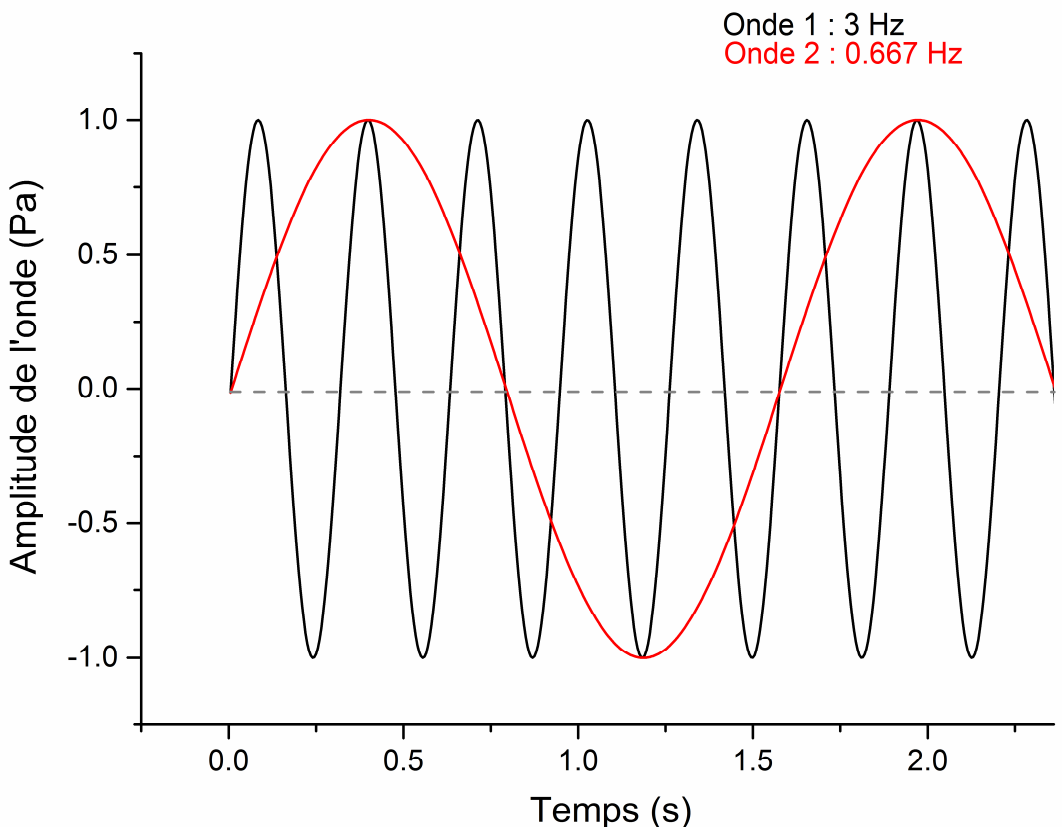

Figure 3. Propagation de deux ondes de deux fréquences différentes. Les ondes 1 et 2 ont la même amplitude (intensité), mais elles ont une fréquence différente. L'onde 1 a une fréquence d'environ 3 Hz et l'onde 2 d'environ 0,667 Hz.

La plupart des sons sont des signaux acoustiques complexes composés de plusieurs ondes sonores additionnées. Pour analyser les sons complexes, on utilise la transformation de Fourier qui permet de décomposer un son complexe en ses fréquences fondamentales et ainsi obtenir ce que l'on appelle le spectre du signal acoustique. Ce spectre nous donne uniquement les fréquences et les intensités des ondes qui composent le son complexe.

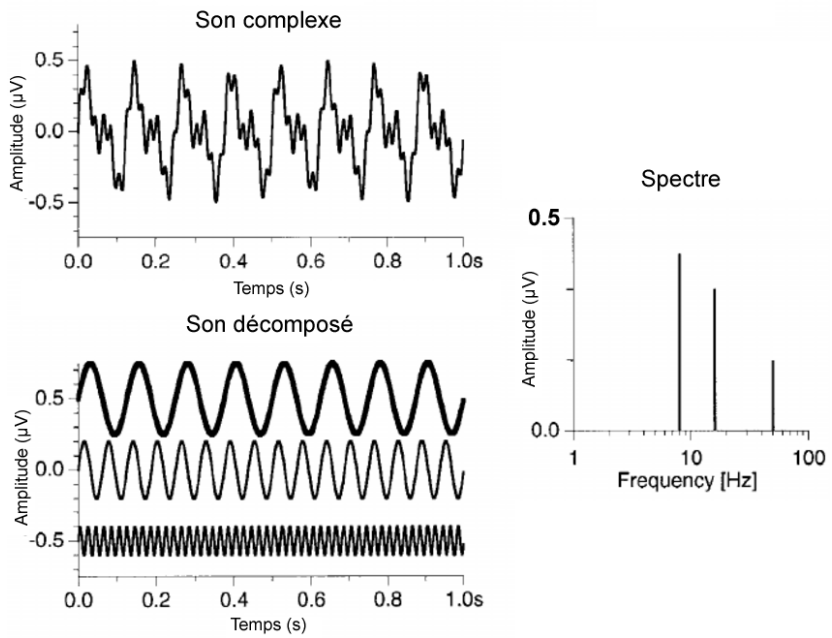

Figure 4. Décomposition d'un son complexe. D'après Bach (Bach and Meigen, 1999). Un son complexe (en haut) est décomposé en ses fréquences fondamentales (en bas) et représenté en spectre après une transformée de Fourrier (à droite).

2. Epidémiologie de la surdité

Selon l'OMS il y a actuellement dans le monde plus de 5% de la population mondiale qui sont atteints de surdité incapacitante soit 430 millions d'adultes et 34 millions d'enfants. Un chiffre qui pourrait doubler d'ici 2050 et atteindre même les 10 % de la population mondiale. Etant donné le rôle essentiel de l'ouïe dans la communication, il a été observé de nombreux impacts de la surdité sur la vie des gens au niveau cognitif (isolement social, solitude, dépression…) mais également au niveau social (accès à l'éducation, à un travail…). C'est donc un enjeu majeur pour le futur qui s'axe principalement sur la prévention et sur le dépistage très précoce des surdités.

3. Dépistage de la surdité chez l'Homme

La surdité se définit par un seuil absolu supérieur à 26 dB (zone fréquence conversationnelle entre 1 et 3 kHz) et se classe en plusieurs catégories : surdité légère (26 à 40 dB), modérée (41 à 55dB), modérément sévère (56 à 70 dB), sévère (71 à 90dB) et profonde (>91dB) (Koffler et al., 2015).

Pour dépister ces surdités, une des méthodes les plus utilisées est la mesure des otoémissions acoustiques (OEAs) correspondants à des émissions acoustiques (échos) de faibles amplitudes produites par la cochlée en réponse à une stimulation sonore (Kemp, 1978). Il existe deux types de test : les otoémissions acoustiques évoquées transitoirement (transient otoacoustic emissions) et les produits de distorsion (Distorstion product otoacoustic emission). Le premier consiste en une stimulation d'un bruit blanc directement dans l'oreille et à l'observation de ces faibles OEAs avec un délai de plusieurs millisecondes. Et le second test consiste en la stimulation simultanée de deux sons purs de fréquences différentes : f_1 et f_2 où $f_1<f_2$ et $f_2/f_1 = 1,2$. L'énergie combinée des deux sons purs va produire de faibles émissions à plusieurs fréquences différentes, les fréquences de produit de distorsion, mais celle qui est le plus souvent mesurée est égale à $f_{DP} = 2f_1-f_2$. En quantifiant l'intensité du son reçu à cette fréquence on peut donc estimer l'activité de la cochlée à capter les sons. Ces méthodes sont rapides, peu invasives et peu coûteuses mais en revanche elles ne permettent pas de détecter toutes les surdités notamment les neuropathies.

Le test des potentiels évoqués auditifs (PEA ou Auditory Brainstem Responses en anglais) est également très utilisé pour le dépistage des surdités. Cette technique permet de mesurer l'activité électrique des voies nerveuses du nerf auditif sortant de la cochlée jusqu'au tronc cérébral via une électrode posée sur le vertex (crâne).

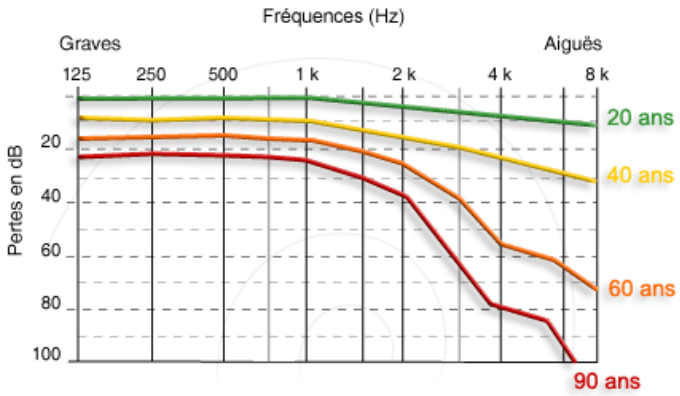

Figure 5. Audiogrammes représentant les pertes auditives moyennes (en dB) d'un individu moyen à différentes fréquences chez l'Homme en fonction de l'âge. D'après : cochlea.eu/exploration-fonctionnelle. Les audiogrammes, d'une même personne, évoluent au cours du temps du fait de la perte auditive liée à l'âge. A 20 ans, on estime l'apogée de la fonction auditive chez l'Homme qui se dégrade ensuite progressivement en impactant préférentiellement les sons de haute fréquence.

Chapitre 2 : Le système auditif chez les mammifères

1. L'oreille externe

Seule partie visible de l'oreille, elle est composée d'une partie cartilagineuse le pavillon auriculaire ou auricule qui donne sur une cavité, la conque, et aboutit sur le conduit auditif externe. L'élasticité et les courbes du pavillon auriculaire ainsi que la résonnance de la cavité formée par la conque permettent d'intensifier la pression au niveau de la membrane tympanique pour augmenter le transfert d'énergie vers l'oreille moyenne. Mais ce n'est pas le seul rôle de l'oreille externe, en effet, il a été observé que la forme particulière du pavillon et de la conque avec leurs courbes et leurs rebords jouent aussi un rôle dans la localisation d'un son. Si un son provient du côté opposé de l'oreille sa trajectoire sera ralentie par ses courbes et ses rebords qui augmenteront le délai de réponse entre les deux oreilles et diminueront son intensité (plus une onde sonore parcourt une distance importante plus elle s'atténue).

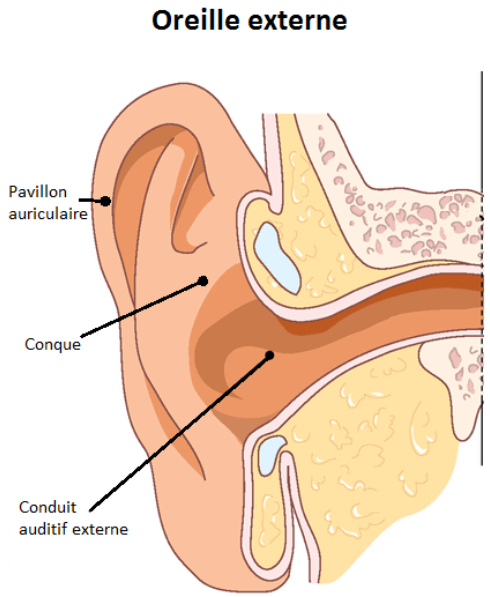

Figure 6. Dessin anatomique de l'oreille externe, d'après Pienkowski (2015)**.** L'oreille externe est composée du pavillon, de la conque et du conduit auditif externe.

2. L'oreille moyenne

Le rôle de l'oreille moyenne est de transmettre l'énergie du son perçue par les vibrations de la membrane tympanique jusqu'à la fenêtre ovale de la cochlée de l'oreille interne. A cet effet l'oreille moyenne dispose de 3 petits osselets appelés marteau, enclume et étrier. L'oreille moyenne joue le rôle important d'adaptateur d'impédance entre le milieu aérien et le milieu aqueux de la cochlée. Il y a un rapport de surface (20 fois) entre la membrane tympanique (60 mm² chez l'Homme) et la membrane de la fenêtre ovale (3,2mm²). De plus, le bras reliant le marteau à l'enclume étant plus grand que le bras reliant l'enclume à l'étrier (2,1 fois plus grand chez l'Homme) permet de créer un effet levier qui augmente également la pression de l'énergie de l'onde perçue sur la fenêtre ovale. Cette architecture permet de compenser en partie la différence d'impédance acoustique entre le milieu aérien extérieur et le milieu aqueux intra-cochléaire. Il est à noter que le marteau et l'étrier sont associés à des petits muscles permettant de contrôler la tension du tympan et de la fenêtre ovale. La contraction de ces muscles réalise ce que l'on appelle le réflexe stapédien qui vise à atténuer le niveau d'intensité des sons transmis à l'oreille interne.

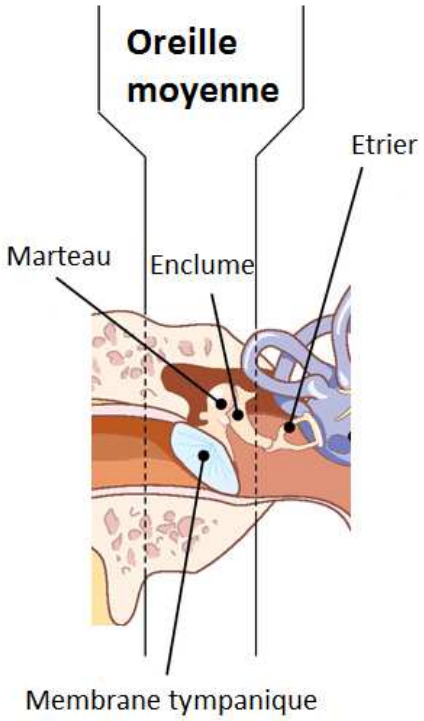

Figure 7. Dessin anatomique de l'oreille moyenne, d'après Pienkowski (2015)**.** On retrouve dans l'oreille moyenne la membrane tympanique associée aux trois osselets : le marteau, l'enclume et l'étrier.

3. L'oreille interne

L'oreille interne renferme les cellules sensorielles du système auditif et vestibulaire. Elle est composée de la cochlée, l'organe de l'ouïe et du vestibule, l'organe de l'équilibre.

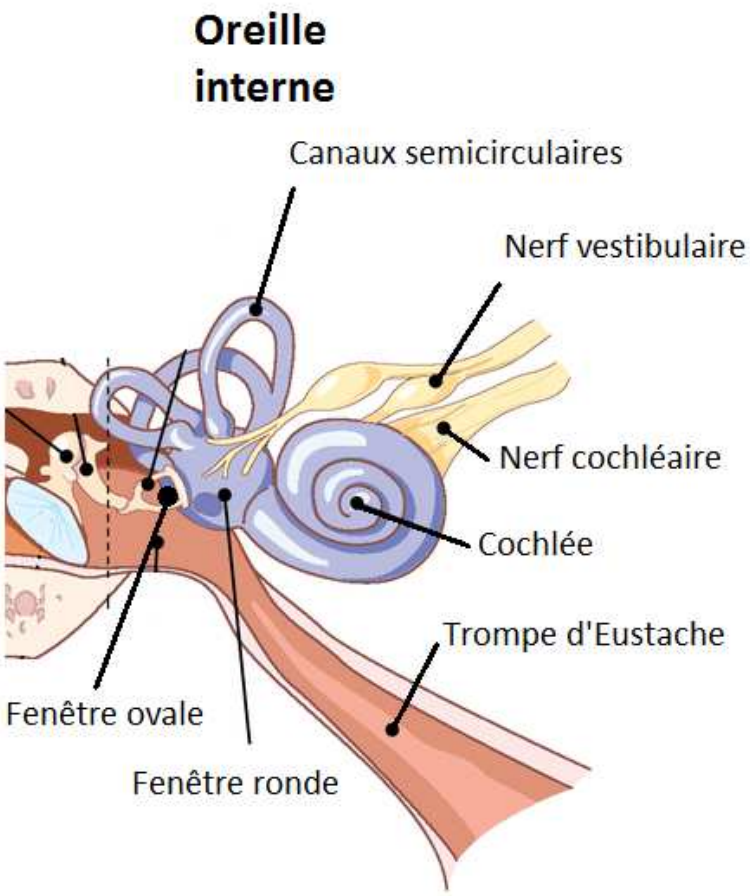

Figure 8. Dessin anatomique de l'oreille interne, d'après Pienkowski (2015)**.** Dans l'oreille interne se trouve la cochlée, l'organe de l'audition, et du vestibule (composée de l'utricule, saccule et des canaux semi-circulaires) qui constitue l'organe de l'équilibre.

A. La cochlée

La cochlée est une cavité osseuse en spirale entourée de la capsule tympanique et encastrée profondément dans l'os temporal ressemblant étrangement à la coquille d'un escargot d'où son nom venant du grec "*kochlias*" signifiant coquillage en spiral, escargot.

Cette cavité est divisée en 3 scalae que l'on appelle aussi canaux ou rampes. Les deux rampes les plus extérieures, la rampe vestibulaire et la rampe tympanique, sont séparées par la rampe cochléaire entre eux tout le long de la spirale.

La rampe vestibulaire et tympanique se rejoignent tout au bout au niveau de l'*hélicotréma*, c'est pourquoi elles contiennent le même fluide que l'on appelle la périlymphe, qui dans sa composition est très similaire à un liquide extracellulaire (riche en Na^+ 140mM et pauvre en K^+ 5mM et Ca^{2+} 1,2mM) et possédant un potentiel plutôt neutre (0mV) (Fettiplace, 2017). La rampe vestibulaire commence au niveau de la fenêtre ovale et comme son nom l'indique communique également avec le vestibule. Alors que la rampe tympanique, elle, commence au niveau de la fenêtre ronde.

La dernière rampe, la rampe cochléaire ou médiane, est complètement isolée du reste de la cochlée. Elle est séparée de la rampe vestibulaire par la membrane de Reissner et de la rampe tympanique par la membrane basilaire. Une des raisons de cet isolement est la composition particulière du fluide qui y circule l'endolymphe, un liquide très riche en K^+ (150mM) et pauvre en Na^+ (1mM) possédant un potentiel positif (+80mV par rapport à la périlymphe) qui fait penser à un liquide intracellulaire. Cette forte concentration en ions K^+ est maintenue activement par la strie vasculaire, riche en pompes ioniques Na/K-ATPase (pour revue voir Ferrary (2007)).

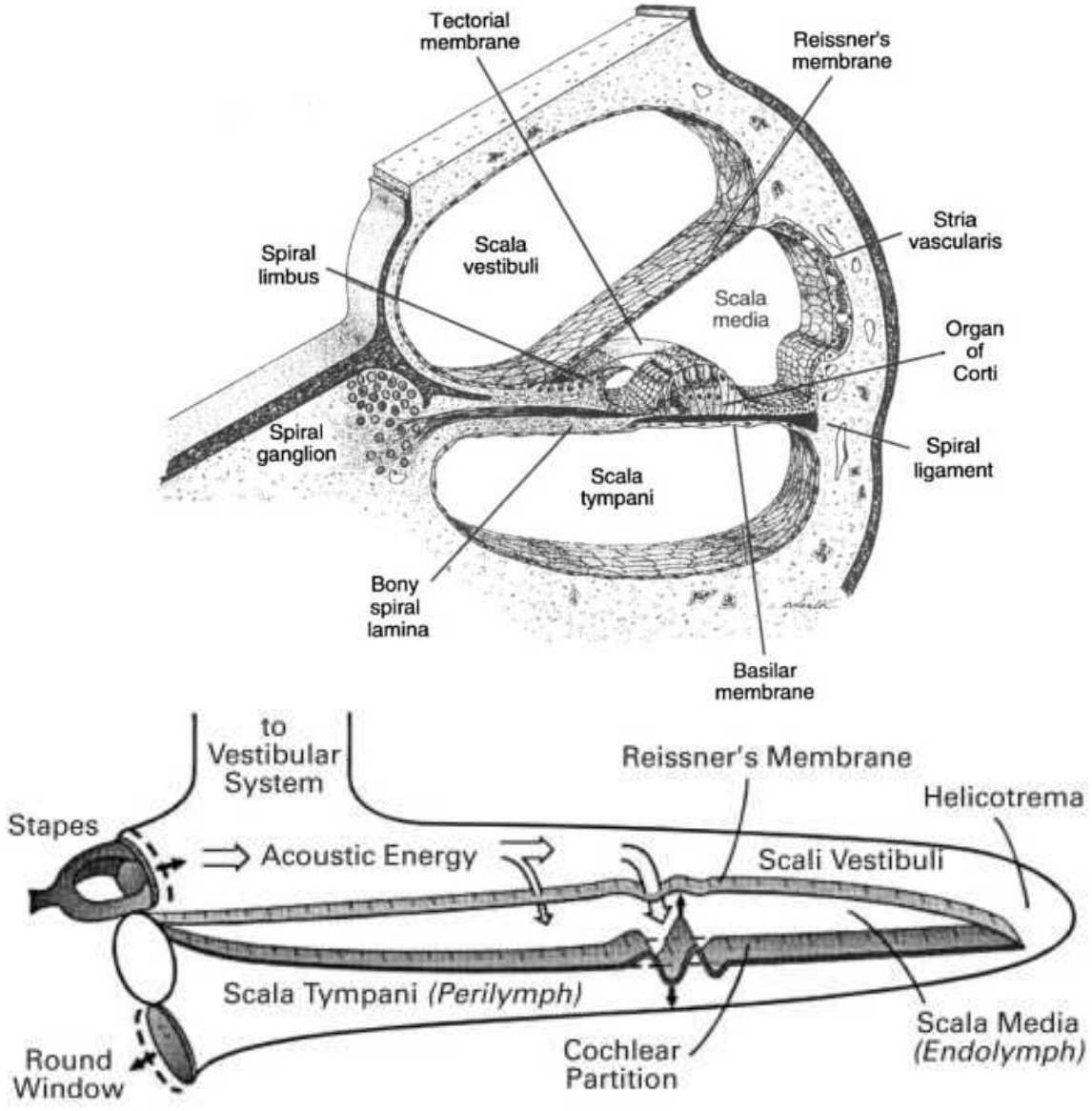

Figure 9. Dessins représentatifs des rampes de la cochlée, d'après Pickles (2013). Le dessin du dessus est une coupe transverse de la cochlée où l'on peut observer les trois rampes qui composent la cochlée. Le dessin en bas représente schématiquement le canal cochléaire ainsi que les rampes vestibulaire et tympanique s'ils étaient complètement déroulés.

Dans cette rampe cochléaire se trouve l'organe de Corti qui repose sur la membrane basilaire. L'organe de Corti est l'épithélium sensoriel qui permet la transduction du son par des cellules mécano-réceptrices : les cellules ciliées. Deux types de cellules ciliées le composent, tout d'abord une rangée de cellules ciliées internes CCI (environ 3 500 chez l'homme et 800 chez la souris), suivi de 3 jusqu'à 5 rangées de cellules ciliées externes CCE (12 000 chez l'homme et 2 500 chez la souris ; (Glueckert et al., 2005)). Les cellules ciliées

sont entourées de cellules de soutien qui ont tout d'abord un rôle structurel pour maintenir en place les cellules ciliées mais aussi elles auraient des rôles fonctionnels sur le maintien de l'homéostasie extracellulaire, la synaptogenèse, la polarité planaire des cellules ciliées et également sur l'élimination et la régénération des cellules ciliées endommagées (Li–dong et al., 2008; Wan et al., 2013). Les cellules de Deiters (ou cellules phalangiennes externes) sont les cellules de soutien qui maintiennent les CCEs dans leur position, elles sont le lien entre la membrane basilaire et les externes, elles joueraient le rôle d'amortisseur des oscillations mécaniques des CCEs (Dulon et al., 1994). Les CCIs, elles, sont maintenues à la membrane basilaire par les cellules bordant des internes du côté médial (Inner border cells) et par les cellules phalangiennes internes du côté latéral (vers les externes), ces cellules joueraient le rôle de cellules gliales captant le glutamate dans la fente synaptique par l'action du transporteur GLAST (Glowatzki et al., 2006). Les cellules du pilier interne et externe séparent les CCIs et les CCEs et créent un espace que l'on appelle le tunnel de Corti. Enfin on peut noter aussi les cellules de Hensen, de Claudius et de Boettcher dont le rôle n'est pas encore bien connu mais bordent le côté latéral des CCEs.

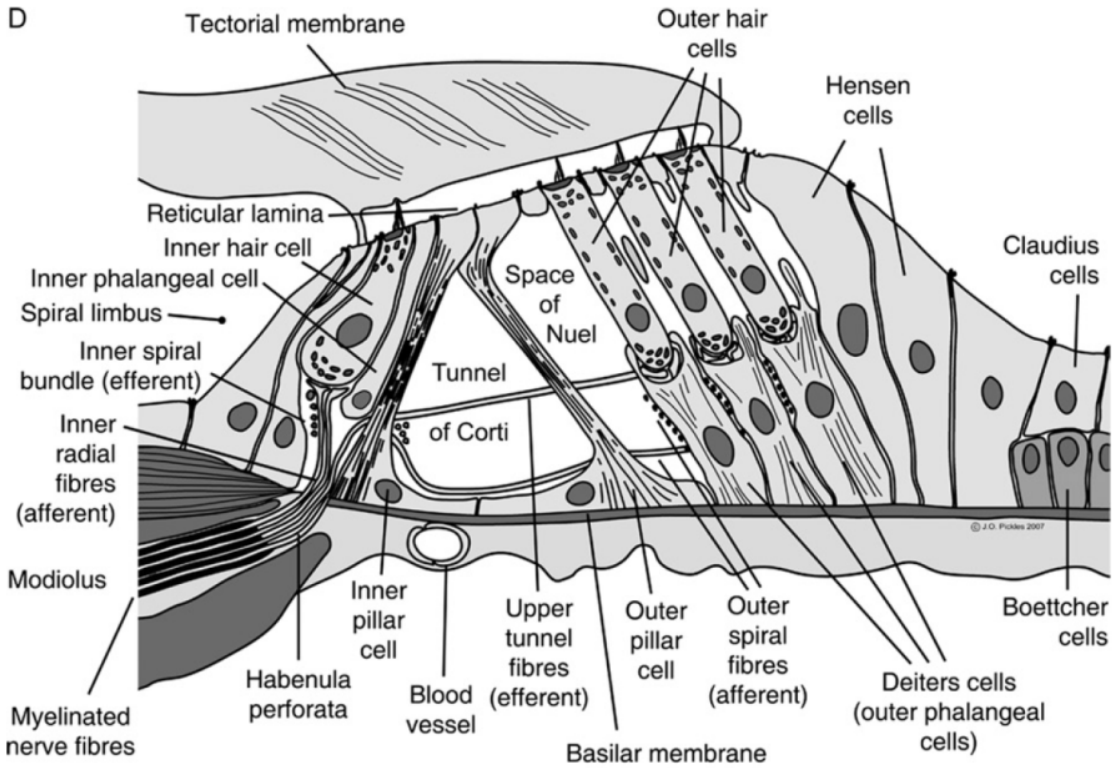

Figure 10. Dessin d'une coupe transverse de l'organe de Corti, d'après Pickles (2013).

Comme leur nom l'indique, les cellules ciliées possèdent des stéréocils au niveau de leur surface apicale. Le mouvement pendulaire ou *déflexion* des stéréocils entraînent l'ouverture de canaux mécano-sensibles permettant la transduction du signal mécanique en signal électrique. Cette transduction mécano-électrique se réalise à la fois au niveau des CCIs et des CCEs mais ce sont les CCIs quasi-exclusivement qui vont réaliser une transmission synaptique vers les fibres afférentes du nerf auditif. Les CCEs ont un rôle d'amplificateur mécanique du signal acoustique (otoémissions) par une transduction secondaire électromécanique utilisant la prestine (Zheng et al., 2000a).

Le mouvement des stéréocils est impulsé par la membrane tectoriale, une structure protéique acellulaire se situant au-dessus des stéréocils. Grâce aux travaux de Georg von Békésy sur la théorie de l'onde propagée cochléaire dans les années 50-60 (récompensé par un prix Nobel en 1961), on sait que l'élasticité de la membrane basilaire varie le long de l'organe de Corti. Elle diminue de la base (hautes fréquences) vers l'apex (basses fréquences). Les ondes traversant la rampe tympanique augmentent d'amplitude le long de la membrane basilaire jusqu'à ce que l'élasticité de celle-ci ne suffise plus à supporter leur fréquence et diminuent drastiquement ensuite ; expliquant l'encodage des sons à hautes fréquences à la base de la cochlée et les basses fréquences à l'apex. Cependant, les seules propriétés mécaniques de la membrane basilaire ne suffisent pas à expliquer la finesse des courbes d'accords neurales et mécaniques enregistrées *in vivo*. C'est l'action d'amplification électromécanique des CCEs tout le long de la membrane basilaires (agissant comme des résonateurs en série) qui donne toute la finesse résolutive des courbes d'accords (pour revue voir Pickles (2013)).

B. Cellules ciliées internes

Les cellules ciliées internes ont une forme de poire (piriforme), elles ont une longueur d'une trentaine de micromètres et une largeur de 10 µm de diamètre au maximum, ces dimensions étant quasi constantes tout le long de la membrane basilaire. Elles encodent la fréquence et l'intensité du signal acoustique en signal électrique au niveau des synapses à ruban associées au fibres afférentes du nerf auditif. Elles ont 3 rangées de stéréocils plutôt linéaires encrées dans la plaque cuticulaire. Ces trois rangées présentent des cils qui

augmentent de taille en escalier de l'intérieur (côté neural) vers le côté extérieur (latéral). Ces stéréocils ont une forme en U aplati. A leur pôle apical, coté plaque cuticulaire, les CCIs ont un diamètre plus resserré probablement dû à la tension mécanique des jonctions serrées et adhérentes entre les CCIs et leurs cellules de soutien. Ces jonctions assurent une étanchéité entre périlymphe et endolymphe mais aussi une cohésion mécanique. Bizarrement, le corps cellulaire piriforme des CCIs a un côté arrondi ou gonflé (relâché) du côté neural et plutôt rectiligne ou tendu du côté pilier. Cette asymétrie pourrait s'expliquer par la tension physique importante des piliers formant le tunnel de Corti. Par ailleurs, une étude récente met en évidence un couplage électrique possible entre les CCIs par un mécanisme de couplage membranaire basolatéral qui permet aussi la diffusion de macromolécules entre CCIs (Jean et al., 2020). Ce couplage membranaire, dont les bases moléculaires restent encore à définir, pourrait permettre aux CCIs de fonctionner en syncytium.

Les zones actives (ZA) des CCIs, faisant face aux boutons synaptiques des fibres afférents du nerf auditif, présentent des structures présynaptiques très particulières, qui apparaissent denses aux électrons en microscopie électronique et que l'on appelle rubans. Ces rubans permettent de concentrer les vésicules synaptiques glutamatergiques au niveau de la ZA pour faciliter et fluidifier leur trafic vers leur site de fusion. Il y a entre 6 et 20 synapses afférentes par CCI, ce chiffre variant selon la tonotopie et l'espèce. En effet, chez la souris dans les fréquences les mieux perçues (12-32 kHz, milieu-apical), il y a le plus grand nombre de rubans et ce nombre diminue en courbe en cloche vers les plus basses et les plus hautes fréquences (Meyer et al., 2009).

C. Cellules ciliées externes

Les cellules ciliées externes (CCEs) ont une forme de tube cylindrique de diamètre 6 à 7 µm et dont la longueur augmente de la base vers l'apex de la cochlée de 25 µm environ à 45 µm chez la souris. Elles possèdent également 3 rangées de stéréocils organisées en V ou W mais contrairement aux CCIs elles ne transmettent pas l'information acoustique vers les centres nerveux car elles ne forment quasiment pas de connexions synaptiques avec les fibres afférentes de type I du nerf auditif. Elles sont connectées par des fibres afférentes de type II qui aurait un rôle dans la nociception auditive (Liu et al., 2015).

Les CCEs, grâce à leurs propriétés électromécaniques permettent d'amplifier le signal acoustique incident et jouent le rôle de résonateurs en série. Pour remplir cette fonction, les CCEs expriment le long de leur membrane basolatérale une protéine moteur piézoélectrique unique, la prestine (Zheng et al., 2000a). Ce moteur est une protéine transmembranaire qui est encodée par le gène SLC26A5 et apparentée à un transporteur d'anions. En réponse à des changements de voltage transmembranaire suite à la déflection des stéréocils, la prestine change de conformation et produit une diminution de l'aire de la membrane basolatérale, cela se traduit par une réduction de la taille globale de la CCE lors d'une dépolarisation du potentiel de membrane et, en revanche, une augmentation de la taille globale de la CCE lors d'une hyperpolarisation (Holley et al., 1992; Matsumoto and Kalinec, 2005). Ce processus est à la base des otoémissions acoustiques. La membrane basolatérale des CCEs contient aussi un cortex d'actin-F capable de modifier sa tension mécanique sous l'action du Ca^{2+} intracellulaire, correspondant à un rétrocontrôle négatif de l'électromotilité prestine-dépendante (Dulon et al., 1990; Dulon and Schacht, 1992).

Il est à noter que les CCEs sont essentiellement contactées par des fibres efférentes cholinergiques issues de l'olive supérieure médiane qui contrôlerait leur activité mécanique. Les CCEs expriment des récepteurs cholinergiques très particuliers de type nicotinique (nAChRs) composés des sous-unités α9-α10 (Elgoyhen et al., 1994; Elgoyhen et al., 2001) perméables aux ions Ca^{2+} (Blanchet et al., 1996).

D. Le vestibule

Le vestibule est constitué de l'utricule et du saccule mais dans le système vestibulaire on peut y rajouter aussi les 3 canaux semi-circulaires. Tout comme la cochlée, le vestibule possède aussi des cellules ciliées divisées en 2 types. Le type I, qui sont des cellules en forme d'amphore entourées par une terminaison nerveuse afférente en calice et le type II qui sont des cellules plutôt cylindriques avec des boutons synaptiques des fibres nerveuses afférentes. Le système vestibulaire permet de détecter l'orientation de la tête dans l'espace grâce aux mouvements liquidiens des canaux semi-circulaires qui sont disposés dans les trois plans de l'espace et communiquent avec l'épithélium sensoriel où reposent les cellules ciliées, appelé la macula, de l'utricule et du saccule. La macula de l'utricule permet de détecter l'orientation horizontale et celle du saccule l'orientation verticale. L'intérieur de la

macula est recouvert d'une couche gélatineuse parsemés de petits cristaux de carbonate de calcium ($CaCO_3$) que l'on appelle otolithes ou organes otolithiques permettant d'appréhender l'inertie, la sensation d'accélération linéaire de la tête (Khan and Chang, 2013).

E. Le nerf auditif

1. Voie afférente

Les fibres afférentes nerveuses provenant du nerf auditif sont localisées au cœur de la cochlée dans le modiolus. Ce sont des neurones majoritairement bipolaires avec leur corps dans le ganglion spiral projetant leur dendrite vers les cellules ciliées et leur axone vers les cellules des noyaux cochléaires dorsaux et ventraux. Il y a environ 30 000 fibres en moyenne chez l'homme et pas loin de 16 000 fibres chez les rongeurs (Nadol, 1988). 90 à 95% des fibres afférentes sont de type I. Chaque fibre afférente de type I est spécifiquement associée à une CCI ce qui renforce la tonotopie le long de la cochlée. Ce sont des fibres myélinisées épaisses qui peuvent avoir une variabilité de réponse en intensité et vélocité permettant de transmettre différents aspects du stimulus acoustique comme le timing, l'intensité et la fréquence qui le composent (Fuchs and Glowatzki, 2015). Les pics de réponses dus au signal acoustique se superposent à une activité spontanée des fibres générée par des potentiels excitateurs postsynaptiques (EPSPs), cette activité spontanée est très hétérogène selon les fibres. Il a été décrit chez le chat que les petites fibres afférentes ont une faible activité spontanée mais un haut seuil d'activation et sont souvent associées à de gros rubans présynaptiques que l'on retrouve côté modiolus, à l'inverse des grosses afférences qui ont une forte activité spontanée et de petits seuils d'activation et sont associées elles aux petits rubans présynaptiques côté latéral (Liberman, 1978; 1982b; a). Ces fibres afférentes innervent majoritairement les CCI du côté où elles se projettent c'est-à-dire le côté modiolus (66%) et minoritairement du côté latéral (33%). Elles possèdent principalement des récepteurs AMPA qui sont sensibles au glutamate relargué par les vésicules synaptiques des CCIs (Puel, 1995). L'encodage de l'intensité acoustique se réaliserait par un relargage synchrone d'un nombre croissant de vésicules synaptiques, c'est ce qu'on appelle la théorie multivésiculaire (Fuchs and Glowatzki, 2015). Ce relargage

multivésiculaire augmente avec la probabilité d'ouverture des canaux calciques dépendants du voltage et implique comme calcium senseur l'otoferline (Vincent et al., 2018).

Le 5 à 10% des fibres restantes sont de type II, elles proviennent également du ganglion spiral mais en passant par le tunnel de Corti font un virage vers la base de la cochlée pour innerver quelques dizaines de micromètres plus loin les CCEs. Elles sont de fines fibres non-myélinisées très faiblement activée et peu sensible au son. On suppose qu'elles auraient un rôle de nocicepteurs et qu'elles ne s'activeraient que lorsque les CCE seraient endommagées en captant de l'ATP via des récepteurs purinergiques P2X et P2Y (Liu et al., 2015).

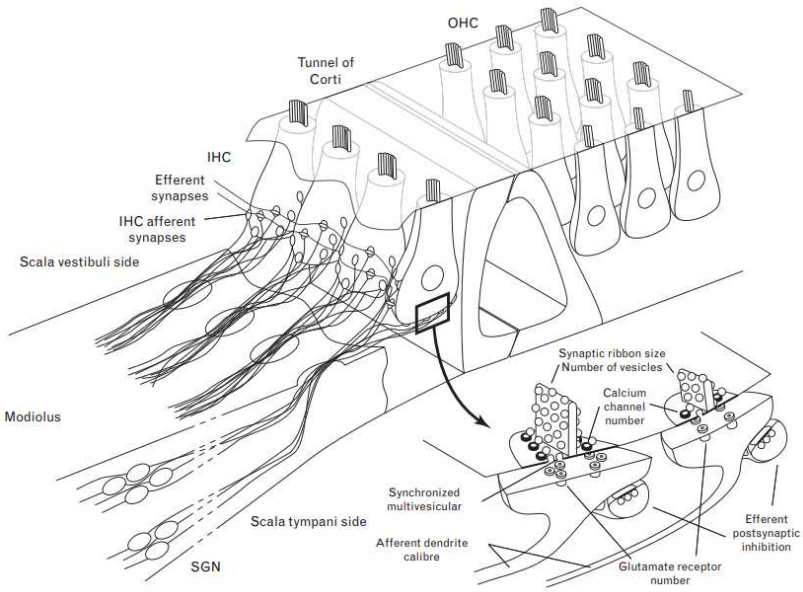

Figure 11. Représentation schématique de l'innervation de l'organe de Corti, d'après Meyer and Moser (2010)**.** En bas à droite, le dessin représente une fibre avec une faible activité spontanée et un seuil élevé associée avec un gros ruban du côté du modiolus (côté interne) et du côté latéral externe de la CCI une fibre afférente avec une forte activité spontanée et un seuil d'activation bas associée à un petit ruban synaptique. On peut aussi observer les fibres efférentes issues de l'olive latérale supérieure régulant l'activité des boutons synaptiques afférents (pour revue voir Nouvian et al. (2015)).

2. Voie efférente

Globalement, il existe deux types de fibres efférentes : celles issus de l'olive médiane supérieure qui projettent sur les CCEs et celles issues de l'olive latérale supérieure qui contactent les boutons afférents synaptiques sous les CCIs. Le système efférent médian permet un rétrocontrôle cholinergique de l'amplification cochléaire des CCEs. Les fibres efférentes latérales contrôle l'activité spontanée et évoquée des fibres afférentes par une voie dopaminergique et cholinergique (voir revue Eybalin et al. (1993) ;(Ruel et al., 2007; Elgoyhen and Katz, 2012)).

Chapitre 3 : La transduction du son

A. La mécano-transduction

1. Les stéréocils

Les stéréocils sont des tubes de 200 nm de diamètre pour les CCEs et presque le double pour les CCIs, composés d'un réseau organisé de filaments d'actine dense. Ces filaments d'actine sont reliés entre eux par des protéines de pont, dont la Plastine-1, la Fascine-1 et l'Espine, qui permettent une organisation hexagonale dense de ces microfilaments à l'intérieur du stéréocil (Zheng et al., 2000b; Shin et al., 2010). Les stéréocils forment 3 rangées en escalier dont les stéréocils les plus hauts sont orientés vers le côté latéral externe de la cochlée. Les stéréocils d'une même rangée sont de taille identique et orientés parallèlement suggérant que leur hauteur et leur orientation planaire sont extrêmement bien contrôlées et régulées (Ezan and Montcouquiol, 2014). Plusieurs protéines ont été identifié comme acteur de ce contrôle dont les protéines EPS8, Myosine XVa et la whirline présentes en abondance au bout apical des stéréocils et semblent toutes trois requises pour une taille normale des stéréocils (Belyantseva et al., 2005; Hertzog et al., 2010; Manor et al., 2011; McGrath et al., 2017). Pour la polarité planaire des stéréocils des cellules ciliées, les protéines Vangl2 and Scrb1 sont essentielles (Montcouquiol et al., 2003).

Ces stéréocils s'ancrent à la partie apicale des CCIs et CCEs dans la plaque cuticulaire. Cette plaque cuticulaire est un maillage de filaments d'actine dense également composé de protéines de structure comme la tropomyosine, l'α-actinine, certaines myosines, la fimbrine, la profiline (Goodyear RJ et al., 2006) et notamment la protéine TRIOBP qui permet l'entremêlement des filaments d'actine (Kitajiri et al., 2010).

Ces stéréocils sont reliés entre eux par des filaments extracellulaires d'environ 150 nm de longueur et 10 nm de diamètre que l'on appelle « Tip-links » (Pickles et al., 1984). Ils sont formés par des protéines dimériques « d'échafaudage » la cadhérine-23 et la protocadhérine-15 (Kazmierczak et al., 2007). La partie haute du « tip-link » composée par la cadhérine-23 qui vient s'ancrer dans le stéréocil supérieur à un complexe protéique formé par l'harmonine-b, la myosine-VIIa et Sans (Grati and Kachar, 2011). Et la partie basse du « tip-link » formée par le dimère de protocadhérine-15 vient s'ancrer au bout apical du

stéréocils inférieur grâce notamment à deux protéines TMIE et LHFPL5 (anciennement le complexe TMHS) et à une protéine fixant le calcium CIB2 (Xiong et al., 2012; Zhao et al., 2014).

La membrane tectoriale est une structure acellulaire essentielle à la déflection des stéréocils, elle est composée d'un réseau dense de fibres de collagène intégré dans une matrice de glycoprotéines comme la tectorine-α (Richardson et al., 1987; Richardson et al., 2008). Comme démontré pour la première fois chez les amphibiens, la déflection excitatrice des stéréocils se fait dans la sens du plus petit vers le plus haut (Hudspeth and Corey, 1977). Ces « tip-links » interciliaires apicaux sont essentiels à la fonction auditive et vestibulaire car ils permettent par une augmentation de leur tension l'ouverture des canaux de mécano-électrique de transduction (« mechanoelectrical transducer channels » MET). A l'inverse, la perte de tension de ces « tip-links » entraînerait leur fermeture.

Il y a une grande différence de potentiel, de 130 à 150 mV environ, entre l'endolymphe extracellulaire (+80 mV) et le cytoplasme intracellulaire des CCIs (-50 à -70 mV ; (Crawford et al., 1991; Fettiplace, 2017)). Cela crée une immense force d'attraction des cations présents dans l'endolymphe, notamment les ions K^+, qui passeront de manière passive lors de l'ouverture des MET vers l'intérieur des CCIs. L'entrée transitoire du K^+ pendant les phases d'alternance entre ouverture et fermeture des canaux de MET lors de la stimulation sonore génère un courant alternatif que l'on peut enregistrer en disposant une électrode sur la fenêtre ronde de la cochlée (A.C ou potentiel microphonique). L'entrée cumulative et soutenue de K^+ peut aussi dépolariser durablement les cellules ciliées, surtout aux fortes intensités acoustiques et hautes fréquences, et ainsi crée un courant continu (D.C or *summating potential*, potentiel de sommation). Parmi les cations entrant dans les cellules ciliées, il y aurait aussi du Ca^{2+} qui activerait les myosines présentes dans les stéréocils et participerait ainsi à l'adaptation de la tension des « tips-links » et donc la fermeture des canaux de MET.

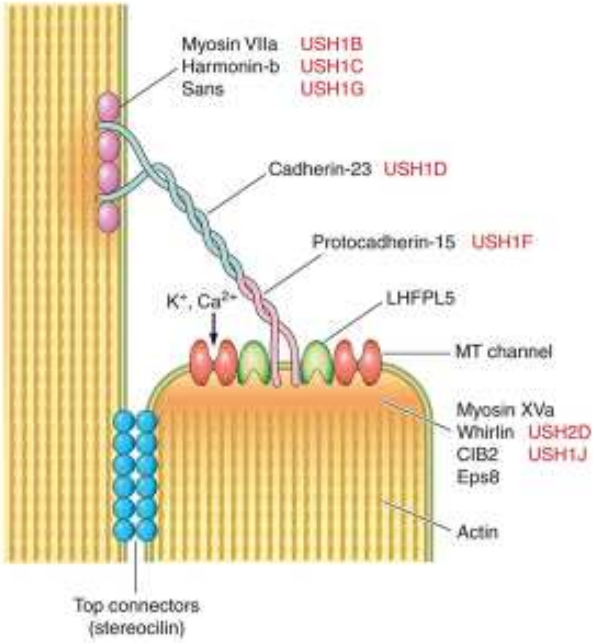

Figure 12. Représentation schématique de l'association mécanique de la partie apicale d'un stéréocil avec son stéréocil adjacent supérieur via le "tip-link", d'après Fettiplace and Kim (2014)**.**
Le "tip-link" est formé par l'association d'un dimère de cadhérine-23 et d'un dimère de protocadhérine-15. Le dimère de cadhérine-23 vient s'ancrer au niveau du stéréocil supérieur dans une densité formée par un complexe formée par la myosine 7a, l'harmonine-b et la protéine sans. Le dimère de protocadhérine-15 s'ancre dans la membrane de la partie apicale du stéréocil inférieur par la protéine LHFPL5 associé aux canaux MET (TMC1/TMC2).

2. Les canaux de mécano-transduction

La fonction de ces canaux est plutôt bien connue mais la nature de ceux-ci beaucoup moins. En effet initialement, la famille des canaux TRP ("Transient Receptor Potential channels") a été découvert dans la fonction visuelle de la drosophile à partir d'expériences de mutations aléatoire. De nombreuses études chez le *zebrafish* (poisson-zèbre) et la souris en faisaient de sérieux candidats pour être les canaux de MET (Sidi et al., 2003; Corey et al., 2004). Cependant le "knock-out" de TRPA1 chez la souris n'altère pas la mécano-transduction des cellules ciliées (Kwan et al., 2006). Malgré ces premiers résultats contradictoires, il est tout de même fort probable que ces canaux partagent de nombreux points communs avec la famille des TRP. En effet, quelques propriétés de ces canaux ont déjà bien été décrites. On sait qu'il y aurait environ 200 canaux de MET par cellule (soit environ 1 à 2 canaux par stéréocils) et que ces canaux ont une impressionnante conductance d'environ 100 pS alors que les canaux cationiques classiques avoisinent les 30 pS comme par

exemple les récepteurs à l'acétylcholine (Crawford et al., 1991; Geleoc et al., 1997; Beurg et al., 2006).

Récemment deux nouveaux candidats sérieux ont été découvert, il s'agirait des protéines TMC1/TMC2 ("Transmembrane channel-like protein"), des canaux possédants entre six et huit domaines transmembranaires très similaires aux sous-unités alpha des canaux potassiques. Il existe plusieurs éléments qui appuient cette hypothèse. Tout d'abord TMC1/TMC2 sont localisées au bout des stéréocils (Kurima et al., 2015; Mahendrasingam and Furness, 2019). Des mutations récessives sur *TMC1* produisent des surdités modérées à sévères DFNB7/11 chez l'Homme (Imtiaz et al., 2016). Chez la souris le knock-out du gène *Tmc1* abolit complètement les courants des canaux MET lors du développement et aboutit à une surdité profonde et une dégénérescence progressive des cellules ciliées à l'âge adulte des souris (Kawashima et al., 2011). De plus, de nombreuses mutations sur le gène *Tmc1* altèrent considérablement la conductance des canaux de MET (Kim et al., 2013; Pan et al., 2013). Les canaux TMC1/TMC2 interagissent directement avec la protéine TMIE qui modulerait l'ouverture des canaux et avec CIB2 qui fixerait ces canaux au bout apical des stéréocils grâce à leur interaction avec la protéine de structure Ankyrine qui se fixe sur le réseau dense des filaments d'actine. Cependant, il semblerait que TMC1/TMC2 n'interagiraient pas directement avec les dimères de protocadhérine-15. Une nouvelle hypothèse propose que l'étirement des "tip-links" entraînerait une déformation de la membrane apicale des stéréocils créant une déformation de la conformation des canaux de MET présents sur cette membrane contrainte par l'étirement et leurs attaches au réseau de filaments d'actine. Ce changement dans la conformation des canaux de MET permettrait leur ouverture (voir figure et revue Zheng and Holt (2021)).

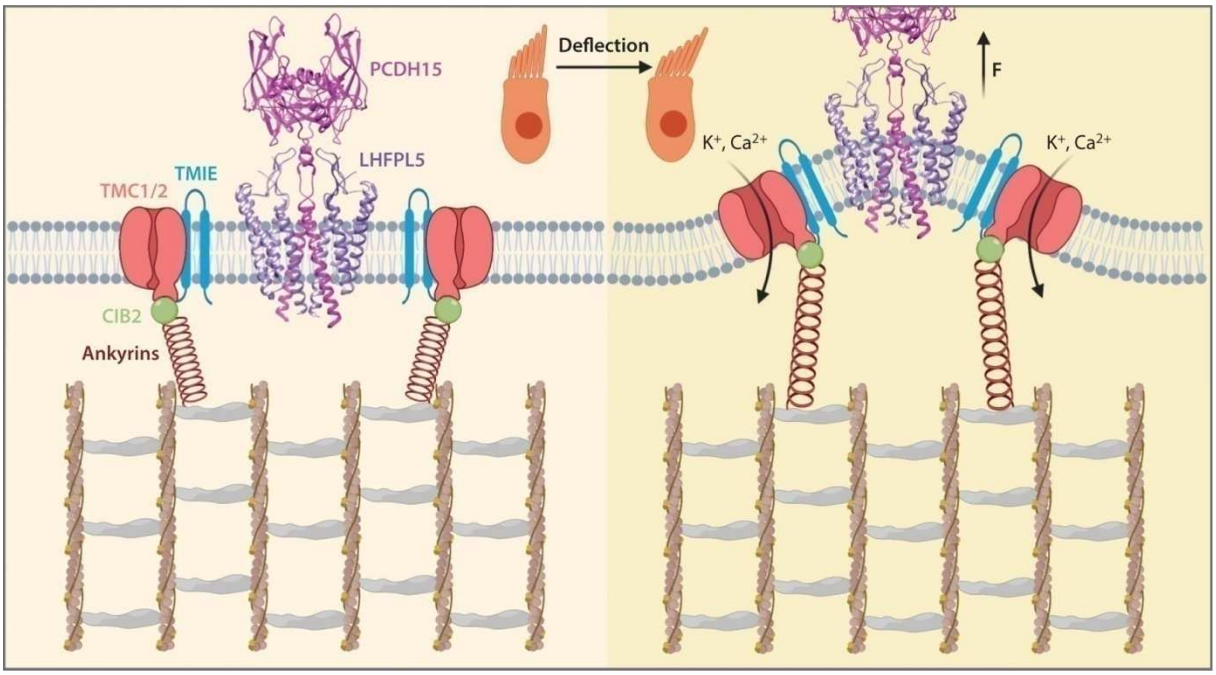

Figure 13. Représentation schématique de l'hypothèse expliquant l'ouverture des canaux MET (TMC1/TMC2) via l'étirement du "tip-link", entraînant une déformation de la membrane plasmique apicale du stéréocil, d'après Zheng et Holt, 2021.Les canaux de MET en rouge sont incrustés dans la membrane plasmique des stéréocils. Ils sont associés avec la protéine TMIE et la protéine CIB2 qui via l'ankyrine leur permettent d'être liés directement avec le réseau dense des filaments d'actine du stéréocil. La contrainte physique exercé par l'étirement des "tip-links" sur la membrane plasmique apicale des stéréocils permettrait l'ouverture de ces canaux de MET et le passage des ions K^+ et Ca^{2+}.

B. Les synapses à ruban

1. Le ruban

Les synapses à ruban, que l'on trouve essentiellement au niveau des CCIs, sont des synapses excitatrices glutamatergiques particulières car elles possèdent une structure anatomique ovoïde en ruban ancrée dans leur zone active (ZA) présynaptique. À la différence des synapses centrales qui encodent un signal binaire (numérique) de même nature en pré- et post-synapse (potentiels d'actions), les synapses à ruban ont la particularité de devoir encoder un signal analogique (potentiel microphonique ou potentiel récepteur gradué et accordé à la fréquence et à l'intensité de la stimulation acoustique) en impulsions électriques au niveau des fibres nerveuses du nerf auditif (exprimé en fréquences de potentiels d'action et avec un *phase-locking* jusqu'au kHz).

En microscopie électronique, cette structure apparait comme dense aux électrons, décorée par des dizaines de vésicules synaptiques. Ces rubans présynaptiques sont retrouvés dans d'autres cellules sensorielles comme par exemple les photorécepteurs de la rétine, les cellules ciliées de la ligne latéral des poissons (*zebrafish*) et aussi les cellules des glandes pinéales de rat (Spiwoks-Becker et al., 2008; Nicolson, 2015; Moser et al., 2020). Les rubans permettent ainsi d'attacher et de concentrer les vésicules synaptiques dans la ZA de la synapse formant un "halo" de vésicules (Glowatzki and Fuchs, 2002). Cette organisation particulière de la synapse lui permet une exocytose infatigable avec une cinétique très rapide (de l'ordre de la milliseconde, en kHz) permettant ainsi une grande précision temporelle (Jean et al., 2018). Chaque ruban des CCI est associé à une terminaison nerveuse postsynaptique issue des afférences des neurones de type I du ganglion spiral. Les CCI possèdent entre 6 et 20 synapses à ruban selon leur localisation tonotopique dans l'organe de corti (voir figure 14 :Meyer et al. (2009)).

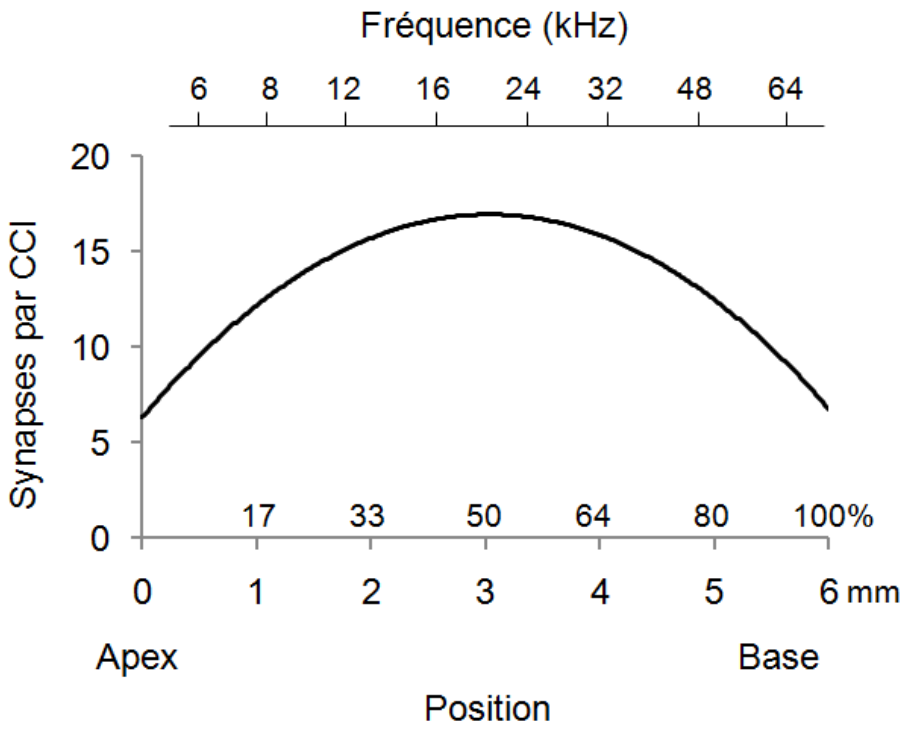

Figure 14. Représentation de la relation entre la distance à partir de l'apex de la cochlée et le nombre moyen de synapses par CCI chez les souris P30 de lignée C57BL/6J, d'après l'étude de Meyer et al. (2009). On observe dans les CCIs de souris P30 C57BL/6J une distribution parabolique du nombre de synapses le long de la cochlée et de l'organe de Corti, allant d'environ 5-6 synapses dans les extrémités jusqu'à une vingtaine dans la partie apicale-milieu de l'organe de corti (entre 2 et 4 mm depuis l'apex). Cette distribution est corrélée avec le cochléogramme de ces mêmes souris, suggérant que la zone des CCI possédant le plus grand nombre de synapses correspondrait environ aux fréquences comprises entre 12 et 32 kHz.

Les fibres afférentes de type I sont généralement classées en trois catégories selon leur activité spontanée et leur seuil de variation de décharge par stimulation acoustique (Liberman, 1978; Taberner and Liberman, 2005). Les fibres bas seuils (haute activité spontanée) ont un large diamètre et présentent un bouton synaptique riche en mitochondries et faisant face à un ruban de petite taille. Ces fibres bas seuils sont situées du côté latéral (abneural ou pilier) des CCIs. Enfin, les fibres à seuils intermédiaires et à haut seuils, contactant des rubans de plus grosse taille, sont les plus nombreuses et sont situées du côté du modiolus (neural ; (Liberman, 1978)).

Le ruban se compose d'un empilement de protéine ribeye encodée par le gène *CtBP2*, un gène qui code pour la protéine CtBP2 qui est ubiquitaire et pour ribeye exprimé uniquement dans les cellules sensorielles. Ribeye est formé d'un domaine A (Ribeye-A) en N-terminal et un domaine B (Ribeye-B) en C-terminal. Le domaine Ribeye-A posséderait plusieurs sites d'interactions avec les autres domaines Ribeye-A et permettrait l'empilement des protéines ribeye. Le domaine Ribeye-B, lui, aurait des interactions avec notamment le NADH qui inhiberait l'empilement des ribeye en se fixant dessus. Le domaine Ribeye-B aurait aussi des interactions direct ou indirect avec les vésicules synaptiques, ce serait lui qui permettrait leur fixation au ruban (Schmitz et al., 2000; Wichmann and Moser, 2015).
Le domaine B de ribeye interagit aussi avec deux protéines de structure appelé bassoon et Piccolo (Dick et al., 2001). Ce sont ces deux protéines qui ancrent vraiment le ruban au niveau de la zone active. Le ruban semble indispensable structurellement à cette synapse et pourtant dans des modèles de souris avec un « knock-out » du gène *Ribeye/CtBP2* la formation des synapses reste normale et les souris n'ont qu'une faible surdité (Becker et al., 2018). Cependant le nombre de vésicules présentes à la ZA présynaptique est largement réduit ainsi que l'exocytose en réponse à des stimulations brèves. Le rôle exact du ruban reste encore un mystère mais l'étude de mutations sur la protéine a permis de proposer quelques hypothèses. Tout d'abord, de par sa présence au niveau de la ZA, le ruban permet le recrutement et la concentration des vésicules synaptiques à cet endroit, et donc facilite la diffusion et l'attachement des vésicules à la membrane de la ZA. Il permet d'avoir un regroupement important de vésicules synaptiques prêt à une fusion rapide que l'on appelle RRP (Readily Releasable Pool of synaptic vesicles) essentiel à la précision temporelle du signal de transmission (Frank et al., 2010; Snellman et al., 2011; Graydon et al., 2014). Le ruban permet également de concentrer les canaux calciques à la ZA et crée une sorte de

barrière physique contre la diffusion de Ca^{2+}. L'augmentation de la concentration de Ca^{2+} localement au niveau de cette ZA permet de synchroniser la fusion multiple des vésicules (Graydon et al., 2011; Vincent et al., 2018). C'est la gradation de cette fusion multivésiculaire qui permettrait d'encoder l'intensité du signal acoustique. Une théorie alternative univésiculaire propose une variation de la taille du pore des vésicules fusionnées pour réaliser cet encodage (Chapochnikov et al., 2014). Il est probable qu'un mix de ces deux processus participe à cette fonction synaptique.

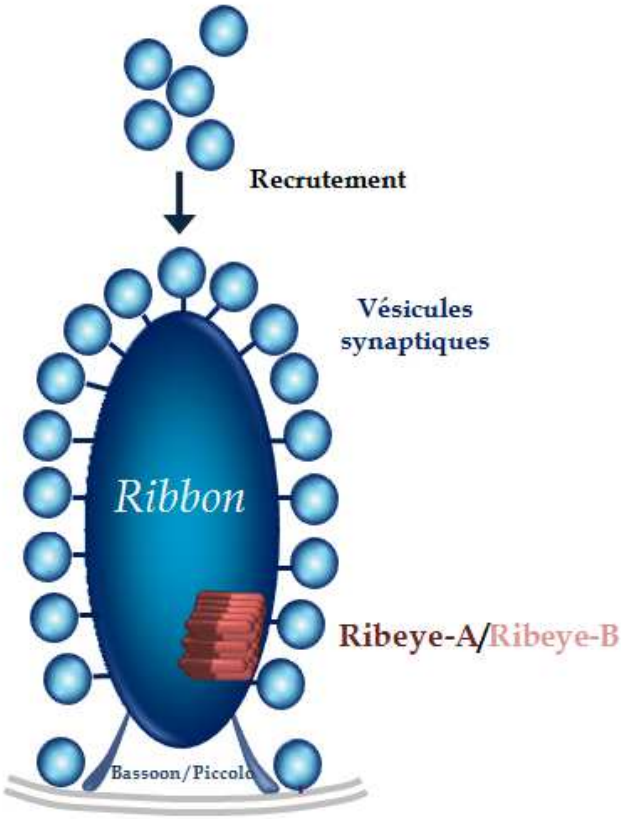

Figure 15. Représentation schématique d'un ruban synaptique inspirée de M. Tertrais et al. 2018 Les protéines ribeye sont empilées en escalier formant ainsi la structure du ruban synaptique. La partie Ribeye-A est impliquée principalement dans cet empilement alors que la partie Ribeye-B permet les liaisons du ruban avec les vésicules synaptiques. Les protéines bassoon et piccolo permettent l'ancrage du ruban synaptique à la membrane plasmique des CCI au niveau des ZA.

A la différence de l'absence de ruban synaptique, le "knock-out" du gène codant pour la protéine de structure bassoon provoque une surdité sévère. Cette surdité s'explique par une désorganisation spatiale des synapses qui provoque une diminution du nombre de ruban, des canaux calciques beaucoup moins nombreux aux niveaux des ZA (Khimich et al., 2005; Frank et al., 2010; Jing et al., 2013). Il semblerait donc que la protéine bassoon serait

indispensable à l'organisation spatiale et structurelle des synapses en associant dans la ZA les acteurs principaux à l'exocytose. Le ruban synaptique, lui, serait important surtout sur l'aspect fonctionnel de la synapse en permettant une synchronicité et une cinétique rapide de la fusion des vésicules synaptiques à la membrane.

2. Les vésicules glutamatergiques

Le neurotransmetteur des synapses à rubans est le glutamate, et les récepteurs postsynaptiques des fibres afférentes des neurones de type I du ganglion spiral sont des récepteurs AMPA (α-amino-3-hydroxy-5-methyl-4-isoxazolepropionic acide ; (Glowatzki and Fuchs, 2002; Sadeghi et al., 2014; Kirk et al., 2017)). Ce sont des récepteurs ionotropiques s'activant par la fixation de glutamate et laissant entrer dans les fibres afférentes des cations (principalement du Na^+) créant ainsi des courants excitateurs (EPSC : excitatory post-synaptic current). Les principales sous-unités impliquées seraient GluA2/3 et GluA4, avec la sous-unité GluA2 donnant une grande perméabilité calcique probablement responsable de l'excitotoxicité lors de traumatisme acoustique (Sebe et al., 2017). Les courants excitateurs postsynaptiques sont proportionnels à la quantité de glutamate délivrée par la fusion des vésicules qui elle-même est proportionnelle aux dépolarisations graduelles des cellules ciliées.

Dans les cellules ciliées, les molécules de glutamate sont massées dans les vésicules synaptiques grâce à la protéine transmembranaire VGLUT3 (Vesicular glutamate transporter 3, voir figure 16), une protéine essentielle au bon fonctionnement de la synapse à ruban, causant la surdité DFNA25 lorsque celle-ci est muté(Ruel et al., 2008; Seal et al., 2008). Le transport de glutamate intra-vésiculaire utilise le gradient H^+ généré par la pompe à protons vésiculaire dépendante de l'ATP : V-ATPase (Karet et al., 1999; Zhao et al., 2019). Le relargage massif multivésiculaire de ces vésicules sera à l'origine de l'acidification des fentes synaptiques un mécanisme de rétrocontrôle limitant l'activité de la synapse par une inhibition des canaux calcique $Ca_V1.3$ (Vincent et al., 2018).

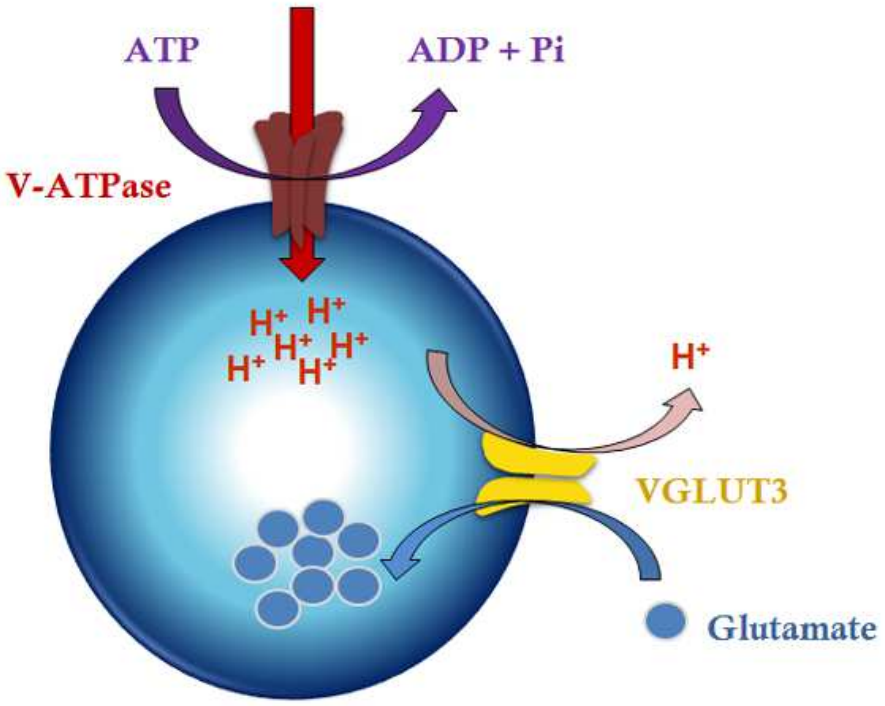

Figure 16. Représentation schématique du mécanisme de remplissage des vésicules synaptiques des CCI en glutamate inspirée de M. Tertrais et al. 2018. Les vésicules glutamatergiques accumulent le glutamate par l'action de la protéine transporteuse VGLUT3 qui utilisent le gradient des protons intra-vésiculaires. Les protons intra-vésiculaires sont activement apportés par la pompe à proton vésiculaire V-ATPase.

Comme décrit précédemment la particularité des synapses à ruban réside dans la vitesse et la précision temporelle de la fusion des vésicules synaptiques à la membrane des ZA. Une partie des vésicules synaptiques sont guidées et amarrées (« docking ») directement au niveau de la membrane cellulaire des CCIs au niveau des ZA pour être prêtes à la fusion (« priming »), ce sont les vésicules du RRP. On sait que dans les synapses neuronales classiques ce sont les protéines du complexe SNARE qui permet cette fonction (Soluble N-éthylmaleimide-sensitive-factor attachment protein receptor, voir figure 17).

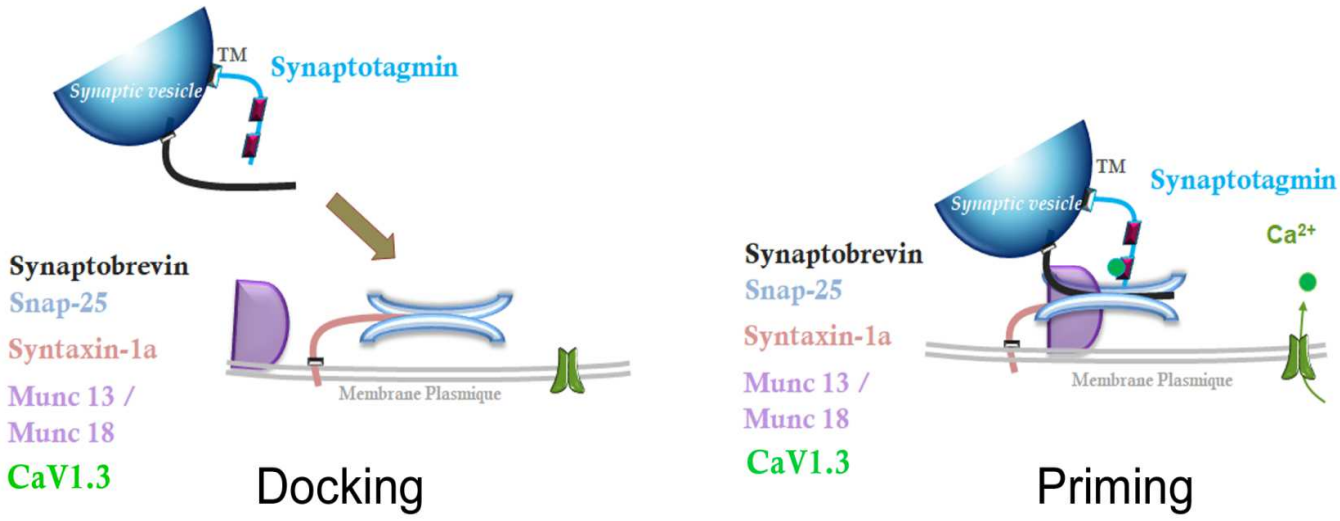

Figure 17. Représentation schématique du « Docking » et « Priming » des vésicules synaptiques dans les synapses neuronales inspirée de M. Tertrais et al. 2018.

Les protéines SNAREs sont divisées en SNARE vésiculaires (v-SNARE, « vesicular ») et SNARE cible (t-SNARE, « target »). Les v-SNAREs comme la Synaptobrévine sont des protéines qui possèdent un domaine transmembranaire dans la membrane des vésicules synaptiques. Les t-SNAREs, comme la Syntaxine-1a ou la SNAP-25 par exemple, sont localisées dans la membrane plasmique des cellules présynaptiques au niveau des ZA. L'association de ces deux types de protéine permet de cibler l'amarrage des vésicules synaptiques au bon endroit. L'expression de ces protéines est aussi retrouvée dans les CCIs grâce à l'étude des ARN messagers (Safieddine and Wenthold, 1999; Shen et al., 2015). Cependant, la présence et l'importance de ces SNAREs dans l'exocytose synaptique des CCIs restent encore à démontrer. La délétion du gène *Snap25* dans des cultures organotypiques de souris indiquent que cette protéine n'est pas essentielle à l'exocytose immature des CCIs (Nouvian et al., 2011). Dans cette étude précédente, l'utilisation de neurotoxines, clivant les SNARES, ne semble pas affecter l'exocytose synaptique des CCIs adultes.

D'autres particularités sont présentes concernant l'exocytose dans les CCIs. Tout d'abord on note l'absence de la protéine Munc-13, indispensable pour l'amarrage des vésicules synaptiques à la membrane dans les synapses centrales (Vogl et al., 2015). Et enfin l'absence de senseurs calciques « classiques » de type synaptotagmines dans les cellules ciliées matures qui sont remplacés progressivement au cours de la maturation par un

senseur calcique un peu particulier, l'otoferline (Beurg et al., 2010). Il est à noter que les CCIs et CCEs immatures présentent une activité électrique spontanée (potentiels d'action Na^+ et Ca^{2+}) avec des synapses afférentes de type neuronales utilisant des synaptotagmines (Beurg et al., 2010).

3. Les senseurs calciques

Les synaptotagmines sont les senseurs calciques de la plupart des synapses neuronales, ce sont de petites protéines possédant un domaine transmembranaire et deux domaines pouvant fixer le Ca^{2+} que l'on appelle C2 : C2A et C2B. Ils permettent d'initier l'exocytose, en présence de Ca^{2+}, en relation avec les protéines SNAREs (voir figure 17 Docking). A l'inverse, l'otoferline est une grande protéine de 1 997 acides aminés possédant également un domaine transmembranaire mais 6 domaines C2 pouvant fixer le Ca^{2+}(de C2A à C2F ; voir figure 18).

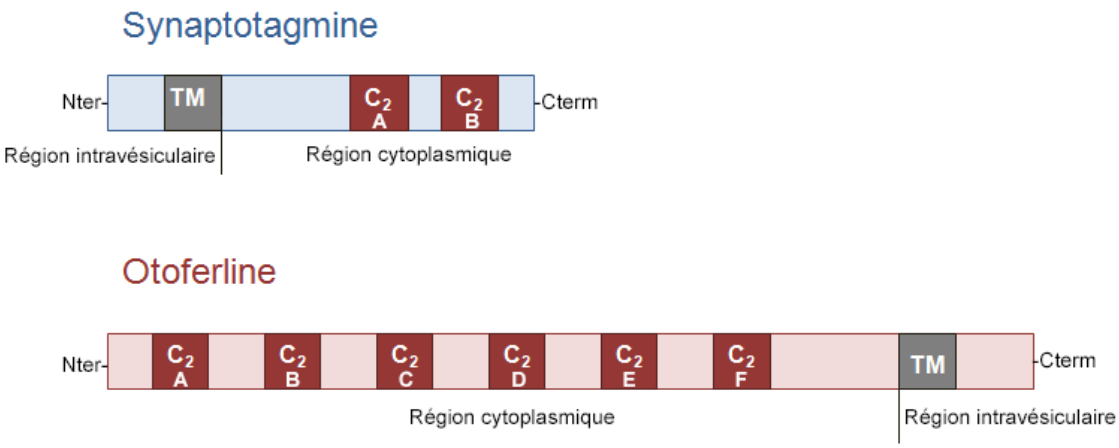

Figure 18. Comparaison de la structure et des domaines C2 des synaptotagmines et de l'otoferline. TM indique la localisation du domaine transmembranaire qui permet l'implantation du senseur dans la membrane des vésicules synaptiques. Les domaines C2 réfèrent à des domaines composer de feuillets β pouvant potentiellement fixer le calcium et interagir avec les phosphoinositides membranaires. (Tertrais et al., 2019). C'est surement la multiplicité de domaines C2 qui confère à l'otoferline une plus grande coopérativité calcique et un encodage graduel du signal acoustique.

L'importance de cette protéine a été démontrée par l'existence de mutations dans le gène *OTOF* provoquant une surdité récessive non-syndromique chez l'Homme appelée

DFNB9 (Yasunaga et al., 1999). Chez la souris le « knock-out » de l'otoferline entraîne également une surdité profonde. Dans ces souris, l'exocytose des CCIs est grandement réduite et ralentie malgré des courants calciques normaux et la présence de rubans synaptiques au niveau des ZA (Roux et al., 2006). L'otoferline apparaît ainsi comme essentielle à la fusion des vésicules synaptiques des CCIs. Le rôle exact des différents domaines C2 dans cette fusion vésiculaire Ca^{2+}-dépendante reste encore à définir. En se basant sur le nombre de mutations portant sur les domaines C2C et C2F on peut supposer que ce sont les deux domaines les plus importants pour l'otoferline. En effet, dans les souris *pachanga* portant une mutation affectant le domaine C2F (Substitution d'un acide aspartique par une glycine) mais pas l'intégrité de l'otoferline, les CCIs ont une exocytose soutenue drastiquement réduite avec une fusion des vésicules synaptiques du RRP toujours présente suggérant que l'otoferline serait surtout importante pour le réapprovisionnement des vésicules synaptiques dans les ZA des CCI (Pangrsic et al., 2012). Une étude similaire sur une mutation portant uniquement sur le domaine C2C de l'otoferline montre également le rôle crucial de la protéine pour la fusion rapide du RRP et le réapprovisionnement soutenu des vésicules synaptiques au niveau des ZA (Michalski et al., 2017). Le domaine C2C semble aussi important pour maintenir la présence de l'otoferline dans les membranes plasmiques via son interaction avec les phospholipides. Une étude récente sur le rôle des différents domaines C2 de l'otoferline, en utilisant des constructions miniaturisées de l'otoferline, démontrent qu'un mini-Otof formée des domaines C2E-C2F permet la restauration d'une exocytose rapide partielle associée à d'une endocytose ultrarapide (Tertrais et al., 2019).

4. Les canaux calciques

a. Généralités

Au niveau des ZA des CCIs, le Ca^{2+} entre via des canaux calciques voltage-dépendant de type L (« Long lasting ») appartenant à la famille des $Ca_V1.3$ sensibles à l'inhibition des dihydropyridines (DHP). Ces canaux sont activés à des hauts voltages du potentiel de membrane (aux environs de -50 mV) et ont une faible inactivation. En plus de leur présence dans le système auditif, ils sont retrouvés dans les neurones et également dans les cellules cardiaques permettant l'activité de « pacemaker » (Platzer et al., 2000).

Le pore des canaux calciques $Ca_V1.3$ est formé par la sous-unité α1D d'où son le nom de son gène *CACNA1D.* Elle possède 4 domaines homologues contenant chacun 6 segments transmembranaires. Mais les canaux calciques sont des protéines hétéro-pentamériques, en plus de la sous-unité α1D, sont associées 4 sous-unités régulatrices : α2, δ, γ et β dont notamment l'isoforme β2 responsable de surdité lorsqu'elle présente une mutation (Neef et al., 2009).

Les souris "knock-out" pour le gène *Cacna1d* présentent une surdité sévère dû à un déficit d'influx calcique et d'exocytose dans les CCIs indiquant que les canaux $Ca_V1.3$ sont les canaux principaux de la neurotransmission auditive afférente (Brandt et al., 2003). Dans ces mêmes souris on observe également un courant calcique résiduel encore présent suggérant la présence d'autres isoformes ou d'autres familles de canaux calciques. À ce jour, il a été démontré la présence de seulement deux isoformes des canaux calciques $Ca_V1.3$ produits par l'épissage alternatif : le premier présentant une forme longue $Ca_V1.3_L$ et le second une forme courte $Ca_V1.3_s$ (Singh et al., 2008; Bock et al., 2011; Vincent et al., 2017).

Ces canaux $Ca_V1.3$ sont regroupés de manière très compacte autour du ruban dans la ZA des CCIs permettant de focaliser l'influx calcique au voisinage des vésicules synaptiques pour initier leur fusion (Wong et al. (2014); voir figure 20). On parle d'organisation topographique en nanodomaine (quelques dizaines de nanomètres) entre vésicules et canaux $Ca_V1.3$, isoforme $Ca_V1.3_S$, et en microdomaine, isoforme $Ca_V1.3_L$, à l'échelle du ruban pour le recrutement actif des vésicules (voir figure 19 ; (Vincent et al., 2017)). La concentration calcique dans ce nanodomaine est amplifiée par la structure géométrique du ruban permettant d'atteindre quelques dizaines de micromolaires très localement et ainsi déclencher une libération multi-vésiculaire synchrone des vésicules synaptiques (Graydon et al., 2011).

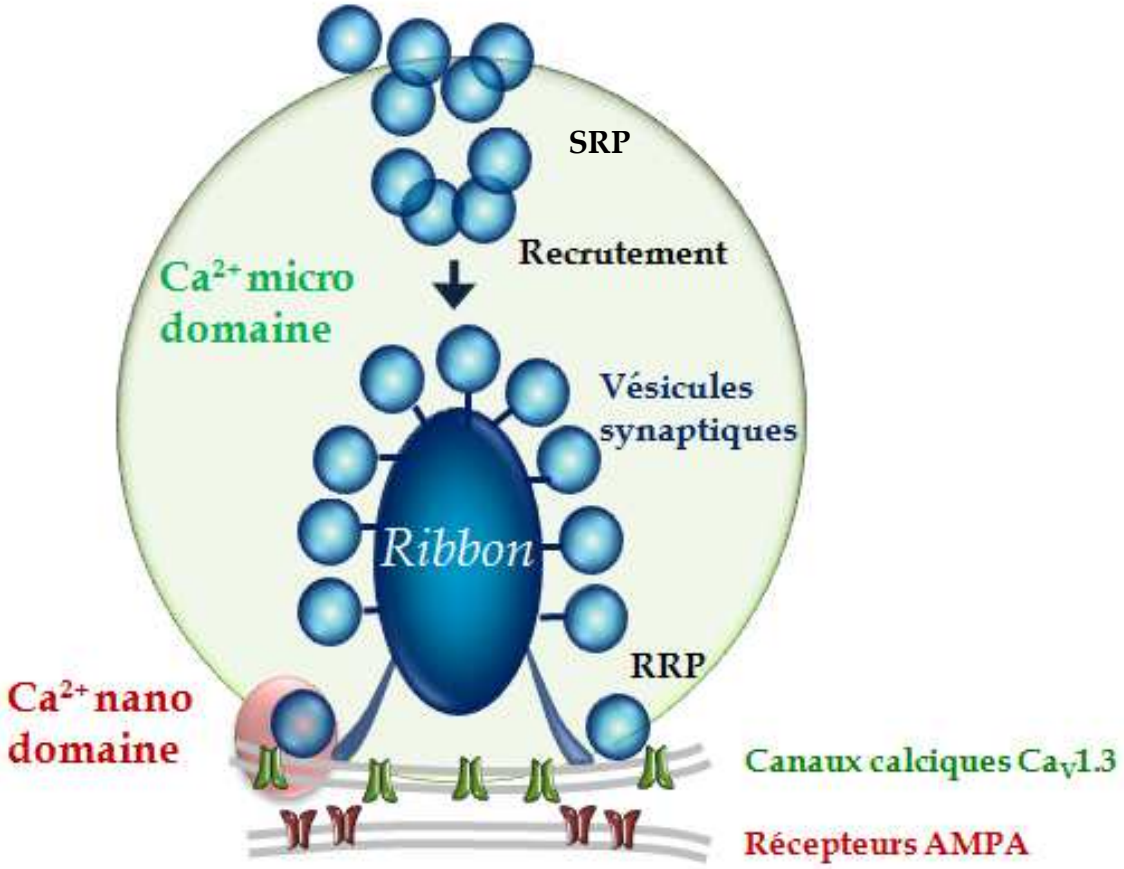

Figure 19. Représentation schématique du nuage calcique (nanodomaine er microdomaine) produit par l'activité des canaux calciques $Ca_V1.3$ situés au niveau des ZA des CCIs inspirée de M. Tertrais et al. 2018. Une association en nanodomaine (quelques dizaines de nm) entre vésicule synaptique et canaux calciques permet l'activation du RRP. L'action synchrone des canaux calcique lors de stimulations prolongées (>20 ms) produit une diffusion large des ions calcium en microdomaine pour stimuler le recrutement des vésicules synaptiques environnant la ZA du ruban (SRP, secondarily releasable pool of vesicles).

b. Inactivation par le voltage et le Ca^{2+}

Les canaux calciques, comme la plupart des canaux dépendant du voltage, s'inactivent en fonction du voltage et de la durée des stimulations grâce à certains segments transmembranaires du pore α1 mais aussi par certaines sous-unités régulatrices comme la β.

En plus de cela, les canaux calciques peuvent également s'inactiver en fonction de la concentration de Ca^{2+} intracellulaire similaire à un processus de rétrocontrôle. Ce processus appelé CDI (pour « calcium dependent inactivation » en anglais) permet de limiter la concentration intracellulaire calcique qui pourrait être néfaste pour les cellules en trop grande quantité. La sous-unité α1 possèdent en position C-terminal des domaines d'interaction, appelé IQ et pre-IQ (motif nommé IQ d'après les 2 premiers acides aminées), avec la protéine calmoduline (CaM) qui induit cette inactivation en changeant de conformation suite à la fixation du Ca^{2+} (Voir figure 20 (Liang et al., 2003; Yang et al., 2006)). Cependant la fixation de la CaM produisant l'inactivation peut être empêcher par la compétition d'autres protéines pouvant fixer le Ca^{2+} (CaBP pour « calcium binding protein » ; Cui et al. (2007)).

c. Inactivation par les protons

Les vésicules synaptiques sont remplies de glutamate grâce à l'échange de protons intra-vésiculaires par la protéine VGLUT3. La présence de protons intra-vésiculaires est alors essentielle, et comme décrit précédemment elle est dû à l'action de la pompe ATPase qui remplit activement les vésicules synaptiques de protons H^+ grâce à l'énergie libérée par la déphosphorylation de l'ATP en ADP + Pi. Cette présence massive de protons dans les vésicules acidifie intensément leur milieu intra-vésiculaire. Lors de la fusion des vésicules à la membrane des CCIs, les molécules de glutamate sont libérées tout autant que les protons dans la fente synaptique. Les protons vont alors acidifier également intensément le milieu extracellulaire des CCIs proche de la membrane plasmique. Ces protons peuvent également fixer les canaux calciques présents à la membrane des ZA et vont les bloquer de façon transitoire (Zhou and Jones, 1996; DeVries, 2001). De la même manière que l'inactivation par le Ca^{2+}, ce processus permet un rétrocontrôle des canaux calciques suite à leur activation pour limiter la libération excessive et nocive de vésicules glutamatergiques à la membrane que l'on appelle : l'excitotoxicité. D'après une récente étude, cette inactivation est permise dans les CCIs grâce au regroupement très serré des canaux calciques à la membrane des ZA. En effet, cette organisation resserrée permet une libération synchrone multivésiculaire des vésicules glutamatergiques. C'est cette quantité de vésicules libérées importante qui permet

de libérer assez de protons pour venir inactiver les canaux calciques. Lors du développement dans les CCIs présentant des synapses immatures, l'organisation des canaux calciques n'étant pas encore assez resserrée on observe une inactivation protonique beaucoup plus faible (Vincent et al., 2018).

d. Les isoformes des canaux calciques

Les canaux calciques sont des protéines hétéro-pentamériques, c'est-à-dire composées de 5 sous-unités différentes. Comme décrit précédemment la sous-unité composant le pore du canal est α1, elle est associée à 4 sous-unités régulatrices : α2, δ, γ et β.

Cependant les canaux calciques $Ca_V1.3$ peuvent subir un épissage alternatif qui les distingue notamment en un isoforme α1présentant un domaine long en C-terminale que l'on appelle $Ca_V1.3_L$et un isoforme α1 présentant un domaine court en C-terminale que l'one appelle $Ca_V1.3_s$ (voir figure 2 ; (Singh et al., 2008; Bock et al., 2011)). Les isoformes long $Ca_V1.3_L$(ou $Ca_V1.3_{43L}$) présentent en C-terminal deux domaines de régulation : un domaine proximal (PCRD : « proximal C-terminal regulatory domain ») et un domaine distal (DCRD : « distal C-terminal regulatory domain »). Ces deux domaines imposants rendraient difficile la fixation de la CaM sur les domaines d'interaction IQ et pre-IQ présents aussi en C-terminale et donc bloqueraient partiellement l'inactivation Ca^{2+}-calmoduline dépendante (Scharinger et al., 2015; Kuzmenkina et al., 2019). En revanche les isoformes courts $Ca_V1.3_s$ (ou $Ca_V1.3_{42A}$) présentent un domaine PCRD tronqué avec les domaines de fixation de la CaM IQ et pre-IQ mais pas de domaine DCRD. L'absence de DCRD permet d'avoir l'espace nécessaire à la fixation de la CaM et donc une inactivation Ca^{2+}-CaM dépendante plus efficace et plus rapide. La présence de ces deux isoformes participerait à un réglage très fin de l'exocytose. En effet, les isoformes courts qui représente environ 25% des canaux seraient spécialisés dans la fusion rapide des vésicules du RRP alors que les isoformes longs (75%) seraient spécialisés dans l'exocytose soutenue des vésicules du SRP (Vincent et al., 2017).

Une étude récente a également mis en évidence des différences significatives dans le potentiel d'activation des isoformes des canaux calciques (Hofer et al., 2021). En effet, les isoformes courts des canaux calciques auraient un potentiel d'activation et d'inactivation plus négatif que les isoformes longs. Ainsi une augmentation de l'expression des isoformes

courts ou une diminution de l'expression des isoformes longs pourraient induire un décalage de la courbe d'activation des canaux calciques des CCIs.

Les sous-unités régulatrices peuvent également permettre la régulation de l'expression des canaux à la surface membranaire, de la cinétique d'activation et de la voltage-dépendance de ces canaux (Arikkath and Campbell, 2003). En effet, par exemple la présence de l'isoforme de la sous-unité auxiliaire $\beta_2$ou $Ca_V\beta_2$ régulerait notamment l'expression des canaux calciques à la membrane (Neef et al., 2009).

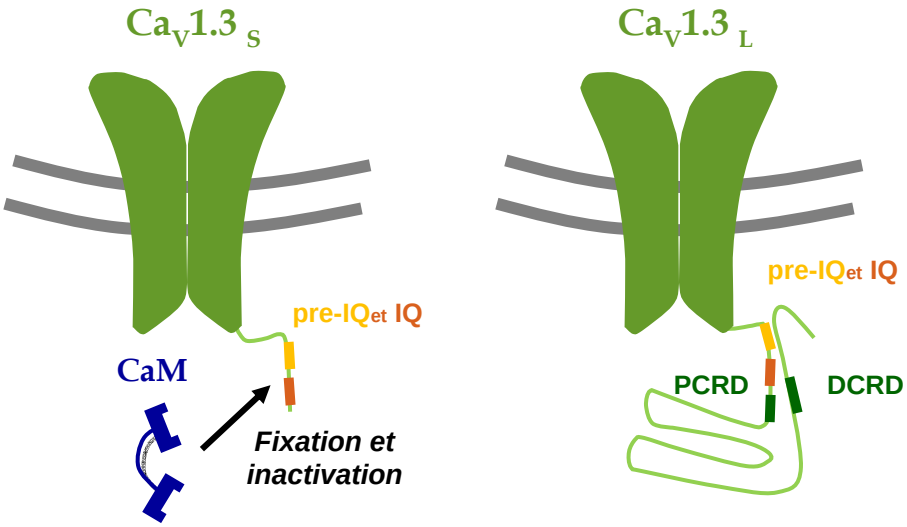

Figure 20. Représentation schématique des canaux calciques $Ca_V1.3$ des CCIs, d'après Tertrais et al. (2019)**.** On trouve essentiellement deux type d'isoformes des canaux $Ca_V1.3$ dans les CCIs (Vincent et al., 2017) :
- une isoforme longue ($Ca_V1.3_L$) qui démontre une inactivation faible et lente car les domaines PCRD et DCRD empêche un binding de la CaM. Cette isoforme serait associé au développement du microdomaine calcique contrôlant le ravitaillement vésiculaire au ruban.
- une isoforme courte ($Ca_V1.3_S$) qui présente une inactivation rapide CaM dépendante qui contrôlerait le RRP.

5. Les canaux potassiques activés par le calcium

a. Les principaux canaux potassiques des cellules ciliées.

Les canaux potassiques activés par le calcium sont divisés en deux grandes catégories, les canaux SK (Small conductance calcium-activated potassium channels) qui ont une petite conductance et les canaux BK (« Big potassium » ou « large conductance calcium-activated potassium channels »), voltage-dépendant, qui ont une grande conductance((Wei et al., 2005) voir revue Pyott and Duncan (2016)). Les canaux SK ont une affinité pour le Ca^{2+} et un temps d'ouverture plus élevés que les canaux BK. Ces canaux permettent de coupler

l'augmentation de la concentration du Ca^{2+} intracellulaire avec l'hyperpolarisation du potentiel de membrane. Ils jouent ainsi un rôle important dans l'excitabilité cellulaire des CCIs et le maintien de l'homéostasie du K^{+}.

C'est la repolarisation rapide des potentiels récepteurs par les canaux BK qui permet d'augmenter l'excitabilité des CCIs et ainsi contrôler la neurotransmission afférente (Skinner et al., 2003; Beurg et al., 2005). L'expression des canaux BK dans les CCIs débute autour du 12ème jour de développement postnatal chez la souris ; c'est-à-dire juste avant l'apparition de l'audition (Hafidi et al., 2005). Cette expression des canaux BK dans les CCIs coïncide avec la disparition des potentiels d'action spontanée et des canaux SK2 (Marcotti et al., 2003; Katz et al., 2004).

Au niveau des CCEs, l'expression des BK suit un gradient tonotopique le long de la cochlée avec une expression décroissante de la base (hautes fréquences) à l'apex (basses fréquences). Cette tonotopie suggère qu'ils participent surtout à la régulation efférente cholinergique médiane de l'audition dans les hautes fréquences (Wersinger et al., 2010). En effet les récepteurs nAChRs (alpha9-alpha10) des CCEs sont perméables aux calciums ce qui permettrait une régulation de l'activité électromécanique des CCEs par les canaux BK. Mais ce sont surtout des canaux de type SK2, associées aux nAChRs des CCEs (Dulon and Lenoir, 1996), qui régule l'hyperpolarisation de ces cellules.

Les souris mutantes KO sur le gène kcnma1 encodant la sous-unité α1 des canaux BK démontre une modification de la réponse temporelle des fibres du nerf auditif (Oliver et al., 2006) et une dégénérescence progressive des cellules ciliées dès la 8me semaine (Ruttiger et al., 2004). Par ailleurs ces souris KO kcnma1 présentent une plus grande sensibilité au bruit (Engel et al., 2006).

b. Propriétés et régulation des canaux BK.

Les canaux BK sont constitués d'un plusieurs sous-unités. La sous-unités α constitue le pore transmembranaire laissant passer les cations. Et les sous-unités β et γ permettent de réguler l'activation du canal (voir figure 3).

Les canaux BK sont principalement régulés par le voltage via certains segments transmembranaires du pore α (domaine Voltage Sensor Domain VSD, S1-S4) mais aussi par la concentration calcique intracellulaire par les 2 domaines RCK1 and RCK2 (regulatory of potassic conductance domain). L'importance des sous-unités régulatrices dans la régulation

des canaux BK *in vivo* n'est pas bien connu. Cependant une étude récente a nouvellement identifié deux sous-unités γ présentes dans les CCIs : LRRC26 (γ1) et LRRC52 (γ2). La fonction précise de LRRC26 n'est pas encore définie. En revanche l'importance de LRRC52 a été démontré, sa présence permet une activation dans un potentiel de membrane beaucoup plus négatif (-60 mV), une propriété assez unique des CCIs. Dans des cellules *in vitro* et des CCI *ex vivo*, il a été démontré que l'absence de LRRC52 conduit à un immense décalage positif (+200 mV). Ces résultats suggèrent que cette sous-unité est essentielle à la maintenance d'une activation des canaux BK à un potentiel de membrane très négatif (Lingle et al., 2019).

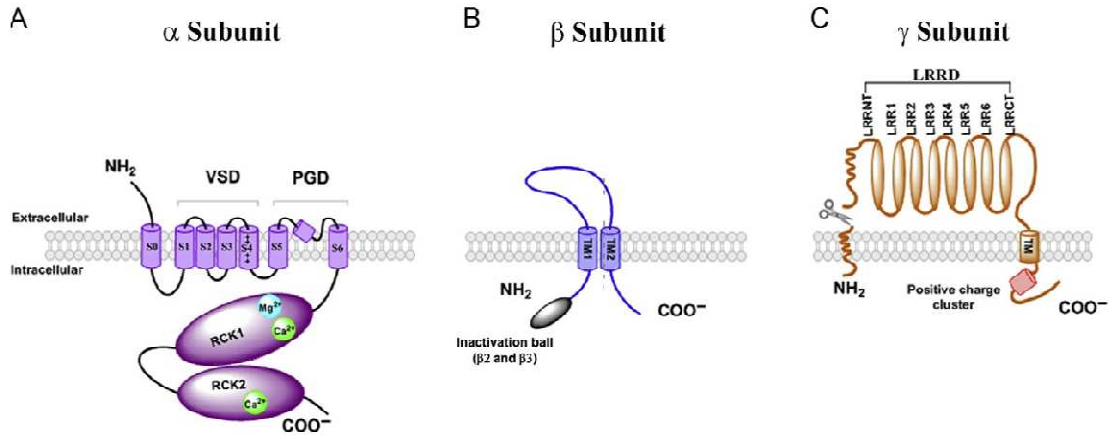

Figure 21. Représentation schématique des sous-unités composant les canaux BK, d'après la revue de Li et Yan, 2016.

A) La sous-unité α constitue le pore du canal : le domaine VSD (Voltage-Sensor Domain) est constitué par les segments transmembranaires S1-S4 et le domaine PGD (Pore-Gated Domain) par les segments S5-S6. Les domaines cytoplasmiques RCK1 et RCK2 constituent les sites de binding et de régulation par le calcium.

B) les sous-unités β sont des éléments de régulation de la voltage-dépendance du canal BK.

C) les sous-unités γ sont des éléments de régulation de l'adressage membranaire et de leur voltage-dépendance.

Chapitre 4 : Surdités

1. Types de surdités

Les surdités d'origine périphérique sont divisées en deux catégories : la perte auditive conductive (ou de transmission) et la perte auditive neurosensorielle. Les surdités de transmission sont liées à des défauts mécaniques provenant de l'oreille externe ou moyenne (membrane tympanique, osselets etc.). Alors que les pertes auditives neurosensorielles sont est associées aux cellules ciliées et/ou au fibres nerveuses du nerf auditif.

2. Surdités Neurosensorielles

Les surdités neurosensorielles peuvent être causées par des molécules médicamenteuses que l'on qualifie d'ototoxiques. Les médicaments ototoxiques les plus connus sont certains anti-inflammatoires (e.g. aspirine), les antibiotiques aminoglycosidiques, certains diurétiques (e.g. bumetanide, furosemide) et également certains traitements anticancéreux dont le plus étudié est le cisplatine. Ces molécules ciblent préférentiellement les cellules ciliées sensorielles et notamment les CCEs dans les hautes fréquences pour les aminosides. Ces molécules sont préférentiellement captées en passant par les canaux de mécano-transduction et perturbent le métabolisme oxydatif des ROS (Dulon, 2012).

Les traumas acoustiques sont également à l'origine de certaines surdités neurosensorielles. En effet l'écoute prolongé de stimulations sonores supérieurs à 90 dB peuvent endommager les cellules ciliées. Dans les cas les moins graves, le trauma va détériorer les "tip-links" des stéréocils et affecter la transduction sonore, et surtout l'amplification des cellules ciliées externes. Mais dans la plupart des cas de trauma acoustiques cette détérioration est réversible. En revanche, dans les cas les plus graves cette détérioration peut être définitive et également accompagnée de défauts synaptiques. En effet, le trauma acoustique peut générer un stress métabolique que l'on appelle stress oxydatif. Ce stress va augmenter la production de ROS et détériorer les structures présynaptiques et induire une réduction du nombre de synapses à ruban. Le trauma acoustique entraîne également une libération beaucoup trop importante de glutamate dans

la fente synaptique créant ainsi une excitotoxicité qui résulte en une entrée massive des cations dans les afférences des neurones du ganglion spiral. Le Ca^{2+} étant toxique en trop grande quantité intracellulaire va alors induire des facteurs de mort cellulaire pour ces neurones (Pujol and Puel, 1999).

Certaines de ces pertes auditives neurosensorielles sont aussi génétiques. En effet, il existe chez l'Homme de nombreuses mutations pouvant entraîner des surdités. Par exemple la mutation sur le gène codant pour la connexine-26 est responsable de la surdité appelé DFNB1 qui représente aux environs de 35% des surdités congénitales.

Protéine	**Surdité**	**Localisation**
Connexine-26 (*Gjb2*)	DFNB1	Strie Vasculaire
Otoferline (*Otof*)	DFNB9	Synapse
Pendrine (*Slc26a4*)	DFNB4	Echangeur d'anions
Cadhérine-23 (*Cdh23*)	USH1C / DFNB12	Tip-link
Tectorine-α (*Tecta*)	DFNA12 / DFNA8 / DFNB21	Membrane tectoriale
Vglut3 (*Slc17a8*)	DFNA25	Vésicule synaptique
Clarine-1 (*Clrn1*)	USH3A	Stéréocils
Myosine VIIa (*Myo7a*)	DFNA11 / DFNB2 / USH1B	Partie supérieure du tip-link

Tableau 1. Liste des protéines les plus couramment impliquées dans des surdités génétiques chez l'Homme.

Les mutations entraînant des surdités congénitales autosomales dominantes sont notées DFNA, celles entraînant des surdités autosomales récessives DFNB (voir tableau). Enfin les mutations entraînant une surdité associée à un défaut visuel font partie du syndrome de Usher décrit par l'ophtalmologiste Charles Usher en 1914 en s'inspirant de travaux antérieurs. La plupart des mutations touchant des protéines localisées à la partie apicale des stéréocils et participant à leur déflection font partie du syndrome de Usher. Parmi celles-ci on retrouve les protéines de la famille des clarines.

Enfin pour finir les pertes auditives neurosensorielles peuvent trouver leur origine dans les effets du vieillissement.

3. Perte de l'audition liée à l'âge

En effet, les CCI et leurs neurones sont des cellules dans un état quiescent qui ne peut se diviser et donc se régénérer, ils sont donc sensibles à tout changement dans leur homéostasie intracellulaire. La perte de l'audition liée à l'âge résulte d'une accumulation de dommages à long terme au niveau des structures des cellules ciliées et de leurs neurones.

Cette perte d'audition commence généralement par la difficulté à discerner la parole de son interlocuteur dans un environnement bruyant. Ensuite vient alors une perte de la sensibilité auditive et la perte de la capacité à localiser l'origine d'un son. Enfin on observe un défaut dans le traitement auditif central.

Le vieillissement cellulaire peut être défini par un processus dépendant du temps, de l'âge qui indique le cumul de perte de fonction et l'augmentation de la vulnérabilité (Fulop et al., 2019). La théorie des radicaux libres (ROS) proposée par Denham Harman en 1956 attribue ces pertes de fonctions dues au vieillissement cellulaire par la conséquence du stress oxydatif (Harman, 1956). Depuis cette théorie a bien évidemment été légèrement mise à jour, notamment sur le concept de vieillissement programmé chronologiquement. En effet, il semblerait plutôt que le vieillissement soit lié à un état de « fragilité » qui augmente avec le temps mais n'est pas programmé (Vina, 2019). Les mécanismes exacts de cette « fragilité » sont encore étudiés mais beaucoup d'études s'accordent à dire que cela viendrait du stress oxydatif et de l'inflammation provoqué par l'augmentation des radicaux libres avec le temps et qui entraînent ces effets délétères (Keithley, 2020).

4. Vieillissement cellulaire dû au stress oxydatif

a. Le stress oxydatif

Le stress oxydatif résulte en un déséquilibre entre la production de facteurs pro-oxydants et la production de facteurs antioxydants. Les facteurs pro-oxydants sont majoritairement représentés par les radicaux libres dérivés réactifs de l'oxygène (ou aussi ROS en anglais pour "reactive oxygen species"). Les ROS comme par exemple le peroxyde d'hydrogène (H_2O_2) sont capables d'échanger un de leur électron avec d'autres molécules d'oxygène dans la cellule. Cependant certaines molécules comme les acides nucléiques

(ADN, ARN), les lipides des membranes plasmiques ou d'autres protéines peuvent être endommagées par cette oxydation (Sies et al., 2017).

Comme décrit précédemment le stress oxydatif peut être provoqué par les médicaments ototoxiques et le trauma acoustique, mais il augmente aussi naturellement avec l'âge. Simultanément on observe également une réduction de l'activité antioxydante des cellules ce qui amplifie le déséquilibre pro- et antioxydants.

Ce sont les mitochondries qui produisent la majorité des ROS via la respiration cellulaire plus spécifiquement du cycle de Krebs et de la phosphorylation oxydative. La production trop importante de ROS endommage directement l'ADN mitochondrial. Ces altérations peuvent entraîner une dérégulation de la phosphorylation oxydative et augmenter encore plus la production de ROS qui induira des dommages cellulaires pouvant stimuler des facteurs pro-apoptotiques (Chinnery, 2015).

En plus de cette production mitochondriale viennent s'ajouter également la production des ROS par les NAD(P)H oxydases ou NOX. Les NOX sont une famille de complexe enzymatique membranaire composées de 7 types d'enzymes chez les mammifères. Chaque type d'enzyme a une fonction et une localisation particulière. Par exemple NOX3 est localisée dans le système vestibulaire et est essentiel pour la biosynthèse des otolithes (Paffenholz et al., 2004). Cependant les NOX partagent toutes la faculté d'oxyder le dioxygène (O_2) en un radical superoxyde O_2^- à partir du NAD(P)H cytosolique via la réaction :

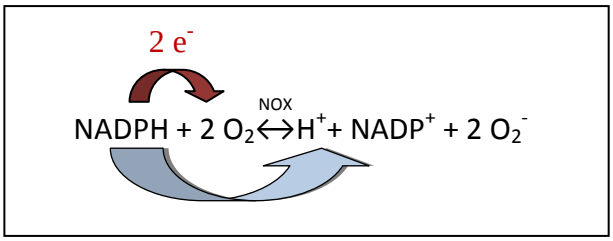

Le NADPH va donner 2 électrons libres, un pour chaque molécule de dioxygène, et va libérer un proton libre H^+. Les molécules de dioxygène acceptant l'électron libre deviennent alors des superoxydes (O_2^-). Ces superoxydes ne sont pas très stables et vont naturellement, ou catalysé par la superoxyde dismutase (SOD), se dismuter avec deux protons libres (H^+) en peroxyde d'hydrogène (H_2O_2) :

$$2\,H^+ + O_2^- \xleftrightarrow{SOD} H_2O_2$$

Comme pour les mitochondries, c'est la suractivation des NOX qui va conduire au stress oxydatif (voir figure 22). C'est le sous-unité p22phox qui est responsable de l'activation des NOX 1 à 4. Dans des souris mutantes où il y a un « knock-out » du gène codant pour la p22phox, on observe une réduction de l'activité de production des ROS par les NOX dans les neurones du ganglion spiral. Cette réduction de production des ROS permet d'atténuer la perte auditive lié à l'âge mais également de conserver une morphologie cochléaire normale comparé aux souris contrôles. C'est pourquoi le ciblage des NOX dans l'oreille interne pourrait présenter un intérêt thérapeutique contre la perte auditive lié à l'âge (Rousset et al., 2020).

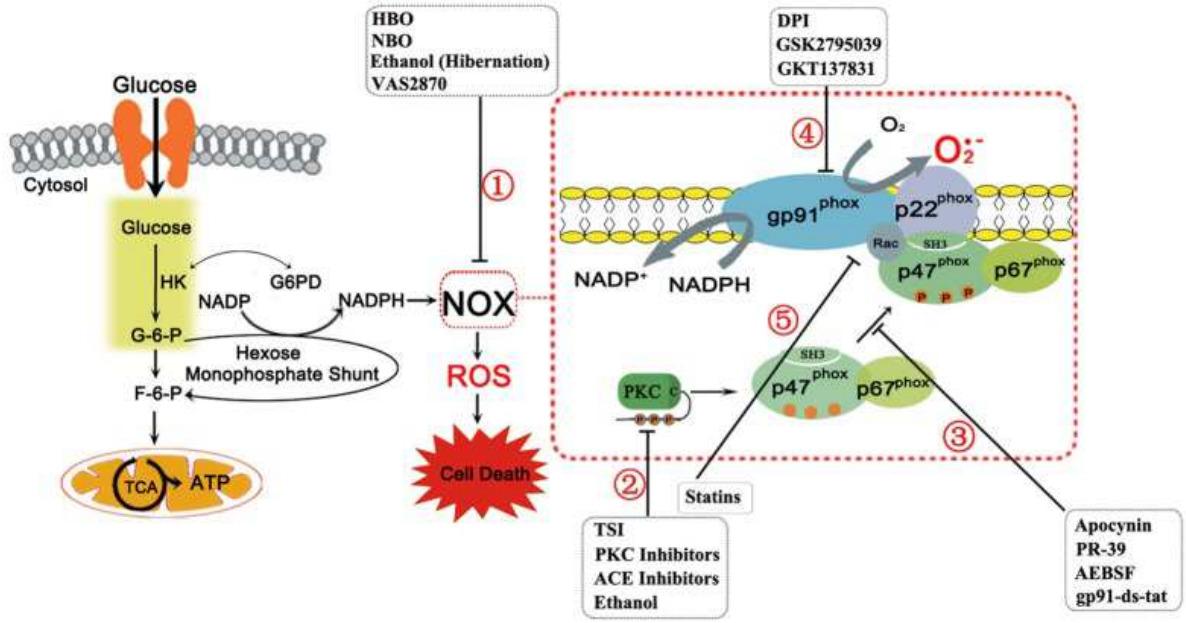

Figure 22. Représentation schématique de la voie d'oxydation des NADPH par le complexe NOX, d'après Rastogi et al. (2016). Le complexe NOX (détaillé dans le rectangle rouge) est constitué d'une partie catalytique composée des sous-unités gp91^{phox} et p22^{phox} et est associé à plusieurs autres sous-unités permettant son assemblage et son activation (e.g. p47^{phox}, p67^{phox}). Le complexe NOX va oxyder le dioxygène en radical superoxyde grâce à la NADPH. Ce superoxyde va se dismuter en peroxyde d'hydrogène. Ces deux réactifs sont ce qu'on appelle des dérivés réactifs de l'oxygène (ROS).

b. L'inflammation dû au vieillissement cellulaire

Le vieillissement cellulaire est souvent accompagné d'une inflammation chronique que l'on appelle en anglais « inflammaging » (contraction de « inflammation » et « aging », le vieillissement cellulaire), et d'une dérégulation du système immunitaire à cause du stress oxydatif (Sanada et al., 2018). Cela crée une activation persistante du système immunitaire

inné et une élévation chronique de certaines cytokines comme les interleukines (IL-6, IL-1β, IL-2) et les facteurs de nécrose tumorale α (TNF-α) qui sont souvent associées à des pertes auditives (Menardo et al., 2012). Cette inflammation chronique provoquée par le stress oxydatif à long terme, augmente à son tour la production de ROS par une rétroactivité positive. Cependant l'inhibition du facteur de transcription NF-κB peut potentiellement médier cette inflammation chronique dû à l'âge (Kanigur Sultuybek et al., 2019). NF-κB peut être activé par la liaison du ligand TNF-α avec son récepteur le TNF-α 1 (TNFR1) qui est impliqué dans la voie apoptotique. TNF-α est également impliqué dans des pertes auditives neurosensorielles. En effet des perfusions intra-cochléaires de TNF-α n'affectent pas directement l'intégrité des cellules ciliées mais réduit considérablement le nombre de synapses fonctionnelles. Il entraîne une dégénération des fibres afférentes des neurones du ganglion spiral (Katsumi et al., 2019). NF-κB est un facteur ambivalent qui selon le niveau de stress oxydative peut aussi bien être à la fois un facteur anti-apoptotique (à faible niveau de stress, faible concentration) et à la fois un facteur pro-apoptotique (à haut niveau de stress et forte concentration). C'est pourquoi sa régulation est crucial lors d'inflammation chronique (Lingappan, 2018).

c. Les voies apoptotiques des cellules ciliées

L'apoptose est un processus qui nécessite d'être finement régulé car il va induire la mort cellulaire. C'est ce processus qui est impliqué dans la majorité des pertes auditives lié à l'âge ayant pour cause la mort des cellules ciliées. L'apoptose est déclenché et régulé dans 3 voies distinctes : la voie du réticulum endoplasmique, la voie intrinsèque et la voie extrinsèque (voir figure 23). Toutes les voies apoptotiques font intervenir des enzymes protéases à cystéines que l'on appelle caspases (venant de la contraction en anglais de « cysteine-aspartic protease ») et sont principalement régulées par les protéines de la famille Bcl-2. Toutes ces voies sont également composées de deux phases : la phase initiatrice et la phase exécutrice.

Dans l'apoptose médiée par les caspases, les voies intrinsèques et extrinsèques ont des phases initiatrices uniques ; mais les deux partagent des voies similaires en phase d'exécution entraînant la mort cellulaire par activation des caspases 3 et 7. La voie extrinsèque s'initie en extracellulaire via la liaison d'un ligand « de mort » (en anglais « death-ligand ») à son récepteur de la famille des TNF, ce ligand pouvant être produit en

réponse au stress oxydatif. Cela stimule une cascade d'événements : tout d'abord activant le complexe de signalisation inducteur de mort (DISC pour « death-inducing signaling complex »), activant ainsi la caspase 8 et enfin la caspase 3 et la caspase 7. La voie intrinsèque est initiée par des facteurs intracellulaires tels que les dommages à l'ADN, la cytotoxicité et les ROS, qui sont détectés par les protéines BID. Les protéines de la grande famille des Bcl-2, dont surtout Bax et Bak, sont stimulées par les protéines BID pour créer un poreau niveau de la membrane externe mitochondriale, permettant la libération du cytochrome C dans le cytoplasme. La translocation de Bax et Bak est inhibée par des protéines anti-apoptotiques de la famille des Bcl-2, y compris Bcl-2 elle-même, prévenant l'apoptose. Le cytochrome C se lie à Apaf-1, activant la caspase 9, l'initiateur de la phase d'exécution. La phase d'exécution dans ces voies implique l'activation des caspases 3, 6 et 7, qui ont pour fonction de détruire les protéines nucléaires, induire la dégradation de l'ADN et de la chromatine, modifier l'arrangement du cytosquelette, et perturber la division cellulaire et la communication. En fin de compte, les fragments de la cellule sont reconnus et phagocyté par les cellules épithéliales et les macrophages (Morrill and He, 2017; Wu et al., 2020). Certaines études suggèrent que les ROS agissent comme des régulateurs de la protéine p53, induisant une activation continue de Bak, et éventuellement conduisant à l'apoptose dans la perte auditive liée à l'âge (Someya and Prolla, 2010). De même, dans le modèle de souris C57BL/6J, la délétion génétique de Bak a empêché l'apoptose des cellules neuronales des cellules ciliées et des ganglions en spirale (Someya et al., 2009).

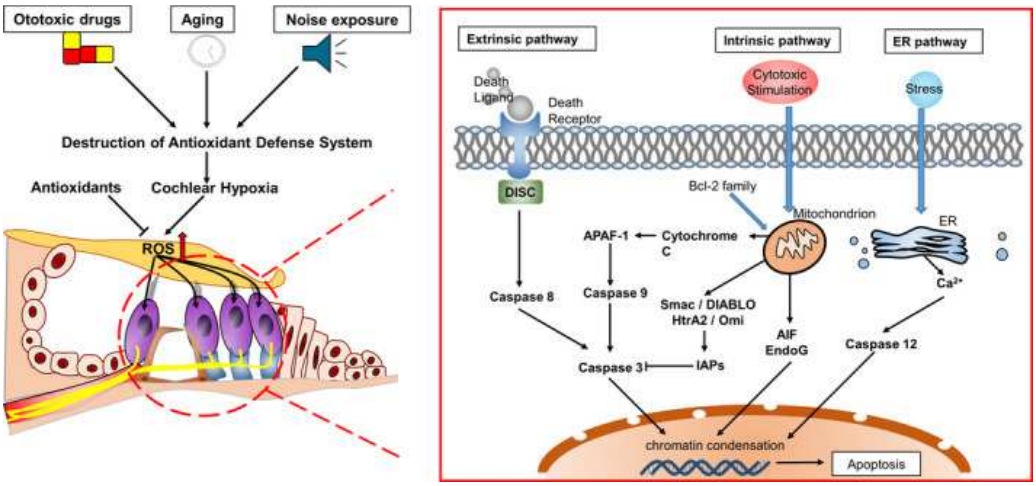

Figure 23. Les voies de signalisation de l'apoptose dans les cellules ciliées, d'après Wu et al., 2020**.** Les médicaments ototoxiques, le trauma acoustique ou encore le vieillissement cellulaire à travers la production de ROS peuvent induire l'apoptose chez les cellules ciliées selon 3 voies distinctes : la voie extrinsèque, la voie intrinsèque et la voie du réticulum endoplasmique.

d. L'autophagie

L'autophagie est un mécanisme de régulation déclenché par les stimuli du stress environnemental de la cellule dont fait partie le stress oxydatif. Le processus désigne le confinement, l'engloutissement et la décomposition des structures intracellulaires anormales ou endommagées qui sont dégradées par l'intermédiaire du lysosome (en acides aminés, nucléotides, acides gras etc.) pour être recyclé (voir figure 24 ; (Ye et al., 2018)). L'autophagie est régulée par la protéine "cible de la rapamycine chez les mammifères" (ou complexe mTOR pour « mammalian target of rapamycin » en anglais). C'est l'inhibition du complexe mTOR par la protéine p53 ou les AMPK (protéines kinases AMP-dépendante) qui active la voie autophagique. En revanche, l'activation du complexe mTOR par la signalisation de la voie MAPK et Akt, atténue l'autophagie. La synthèse des protéines se produit essentiellement dans le réticulum endoplasmique (RE). Le RE évalue les protéines synthétisées pour savoir si elles ont eu un bon assemblage grâce à cette voie d'autophagie ou également grâce au système ubiquitine-protéasome. Une fois identifiées, il va initier leur destruction et leur recyclage. Environ un tiers des protéines produites subissent ce processus, appelé la réponse UPR (pour « Unfold protein response »). Cette réponse UPR peut aussi déclencher l'apoptose via la libération de caspase 12. Enfin le stress du RE peut aussi déclencher la production de ROS elle-même via l'activation du facteur NF-κB (Jung et al., 2020).

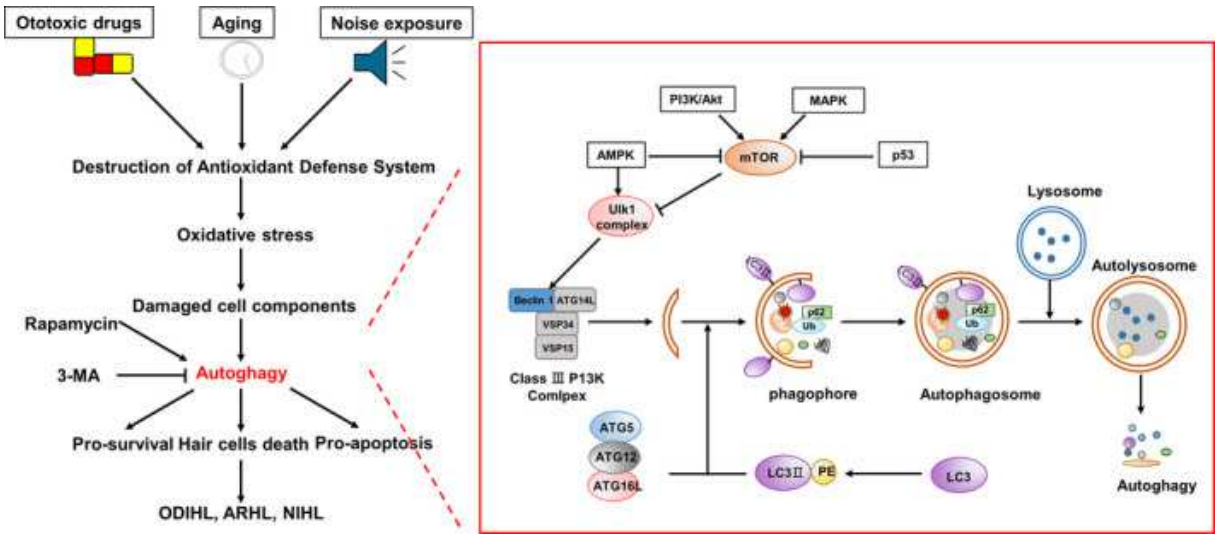

Figure 24. Voie de signalisation de l'autophagie dans les cellules ciliées, d'après Wu et al., 2020.

Chapitre 5: Objectifs de la thèse

L'exocytose des vésicules synaptiques glutamatergiques des CCIs est régulée par l'activité voltage-dépendante des canaux calciques de type $Ca_V1.3$ et du senseur calcique l'otoferline. L'organisation moléculaire fonctionnelle de ces deux acteurs restent encore à préciser. Nous avons ici abordé trois aspects du fonctionnement des synapses à ruban des CCIs :

1. Caractériser le rôle de la clarine-2

La clarine-2 est une petite protéine de type *tetraspan* (quatre domaines transmembranaires) récemment identifiée et appartenant à la famille de la clarin-1 (Usher-III syndrome protein). Tandis que la clarine-1 est montrée comme essentielle à la morphogénèse des stéréocils et à l'organisation spatiale resserrée des canaux $Ca_V1.3$ aux ZA des CCIs, l'implication de la clarin-2 dans les synapses à ruban reste encore à déterminer. Une mutation délétère de clarin-2 chez la souris provoque une surdité profonde qui a pour origine une désorganisation des stéréocils. Pour explorer le rôle synaptique éventuel de la clarin-2, nous avons aussi caractérisé les courants calciques et potassiques, ainsi que l'exocytose des CCIs de souris n'exprimant pas la clarin-2. Des expériences de restauration par injection intra-cochléaire de particules virales AAV contenant la séquence codante de clarin-2 nous permettrons de déterminer si les défauts synaptiques proviennent bien directement de l'absence de clarine-2.

2. Etudier le rôle de SNAP-25

L'implication des SNAREs dans le fonctionnement des synapses à ruban des CCIs reste encore largement débattue, notamment le rôle de la SNAP-25 (t-SNARE). Il est à noter que ces SNAREs sont essentielles à l'exocytose synaptique neuronale. Notre objectif était ici de démontrer directement le rôle de la SNAP-25 dans l'exocytose vésiculaire des cellules ciliées. Pour cela nous avons généré un modèle de souris KO conditionnel SNAP-25 où le gène encodant cette protéine est spécifiquement supprimé dans les cellules ciliées. L'impact sur

la fonction auditive et vestibulaire de ces souris sera étudié. L'exocytose et les courants calciques des cellules ciliées auditives et vestibulaires seront caractérisés.

3. Caractériser les changements fonctionnels et structurels lors du vieillissement

Le vieillissement de la fonction auditive, notamment chez la souris C57BL/6J est en premier lieu associé à une dégénérescence progressive des synapses à ruban, bien avant une perte de cellules ciliées ou de neurones du ganglion spiral. Les changements fonctionnels progressif des synapses à ruban résiduelles avec l'âge ne sont pas encore précisément définis. Nous étudierons ici au niveau cellulaire les changements des réponses calciques et de l'exocytose sur des CCIs de souris C57BL/6J avec l'âge.

RESULTATS

Article 1

Clarin-2 is essential for hearing by maintaining stereocilia integrity and function

Publié dans

EMBO Molecular Medicine

le 26 Août 2019

https://doi.org/10.15252/emmm.201910288

Introduction

La clarine-2 est une protéine de type tetraspan encodée par un gène paralogue de la clarine-1. Chez l'Homme, des mutations sur le gène codant pour la clarine-1 sont à l'origine du syndrome de Usher de type 3A (USH3A) qui se caractérise par une surdité progressive, une perte de la vue et dans certains cas, un trouble vestibulaire (Adato et al., 2002; Bonnet and El-Amraoui, 2012). Un modèle d'étude chez la souris a été généré par le "knock-out" du gène de la clarine-1. Ce modèle de souris présente une surdité progressive précoce sévère dû à un déficit dans la morphogénèse des stéréocils (Geng et al., 2009; Geng et al., 2012). Le gène codant pour la clarine-2 est également associé à un syndrome de surdité chez l'Homme (Vona et al., 2021). Nous avons identifié une mutation sur le gène *Clrn2*, induite par un agent mutagène (ENU), provoquant une surdité progressive sévère chez les souris mutantes *clarinette*. Nous avons caractérisé le rôle important de clarine-2 dans la maintenance des stéréocils et de la mécanotransduction.

Résultats

Les souris mutantes *clarinette* présentent une surdité progressive sévère précoce affectant les CCIs et les CCEs.

La clarine-2 est exprimée à l'apex des stéréocils des CCIs et des CCEs. Mais son expression commence tardivement dans la cochlée (P12). De ce fait, la clarine-2 n'est pas requise pour la morphogénèse des stéréocils, ni pour le développement de leur architecture en escalier ou leur organisation en U ou en V.

La clarine-2 a un rôle essentiel dans la maintenance des stéréocils. Dans les souris mutantes clarinette, à partir de P8, la taille des premières rangées de stéréocils est significativement réduite. De plus, le bout apical des stéréocils, normalement ellipsoïdal, est sphérique et aplatie, reflétant une perte de tension des liens entre les stéréocils que l'on appelle "tip-links".

Dans les souris mutantes clarinette, l'harmonine-b, une protéine essentielle du complexe de mécanotransduction, se retrouve délocalisée au bout des stéréocils. De plus, dans les CCIs et les CCEs des souris mutantes clarinette, les courants des MET sont drastiquement réduits.

Conclusion

Les souris clarinette, possédant une mutation délétère sur le gène Clrn2, présentent une surdité progressive précoce sévère. La clarine-2 est une petite protéine de 232 acides aminés de type tetraspan. Grâce à ce modèle murin, nous avons pu démontrer le rôle de clarine-2 dans la maintenance de la morphologie des stéréocils et de la mécanotransduction.

Article

TRANSPARENT PROCESS OPEN ACCESS

EMBO Molecular Medicine

Clarin-2 is essential for hearing by maintaining stereocilia integrity and function

Lucy A Dunbar[1], Pranav Patni[2], Carlos Aguilar[1], Philomena Mburu[1], Laura Corns[3], Helena RR Wells[4], Sedigheh Delmaghani[2], Andrew Parker[1], Stuart Johnson[3], Debbie Williams[1], Christopher T Esapa[1], Michelle M Simon[1], Lauren Chessum[1], Sherylanne Newton[1], Joanne Dorning[1], Prashanthini Jeyarajan[1], Susan Morse[1], Andrea Lelli[5], Gemma F Codner[6], Thibault Peineau[7], Suhasini R Gopal[8], Kumar N Alagramam[8], Ronna Hertzano[9], Didier Dulon[7], Sara Wells[6], Frances M Williams[4], Christine Petit[5], Sally J Dawson[10], Steve DM Brown[1], Walter Marcotti[3], Aziz El-Amraoui[2,*,†] & Michael R Bowl[1,†,**]

Abstract

Hearing relies on mechanically gated ion channels present in the actin-rich stereocilia bundles at the apical surface of cochlear hair cells. Our knowledge of the mechanisms underlying the formation and maintenance of the sound-receptive structure is limited. Utilizing a large-scale forward genetic screen in mice, genome mapping and gene complementation tests, we identified *Clrn2* as a new deafness gene. The *Clrn2*$^{clarinet/clarinet}$ mice (p.Trp4* mutation) exhibit a progressive, early-onset hearing loss, with no overt retinal deficits. Utilizing data from the UK Biobank study, we could show that *CLRN2* is involved in human non-syndromic progressive hearing loss. Our in-depth morphological, molecular and functional investigations establish that while it is not required for initial formation of cochlear sensory hair cell stereocilia bundles, clarin-2 is critical for maintaining normal bundle integrity and functioning. In the differentiating hair bundles, lack of clarin-2 leads to loss of mechano-electrical transduction, followed by selective progressive loss of the transducing stereocilia. Together, our findings demonstrate a key role for clarin-2 in mammalian hearing, providing insights into the interplay between mechano-electrical transduction and stereocilia maintenance.

Keywords hair cells; mechanotransduction; mouse models; mutagenesis; stereocilia

Subject Categories Genetics, Gene Therapy & Genetic Disease; Molecular Biology of Disease

DOI 10.15252/emmm.201910288 | Received 9 January 2019 | Revised 23 July 2019 | Accepted 26 July 2019

EMBO Mol Med (2019) 11: e10288

Introduction

The process of hearing requires the transduction of sound wave-induced mechanical energy into neuronal signals. This process is achieved by the mechanosensitive inner ear hair cells located in the cochlea. These specialized sensory cells, named inner hair cells (IHCs) and outer hair cells (OHCs), have an array of actin-filled stereocilia protruding from their apical surface. Each hair cell stereocilia bundle is arranged as 3–4 rows in a highly ordered "staircase-like" structure, which is essential for function. Each taller stereocilium is connected to a shorter neighbour, in an adjacent row, by an extracellular tip link (Kazmierczak *et al*, 2007), with the upper end of the tip link extending from the side of a taller-row stereocilium to the tip of a shorter-row stereocilium, where it is tethered to the transduction channel complex. In response to sound-induced fluid movement within the inner ear, hair cell bundles are deflected towards the tallest stereocilia

1 Mammalian Genetics Unit, MRC Harwell Institute, Harwell, UK
2 Déficits Sensoriels Progressifs, Institut Pasteur, INSERM UMR-S 1120, Sorbonne Universités, Paris, France
3 Department of Biomedical Science, University of Sheffield, Sheffield, UK
4 Department of Twin Research & Genetic Epidemiology, King's College London, London, UK
5 Génétique et Physiologie de l'Audition, Institut Pasteur, INSERM UMR-S 1120, Collège de France, Sorbonne Universités, Paris, France
6 Mary Lyon Centre, MRC Harwell Institute, Harwell, UK
7 Laboratoire de Neurophysiologie de la Synapse Auditive, Université de Bordeaux, Bordeaux, France
8 Department of Otolaryngology – Head and Neck Surgery, University Hospitals Cleveland Medical Center, Case Western Reserve University, Cleveland, OH, USA
9 Department of Otorhinolaryngology Head and Neck Surgery, Anatomy and Neurobiology and Institute for Genome Sciences, University of Maryland School of Medicine, Baltimore, MD, USA
10 UCL Ear Institute, University College London, London, UK
*Corresponding author. Tel: +33 1 45 68 88 92; E-mail: aziz.el-amraoui@pasteur.fr
**Corresponding author. Tel: +44 1235 841161; E-mail: m.bowl@har.mrc.ac.uk
†These authors contributed equally to this work

© 2019 The Authors. Published under the terms of the CC BY 4.0 license

causing tension in the tip links, which opens the mechanically gated transduction channels, allowing the influx of K^+ and Ca^{2+} ions into the hair cell, leading to depolarization and release of neurotransmitter (Corey & Hudspeth, 1983; Schwander *et al*, 2010). Components of the elusive transduction channel complex include LHFPL tetraspan subfamily member 5 (LHFPL5), transmembrane inner ear (TMIE) and transmembrane channel-like 1 (TMC1) and TMC2 (Kawashima *et al*, 2011; Kurima *et al*, 2015; Corns *et al*, 2016, 2017; Fettiplace, 2016; Beurg *et al*, 2018). All these proteins are reported to interact with protocadherin-15 (PCDH15), a component of the tip link, anchoring it to the stereocilia membrane (Xiong *et al*, 2012; Maeda *et al*, 2014; Zhao *et al*, 2014). The development and maintenance of the "staircase" stereocilia bundle, and the inter-stereociliary tip links, are therefore critical for auditory transduction and essential for hearing. Currently, our knowledge of the mechanisms underlying stereocilia bundle formation and maintenance is limited, and the precise molecular composition of the transduction channel complex remains elusive.

The Clarin (CLRN) proteins belong to a superfamily of small integral proteins with four alpha-helical transmembrane domains, which also includes Tetraspanins, Connexins, Claudins, Occludins and calcium channel gamma subunit-like proteins (Adato *et al*, 2002; Aarnisalo *et al*, 2007). In humans, the CLRN family comprises three proteins encoded by the paralogous genes *CLRN1*, *CLRN2* and *CLRN3*, which contain no known functional domains apart from their four transmembrane domains and a C-terminal class-II PDZ-binding motif (PBM type II) (Fig 1A). In humans, *CLRN1* mutations have been found to cause Usher syndrome type 3A (USH3A), which is characterized by post-lingual, progressive hearing loss, variable vestibular dysfunction and onset of retinitis pigmentosa leading to vision loss (Adato *et al*, 2002; Bonnet & El-Amraoui, 2012). Similarly, *Clrn1* knockout ($Clrn1^{-/-}$) mice are reported to show early-onset profound hearing loss, and consistent with this, these mice exhibit disrupted stereocilia bundles in the early postnatal period (Geng *et al*, 2009, 2012). However, to date *Clrn2* has not been associated with any disease and has never been the focus of a scientific paper.

Utilizing an unbiased forward genetic screen, we have identified an ENU-induced *Clrn2* mutation as the cause of deafness in the *clarinet* mouse mutant ($Clrn2^{clarinet}$). Moreover, we have employed $Clrn2^{clarinet}$ mice and a second CRISPR/Cas9-induced mutant ($Clrn2^{del629}$) to investigate the requirement of clarin-2 in the auditory, vestibular and visual systems. While clarin-2 appears to have a nonessential role in the retina and vestibular apparatus, its absence leads to an early-onset progressive hearing loss. In addition, we identify that genetic variation at the human *CLRN2* locus is highly associated with adult hearing difficulty in the UK Biobank Cohort. Expression of tagged clarin-2 in cochlear cultures shows enrichment of the protein in hair cell stereocilia. We demonstrate that clarin-2 is not required for the initial patterning, or formation, of the "staircase" stereocilia bundle, but instead is essential for the process of maintenance of the stereocilia bundle and mechano-electrical transduction. This study establishes a critical role for the tetraspan protein clarin-2 in the function of the mammalian auditory system.

Results

Clarin-2, a novel protein essential for mammalian hearing

During a recent phenotype-driven ENU-mutagenesis screen undertaken at the MRC Harwell Institute, pedigree MPC169 was identified as containing mice with hearing impairment (Potter *et al*, 2016). In a G_3 cohort of 69 mice, 8 were found to have severely elevated auditory brainstem response (ABR) thresholds at 3 months of age (Fig 1A). A genome scan and subsequent single nucleotide polymorphism (SNP) mapping of affected (deaf) and unaffected (hearing) G_3 mice demonstrated linkage to a ~12-Mb region on Chromosome 5 (Fig EV1A). Whole-genome sequencing of an affected mouse identified a homozygous mutation within the critical interval consisting of a non-synonymous G-to-A transition at nucleotide 12 of the *Clrn2* gene (ENSMUST00000053250). The *Clrn2* mutation, confirmed using Sanger sequencing (Fig EV1B), leads to a tryptophan-to-stop (p.Trp4*) nonsense mutation in the encoded clarin-2 protein, a tetraspan-like glycoprotein with a class-II PDZ-binding motif (Fig 1B and C). We subsequently named this mutant *clarinet* and backcrossed the $Clrn2^{clarinet}$ allele to C57BL/6J for ten generations.

To confirm $Clrn2^{clarinet}$ is the causal mutation underlying the auditory dysfunction observed in *clarinet* mice, we first used a CRISPR/Cas9 approach to engineer a second *Clrn2* mutant mouse model, named $Clrn2^{del629}$. This allele consists of a 629 nucleotide deletion that encompasses exon 2 (ENSMUSE00000401986) of the *Clrn2* gene, which encodes the second, and part of the third, transmembrane domains of clarin-2. As such, while the remaining exons 1 and 3 splice together and are in-frame, any translated protein is predicted to have reduced, or absent, function (Figs 1D and EV1C). Next, we undertook a complementation test crossing together these two *Clrn2* mutant lines (Figs 1E and EV1D). ABR measurements, recorded in postnatal day 28 (P28) mice in response to click and tone-burst stimuli, showed that compound heterozygous ($Clrn2^{clarinet/del629}$) mice display very elevated thresholds (> 80 decibel sound pressure level (dB SPL)) at all frequencies tested: 8, 16 and 32 kHz, whereas $Clrn2^{clarinet/+}$ and $Clrn2^{del629/+}$ mice exhibit thresholds comparable with those of wild-type ($Clrn2^{+/+}$) littermates (< 40 dB SPL) (Figs 1E and EV1D), demonstrating the absence of a heterozygous auditory phenotype. Failure of complementation in $Clrn2^{clarinet/del629}$ mice confirms the gene *Clrn2* is essential for hearing.

Utilizing the UK Biobank Cohort (Sudlow *et al*, 2015), a multi-phenotype study of 500,000 people aged between 40 and 69 years, we also sought whether genetic variation at the *CLRN2* locus is related to self-reported human hearing difficulty. The association was performed using a case–control design (n = 250,389) based on answers to questions regarding participants' self-assessed hearing ability and self-reported hearing difficulty in the presence of background noise. An association was tested between all 484 UK Biobank genotyped and imputed SNPs within 100 kb of the *CLRN2* gene. Within this region, 36 SNPs were significantly associated with the hearing difficulty phenotype, including a cluster of five highly associated SNPs that lie within or very close to the *CLRN2* gene (Fig 1F). Within the 20 most highly associated SNPs, the majority are either intronic or intergenic (Table EV1). The rs35414371 SNP with the highest association has a P-value of 1.60E-11 and lies just 2 kb downstream of the *CLRN2* gene. The second most associated

 © 2019 The Authors

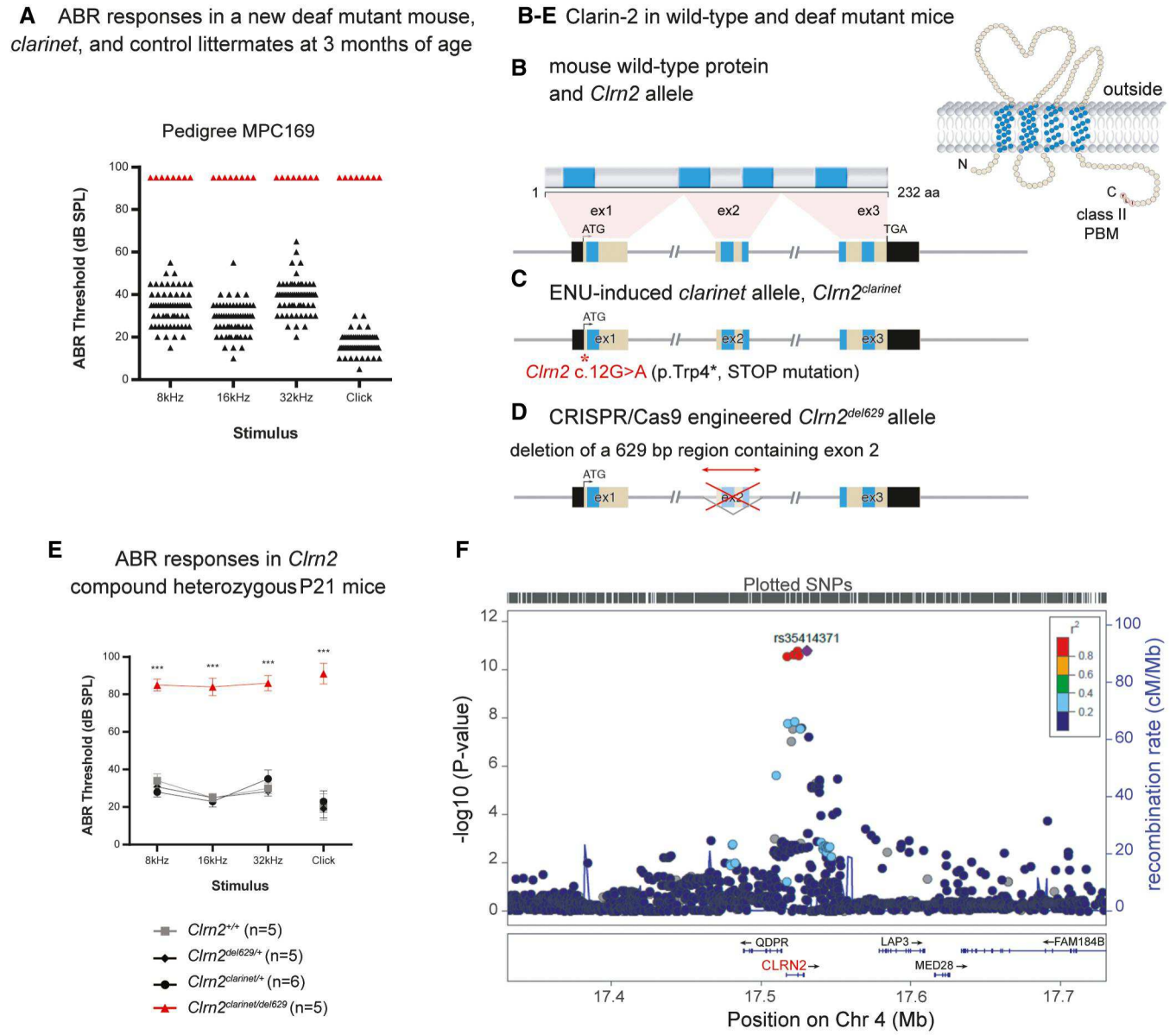

Figure 1. *Clrn2* is essential for mammalian hearing.

A Identification of the ENU-induced hearing loss pedigree MPC169, subsequently named *clarinet*. ABR phenotyping of pedigree Muta-Ped-C3PDE-169 at 3 months of age identified 8 mice with elevated hearing thresholds (red triangles) compared to their normal hearing colony mates (n = 61, black triangles). Indeed, all eight affected mice were found to not respond to the highest intensity stimulus (90 dB SPL) at the three frequencies tested, or the click stimulus, and so their thresholds are shown as 95 dB SPL.

B–D The genomic structure of mouse *Clrn2* (ENSMUST00000053250), and domains of the encoded tetraspan-like glycoprotein (232 amino acids). Black-filled boxes represent untranslated region of *Clrn2*. The positions of the transmembrane (TM) domains (blue) and the structure of $Clrn2^{clarinet}$ (C) and $Clrn2^{del629}$ (D) alleles are indicated. The *clarinet* mutation, $Clrn2^{clarinet}$ (c.12G > A) (red asterisk), is predicted to lead to a premature stop codon at position 4 (p.Trp4*) (C), whereas the $Clrn2^{del629}$ allele consists of a CRISPR/Cas9-mediated 629 nucleotide deletion encompassing exon 2, leading to splicing of exon 1 to exon 3, which if translated would produce a protein lacking 2 (TM2 and TM3) of the 4 transmembrane domains (D).

E Averaged ABR thresholds for $Clrn2^{clarinet/del629}$ compound heterozygotes at P21, showing significantly elevated thresholds compared to $Clrn2^{+/+}$, $Clrn2^{clarinet/+}$ and $Clrn2^{del629/+}$ control colony mates. All five $Clrn2^{clarinet/del629}$ mice were found to not respond at the highest intensity stimulus (90 dB SPL) for at least one frequency/click stimulus. Data shown are mean ± SD ***P < 0.001, one-way ANOVA (Please see Appendix Table S1 for exact P-values).

F Regional plot of P-values for SNP association with hearing difficulty around the *CLRN2* gene locus. The genes within the region are annotated, and the direction of the transcripts is shown by arrows. Colouring is based on linkage disequilibrium (LD) across the region with the most associated SNP, rs35414371, shown in purple.

SNP, rs13147559 (P = 1.70E-11), is in exon 2 of the *CLRN2* gene at coding nucleotide position 337 (c.337, ENST00000511148.2). Presence of the ancestral allele (cytosine, c.337C) encodes for leucine (p.113Leu), whereas presence of the minor allele (guanine, c.337G) encodes for valine (p.113Val). As such, this SNP (c.337C > G) represents a missense variant (p.Leu113Val) within the predicted

© 2019 The Authors

transmembrane domain 2 of the clarin-2 protein (NP_001073296). *In silico* studies show that the leucine at position 113 is evolutionarily conserved across species. Furthermore, two prediction tools, PolyPhen-2 and MutationAssessor, suggest that substitution of a valine at this position might be detrimental to clarin-2 function returning scores of "possibly damaging" and "medium", respectively.

Together, our findings indicate that clarin-2 is key to hearing in both mice and humans.

Clarin-2 is essential for hearing function

Clarin-2 displays 56% amino acid similarity with clarin-1, the USH3A protein. Indeed, *CLRN1* loss of function has been shown to cause progressive hearing loss, variable vestibular dysfunction and progressive retinitis pigmentosa, which prompted us to seek whether *Clrn2* is a candidate Usher gene. RT–PCR analyses from wild-type P30 mice revealed the presence of *Clrn2* transcripts in the inner ear (notably in the auditory hair cells) and the eye, but not in brain or muscle (Fig 2A and B). Thus, functional measurements were performed to characterize hearing, vestibular and visual phenotypes in *clarinet* mice.

To establish the onset and progression of auditory impairment in $Clrn2^{clarinet/clarinet}$ mice, ABR measurements were undertaken at P16, which is just after the onset of hearing in mice (~P12), and longitudinally at P21, P28 and P42. At P16, $Clrn2^{clarinet/clarinet}$ mice display elevated hearing thresholds (e.g. mean click threshold 64 dB SPL ± 15 SD) compared with their littermate controls (mean click threshold < 30 dB SPL ± 6 SD for $Clrn2^{+/+}$ mice) (Fig 2C). At P21, $Clrn2^{clarinet/clarinet}$ mice display increased auditory thresholds (mean click threshold 80 dB SPL ± 16 SD) compared with P16 $Clrn2^{clarinet/clarinet}$ mice, and thresholds continue to increase by P28, and P42 (mean click threshold 89 dB SPL ± 5 SD; Fig 2D–F). To further assess cochlear function, distortion product otoacoustic emissions (DPOAEs) were measured in P28 $Clrn2^{clarinet/clarinet}$ mice. Compared to their $Clrn2^{+/+}$ and $Clrn2^{clarinet/+}$ littermates, $Clrn2^{clarinet/clarinet}$ mice have reduced DPOAEs (Fig 2G) suggesting impaired OHC function. These results show that lack of clarin-2 causes an early-onset hearing loss, characterized by a fast-progressive deterioration of hearing function likely affecting both inner and outer hair cells.

To assess for potential vestibular deficits, *clarinet* and control mice were subject to various tests, including platform, trunk-curl, contact righting and swim tests (Hardisty-Hughes *et al*, 2010). Regardless of the test employed, no overt difference between $Clrn2^{clarinet/clarinet}$ mice ($n = 12$) and age-matched $Clrn2^{clarinet/+}$ control mice ($n = 10$) was observed at P28 or at P60, indicating normal balance function in young animals despite the absence of clarin-2 (Fig 3A; $P > 0.05$).

To investigate for possible visual deficits in *clarinet* mice, we measured the retinal-evoked potential responses, characterized by an initial negative deflection (the a-wave) followed by a positive peak (the b-wave), the amplitudes of which vary with light intensity. Functional electroretinogram (ERG) measurements, under scotopic (Fig 3B, D and E) or photopic (Fig 3C and F) conditions, indicated that rod and cone functions are normal in $Clrn2^{clarinet/clarinet}$ mutant mice at both 3 months and 6–7 months. The ERG responses were almost normal in shape, with unaffected time-to-peak values for the a- and b-waves (Fig 3B and C). The amplitudes measured at the peak of both the a- and b-waves were also similar for control ($Clrn2^{clarinet/+}$) and $Clrn2^{clarinet/clarinet}$ mice at 6–7 months (a-wave, Fig 3D: 172 ± 14 and 207 ± 17, respectively; b-wave, Fig 3E: 299 ± 15 and 242 ± 39, respectively; photopic ERGs, Fig 3F: 61 ± 7 and 67 ± 8, respectively). Consistent with ERG findings, the overall laminar organization of the retina in control $Clrn2^{clarinet/+}$ and mutant $Clrn2^{clarinet/clarinet}$ mice, examined on cryosections from mice aged 6–7 months, is normal, with normal retinal pigment epithelium, clearly distinguishable neuroretinal layers, and normal targeting and restriction of the short wavelength-sensitive opsin 1 (S opsin) and rhodopsin to the outer segment in blue cone and rod photoreceptor cells, respectively (Fig EV2A and B). No pyknotic nuclei, indicative of degenerating cells, were observed in any of the retinal cell layers, and TUNEL assays detected no apoptosis (Fig EV2C). The Iba1-immunoreactive microglial cells in the retinas of $Clrn2^{clarinet/clarinet}$ mice had features typical of the resting state similar to age-matched controls, including long thin neurites and lack of immunostaining in the photoreceptor cell-containing layer (Fig EV2D).

Together, our findings indicate that the absence of clarin-2 leads to an early-onset, progressive hearing loss, without overt retinal deficits.

Clarin-2 is not required for the formation and proper polarization of the hair bundle

To investigate the cause of hearing loss in $Clrn2^{clarinet/clarinet}$ mice, and considering the previously reported disrupted organization of auditory hair bundles in neonatal *Clrn1* mutant mice (Geller *et al*, 2009; Geng *et al*, 2009, 2012; Dulon *et al*, 2018), we used confocal and scanning electron microscopy to monitor the progression of hair cell stereocilia bundle development and maturation from birth (Figs 4 and 5).

At P6, towards the end of the first postnatal week, $Clrn2^{clarinet/clarinet}$ cochlear OHC and IHC hair bundles have a cohesive appearance, with the expected V- and U-shape organization, respectively, compared to heterozygous controls (Fig 4A and B). Moreover, throughout $Clrn2^{clarinet/clarinet}$ cochleae, stereocilin localizes as expected at the tips of the tallest stereocilia (Fig 4C and E, $n = 3$), indicating normal coupling between OHC stereocilia and the overlying tectorial membrane (Verpy *et al*, 2008). These data contrast with the grossly misshapen auditory OHC hair bundles exhibited by *Clrn1* mutant mice (Geller *et al*, 2009; Geng *et al*, 2009; Dulon *et al*, 2018) (see also Fig 4D). By P8, scanning electron microscopy shows $Clrn2^{clarinet/clarinet}$ mutants do not exhibit any gross patterning defects, or differences in the overall number of OHC and IHC bundles compared to controls (Fig 4F and G). Mutant hair bundles throughout the cochlea still displayed the 3–4 rows of stereocilia arranged in a regular "staircase-like" pattern as in age-matched control mice (see Fig 5A and B). Also, cochlear OHC apical circumferences have lost their immature rounded shape, to acquire a non-convex form moulded to the V-shape of the overlying hair bundle (arrowheads in Fig 4A, B, F and G).

The first notable morphological defect in $Clrn2^{clarinet/clarinet}$ mice was observed in the auditory hair cells of the cochlea towards the end of the first postnatal week. Detailed analyses at P8 revealed that the shortest row stereocilia in mutant OHCs appear shorter than those of $Clrn2^{+/+}$ littermates (Fig 5A and C). In addition, the tips of

 © 2019 The Authors

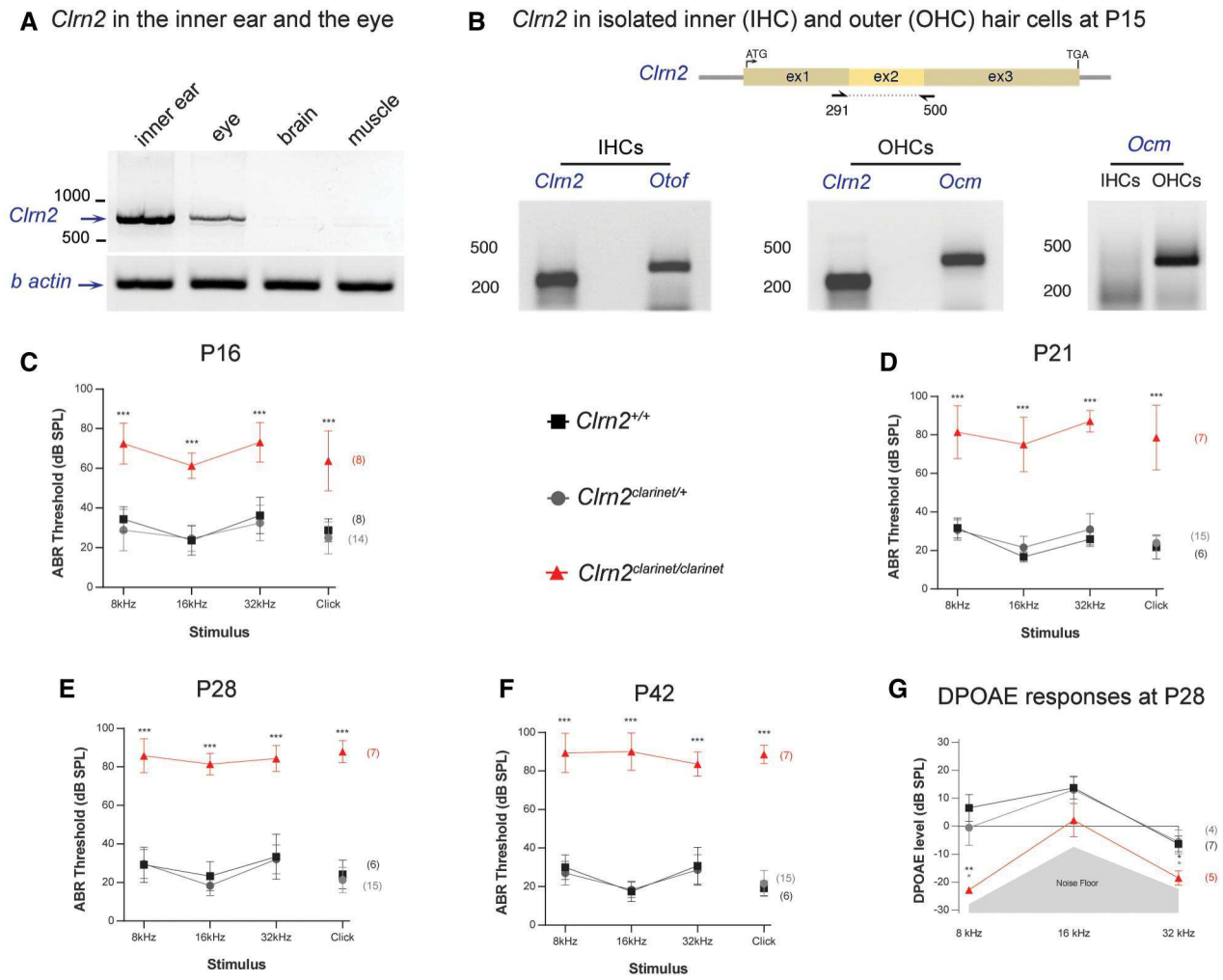

Figure 2. Clarin-2 is required for hearing function.

A RT–PCR analysis in P30 mice showing the presence of *Clrn2* transcripts in the inner ear and eye, but not in brain or muscle. β-actin was used as a positive control.

B *Clrn2* transcripts could be detected in both inner (IHCs) and outer (OHCs) hair cells of P15 wild-type mice. Otoferlin (*Otof*) and oncomodulin (*Ocm*) transcripts were used as positive controls for IHCs and OHCs, respectively. *Ocm* transcripts were only present in the OHC lysate, demonstrating that the IHC sample had not been contaminated with OHCs.

C–F Auditory phenotyping of *clarinet* mice at P16 (C), P21 (D), P28 (E) and P42 (F). ABR threshold measurements show that $Clrn2^{clarinet/clarinet}$ mice (red) exhibit a severe-to-profound hearing loss affecting all frequencies tested. At 16 kHz in $Clrn2^{clarinet/clarinet}$ mice, the mean ABR hearing thresholds vary from 55–65 dB SPL at P16, 60–90 dB SPL at P21 and to 80–100 dB SPL at P28 and P42. Age-matched $Clrn2^{+/+}$ (black) and $Clrn2^{clarinet/+}$ (grey) controls display thresholds within the expected range (15–45 dB SPL) at all frequencies and timepoints tested. At P16, all eight $Clrn2^{clarinet/clarinet}$ mice exhibited recordable ABR responses for each frequency tested and the click stimulus. For the longitudinal ABR study, at P21 and P28 three of the seven $Clrn2^{clarinet/clarinet}$ mice were found to not respond at the highest intensity stimulus (90 dB SPL) for at least one frequency-specific/click stimulus. By P42, five of the $Clrn2^{clarinet/clarinet}$ mice were found to not respond at the highest intensity stimulus (90 dB SPL) for at least two frequency-specific/click stimuli. ABR data shown are mean ± SD ***$P < 0.001$, one-way ANOVA.

G Averaged DPOAE responses for *clarinet* mice at P28, showing significantly reduced responses in $Clrn2^{clarinet/clarinet}$ mutants at all frequencies tested. DPOAE data shown are mean ± SD. *$P < 0.02$, **$P < 0.01$, one-way ANOVA. Please see Appendix Table S1 for exact *P*-values.

the middle and shortest row stereocilia in $Clrn2^{clarinet/clarinet}$ mutant IHCs are less prolate compared to $Clrn2^{+/+}$ littermates, instead displaying a rounded appearance (Fig 5B). Focusing on the second stereocilia row in both IHCs and OHCs, we used cochlear mid-turn electron micrographs from control and clarin-2-deficient hair bundles at P8 to score prolateness. At least 80 tip images per genotype were used—3 animals per genotype, 3 bundles per animal. We found a high prevalence of a rounded shape of the stereocilia from *clarinet* mice, as compared to age-matched wild-type mice, where the normal prolate shape is far more common ($P < 0.005$ for all cases, χ^2) (Fig EV3). To further characterize the bundle architecture, we measured the heights of OHC and IHC stereocilia (tallest, middle and shortest rows) within individual hair cell bundles from the mid-region of the cochlea (≥ 9 stereocilia per bundle, ≥ 2 bundles per animal, 3 animals per genotype). At P8 in OHC bundles, the average heights of stereocilia in all three rows are significantly shorter in $Clrn2^{clarinet/clarinet}$ mice relative to $Clrn2^{+/+}$ littermates (tallest −13%, middle −25%, shortest −52%) (Fig 5C). However, at P8 in

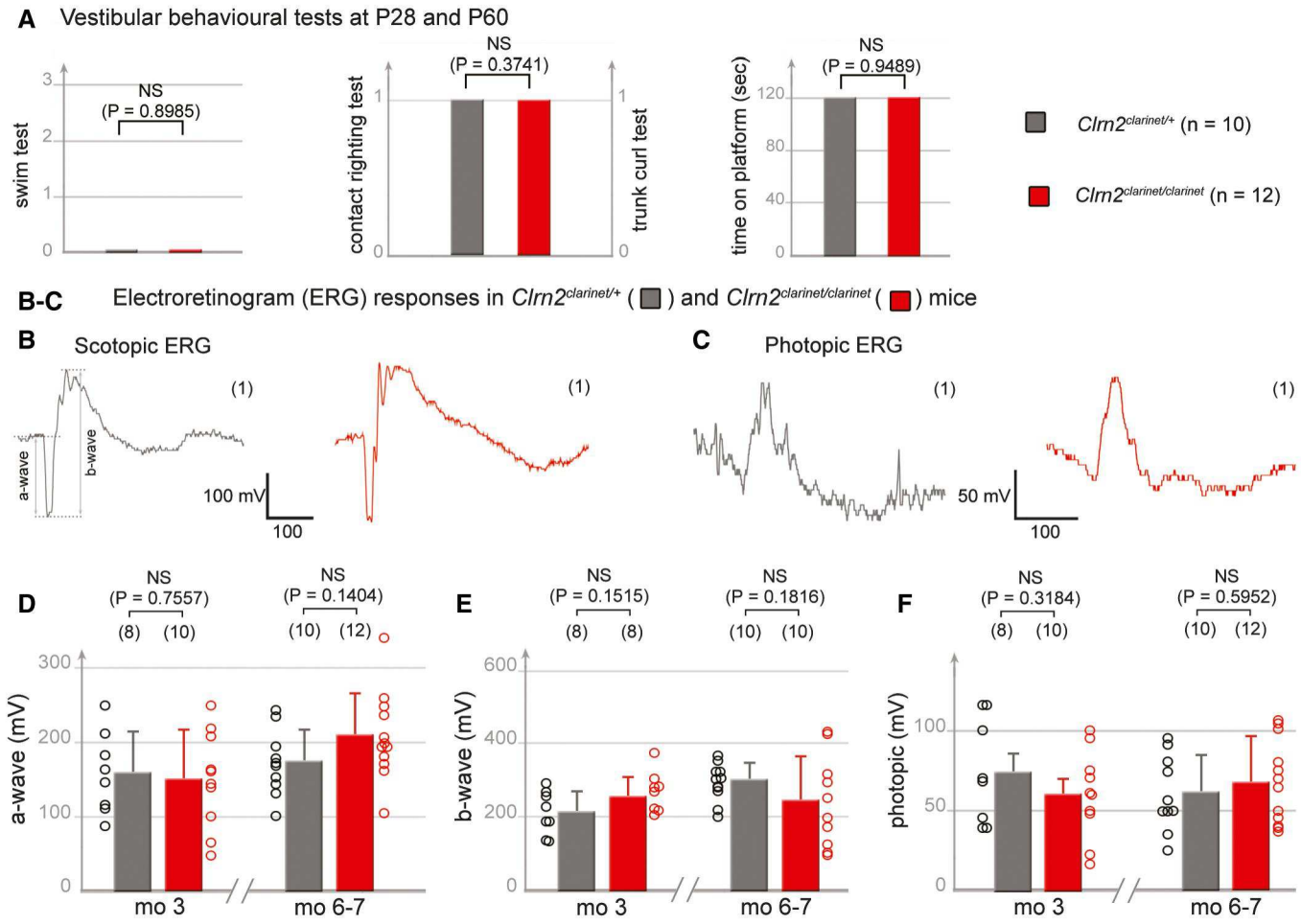

Figure 3. Clarin-2 is dispensable for balance and vision.

A Vestibular behavioural tests (swim tests, contact-righting, trunk-curl and platform). The *Clrn2*$^{clarinet/clarinet}$ mice (red, P28, n = 5, and P60, n = 7) have no vestibular dysfunction, displaying similar performances to age-matched control *Clrn2*$^{clarinet/+}$ mice (grey, P28, n = 3, and P60, n = 7) (Student's t-test was used for the platform assay, and the Pearson's Chi-squared test for other experiments). Being similar, the values at P28 and P60 were combined.

B–F Electroretinogram (ERG) measurements from control *Clrn2*$^{clarinet/+}$ (grey) and mutant *Clrn2*$^{clarinet/clarinet}$ (red) mice. Each trace in (B, C) is representative of an ERG response from the eye of age-matched *Clrn2*$^{clarinet/+}$ and *Clrn2*$^{clarinet/clarinet}$ mice, showing no significant difference in a- or b-wave amplitudes. (D–F) The lack of change in ERG amplitude responses in *Clrn2*$^{clarinet/clarinet}$ mice (aged 3 or 6–7 months), regardless of the test conditions: scotopic (D, E) or photopic (F) indicates normal photoreceptor kinetics and no change in the sensitivity of photoreceptor cells. The data shown are mean ± SEM. (NS) indicates a statistically non-significant difference ($P > 0.1$, Student's t-test).

IHC bundles we do not identify any significant differences in the average heights of stereocilia between *Clrn2*$^{clarinet/clarinet}$ mutants and *Clrn2*$^{+/+}$ controls in any row (Fig 5D). By P16 in OHC bundles, the average height of stereocilia in all three rows continue to be shorter in *Clrn2*$^{clarinet/clarinet}$ mice relative to *Clrn2*$^{+/+}$ littermates (tallest −9%, middle −25%, shortest −87%), with many short row stereocilia now missing (Fig 5C), and by P28, this row is entirely absent (Fig 5E, left panels). At P16 in IHC bundles, similar to P8 we do not identify any differences in the average heights of IHC stereocilia between *Clrn2*$^{clarinet/clarinet}$ mutants and *Clrn2*$^{+/+}$ controls in any row (Fig 5B and D). However, the tips of the middle and shortest row IHC stereocilia in *Clrn2*$^{clarinet/clarinet}$ mice continue to display a rounded appearance, unlike the pronounced prolate shape observed in *Clrn2*$^{+/+}$ littermates (Fig 5B). Furthermore, the height of the shorter-row stereocilia is more variable with some very short stereocilia measured (Fig 5D). Moreover, by P28 the heights of the middle and short row are visibly more variable in *Clrn2*$^{clarinet/clarinet}$ mice, and missing short row IHC stereocilia are evident (Fig 5E, right panels).

These data suggest that while clarin-2 is dispensable for patterning and establishment of the "staircase" bundle in young postnatal hair cells, it is critical for the maintenance of the transducing stereocilia in functionally mature inner and outer hair cells.

Clarin-2 is targeted to the hair bundles of the hair cells

To analyse the expression profile of *Clrn2*, whole-cochlea RNA extracts were prepared from wild-type mice at different embryonic and postnatal timepoints and utilized for quantitative RT–PCR (qRT–PCR) analysis of *Clrn2* transcripts. This shows that the relative abundance of *Clrn2* transcripts in the cochlea is stable from late embryonic stages to P12 (the onset of hearing in mice), but

 © 2019 The Authors

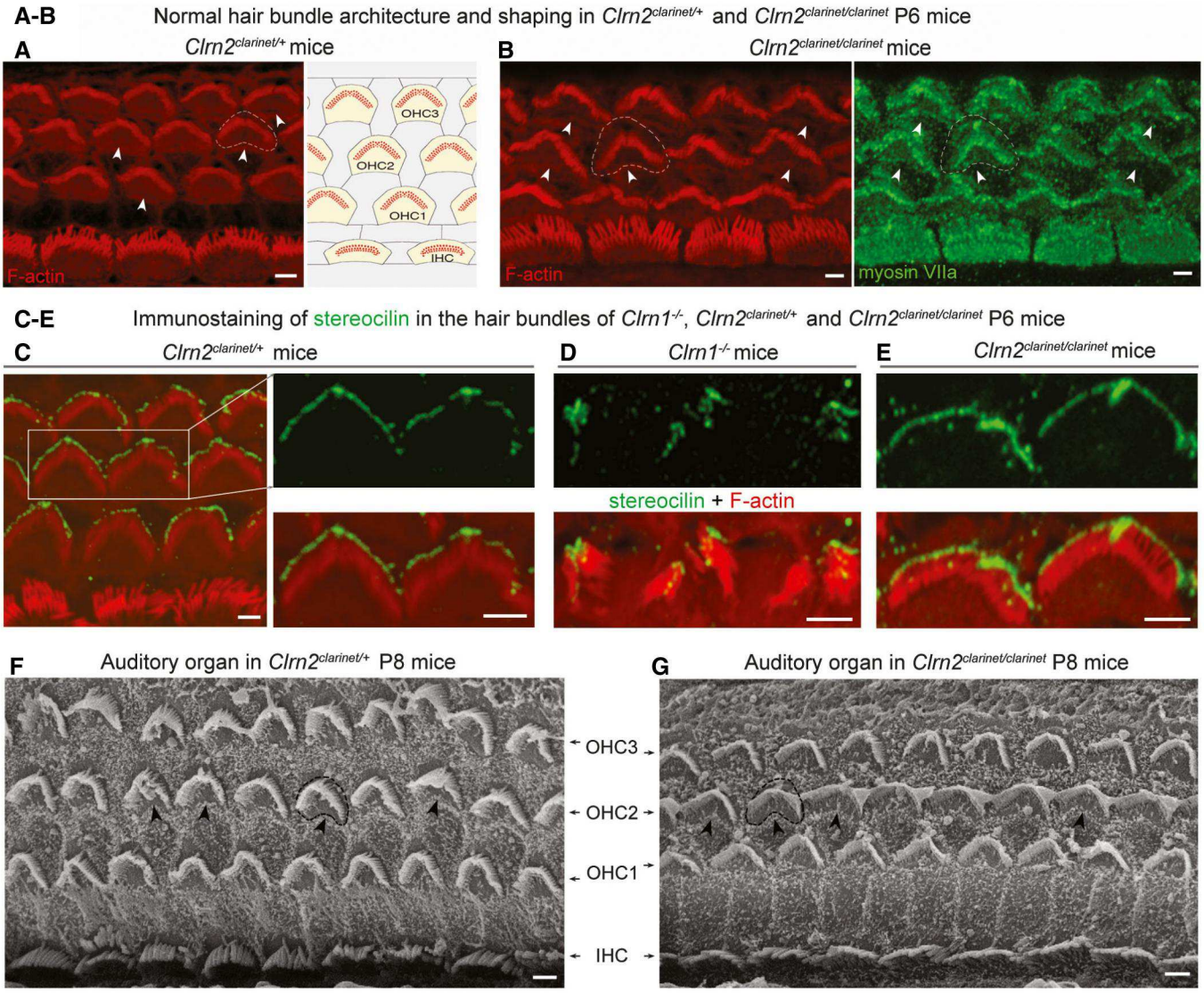

Figure 4. Normal architecture of cochlear hair bundles in *clarinet* mice.

A, B Confocal microscopy images of whole-mount preparations of mid-basal cochlear sensory epithelia from *Clrn2*$^{clarinet/+}$ (A) and *Clrn2*$^{clarinet/clarinet}$ (B) P6 mice immunostained for actin. Despite lack of clarin-2, the developing sensory epithelium of mutants is similar to that of heterozygous controls.

C–E Confocal microscopy images of whole-mount preparations of cochlear sensory epithelia from *Clrn2*$^{clarinet/+}$ (C), *Clrn1*$^{-/-}$ (D) and *Clrn2*$^{clarinet/clarinet}$ (E) P6 mice immunostained for stereocilin (green) and actin (red). Unlike the fragmented immunostaining in *Clrn1*$^{-/-}$ mice (mirroring the fragmentation of the hair bundle), stereocilin immunostaining in *Clrn2*$^{clarinet/clarinet}$ mice reflects the normally V-shaped bundles of OHCs, similar to *Clrn2*$^{clarinet/+}$ OHCs.

F, G Representative scanning electron micrographs of the sensory epithelium of *Clrn2*$^{clarinet/+}$ (F) and *Clrn2*$^{clarinet/clarinet}$ (G) P8 mice, showing no apparent differences in the gross patterning of IHCs and OHCs.

Data information: Arrowheads in (A, B) (white), (F, G) (black) illustrate the convex shape of the apical circumference of OHCs. Scale bars: 2 μm (A-E), 10 μm (F, G).

thereafter increases (Fig EV4A). Consistent with this finding, *in silico* analyses of the expression of *Clrn2* at different inner ear developmental and adult stages using the gEAR portal (*umgear.org*) reveal that while the *Clrn2* transcript is lowly expressed in the newborn inner ear and early postnatal stages, it is readily detected in P15 single-cell and adult-sorted hair cells (Liu *et al*, 2014, 2018; Ranum *et al*, 2019). In addition, the expression of *Clrn2* is detected in zebrafish hair cells (Steiner *et al*, 2014; Erickson & Nicolson, 2015). Interestingly, *Clrn2* transcripts were detected also in the auditory cortex (A1) and increased in levels between P7 and adult mice (Guo *et al*, 2016). The *Clrn2* expression in both IHCs and OHCs was confirmed by RT–PCR on isolated auditory hair cells from P15 mice (Fig 2B). Regarding protein localization, several attempts were made to immunodetect endogenous mouse clarin-2, including raising an antibody against mouse clarin-2. While this purified antibody was able to recognize overexpressed clarin-2 in transfected cells, it does not detect endogenous clarin-2 despite various tests using cochlear whole mounts from different postnatal stages, and under various conditions of fixation and antigen-retrieval (Fig EV4B–E). Therefore, an

© 2019 The Authors

injectoporation approach (Xiong *et al*, 2014) was utilized to deliver a GFP-tagged clarin-2 expression construct to P2 cochlear cultures (see Fig 6A). After incubation, the injectoporated organs of Corti were fixed and co-stained with an anti-GFP antibody to detect the clarin-2 fusion protein, and phalloidin to visualize the stereocilia. In contrast to supporting cells, where the GFP-tagged clarin-2 is distributed diffusely throughout the cytoplasm (Fig 6B and C), in auditory hair cells, clarin-2 is enriched in the apical stereocilia (Fig 6D–F).

Lack of clarin-2 causes selective defects in the mechano-electrical transduction machinery

To study molecular underpinnings of the bundle stereocilia remodelling in *clarinet* mice, we explored the distribution of myosin VIIa (used as a hair cell marker, Fig EV5A) and some selected proteins key to stereocilia growth and hair bundle organization (Figs 7 and EV5B–D). Considering the clarin-2 C-terminal class-II PDZ-binding motif, we investigated whether the absence of clarin-2 might

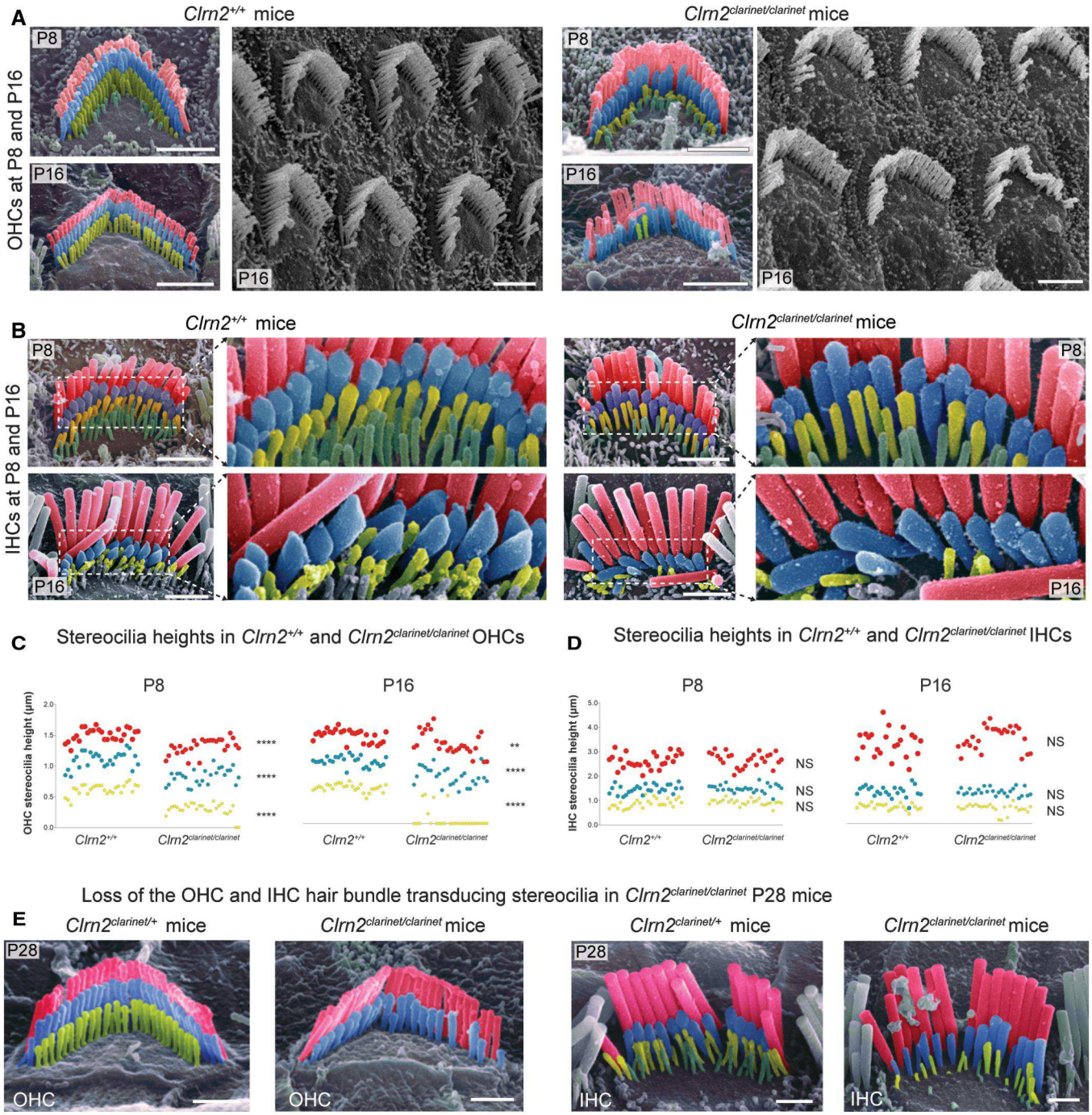

Figure 5.

© 2019 The Authors

Figure 5. Sensory hair cell bundle patterning and measurements in *clarinet* mice.

A, B Pseudo-coloured scanning electron micrographs of individual outer and inner hair cell bundles from *clarinet* mice at P8 and P16, showing that gross morphology of OHC and IHC bundles is similar between *Clrn2*$^{+/+}$ and *Clrn2*$^{clarinet/clarinet}$ mice. Representative images from the mid-region of the cochlear spiral are shown, and close-up views illustrate the three full rows, tallest (red), middle (blue) and short (yellow), of stereocilia in IHC and OHC hair bundles. At P8 and P16 (upper panels in A and B), the three stereocilia rows are observed in *Clrn2*$^{clarinet/clarinet}$ OHCs (A) and IHCs (B), although the shortest and middle rows of IHC stereocilia appear less prolate compared to controls.

C, D Distribution of individual stereocilia measures across genotypes at P8 and P16. (C) The OHC stereocilia measurements at both P8 and P16 (C) show a significant difference in height of *Clrn2*$^{+/+}$ stereocilia compared to *Clrn2*$^{clarinet/clarinet}$ in: e.g. for the shortest row at P8: *Clrn2*$^{+/+}$: 0.6188 ± 0.0944 p.μm (n = 27); *Clrn2*$^{clarinet/clarinet}$: 0.2948 ± 0.1029 p.μm (n = 27) (P < 0.0001, Mann–Whitney ranks comparison), and at P16: *Clrn2*$^{+/+}$: 0.579 ± 0.06179 p.μm (n = 27); *Clrn2*$^{clarinet/clarinet}$: 0.07282 ± 0.1626 p.μm (n = 27) (P < 0.0001, Mann–Whitney ranks comparison). Note the amount of value points equal to zero at P16. (D) Conversely, IHC stereocilia measurements at P8 and P16 did not show a difference between *Clrn2*$^{+/+}$ and *Clrn2*$^{clarinet/clarinet}$ in: for the shortest row at P8: *Clrn2*$^{+/+}$: 0.8808 ± 0.1753 p.μm (n = 27); *Clrn2*$^{clarinet/clarinet}$: 0.9313 ± 0.1217 p.μm (n = 27) (P = 0.2244, unpaired t-test); and at P16: *Clrn2*$^{+/+}$: 0.6784 ± 0.1171 p.μm (n = 23); *Clrn2*$^{clarinet/clarinet}$: 0.6063 ± 0.1855 p.μm (n = 26) (P = 0.2436, Mann–Whitney ranks comparison). **P < 0.01; ****P < 0.0001; NS P > 0.05.

E Pseudo-coloured scanning electron micrographs of individual OHC (left panels) and IHC (right panels) hair bundles from *clarinet* mice at P28. *Clrn2*$^{clarinet/clarinet}$ mutants have only two rows of OHC stereocilia, and the middle row of stereocilia is less uniform in height compared to controls. The middle and short rows of stereocilia in *Clrn2*$^{clarinet/clarinet}$ IHC bundles appear fewer in number, and heterogeneous in height.

Data information: Scale bars, 2 μm.

interfere with the subcellular distribution of PDZ-containing proteins, namely whirlin, PDZD7 and harmonin. These deafness defective PDZ-containing adaptor proteins have been shown to anchor stereocilia integral membrane proteins to the underlying cytoskeleton (Boeda *et al*, 2002; Mburu *et al*, 2003; Grati *et al*, 2012). Within stereocilia, the subcellular distribution of whirlin and PDZD7 immunostainings were identical in *Clrn2*$^{clarinet/clarinet}$ mice and *Clrn2*$^{clarinet/+}$ littermates, consistent with normal growth and proper shaping of the auditory hair bundles, respectively (Figs 7A and B, and EV5B; n = 5). Interestingly, in *Clrn2*$^{clarinet/clarinet}$ mice, the PDZD7 immunoreactive spots were arranged mostly in one row, between middle and tallest stereocilia (arrow), while in age-matched *Clrn2*$^{clarinet/clarinet}$ control mice, PDZD7 was additionally detected between short and middle stereocilia (arrowhead) rows (Figs 7A and EV5B).

We also investigated the distribution of the harmonin-b isoform, a core component in mechano-electrical transducer (MET) transduction machinery (Grillet *et al*, 2009; Michalski *et al*, 2009), which has been shown to directly bind to actin filaments anchoring the apical-most tip link component, cadherin-23, to the stereocilia underlying cytoskeleton (Kazmierczak *et al*, 2007). In wild-type mice, between P1 and P5, harmonin-b localization switches from the stereocilia tips to a region below the tip of tall and medium stereocilia, corresponding to the upper attachment point of the tip link (Lefevre *et al*, 2008). This switch also occurs in the absence of clarin-2, since almost all *Clrn2*$^{clarinet/clarinet}$ stereocilia tips are devoid of harmonin-b staining (Fig 7C and D). Nevertheless, the harmonin-b immunoreactive spots were mispositioned; being located much closer to the stereocilia tip in *Clrn2*$^{clarinet/clarinet}$ mice compared to age-matched P6 controls (Figs 7C and D, and EV5C). We used confocal micrographs to quantify the positioning of harmonin-b immunoreactive spots in the stereocilia at the mid-basal region of the cochlea (Fig 7E). Measurements were performed using IHC, rather than OHC, bundles, focusing on the tallest stereocilia to allow accurate measurements of the distance of the harmonin-b immunoreactive spot from the stereocilium tip in *Clrn2*$^{clarinet/+}$ and *Clrn2*$^{clarinet/clarinet}$ P6 mice (Fig 7E). The positioning of the harmonin-b immunoreactive spots, relative to the tip of the tallest stereocilium, was observed on average at 575 ± 23 nm (mean ± SEM; n = 35 hair bundles from 5 mice) in *Clrn2*$^{clarinet/clarinet}$ mice, as compared to 850 ± 28 nm (mean ± SEM; n = 31 hair bundles from 5 mice) in *Clrn2*$^{clarinet/+}$ mice (Fig 7F) (P < 0.0001, Student's t-test).

Given the reported function of clarin-1 in maturation of IHC ribbon synapses (Zallocchi *et al*, 2012; Ogun & Zallocchi, 2014), we also used immunolabelling to examine the ribbon synapse in *clarinet* cochlear whole mounts. In P21 apical-coil IHCs, a similar number of pre-synaptic ribbons (Ribeye-positive puncta) and post-synaptic densities (GluR2-positive puncta) were observed in *Clrn2*$^{+/+}$ and *Clrn2*$^{clarinet/+}$ control and *Clrn2*$^{clarinet/clarinet}$ mutant mice (Fig 7G and H). Furthermore, Ribeye-positive puncta and GluR2-positive puncta were juxtaposed in all genotypes (Fig 7G and H), as previously described (Brandt *et al*, 2005; Valeria *et al*, 2013), indicating normal coordination of synaptic body components and functional IHC ribbon synapses.

Lack of clarin-2 disrupts hair cell transducer currents in auditory hair cells

Harmonin-b relocation to the upper link tip link density has been ascribed to its interaction with the tip link component cadherin-23 (Boeda *et al*, 2002; Grillet *et al*, 2009; Michalski *et al*, 2009). Harmonin-b mispositioning in the absence of clarin-2 (Fig 7D–F) might infer a decrease in the MET-induced tension forces, which is consistent with the high prevalence of round- and oblate-shaped stereocilia tips at this stage in *Clrn2*$^{clarinet/clarinet}$ mice (Figs 5B and EV3). To further investigate hair cell function, MET currents were recorded from P6–8 apical-coil OHCs by displacing their hair bundles in the excitatory and inhibitory direction using a piezo-driven fluid jet (Corns *et al*, 2014, 2016). At hyperpolarized membrane potentials (−121 mv), the displacement of the hair bundle in the excitatory direction (i.e. towards the taller stereocilia) elicited a large inward MET current in OHCs from both *Clrn2*$^{clarinet/+}$ and *Clrn2*$^{clarinet/clarinet}$ mice (Fig 8A and B). The maximal MET current in 1.3 mM Ca^{2+} was significantly different (P < 0.0001) between *Clrn2*$^{clarinet/+}$ (−1,842 ± 66 pA at −121 mV, n = 7) and *Clrn2*$^{clarinet/clarinet}$ (−902 ± 39 pA, n = 9) OHCs (Fig 8C). The resting current flowing through open MET channels in the absence of mechanical stimulation was reduced when bundles were moved in the inhibitory direction (i.e. away from the taller stereocilia) in all OHCs tested (Fig 8A and B, arrows). Despite the different size of the maximal MET current, the open probability

© 2019 The Authors

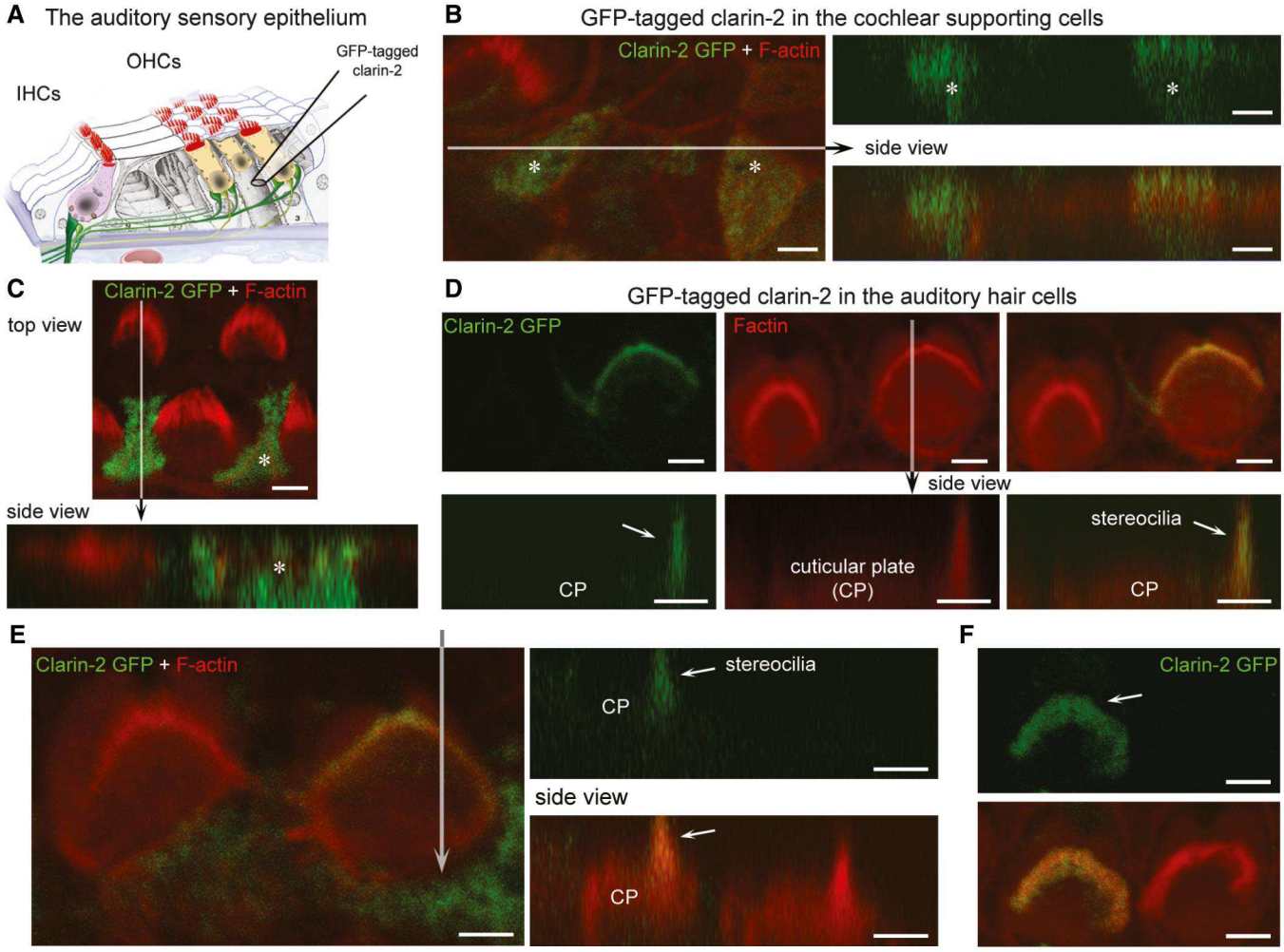

Figure 6. Expression of clarin-2 in the hair bundle of auditory hair cells.

A Schematic representation of the auditory sensory organ, illustrating the positioning of the electrode used for injectoporation of GFP-tagged clarin-2 construct into cochlear supporting and hair cells.

B–F Top and side views of representative images of supporting cells (asterisk) and hair cells expressing clarin-2. In supporting cells, GFP-tagged clarin-2 (green) was distributed diffusely throughout the cytoplasm (B, C). By contrast, in all injectoporated hair cells, the majority of clarin-2 was observed in the apical stereocilia (D–F). Arrows indicate position of the hair bundle stereocilia. Scale bars, 2 μm.

of MET channels was similar between *Clrn2*$^{clarinet/+}$ and *Clrn2*$^{clarinet/clarinet}$ OHCs (Fig 8D and E). Because the MET current reverses near 0 mV, it became outward when excitatory bundle stimulation was applied during voltage steps positive to its reversal potential (Fig 8A–C). At positive membrane potentials (+99 mV), the larger resting MET current (Fig 8A and B, arrowheads), which is due to an increased open probability of the transducer channel resulting from a reduced driving force for Ca^{2+} influx (Crawford *et al*, 1989; Corns *et al*, 2014), was also similar between the two genotypes (Fig 8D). Similar findings were also observed in basal-coil OHCs (Fig 8E) and apical-coil IHCs (Fig 8F–H), with a significant reduction in the maximum MET current in *Clrn2*$^{clarinet/clarinet}$ mutants ($P < 0.0001$ for both hair cell types), but similar resting open probability, between *Clrn2*$^{clarinet/+}$ and *Clrn2*$^{clarinet/clarinet}$ mice.

Overall, these data show that clarin-2 is required for normal MET current in developing cochlear hair cells.

Clarin-2 is required for the functional differentiation of IHCs, but not OHCs

In the mouse cochlea, the onset of adult-like characteristics in OHCs occurs at around P8 with the expression of the negatively activated K^+ current $I_{K,n}$ (Marcotti & Kros, 1999) carried by the KCNQ4 channel (Kubisch *et al*, 1999). Potassium currents in apical-coil OHCs from P22 *clarinet* mice were elicited by applying a series of depolarizing voltage steps in 10 mV increments from −144 mV (holding potential was −84 mV). We found that adult OHCs from *Clrn2*$^{clarinet/+}$ and *Clrn2*$^{clarinet/clarinet}$ mice express the same complement of K^+ currents (Fig 9A–C). The size of the total outward K^+ current at 0 mV, which includes $I_{K,n}$ and the classical delayed rectified outward K^+ current I_K (Marcotti & Kros, 1999), was similar between *Clrn2*$^{clarinet/+}$ (2.9 ± 0.6 nA, $n = 5$) and *Clrn2*$^{clarinet/clarinet}$ (3.2 ± 0.5 nA, $n = 6$) P22 OHCs. The size of $I_{K,n}$ was also similar

 © 2019 The Authors

between the two genotypes. These results indicate that absence of clarin-2 does not influence the acquisition of the adult-like basolateral membrane properties of OHCs.

Different to the OHCs, the onset of adult-like characteristics in IHCs occurs at around P12 (Kros *et al*, 1998; Marcotti, 2012). The IHC functional maturation is achieved by the down-regulation of immature-type currents (e.g. Na^+ current and the small conductance Ca^{2+}-activated K^+ current carried by SK2 channels) and inward rectifier (K1) currents) and expression of $I_{K,n}$ and the fast-activating large-conductance Ca^{2+}-activated K^+ current ($I_{K,f}$: carried by BK

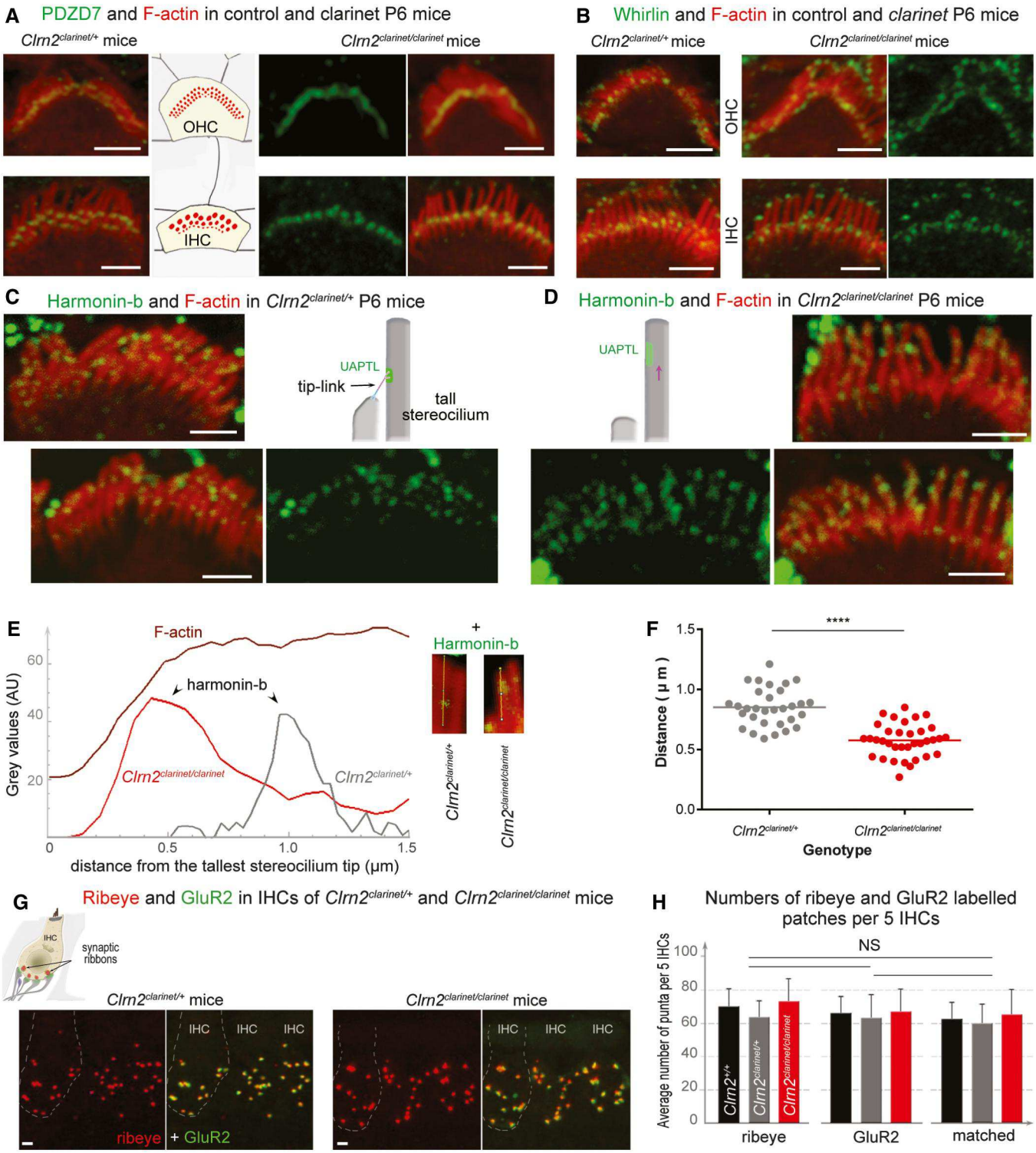

Figure 7.

Figure 7. The distribution of hair bundle and synaptic proteins in *clarinet* mice.

A, B Confocal images of IHC and OHC hair bundles of *Clrn2*$^{clarinet/clarinet}$ mice and heterozygous littermates at P6 immunostained for PDZD7 (A, green) and whirlin (B, green) and actin (red in both figures). The PDZD7 immunostaining is normally restricted to the base of stereocilia in both *Clrn2*$^{clarinet/+}$ and *Clrn2*$^{clarinet/clarinet}$ P6 mice (A). Whirlin immunostaining is properly located at the stereocilia tips of IHC and OHC hair bundles (B).

C–F Harmonin-b immunostaining in IHC hair bundles. In *Clrn2*$^{clarinet/clarinet}$ mice (D), the harmonin-b immunoreactive puncta (green) were still observable on the stereocilia, but unlike in age-matched heterozygote littermates (C), were located much closer to the tip of stereocilia (indicated by the purple arrow). The two diagrams in (C) and (D) illustrate the position of harmonin-b immunostaining (green) corresponding to the site of the upper attachment point of the tip link (UAPTL), facing the tip link. The bright green signal outside stereociliary bundles are non-specific. The change of harmonin-b localization along the stereocilium in *Clrn2*$^{clarinet/clarinet}$ mice is illustrated further by line scan (E) and quantification (F) analyses. The insets in (E) show images of individual stereocilia used for the line scan signal analysis. The harmonin-b immunoreactive puncta were located within 850 ± 28 nm (mean ± SEM) distance from the tip of the tallest stereocilia in *Clrn2*$^{clarinet/+}$ mice (n = 31 hair bundles from 5 mice) (F), and within 575 ± 23 nm in *Clrn2*$^{clarinet/clarinet}$ mice (n = 35 hair bundles from 5 mice). Individual data points are shown and mean indicated by a horizontal bar. ****$P < 0.0001$, Student's t-test.

G, H (G) Cochlear whole mounts from P21 *clarinet* mice, labelled with the IHC pre-synaptic ribbon marker Ribeye (red) and the post-synaptic density marker GluR2 (green), showing a similar number of total and matched Ribeye-positive and GluR2-positive puncta in *Clrn2*$^{clarinet/clarinet}$ mutant cochleae compared to *Clrn2*$^{clarinet/+}$ littermates, which is reflected in puncta counted per five hair cells (H) n = 4 per genotype. Data shown are mean ± SD, one-way ANOVA.

Data information: Scale bars, 2 μm.

channels) (Marcotti *et al*, 2003). Initially, we measured the size of the total outward K^+ current at 0 mV in P22 IHCs and found that it was similar between *Clrn2*$^{clarinet/+}$ controls (11.6 ± 1.6 nA, n = 4) and *Clrn2*$^{clarinet/clarinet}$ mutants (10.7 ± 1.0 nA, n = 5). For these experiments, currents were elicited by applying depolarizing voltage steps in 10 mV nominal increments from –124 mV up to + 30 mV, starting from the holding potential of −84 mV. However, a close inspection of the time-course of current activation showed some differences, which were evaluated in more detail by delivering a voltage protocol that allowed the evaluation of both $I_{K,n}$ and $I_{K,f}$ (Fig 9D–F). IHCs were held at −64 mV and subjected to depolarizing voltages in 10 mV nominal increments from −144 mV to more positive values. We found that while *Clrn2*$^{clarinet/+}$ IHCs exhibit both $I_{K,n}$ and $I_{K,f}$, *Clrn2*$^{clarinet/clarinet}$ IHCs fail to show the above currents and instead express I_{K1} (Fig 9D–F), which is characteristic of a pre-hearing IHC (Marcotti *et al*, 1999). The physiological consequence of the above abnormalities was that adult *Clrn2*$^{clarinet/clarinet}$ IHCs did not acquire the fast-graded voltage responses to stimulation normally present in mature cells (Fig 9G and H) and, in some cases, retained the ability to fire an initial Ca^{2+}-dependent action potentials (Fig 9I) that is characteristic of immature cells (Kros *et al*, 1998; Marcotti *et al*, 2003). We found that immature-type currents were not down-regulated in *Clrn2*$^{clarinet/clarinet}$ IHCs, and as such, their functional differentiation into mature cells was prevented.

Discussion

We demonstrate that *Clrn2* is a novel deafness gene required for maintenance of transducing stereocilia in the sensory cochlear hair cells. Our results show that the absence of clarin-2 leads to an early-onset hearing loss in *clarinet* mice, which is moderate-to-severe at P16, but rapidly progresses to profound hearing loss after P21. Moreover, our morpho-functional and molecular studies of clarin-2-deficient mice demonstrate this protein is critically required for late-stage cochlear hair bundle maintenance and function. In particular, we show that while clarin-2 is dispensable for the acquisition of polarized and assembled stereocilia bundles, the protein is essential for maintaining bundle integrity and normal sound-induced mechano-electrical transduction.

Hair bundle formation and polarization is a multi-step process with three main phases reported in the mouse—initial (E15-P0), intermediate (P1-P5) and final (P6-P15) stages (Lefevre *et al*, 2008). During phase 1, growth of the stereocilia rows is uniform, whereas in phase 2 differential elongation leads to the staircase pattern, with concomitant regression of supernumerary stereocilia in the mature hair bundle (Kaltenbach *et al*, 1994). Previous work has shown that clarin-1 is critically involved in formation of properly shaped IHC and OHC hair bundles (Geller *et al*, 2009; Geng *et al*, 2009, 2012; Dulon *et al*, 2018). Importantly, no such disorganization occurs in the absence of clarin-2. We show that during cochlear development and maturation, the OHC and IHC hair cell bundles in clarin-2-deficient mice appear to grow normally up to ~P5, developing their characteristic "staircase" architecture, and typical V- and U-shape organization, respectively. Indeed, by P6 almost all cochlear OHC apical circumferences have lost their immature rounded shape, to acquire a non-convex form moulded to the V-shape of the overlying hair bundle (arrowheads in Fig 4A, B, F and G). Together, these findings suggest that polarity cues (Kelly & Chen, 2007; Ezan & Montcouquiol, 2013), as well as the interactions and cellular remodelling between supporting and sensory hair cells necessary for normal patterning of the auditory organ (Keller *et al*, 2000; Etournay *et al*, 2010), occur normally in the absence of clarin-2. Furthermore, the persistence of immunostaining for PDZD7, a key member of the ankle link complex at the stereocilia base, correlates with the proper shaping of the V- and U-shaped hair bundles (Grati *et al*, 2012). Also, the persistence of whirlin (Fig 7B) and EPS8 (Fig EV5D), two proteins key for actin polymerization, at the tips of the differentiating stereocilia (Mburu *et al*, 2003; Manor *et al*, 2011; Zampini *et al*, 2011) are consistent with normal stereocilia elongation up to at least P8 in the absence of clarin-2. Moreover, stereocilin is properly targeted to the distal tips of the tallest row stereocilia, indicating normal anchoring of these OHC stereocilia into the overlying tectorial membrane. Thus, we conclude that the first molecular and structural steps of hair bundle morphogenesis (initial and intermediate phases) are not affected in the absence of clarin-2.

Our qRT–PCR analyses show a postnatal increase of *Clrn2* transcripts in wild-type mouse cochleae, indicating a potential key function after the onset of hearing (~P12 in mice). We show that upon injectoporation into cochlear organs, clarin-2 localizes to stereocilia. Interestingly, only in hair cells does GFP-tagged clarin-2 target to apical surface cell membranes, indicating that additional hair cell-specific co-factors are likely required for proper

 © 2019 The Authors

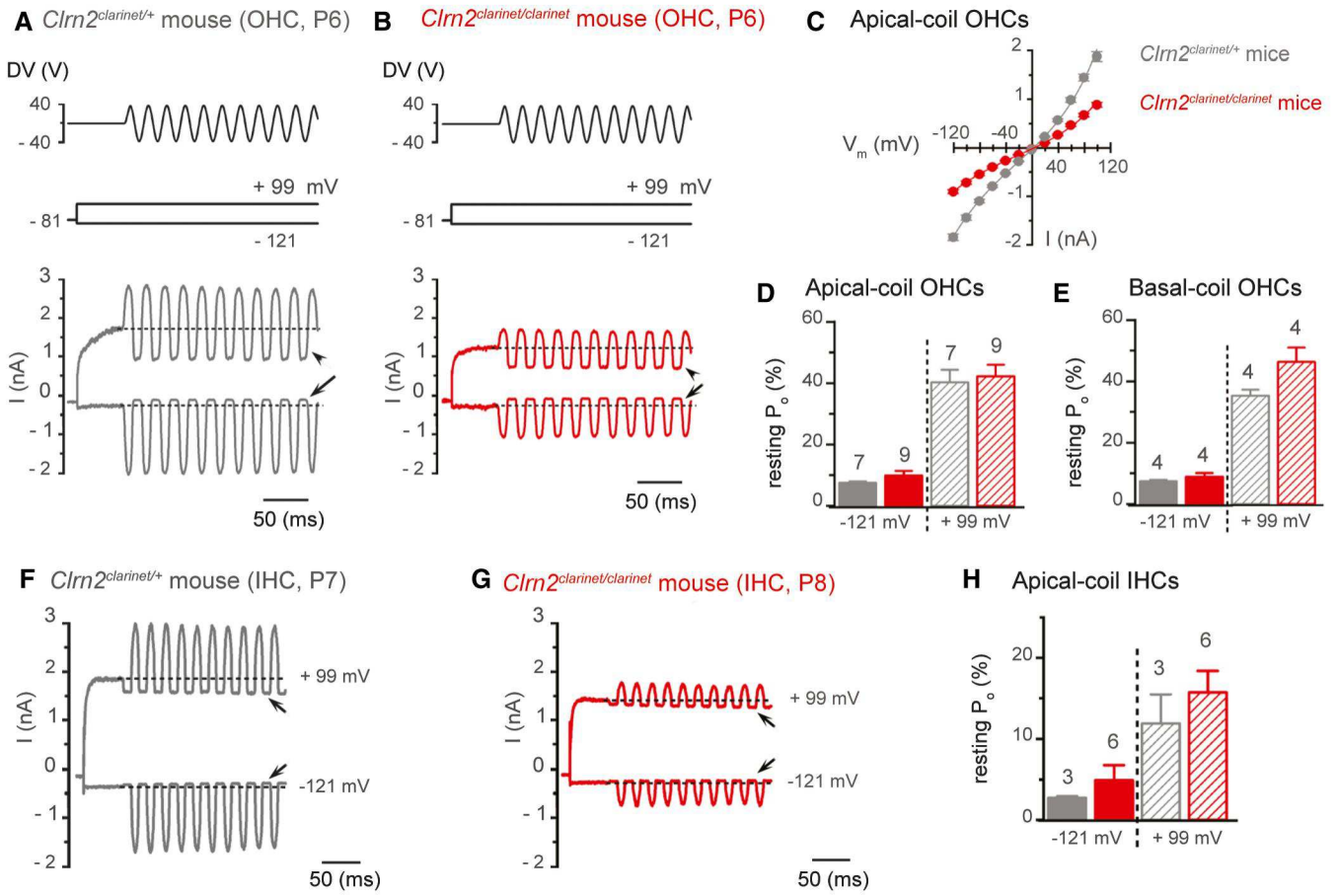

Figure 8. *Clrn2* is required for the acquisition of normal mechano-electrical transducer (MET) function in immature cochlear hair cells.

A, B Saturating MET currents recorded from P6 *Clrn2*$^{clarinet/+}$ (A) and *Clrn2*$^{clarinet/clarinet}$ (B) apical-coil OHCs by applying sinusoidal force stimuli of 50 Hz to the hair bundles at −121 mV and +99 mV. The driver voltage (DV) signal of ± 40 V to the fluid jet is shown above the traces (positive deflections of the DV are excitatory). The holding potential was −81 mV. Extracellular Ca^{2+} concentration was 1.3 mM. Arrows and arrowheads indicate the closure of the MET currents (i.e. resting MET current) elicited during inhibitory bundle displacements at hyperpolarized and depolarized membrane potentials, respectively. Dashed lines indicate the holding current, which is the current at the holding membrane potential.

C Average peak-to-peak current–voltage curves recorded from *Clrn2*$^{clarinet/+}$ (grey, P6, n = 7) and *Clrn2*$^{clarinet/clarinet}$ (red, P6-7, n = 9) apical-coil OHCs.

D, E Resting open probability (P_o) of the MET current at the membrane potential of −121 mV and +99 mV from apical- (D) and basal-coil (E) OHCs. Number of OHCs investigated is shown above the columns. Data shown are mean ± SEM.

F, G Saturating MET currents recorded from a P7 *Clrn2*$^{clarinet/+}$ (F) and a P8 *Clrn2*$^{clarinet/clarinet}$ (G) apical-coil IHC using the same experimental protocol described above.

H Average P_o of the MET current measured in apical-coil IHCs at the membrane potential of −121 mV and +99 mV from *Clrn2*$^{clarinet/+}$ (P7, n = 3) and *Clrn2*$^{clarinet/clarinet}$ (P7-8, n = 6) apical-coil IHCs. Data shown are mean ± SEM.

subcellular targeting of clarin-2 to the plasma membrane of stereocilia. In the *Clrn2*$^{clarinet/clarinet}$ mice, despite normal shape organization, the absence of clarin-2 leads to a progressive reduction in height of the middle and shortest row stereocilia, which is evident first in OHCs by P8, and then later in IHCs at P16. It is noteworthy that an abnormal shortening of mechanotransducing stereocilia has also been reported in mice deficient for several components of the mechano-electrical transduction machinery, namely the TMC1/TMC2 channel complex (Kawashima *et al*, 2011), TMIE (Zhao *et al*, 2014), LHFPL5 (Xiong *et al*, 2012), and sans or cadherin-23 (Caberlotto *et al*, 2011) and PCDH15 (Pepermans *et al*, 2014). Furthermore, Velez-Ortega and colleagues recently showed that reducing mechano-electrical transduction currents in wild-type mouse or rat hair cells, using pharmacological channel blockers or disruption of tip links, leads to reduction in the height of the middle and shortest row "transducing" stereocilia (Velez-Ortega *et al*, 2017). Thus, it is possible that the stereocilia phenotype observed in *clarinet* mutant mice is a downstream consequence of a defect in mechano-electrical transduction. Indeed, the onset of regression of the mechanotransducing stereocilia, occurring in the absence of clarin-2, is concomitant with the loss of normal MET responses, which are already identifiable by P6-7 at both the molecular and functional levels. First, from P8 onwards, instead of the normal prolate-shaped tips of the transducing stereocilia evident in wild-type mice, which is believed to be a result of the traction force exerted by the tip link on the stereocilium apical membrane (Rzadzinska *et al*, 2004; Prost *et al*, 2007), clarin-2-deficient transducing

© 2019 The Authors

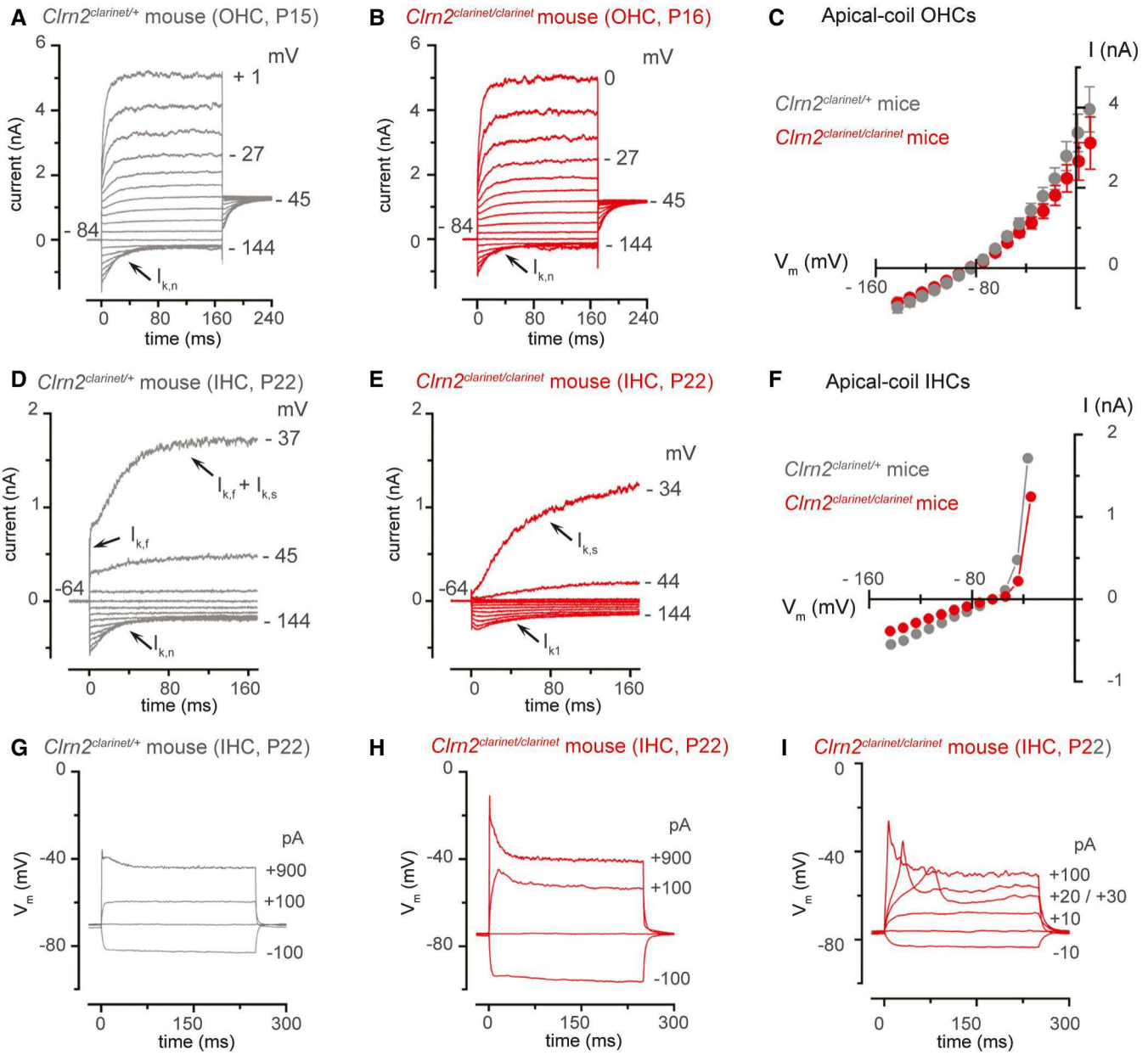

Figure 9. IHCs, but not OHCs, fail to acquire adult-like basolateral currents in *clarinet* mice.

A, B Potassium currents recorded from mature *Clrn2*$^{clarinet/+}$ (A, P15) and *Clrn2*$^{clarinet/clarinet}$ (B, P16) apical-coil OHCs. Currents were elicited by depolarizing voltage steps (10 mV nominal increments) from −144 mV to more depolarized values from the holding potential of −84 mV. Note that the current characteristic of mature OHCs. The size of $I_{K,n}$, measured in isolation as the deactivating tail currents (difference between instantaneous and steady-state inward currents) for voltage steps from the holding potential to −124 mV, was 545 ± 115 pA (n = 5) *in Clrn2*$^{clarinet/+}$ and 595 ± 67 pA (n = 7) in *Clrn2*$^{clarinet/clarinet}$ OHCs.

C Average peak current–voltage relation for the total K^+ current recorded from *Clrn2*$^{clarinet/+}$ (P15-16, n = 7) and *Clrn2*$^{clarinet/clarinet}$ (P15-16, n = 5) OHCs. Data shown are mean ± SEM.

D, E Potassium currents recorded from P22 mature *Clrn2*$^{clarinet/+}$ and *Clrn2*$^{clarinet/clarinet}$ apical-coil IHCs, respectively, using the same voltage protocol described above. Holding potential of −64 mV.

F Peak current–voltage relation for the total K^+ current recorded from the IHCs shown in panel (A) and (B).

G–I Voltage responses from P22 *Clrn2*$^{clarinet/+}$ (G) and *Clrn2*$^{clarinet/clarinet}$ (H,I) IHCs. Note that Ca^{2+}-dependent action potentials could be induced in mature IHCs (I).

stereocilia display round, oblate apical stereocilia wedges (Fig EV3). Second, the number of PDZD7 immunoreactive spots, essentially between the short and middle transducing stereocilia, is decreased in the absence of clarin-2, indicating loss of cytoskeleton–membrane crosslinkers that probably accompanies the regression of the short stereocilia row (morphologically visible at later stages, about P16 in OHCs). Third, the actin-binding USH1C protein harmonin-b (Boeda *et al*, 2002), a core component of the MET machinery (Grillet *et al*, 2009; Michalski *et al*, 2009), is mislocalized in the absence of clarin-2 at P6. A similar

 © 2019 The Authors

harmonin-b mislocation has been observed in mutant mice lacking cadherin 23- and PCDH15-composed tip links (Lefevre *et al*, 2008), which implies the necessity of mechano-electrical transduction-induced tension forces to maintain the recruitment of harmonin-b to the upper attachment point of the tip link, facing the tips of the adjacent shorter stereocilia actin core. Finally, detailed electrophysiological recordings in IHCs and OHCs at P6-8 showed that in the absence of clarin-2 the properties of the MET channel are normal, as shown by the similar resting open probability at positive membrane potentials, indicative of reduced adaptation in the unstimulated bundle from both genotypes (Corns *et al*, 2014). However, the maximal current is significantly reduced by approximately 50% in mutant IHCs and OHCs, indicating there are less available functional channels. This reduction could result from missing tip links and/or lack of sustaining tension on still present tip links, which would also be consistent with our finding of non-prolate middle and shortest row stereocilia. The presence of a functional MET current in pre-hearing IHCs, but not OHCs, has been shown to be crucial for their functional maturation into fully functional sensory receptors (Corns *et al*, 2018).

In humans, recessive *CLRN1* mutations cause Usher syndrome type IIIA (USH3A, MIM276902), characterized by post-lingual, progressive hearing loss, and variable balance and vision loss deficits (Adato *et al*, 2002). Interestingly, almost all USH3A patients develop normal speech, and a number display only mild-to-moderate hearing threshold elevation at the time of hearing loss diagnosis, at an age of 30–40 years (Ness *et al*, 2003). This contrasts with the phenotype of *Clrn1* knockout mice, where lack of clarin-1 has been shown to cause an early profound hearing loss (Geller *et al*, 2009; Geng *et al*, 2009, 2012; Dulon *et al*, 2018). Additionally, $Clrn1^{N48K}$ mouse mutants exhibit profound hearing loss by P25, even though USH3A patients with the $CLRN1^{N48K}$ mutation display post-lingual progressive hearing loss (Ness *et al*, 2003; Geng *et al*, 2012). Furthermore, *Clrn1* knockout mice do not exhibit overt retinal deficits, and so do not model this aspect of USH3A. Our characterization of the *clarinet* mutant establishes that lack of clarin-2 results in a progressive, early-onset hearing loss in mice, with no overt retinal deficits. However, given the interspecies difference in phenotypic presentation observed with *Clrn1*, we cannot exclude the possibility that pathogenic *CLRN2* mutations in humans might give rise to an Usher syndrome-like phenotype. Moreover, our studies show that clarin-2, unlike clarin-1 which is required during embryonic stages, is dispensable for the patterning and establishment of the "staircase" bundle in young postnatal hair cells. This finding supports our hypothesis that clarin-2 has an important role in functionally mature cochlear hair cells to maintain proper integrity of the transducing stereocilia. Accordingly, we investigated the UK Biobank cohort and found that genetic variation at the human *CLRN2* locus is highly associated with adult hearing difficulty in this cohort.

Our analysis revealed a cluster of SNPs that lie within, or close to, the *CLRN2* gene, which are significantly associated with an adult hearing difficulty phenotype. Within the 20 most highly associated SNPs, the majority are either intronic or intergenic (Table EV1). As such, it is probable that these do not directly affect *CLRN2* expression. Instead, these SNPs are likely in linkage disequilibrium with an, as yet unidentified, causal variant(s) within the UK Biobank population cohort. However, the second most associated SNP (rs13147559) is located within the *CLRN2* gene coding sequence (c.337C > G), with presence of the minor allele causing a leucine-to-valine missense variation at codon 113 (p.Leu113Val). This leucine residue, based on comparison to the 3D modelling prediction of hsCLRN1 (Gyorgy *et al*, 2019), is located within the second transmembrane domain of hsCLRN2 and is evolutionarily conserved across species. While this variation involves two hydrophobic amino acids that possess similar structures, valine does have a shorter side chain. Furthermore, prediction tools suggest that this substitution might be detrimental to protein function returning scores of "possibly damaging" and "medium". Interestingly, similar substitutions located in the highly conserved transmembrane domains of presenilin, encoded by the gene *PSEN1*, have been reported in patients with Alzheimer's disease. These missense variants (p.Leu250Val and p.Leu153Val) have been proposed to interfere with the helix alignment of the transmembrane domain altering protein optimal activity, thus accounting for disease expression (Furuya *et al*, 2003; Larner, 2013). However, additional studies are needed to determine whether the hsCLRN2 p.Leu113Val missense variant is causal of, or merely associated with, the adult hearing difficulty trait. Perhaps it may be that "mild" *CLRN2* hypomorphic mutations, such as p.Leu113Val may represent, is likely to predispose to a progressive, late-onset hearing loss phenotype. Conversely, it is possible that more pathogenic *CLRN2* mutations may elicit a more severe, early-onset hearing loss phenotype. There are examples of this, for instance *TMPRSS3*, encoding transmembrane protease serine 3, has been reported to cause severe-to-profound prelingual hearing loss (DFNB10) as well as progressive hearing impairment with post-lingual onset (DFNB8) due to differential pathogenic mutations (Gao *et al*, 2017). Of note, a recent work by Gopal S. and colleagues reported a recessively inherited non-syndromic sensorineural hearing loss in a consanguineous Iranian family caused by a *CLRN2* mutation that results in a missense mutation in the encoded protein (Gopal *et al*, 2019). Affected patients develop post-lingual moderate-to-profound hearing loss with no indication of balance or vision deficits. Altogether, while mutations in *CLRN1* unambiguously lead to USH3A, current findings suggest that *CLRN2* mutation most likely causes non-syndromic hearing loss. However, additional cases need to be identified to clarify the genotype–phenotype relationship between the impaired extent of activity of the mutated clarin-2 protein, the age of onset, the severity and the extent of the disease phenotype. Nonetheless, our study demonstrates the utility of interrogating human large cohort study data as a means to help validate candidate genes arising from forward genetic, or whole-genome sequencing, screens.

Conclusion

$Clrn2^{clarinet}$ mice are ENU-induced mutants that exhibit early-onset sensorineural hearing loss, associated with a nonsense mutation in the encoded tetraspan protein clarin-2. Utilizing these mice, we demonstrate that clarin-2 is required for the maintenance of stereocilia bundle morphology, and show that its loss leads to decreased mechano-electrical transduction and progressive hearing impairment. Moreover, utilizing data from the UK Biobank study, *CLRN2* is identified as a novel candidate gene for human non-syndromic progressive age-related hearing loss. Our study of the *clarinet* mouse

© 2019 The Authors

mutant provides insight into the interplay between mechano-electrical transduction and stereocilia bundle maintenance.

Materials and Methods

Mice

The *clarinet* mutant was identified from the MRC Harwell Institute phenotype-driven *N*-ethyl-*N*-nitrosourea (ENU) Ageing Screen (Potter *et al*, 2016). In this screen, ENU-mutagenized C57BL/6J males were mated with wild-type "sighted C3H" (C3H.Pde6b+) females (Hoelter *et al*, 2008). The resulting G_1 males were crossed with C3H.Pde6b+ females to produce G_2 females, all of which were screened for the *Cdh23*^{ahl} allele (Johnson *et al*, 2006). *Cdh23*$^{+/+}$ G_2 females were then backcrossed to their G_1 fathers to generate recessive G_3 pedigrees, which entered a longitudinal phenotyping pipeline. Auditory phenotyping comprised clickbox testing at 3, 6, 9 and 12 months of age and ABR at 9 months of age. Initial linkage was determined using SNP mapping (Tepnel Life Sciences), delineating a critical interval containing the *clarinet* mutation on Chromosome 5. Whole-genome sequencing was undertaken using DNA from an affected G_3 mouse (Oxford Genomics Centre, Wellcome Trust Centre for Human Genetics, University of Oxford) and putative lesions validated by standard PCR and Sanger sequencing. *Clrn2*$^{clarinet/+}$ carrier mice were subsequently backcrossed to C57BL/6J for ten generations until congenic. The *Clrn2*^{del629} mutant line was generated on a C57BL/6N background by the Molecular and Cellular Biology group at the Mary Lyon Centre (MLC), MRC Harwell Institute using CRISPR-Cas9 genome editing (Mianne *et al*, 2016; Codner *et al*, 2018) (Table EV2). Within the MLC, all mice were housed and maintained under specific pathogen-free conditions in individually ventilated cages, with environmental conditions as outlined in the Home Office Code of Practice. Animals were housed with littermates until weaned and then housed with mice of the same gender and of similar ages, which was often their littermates. Both male and female animals were used for all experiments.

Animal procedures at the MRC Harwell Institute and University of Sheffield were licensed by the Home Office under the Animals (Scientific Procedures) Act 1986, UK, and additionally approved by the relevant Institutional Ethical Review Committees. Animal procedures at the Institut Pasteur were accredited by the French Ministry of Agriculture to allow experiments on live mice [accreditation 75-15-01, issued on 6 September 2013 in appliance of the French and European regulations on care and protection of the Laboratory Animals (EC Directive 2010/63, French Law 2013-118, 6 February 2013)]. Protocols were approved by the veterinary staff of the Institut Pasteur animal facility and were performed in compliance with the NIH Animal Welfare Insurance #A5476-01 issued on July 31, 2012.

Association analysis of human hearing with *CLRN2* variation in the UK Biobank Cohort

The cohort used for the human association analysis consisted of 500,000 UK Biobank (UKBB) participant (Sudlow *et al*, 2015) with "White British" ancestry. Samples with excess heterozygosity, excess relatedness and sex discrepancies were identified and removed prior to analysis. Samples were genotyped on one of two arrays; 50,000 samples were genotyped on the Affymetrix UK BiLEVE Axiom array, while the remaining 450,000 were genotyped on the Affymetrix UK Biobank Axiom® array. The two arrays shared 95% coverage resulting in > 800,000 genotyped SNPs. Imputation was carried out centrally by UKBB, primarily using the HRC reference panel and IMPUTE2 (Howie *et al*, 2009, 2011). Analysis in this study was conducted with version 3 of the UK Biobank imputed data.

For association testing, cases and controls were defined based on participants' responses to questions regarding hearing ability. Briefly, participants who answered YES to both "Do you have any difficulty with your hearing?" and "Do you find it difficult to follow a conversation if there is background noise (such as TV, radio, children playing)?" were defined as cases, $n = 102{,}832$. Those who answered NO to the same questions were defined as controls. Any individuals who said they used a hearing aid were removed from the control group. Finally, individuals below the age of 50 years of age were removed from the controls to ensure a similar age distribution to cases, resulting in a sample with $n = 163{,}333$ for the control group.

A linear mixed models approach was used to test for association for all SNPs within 100 kb of the *CLRN2* gene using BOLT-LMM v.2[3] (Loh *et al*, 2018) for the association analysis, which corrects for population stratification and within-sample relatedness. In addition, analysis was adjusted for age, sex, UK Biobank genotyping platform and UK Biobank PCs1-10. For quality control, SNPs were filtered based on the two thresholds: (i) minor allele frequency > 0.01 (ii) INFO score > 0.7. Individuals with < 98% genotype call rate were removed. Following genomic quality control filters and selection for White British samples, association analysis was performed on the remaining 87,056 cases and 163,333 controls. To adjust for multiple testing, the Bonferroni-adjusted significance threshold for this analysis is set at 0.0009 based on calculating the effective number of independent SNPs within this region ($n = 55$) (Li *et al*, 2012).

Utilization of the UK Biobank Resource was conducted under Application Number 11516.

Auditory phenotyping

Auditory brainstem response (ABR) tests were performed using a click stimulus and frequency-specific tone-burst stimuli (at 8, 16 and 32 kHz) to screen mice for auditory phenotypes and investigate auditory function (Hardisty-Hughes *et al*, 2010). Mice were anaesthetized by intraperitoneal injection of ketamine (100 mg/ml at 10% v/v) and xylazine (20 mg/ml at 5% v/v) administered at the rate of 0.1 ml/10 g body mass. Once fully anaesthetized, mice were placed on a heated mat inside a sound-attenuated chamber (ETS Lindgren) and recording electrodes (Grass Telefactor F-E2-12) were placed subdermally over the vertex (active), right mastoid (reference) and left mastoid (ground). ABR responses were collected, amplified and averaged using TDT System 3 hardware and BioSig software (Tucker Davies Technology, Alachua, FL, USA). The click stimulus consisted of a 0.1-ms broadband click presented at a rate of 21.1/s. Tone-burst stimuli were of 7-ms duration including rise/fall gating using a 1-ms Cos2 filter, presented at a rate of 42.5/s. All stimuli were presented free-field to the right ear of the mouse,

 © 2019 The Authors

starting at 90 dB SPL and decreasing in 5 dB increments until a threshold was determined visually by the absence of replicable response peaks. For graphical representation, mice not showing an ABR response at the maximum level tested (90 dB SPL) were recorded as having a threshold of 95 dB SPL. These mice/thresholds were included when calculating genotype average thresholds. All ABRs were performed blind to genotype, to ensure thresholds were obtained in an unbiased manner. Mice were recovered using 0.1 ml of anaesthetic reversal agent atipamezole (Antisedan™, 5 mg/ml at 1% v/v), unless aged P16, when the procedure was performed terminally.

Distortion product otoacoustic emission tests were performed using frequency-specific tone-burst stimuli from 8 to 32 kHz with the TDT RZ6 System 3 hardware and BioSig RZ software (Tucker Davis Technology, Alachua, FL, USA) software. An ER10B+ low-noise probe microphone (Etymotic Research) was used to measure the DPOAE near the tympanic membrane. Tone stimuli were presented via separate MF1 (Tucker Davis Technology) speakers, with f1 and f2 at a ratio of f2/f1 = 1.2 (L1 = 65 dB SPL, L2 = 55 dB SPL). Mice were anaesthetized via intraperitoneal injection of ketamine (100 mg/ml at 10% v/v), xylazine (20 mg/ml at 5% v/v) and acepromazine (2 mg/ml at 8% v/v) administered at a rate of 0.1 ml/10 g body mass. Once surgical anaesthesia was confirmed by the absence of a pedal reflex, a section of the pinna was removed to enable unobstructed access to the external auditory meatus. Mice were then placed on a heated mat inside a sound-attenuated chamber (ETS Lindgren), and a pipette tip containing the DPOAE probe assembly was inserted into the ear canal. In-ear calibration was performed before each test. The f1 and f2 tones were presented continuously, and a fast-Fourier transform was performed on the averaged response of 356 epochs (each ~21 ms). The level of the 2f1-f2 DPOAE response was recorded and the noise floor calculated by averaging the four frequency bins either side of the 2f1-f2 frequency.

Clrn2 expression in tissues and isolated auditory hair cells

To allow analysis of the *Clrn2*^{del629} allele, whole cochlear ducts were collected from P21 (+/− 1 day) *Clrn2*$^{+/+}$, *Clrn2*$^{+/del629}$ and *Clrn2*$^{del629/del629}$ littermate mice, and stored in RNA *later* Stabilising Solution (Invitrogen) at −20°C until processed. Total RNA was extracted using TRIzol Reagent (Invitrogen) and used as template for cDNA generation using the High Capacity cDNA Reverse Transcription kit (Applied Biosystems). Subsequent PCR amplification was undertaken utilizing *Clrn2*-specific primers: *Clrn2-Exon 1 For (CTCATTAGTATGCCTGGATGG)/Clrn2-Exon 3 Rev (TTAGTCTT GATTTCTGGAAGGG)* and then electrophoresed on a 2% agarose gel. PCR products were excised and purified using the GENECLEAN II kit (MP Biomedical) and subject to Sanger sequencing (Oxford Source Bioscience). Data were analysed using the SeqMan Pro (DNASTAR) software. For RT–PCR analyses of tissues and hair cells, fresh tissues (inner ear, eye, brain and muscle) of P30 wild-type C57BL/6J mice and isolated auditory hair cells from P15 mice were collected and quickly frozen in liquid nitrogen and stored at −80°C until processing. Auditory hair cells were isolated under direct visual microscope observation. Only solitary IHCs and OHCs identified based on their typical morphology (cylindrical OHCs and pear-shaped IHCs) were taken into consideration, hair cells with ambiguous morphology were excluded. Total RNAs were isolated with TRIzol Reagent (Invitrogen) according to the manufacturer's instructions. Total RNA (400 ng) was reverse-transcribed with the Superscript One-Step RT–PCR system (Invitrogen). For tissue-specific *Clrn2* expression studies, the primers employed were as follows: *Clrn2-F1* (*ATGCCTGGATGGTTCAAAAAG*)/*Clrn2-R1* (*TCAC AAGGTGTACGCAGGAGTCAG*), and a β-actin control: *β-actin-F* (*ACC TGACAGACTACCTCAT*)/*β-actin-R* (*AGACAGCACTGTGTTGGCAT*). For hair cell type-specific *Clrn2* expression, the primers employed were as follows: *Clrn2-F2* (*GGGACGCCAGTCCCAATTTA*)/*Clrn2-R2* (*ACTCCACCTGCGAGGACATT*), with hair cell-specific controls: *Otoferlin* (IHC positive control) *Otof-F* (*CATCGAGTGTGCAGG AAAGG*)/*Otof-R* (*ACCTGACCACAGCATCAGA*); and *Oncomodulin* (OHC positive control) *Ocm-F* (*CGGCCCTGCAGGAATGCCAA*)/*Ocm-R* (*GCTTCAGGGGGACTTGGTAAA*). PCR products were separated by electrophoresis on 2% agarose gels.

Behavioural tests

Multiple behavioural tests were used to assess the vestibular function of *clarinet* mice, as described previously (Hardisty-Hughes *et al*, 2010). In the platform test, mice were placed on a small platform (7 × 7 cm, at a height of 29 cm) and the time on the platform was recorded over a period of 2 min. The contact righting test consisted of placing a mouse in a closed transparent tube and determining whether it was able to successfully regain standing position upon a 180° rotation of the tube (score 1) or fail (score 0). For the swim test, each mouse was placed in a container filled with water at 22–23°C and given a score determined as follows: score 0 = normal swimming; score 1 = irregular swimming; score 2 = immobile floating; score 3 = underwater tumbling.

Electroretinogram response measurements

To measure electroretinograms (ERGs), animals were kept in the dark to adapt to darkness overnight as previously described (Michel *et al*, 2017). Each mouse was anesthetized with a mixture of ketamine (80 mg/kg, Axience, France) and xylazine (8 mg/kg, Axience, France), and placed over a warming pad to maintain body temperature at 37°C. Their pupils were dilated with tropicamide (Mydriaticum; Théa, Clermont-Ferrand, France) and phenylephrine (Neosynephrine; Europhta, Monaco). The cornea was locally anesthetized with oxybuprocaine chlorhydrate (Théa, Clermont-Ferrand, France). Upper and lower lids were retracted to keep eyes open and bulging. Retinal responses were recorded with a gold-loop electrode brought into contact with the cornea through a layer of lubrithal (Dechra, France), with needle electrodes placed in the cheeks and back used as reference and ground electrodes, respectively (Yang *et al*, 2009). The light stimuli were provided by an LED in a Ganzfeld stimulator (SIEM Bio-médicale, France). Responses were amplified and filtered (1 Hz-low and 300 Hz-high cut-off filters) with a one-channel DC-/AC amplifier. One level of stimulus intensity (8 cd.s/m^2) was used for scotopic ERG recording. Each of the response obtained was averaged over five flash stimulations. Photopic cone ERGs were recorded in a rod-suppressing background light of 20 cd.s/m^2, after a 5-min adaptation period. An 8 cds/m^2 level of stimulus intensity was used for the light-adapted ERGs. Each cone photopic ERG response presented was averaged over ten consecutive flashes.

© 2019 The Authors

Immunolabelling

For the synaptic labelling experiments, mice were culled by cervical dislocation and inner ears were fixed in 4% paraformaldehyde (PFA) in PBS for 1 h at room temperature (RT). Post-fixation, ears were fine dissected to expose the sensory epithelium then permeabilized using 0.1% Triton X-100 in PBS for 10 min at RT. Samples were blocked in 5% donkey serum (Sigma) for 1 h at RT and immunolabelled with primary antibodies overnight at 37°C. To enable detection, samples were incubated with fluorophore-coupled secondary antibodies for 1 h at 37°C then stained with DAPI (1:2,500, Thermo Fisher) for 5 min at RT. Samples were mounted onto slides in SlowFade® Gold (Life Technologies) and visualized using a Zeiss LSM 710 fluorescence confocal microscope. Primary antibodies: rabbit anti-Ribeye (Synaptic Systems; 192103; 1:200); mouse anti-GluR2 (Millipore; MABN1189; 1:200). Secondary antibodies: Alexa Fluor® donkey anti-rabbit 568 (Invitrogen; 1:200); Alexa Fluor® donkey anti-mouse 488 (Invitrogen; 1:500).

For all other immunofluorescence experiments, samples were processed as previously described (Michel *et al*, 2017). Briefly, for cochlear whole-mount preparations, micro-dissected, fixed mouse organs of Corti (4% PFA in PBS, pH 7.4 for 1 h at RT) were rinsed, then blocked by incubation in PBS supplemented with 20% normal goat serum and 0.3% Triton X-100 for 1 h at RT. After incubation with primary antibodies in PBS 1% bovine serum albumin overnight at 4°C, samples were rinsed in PBS then incubated with specific secondary antibodies (and phalloidin for actin staining when required) for 1 h at RT. They were then immersed in DAPI (Sigma) for nuclear labelling and rinsed before mounting using Fluorsave (Calbiochem, La Jolla, CA).

To test the occurrence of apoptosis in the retina, cryosections from control and *clarinet* mice were analysed using the in-situ Cell Death Detection Kit, Fluorescein (Roche), according to the manufacturer's instructions.

To detect clarin-2 protein, the cDNA encoding amino acid residues 159–232 (VKFHDLTERIANFQERLFQFVVVEEQYEESFWIC VASASAHAANLVVVAISQIPLPEIKTKMEEATVTPEDILY) of mouse *Clrn2* were amplified by PCR, cloned into pRSET (Life Technologies) and transformed into BL21(DE3)pLysS competent cells (Life Technologies) for protein production. The fusion protein was purified using cobalt chloride-charged chelating sepharose fast flow resin (GE Healthcare Life Sciences) and used to immunize rabbits (Covalab). The antisera were purified by affinity chromatography using the fusion protein (antigen) coupled to SulfoLink resin (Pierce), according to the manufacturer's instructions. We checked the specificity of the affinity-purified antibodies by immunofluorescence using transfected cells and mouse organs of Corti (*clarinet* samples were used as negative controls). The purified homemade, but not commercial, anti-clarin-2 antibodies did detect both GFP- and FLAG-tagged clarin-2 in transfected cells (Fig EV4B–D). However, repeated attempts to detect endogenous clarin-2 in the mouse auditory sensory organ at different postnatal stages, under various conditions of fixation and antigen-retrieval, were unsuccessful. Similar observations were made using commercially available rabbit polyclonal anti-clarin-2 antibodies: the anti-clarin-2 from Proteintech (1:100, 23994-1-AP) and from Atlas (HPA042407; 1:100). The absence of specific immuno-detection in hair cells could reflect a low level of endogenous expression (Fig EV4).

To detect PDZD7, we used a newly generated homemade polyclonal rabbit antibody. It is derived against a mouse PDZD7 fusion protein (amino acid 2–83, accession number NP_001182194.1) and has been validated in transfected cells and mouse organs of Corti. The following other primary antibodies were used: rabbit anti-myosin VIIa (1:500), rabbit anti-harmonin-b (1:50) and rabbit anti-whirlin (1:100) (Sahly *et al*, 2012). Other primary antibodies were used: rabbit anti-stereocilin (1:150)(Verpy *et al*, 2008), mouse anti-EPS8 (1:200; 610144; BD Bioscience) mouse and rabbit anti-CtBP2 (1:200; Goat polyclonal, Santa Cruz, USA; SC-5966) to detect the ribbon protein ribeye, rabbit anti-GluR2/3 (1:200; Millipore), rabbit anti-opsin, blue (1:100; AB5407, Merck-Millipore), mouse anti-Iba1 (1:200; MABN92, Merck-Millipore), mouse anti-rhodopsin (1:500; MAB5316, Merck-Millipore), mouse anti-FLAG2 (1:120, F3165, Sigma-Aldrich) and rabbit anti-GFP (1:250, Invitrogen). The following specific secondary antibodies were used: ATTO 488-conjugated goat anti-rabbit IgG (1:500, Sigma-Aldrich) and ATTO 500 goat anti-mouse IgG antibody (1:500, Sigma-Aldrich). ATTO 565 phalloidin (1:700; Sigma-Aldrich) was also used to label F-actin.

Samples were imaged at RT with a confocal microscope (LSM 700; Carl Zeiss) fitted with a Plan-Apochromat 63× NA 1.4 oil immersion objective from Carl Zeiss. To quantify the positioning of the harmonin-b immunoreactive area relative to the tip of the taller stereocilium, we used ImageJ software (NIH). Quantification was made using IHC, rather than OHC, bundles as it is easier to define individual stereocilia, allowing accurate measurements of the distance of the harmonin-b immunoreactive spot relative to the tip of the stereocilium. For each *clarinet* ($n = 4$) and wild-type ($n = 4$) mouse, confocal images of 8–10 IHCs with well-preserved tallest stereocilia were considered for measurements. For each cell, the distance value taken into consideration is an average value from 3 stereocilia of the same cell: for each stereocilium, we measure the distance between the stereocilium tip to the centre of harmonin-b-immunoreactive spot located on the side of the same stereocilium. Measurements were analysed using Student's *t*-test.

Scanning electron microscopy

Mice were euthanized by cervical dislocation, and inner ears were removed and fixed in 2.5% glutaraldehyde (TAAB Laboratories Equipment Ltd.) in 0.1 M phosphate buffer (Sigma-Aldrich) overnight at 4°C. Following decalcification in 4.3% EDTA, cochleae were sub-dissected to expose the sensory epithelium then "OTO processed" with alternating incubations in 1% osmium tetroxide (TAAB Laboratories Equipment Ltd.) in 0.1 M sodium cacodylate (Sigma-Aldrich) and 1% thiocarbohydrazide (Sigma-Aldrich) in ddH_2O. Ears were dehydrated through a graded ethanol (Fisher Scientific) series (25–100%) at 4°C and stored in 100% acetone (VWR Chemicals) until critical point drying with liquid CO_2 using an Emitech K850 (EM Technologies Ltd). Ears were mounted onto stubs using silver paint (Agar Scientific), sputter coated with palladium using a Quorum Q150R S sputter coater (Quorum Technologies) and visualized with a JSM-6010LV Scanning Electron Microscope (JEOL).

To analyse prolateness of the stereocilia tips between control and clarin-2-deficient hair bundles, scanning electron micrographs were utilized and small square selections framing the tips of individual

 © 2019 The Authors

second row stereocilia were delimited and extracted to create an array of tip images using ImageJ (Fiji). Consistency between the images captured was maintained by ensuring the side of the square selection was parallel to the distal edge of the stereocilium, and ensuring that a constant distance was kept from the upper edge. Stereocilia from OHC bundles were imaged at a ~45° angle from the perspective plane. All images were taken to scale after calibration to the scanning electron microscope software-generated scale bar. The image array for each genotype was then loaded as a pseudo z-stack and a median-intensity z-projection generated. For each projection, at least 80 tip images per genotype were used—3 animals per genotype, 3 bundles per animal, with all bundles from the mid-region of the cochlea. These projections were processed using auto-tone and then pseudo-coloured in Adobe Photoshop, before a perimeter outline was drawn using Adobe Illustrator in order to show the shape of the median Z-projected stereocilia tip (see Fig EV3).

To assess stereocilia heights, at least three ears (one ear per mouse) were analysed for each genotype at each time point. Duplicate images of the middle turn (180° to 360°) of the cochlea were taken, with a 5° tilt between them. IHC bundles were imaged at 8,000× magnification and OHC bundles at 15,000× magnification, all at a constant working distance of 20 μM. Three different bundles were analysed per animal, with up to nine different measurements taken per bundle: three measurements from the tallest row of stereocilia, three from the middle row and three from the shortest row (if present). IHC and OHC measurements were obtained using ImageJ software (NIH) and corrected using a pseudo-eucentric tilting approach (Bariani *et al*, 2005). A single measure x_1 (e.g. length of the tallest row of one stereocilium) was taken on a first micrograph and measured again (x_2) on the corresponding 5°-tilted repeat micrograph. Perpendicular countermeasures (y_1 and y_2) to x_1 and x_2 were also taken in every instance. Later, countermeasures were fed onto equation (1), in order to estimate uncertainty (ζ) due to plane rotation. Every pair of tilted-coupled measures (x_1 and x_2) was then fed onto equation (2), along with the uncertainty estimate (ζ) from equation (1), thus obtaining a close approximation (ξ) of the true measure of the structures investigated.

$$\zeta = \frac{(\Delta y)\cos\Delta\varphi + (2y_1(y_1 - \Delta y)/d)\sin\Delta\varphi}{(1 + y_1(y_1 - \Delta y)/d^2\sin\Delta\varphi) + (\Delta y/d)\cos(2\Delta\varphi)}; \quad (1)$$

$$\xi = \frac{2d - 2\zeta\cos\Delta\varphi}{d/x_1 + d/x_2}; \quad (2)$$

where, ζ = uncertainty estimate; $y_{1,2}$ = perpendicular countermeasures to measures $x_{1,2}$; Δy = arithmetic difference of countermeasures y_1 and y_2; $\Delta\varphi$ = tilting angle (5°); d = working distance (20 μM); $x_{1,2}$ = tilted paired-measures of structure of interest; ξ = estimate of true size of structure of interest.

Clrn2 expression in whole cochlea

Total RNA samples were extracted from wild-type C57BL/6J mouse whole cochleae at E17.5 (embryonic day 17.5), P4, P8, P12, P16 and P28 using a Direct-zol RNA MiniPrep Kit (Zymo Research). Five separate samples were prepared for each age, comprising whole-cochlea mouse RNA extracted from both ears. In each case, quintuplicate samples from independent mice were analysed for each stage. Complementary DNAs were generated from 1 μg total RNA using the High Capacity cDNA synthesis kit (Applied Biosystems) following the manufacturer's instructions. Amplifications were performed using TaqMan Gene Expression Assays with Fast Universal PCR Master Mix. A β-actin primer/probe set (*Mm00607939_s1*) was used as an internal control, and a custom TaqMan assay was designed to allow the specific amplification of the *Clrn2* transcripts using the following forward and reverse primers, and TaqMan Gene Expression Assay: *Clrn2*-F 5′-*AAGATGTC CACTTGCCCAAC*-3′, *Clrn2*-R 5′-*GACCAGGGTTCTTGTGCTTC*-3′, *Mm03990594_m1*. PCRs were run in triplicate in the Applied Biosystems real-time PCR device (7500 Fast Real-Time PCR System) in 20-μl reactions containing 10 μl Fast TaqMan Master Mix, 1 μl TaqMan assay, 4 μl ddH_2O and 5 μl complementary DNA (5 ng/μl), using the following cycles: 95°C for 20 s and 40 cycles at 95°C for 3 s and 60°C for 30 s. Amplification data were recorded and relative quantification performed using the 7500 software version 2.0.6 software (Applied Biosystems) comparing threshold cycles (C_t). *Clrn2* mRNA levels were first normalized to *Actin* ($\Delta Ct = Ct_{Nptn} - Ct_{Actin}$) at each age, and changes in expression relative to P4 were calculated as $2^{-(\Delta Ct - \Delta CtP4)}$.

Injectoporation

The injectoporation experiments of cochlear explants were performed as previously described (Xiong *et al*, 2014), with a few modifications. In brief, cochleae were dissected from P2 wild-type mice, cut into 4–6 pieces and cultured for 6 h in DMEM/F12 medium with 100 ng/μl ampicillin. Next, adherent cochlear explants were placed between two platinum wire electrodes (Surepure Chemetals) and a patch pipette (2 μm diameter) placed between the second and third row of OHCs was used to deliver the plasmid (1 μg/μl in 1× HBSS) to the hearing organ. The pipette and electrode were positioned using an Axioscope 2 Carl Zeiss microscope with a 40× objective (Olympus) and two micromanipulators (Sutter MPC-200). To trigger plasmid entry into cells, 3 square-pulses with a magnitude of 60 V (15 ms length, 1-s intervals) were applied, using an ECM 830 electroporator (Harvard Apparatus). Organs of Corti were cultured for another 12 h in DMEM/F12 and fixed in 4% PFA for 1 h before immunostaining. Samples were analysed at RT with a confocal microscope (LSM 700; Carl Zeiss) fitted with a Plan-Apochromat 63× NA 1.4 oil immersion objective from Carl Zeiss.

Electrophysiology

Electrophysiological recordings were made from apical-coil OHCs and IHCs of *clarinet* mice aged P6-22. A number of basal-coil OHCs were also investigated at P7-8. Cochleae were dissected in normal extracellular solution (in mM): 135 NaCl, 5.8 KCl, 1.3 $CaCl_2$, 0.9 $MgCl_2$, 0.7 NaH_2PO_4, 5.6 D-glucose, 10 HEPES-NaOH. Sodium pyruvate (2 mM), MEM amino acids solution (50X, without L-Glutamine) and MEM vitamins solution (100×) were added from concentrates (Fisher Scientific, UK). The pH was adjusted to 7.5 (308 mosmol/kg). The dissected cochleae were transferred to a microscope

© 2019 The Authors

chamber, immobilized with a nylon mesh (Corns *et al*, 2016) and continuously perfused with a peristaltic pump using the above extracellular solution. The organs of Corti were viewed using an upright microscope (Leica DMLMF, Germany; Nikon FN1, Japan) with Nomarski optics (x60 or x63 objectives).

MET currents were elicited by stimulating the hair bundles of OHCs and IHCs using a fluid jet from a pipette (tip diameter 8–10 μm) driven by a piezoelectric disc (Corns *et al*, 2014). The pipette tip of the fluid jet was positioned near to the bundles to elicit a maximal MET current. Mechanical stimuli were applied as 50 Hz sinusoids (filtered at 0.25 kHz, 8-pole Bessel) with driving voltages of ± 40 V. MET currents were recorded with a patch pipette solution containing (in mM): 106 Cs-glutamate, 20 CsCl, 3 $MgCl_2$, 1 EGTA-CsOH, 5 Na_2ATP, 0.3 Na_2GTP, 5 HEPES-CsOH, 10 sodium phosphocreatine (pH 7.3). Membrane potentials were corrected for the liquid junction potential (LJP) of −11 mV, measured between electrode and bath solutions.

Patch clamp recordings were performed using an Optopatch (Cairn Research Ltd, UK) amplifier. Patch pipettes were made from soda glass capillaries with a typical resistance in the extracellular solution of 2–3 MΩ. In order to reduce the electrode capacitance, patch electrodes were coated with surf wax (Mr Zoggs SexWax, USA). Basolateral membrane recordings were performed using an intracellular solution containing (in mM): 131 KCl, 3 $MgCl_2$, 1 EGTA-KOH, 5 Na_2ATP, 5 HEPES-KOH, 10 Na_2-phosphocreatine (pH 7.3; osmolality ~296 mmol/kg). Data acquisition was controlled by pClamp software using Digidata 1440A boards (Molecular Devices, USA). Recordings were low-pass filtered at 2.5 kHz (8-pole Bessel), sampled at 5 kHz and stored on computer for off-line analysis (Origin: OriginLab, USA). Membrane potentials in voltage clamp were corrected for the voltage drop across the uncompensated residual series resistance and for a LJP of −4 mV measured between electrode and bath solutions. All recordings were performed at RT.

Statistical analysis

Unless stated, data were analysed using Student's two-tailed *t*-test (two study groups) or one-way ANOVA followed by Tukey's post-hoc test (three study groups) using GraphPad Prism. Graphs are presented as mean ± SD, unless stated, and $P < 0.05$ indicates statistical significance. Using data obtained from the original MPC169 cohort, we used GraphPad StatMate to carry out power calculations to determine sample size in an unpaired *t*-test using the standard deviation of the measured hearing thresholds, a significance level of $P = 0.01$ (two-tailed) and a power of 95%. As such, an effect size was estimated using real data corresponding to the *clarinet* hearing loss phenotype comparing hearing thresholds of wild-type and homozygous littermates. This determined that a cohort size of ≥ 4 mice/genotype would be sufficient to detect an auditory threshold difference. All phenotyping was performed blind to genotype, and no data were excluded from analysis.

Availability of materials

$Clrn2^{clarinet}$ and $Clrn2^{del629}$ mice are available on request from the MRC Harwell Institute.

The paper explained

Problem
Hearing loss is a very prevalent condition that can result from environmental causes, genetic predisposition or an interaction of both. Over the last two decades, while much progress has been made in understanding the genetic bases of congenital and early-onset hearing loss, we have only just begun to elaborate upon the genetic landscape of age-related hearing loss. Going forward, increased knowledge of the genes and molecular pathways required for the maintenance of hearing function will likely provide opportunities for the design of therapeutic approaches to prevent progressive hearing loss.

Results
Utilizing a forward genetic screen in mice, we identified a mutation within the *Clrn2* gene as the cause of hearing loss in the *clarinet* mutant. Loss of the encoded tetraspan-like protein clarin-2 leads to an early-onset, progressive hearing loss. Interestingly, analysis of a large cohort of patients with adult hearing difficulties from the UK Biobank study we identify *CLRN2* as a novel candidate gene for human non-syndromic progressive age-related hearing loss. Our morphological, molecular and functional investigations of the clarin-2-deficient mice establish that while the protein is not required for the initial formation of cochlear sensory hair cell stereocilia bundles, it is critical for maintaining normal bundle integrity and functioning. In the differentiating hair bundles, lack of clarin-2 leads to loss of mechano-electrical transduction, followed by selective progressive loss of the transducing stereocilia.

Impact
Integrated mouse and human approaches continue to elaborate upon our understanding of the genetic mechanisms required for mammalian hearing. In this study, we establish that *Clrn2* is a novel deafness gene associated with progressive hearing loss in both mice and humans, and as such, severe loss-of-function *CLRN2* mutations should be considered in the aetiology of human autosomal recessive hearing loss. Moreover, our findings demonstrate a key role for clarin-2 in mammalian hearing, providing insights into the interplay between mechano-electrical transduction and stereocilia architecture maintenance.

Expanded View for this article is available online.

Acknowledgements
We would like to thank L. Vizor, R. Kent, M. Hutchison, S. Nouaille and MLC Ward staff for their assistance with the breeding of *clarinet* and *del629* animals; Y. Bouleau for help with isolation of hair cells; J. Sanderson for his technical assistance with the immunolabelling experiments; and the Molecular and Cellular Biology group at the Harwell Institute for generating the $Clrn2^{del629}$ mice. This work was supported by: Medical Research Council (MC_U142684175 to S.D.M.B. and MC_UP_1503/2 to M.R.B), Wellcome Trust (102892 to W.M.); the French National Research Agency (ANR) as part of the second "Investissements d'Avenir" programme (light4deaf, ANR-15-RHUS-0001) and LHW-Stiftung (to C.P. & A.E.); ANR-HearInNoise-(ANR-17-CE16-0017 to A.E.); NIDCD/NIH (R01DC013817), NIMH/NIH (R24MH114815) and the Hearing Restoration Program of the Hearing Health Foundation (to R.H.); and an Action on Hearing Loss PhD studentship (to F.W. and S.Da.), which was supported by the National Institute for Health Research University College London Hospitals Biomedical Research Centre. L.D. is a Medical Research Council PhD student. P.P. benefited from a fellowship from the European Union's Horizon 2020

 © 2019 The Authors

Marie Sklodowska-Curie grant No 665807. S.L.J. is a Royal Society University Research Fellow.

Author contributions

LAD, PP, CA, PM, AP, DW, CTE, MMS, SDe, RH, DD, WM, AE and MRB designed and interpreted the experiments. LAD, PP, CA, PM, SDe, AP, LCh, SN, JD, PJ, SM, AL, GFC and TP performed the experiments. LCo, SJ and WM carried out the electrophysiology experiments and analysis. HRRW, FMW and SJDa undertook the UK BioBank association study. SW aided in the management of the *clarinet* colony. SRG, KNA and CP provided support; LAD, CA, LCh, SJDa, SDMB, WM, AE and MRB wrote the manuscript, AE and MRB conceived and coordinated the study.

Conflict of interest

The authors declare that they have no conflict of interest.

References

Aarnisalo AA, Pietola L, Joensuu J, Isosomppi J, Aarnisalo P, Dinculescu A, Lewin AS, Flannery J, Hauswirth WW, Sankila EM *et al* (2007) Anti-clarin-1 AAV-delivered ribozyme induced apoptosis in the mouse cochlea. *Hear Res* 230: 9–16

Adato A, Vreugde S, Joensuu T, Avidan N, Hamalainen R, Belenkiy O, Olender T, Bonne-Tamir B, Ben-Asher E, Espinos C *et al* (2002) USH3A transcripts encode clarin-1, a four-transmembrane-domain protein with a possible role in sensory synapses. *Eur J Hum Genet* 10: 339–350

Bariani P, De Chiffre L, Hansen HN, Horsewell A (2005) Investigation on the traceability of three dimensional scanning electron microscope measurements based on the stereo-pair technique. *Prec Eng* 29: 219–228

Beurg M, Cui R, Goldring AC, Ebrahim S, Fettiplace R, Kachar B (2018) Variable number of TMC1-dependent mechanotransducer channels underlie tonotopic conductance gradients in the cochlea. *Nat Commun* 9: 2185

Boeda B, El-Amraoui A, Bahloul A, Goodyear R, Daviet L, Blanchard S, Perfettini I, Fath KR, Shorte S, Reiners J *et al* (2002) Myosin VIIa, harmonin and cadherin 23, three Usher I gene products that cooperate to shape the sensory hair cell bundle. *EMBO J* 21: 6689–6699

Bonnet C, El-Amraoui A (2012) Usher syndrome (sensorineural deafness and retinitis pigmentosa): pathogenesis, molecular diagnosis and therapeutic approaches. *Curr Opin Neurol* 25: 42–49

Brandt A, Khimich D, Moser T (2005) Few CaV1.3 channels regulate the exocytosis of a synaptic vesicle at the hair cell ribbon synapse. *J Neurosci* 25: 11577–11585

Caberlotto E, Michel V, Foucher I, Bahloul A, Goodyear RJ, Pepermans E, Michalski N, Perfettini I, Alegria-Prevot O, Chardenoux S *et al* (2011) Usher type 1G protein sans is a critical component of the tip-link complex, a structure controlling actin polymerization in stereocilia. *Proc Natl Acad Sci USA* 108: 5825–5830

Codner GF, Mianne J, Caulder A, Loeffler J, Fell R, King R, Allan AJ, Mackenzie M, Pike FJ, McCabe CV *et al* (2018) Application of long single-stranded DNA donors in genome editing: generation and validation of mouse mutants. *BMC Biol* 16: 70

Corey DP, Hudspeth AJ (1983) Kinetics of the receptor current in bullfrog saccular hair cells. *J Neurosci* 3: 962–976

Corns LF, Johnson SL, Kros CJ, Marcotti W (2014) Calcium entry into stereocilia drives adaptation of the mechanoelectrical transducer current of mammalian cochlear hair cells. *Proc Natl Acad Sci USA* 111: 14918–14923

Corns LF, Johnson SL, Kros CJ, Marcotti W (2016) Tmc1 point mutation affects Ca2+ sensitivity and block by dihydrostreptomycin of the mechanoelectrical transducer current of mouse outer hair cells. *J Neurosci* 36: 336–349

Corns LF, Jeng JY, Richardson GP, Kros CJ, Marcotti W (2017) TMC2 modifies permeation properties of the mechanoelectrical transducer channel in early postnatal mouse cochlear outer hair cells. *Front Mol Neurosci* 10: 326

Corns LF, Johnson SL, Roberts T, Ranatunga KM, Hendry A, Ceriani F, Safieddine S, Steel KP, Forge A, Petit C *et al* (2018) Mechanotransduction is required for establishing and maintaining mature inner hair cells and regulating efferent innervation. *Nat Commun* 9: 4015

Crawford AC, Evans MG, Fettiplace R (1989) Activation and adaptation of transducer currents in turtle hair cells. *J Physiol* 419: 405–434

Dulon D, Papal S, Patni P, Cortese M, Vincent PF, Tertrais M, Emptoz A, Tlili A, Bouleau Y, Michel V *et al* (2018) Clarin-1 gene transfer rescues auditory synaptopathy in model of Usher syndrome. *J Clin Invest* 128: 3382–3401

Erickson T, Nicolson T (2015) Identification of sensory hair-cell transcripts by thiouracil-tagging in zebrafish. *BMC Genom* 16: 842

Etournay R, Lepelletier L, Boutet de Monvel J, Michel V, Cayet N, Leibovici M, Weil D, Foucher I, Hardelin JP, Petit C (2010) Cochlear outer hair cells undergo an apical circumference remodeling constrained by the hair bundle shape. *Development* 137: 1373–1383

Ezan J, Montcouquiol M (2013) Revisiting planar cell polarity in the inner ear. *Semin Cell Dev Biol* 24: 499–506

Fettiplace R (2016) Is TMC1 the hair cell mechanotransducer channel? *Biophys J* 111: 3–9

Furuya H, Yasuda M, Terasawa KJ, Tanaka K, Murai H, Kira J, Ohyagi Y (2003) A novel mutation (L250V) in the presenilin 1 gene in a Japanese familial Alzheimer's disease with myoclonus and generalized convulsion. *J Neurol Sci* 209: 75–77

Gao X, Yuan YY, Wang GJ, Xu JC, Su Y, Lin X, Dai P (2017) Novel mutations and mutation combinations of TMPRSS3 cause various phenotypes in one Chinese family with autosomal recessive hearing impairment. *Biomed Res Int* 2017: 4707315

Geller SF, Guerin KI, Visel M, Pham A, Lee ES, Dror AA, Avraham KB, Hayashi T, Ray CA, Reh TA *et al* (2009) CLRN1 is nonessential in the mouse retina but is required for cochlear hair cell development. *PLoS Genet* 5: e1000607

Geng R, Geller SF, Hayashi T, Ray CA, Reh TA, Bermingham-McDonogh O, Jones SM, Wright CG, Melki S, Imanishi Y *et al* (2009) Usher syndrome IIIA gene clarin-1 is essential for hair cell function and associated neural activation. *Hum Mol Genet* 18: 2748–2760

Geng R, Melki S, Chen DH, Tian G, Furness DN, Oshima-Takago T, Neef J, Moser T, Askew C, Horwitz G *et al* (2012) The mechanosensory structure of the hair cell requires clarin-1, a protein encoded by Usher syndrome III causative gene. *J Neurosci* 32: 9485–9498

Gopal SR, Vona B, Azaiez H, Mazaheri N, Booth KT, Maroofian R, Clancy K, Shariati G, Sedaghat A, Stepanyan R *et al* (2019) Mutation in the clarin-2 gene cause hearing loss in human and a zebrafish model reveals the likely cause of that hearing loss. *ARO Abstr PD* 84: 520

Grati M, Shin JB, Weston MD, Green J, Bhat MA, Gillespie PG, Kachar B (2012) Localization of PDZD7 to the stereocilia ankle-link associates this scaffolding protein with the Usher syndrome protein network. *J Neurosci* 32: 14288–14293

Grillet N, Xiong W, Reynolds A, Kazmierczak P, Sato T, Lillo C, Dumont RA, Hintermann E, Sczaniecka A, Schwander M *et al* (2009) Harmonin

© 2019 The Authors

mutations cause mechanotransduction defects in cochlear hair cells. *Neuron* 62: 375 – 387

Guo Y, Zhang P, Sheng Q, Zhao S, Hackett TA (2016) lncRNA expression in the auditory forebrain during postnatal development. *Gene* 593: 201 – 216

Gyorgy B, Meijer EJ, Ivanchenko MV, Tenneson K, Emond F, Hanlon KS, Indzhykulian AA, Volak A, Karavitaki KD, Tamvakologos PI *et al* (2019) Gene transfer with AAV9-PHP.B rescues hearing in a mouse model of usher syndrome 3A and transduces hair cells in a non-human primate. *Mol Ther Meth Clin Dev* 13: 1 – 13

Hardisty-Hughes RE, Parker A, Brown SD (2010) A hearing and vestibular phenotyping pipeline to identify mouse mutants with hearing impairment. *Nat Protoc* 5: 177 – 190

Hoelter SM, Dalke C, Kallnik M, Becker L, Horsch M, Schrewe A, Favor J, Klopstock T, Beckers J, Ivandic B *et al* (2008) "Sighted C3H" mice–a tool for analysing the influence of vision on mouse behaviour? *Front Biosci* 13: 5810 – 5823

Howie BN, Donnelly P, Marchini J (2009) A flexible and accurate genotype imputation method for the next generation of genome-wide association studies. *PLoS Genet* 5: e1000529

Howie B, Marchini J, Stephens M (2011) Genotype imputation with thousands of genomes. *G3* 1: 457 – 470

Johnson KR, Zheng QY, Noben-Trauth K (2006) Strain background effects and genetic modifiers of hearing in mice. *Brain Res* 1091: 79 – 88

Kaltenbach JA, Falzarano PR, Simpson TH (1994) Postnatal development of the hamster cochlea. II. Growth and differentiation of stereocilia bundles. *J Comp Neurol* 350: 187 – 198

Kawashima Y, Geleoc GS, Kurima K, Labay V, Lelli A, Asai Y, Makishima T, Wu DK, Della Santina CC, Holt JR *et al* (2011) Mechanotransduction in mouse inner ear hair cells requires transmembrane channel-like genes. *J Clin Invest* 121: 4796 – 4809

Kazmierczak P, Sakaguchi H, Tokita J, Wilson-Kubalek EM, Milligan RA, Muller U, Kachar B (2007) Cadherin 23 and protocadherin 15 interact to form tip-link filaments in sensory hair cells. *Nature* 449: 87 – 91

Keller R, Davidson L, Edlund A, Elul T, Ezin M, Shook D, Skoglund P (2000) Mechanisms of convergence and extension by cell intercalation. *Philos Trans R Soc Lond B Biol Sci* 355: 897 – 922

Kelly M, Chen P (2007) Shaping the mammalian auditory sensory organ by the planar cell polarity pathway. *Int J Dev Biol* 51: 535 – 547

Kros CJ, Ruppersberg JP, Rusch A (1998) Expression of a potassium current in inner hair cells during development of hearing in mice. *Nature* 394: 281 – 284

Kubisch C, Schroeder BC, Friedrich T, Lutjohann B, El-Amraoui A, Marlin S, Petit C, Jentsch TJ (1999) KCNQ4, a novel potassium channel expressed in sensory outer hair cells, is mutated in dominant deafness. *Cell* 96: 437 – 446

Kurima K, Ebrahim S, Pan B, Sedlacek M, Sengupta P, Millis BA, Cui R, Nakanishi H, Fujikawa T, Kawashima Y *et al* (2015) TMC1 and TMC2 localize at the site of mechanotransduction in mammalian inner ear hair cell stereocilia. *Cell Rep* 12: 1606 – 1617

Larner AJ (2013) Presenilin-1 mutations in Alzheimer's disease: an update on genotype-phenotype relationships. *J Alzheimer's Dis* 37: 653 – 659

Lefevre G, Michel V, Weil D, Lepelletier L, Bizard E, Wolfrum U, Hardelin JP, Petit C (2008) A core cochlear phenotype in USH1 mouse mutants implicates fibrous links of the hair bundle in its cohesion, orientation and differential growth. *Development* 135: 1427 – 1437

Li MX, Yeung JM, Cherny SS, Sham PC (2012) Evaluating the effective numbers of independent tests and significant p-value thresholds in commercial genotyping arrays and public imputation reference datasets. *Hum Genet* 131: 747 – 756

Liu H, Pecka JL, Zhang Q, Soukup GA, Beisel KW, He DZ (2014) Characterization of transcriptomes of cochlear inner and outer hair cells. *J Neurosci* 34: 11085 – 11095

Liu H, Chen L, Giffen KP, Stringham ST, Li Y, Judge PD, Beisel KW, He DZZ (2018) Cell-specific transcriptome analysis shows that adult pillar and deiters' cells express genes encoding machinery for specializations of cochlear hair cells. *Front Mol Neurosci* 11: 356

Loh PR, Kichaev G, Gazal S, Schoech AP, Price AL (2018) Mixed-model association for biobank-scale datasets. *Nat Genet* 50: 906 – 908

Maeda R, Kindt KS, Mo W, Morgan CP, Erickson T, Zhao H, Clemens-Grisham R, Barr-Gillespie PG, Nicolson T (2014) Tip-link protein protocadherin 15 interacts with transmembrane channel-like proteins TMC1 and TMC2. *Proc Natl Acad Sci USA* 111: 12907 – 12912

Manor U, Disanza A, Grati M, Andrade L, Lin H, Di Fiore PP, Scita G, Kachar B (2011) Regulation of stereocilia length by myosin XVa and whirlin depends on the actin-regulatory protein Eps8. *Curr Biol* 21: 167 – 172

Marcotti W, Kros CJ (1999) Developmental expression of the potassium current IK, n contributes to maturation of mouse outer hair cells. *J Physiol* 520(Pt 3): 653 – 660

Marcotti W, Geleoc GS, Lennan GW, Kros CJ (1999) Transient expression of an inwardly rectifying potassium conductance in developing inner and outer hair cells along the mouse cochlea. *Pflugers Arch* 439: 113 – 122

Marcotti W, Johnson SL, Holley MC, Kros CJ (2003) Developmental changes in the expression of potassium currents of embryonic, neonatal and mature mouse inner hair cells. *J Physiol* 548: 383 – 400

Marcotti W (2012) Functional assembly of mammalian cochlear hair cells. *Exp Physiol* 97: 438 – 451

Mburu P, Mustapha M, Varela A, Weil D, El-Amraoui A, Holme RH, Rump A, Hardisty RE, Blanchard S, Coimbra RS *et al* (2003) Defects in whirlin, a PDZ domain molecule involved in stereocilia elongation, cause deafness in the whirler mouse and families with DFNB31. *Nat Genet* 34: 421 – 428

Mianne J, Chessum L, Kumar S, Aguilar C, Codner G, Hutchison M, Parker A, Mallon AM, Wells S, Simon MM *et al* (2016) Correction of the auditory phenotype in C57BL/6N mice via CRISPR/Cas9-mediated homology directed repair. *Genome Med* 8: 16

Michalski N, Michel V, Caberlotto E, Lefevre GM, van Aken AF, Tinevez JY, Bizard E, Houbron C, Weil D, Hardelin JP *et al* (2009) Harmonin-b, an actin-binding scaffold protein, is involved in the adaptation of mechanoelectrical transduction by sensory hair cells. *Pflugers Arch* 459: 115 – 130

Michel V, Booth KT, Patni P, Cortese M, Azaiez H, Bahloul A, Kahrizi K, Labbe M, Emptoz A, Lelli A *et al* (2017) CIB2, defective in isolated deafness, is key for auditory hair cell mechanotransduction and survival. *EMBO Mol Med* 9: 1711 – 1731

Ness SL, Ben-Yosef T, Bar-Lev A, Madeo AC, Brewer CC, Avraham KB, Kornreich R, Desnick RJ, Willner JP, Friedman TB *et al* (2003) Genetic homogeneity and phenotypic variability among Ashkenazi Jews with Usher syndrome type III. *J Med Genet* 40: 767 – 772

Ogun O, Zallocchi M (2014) Clarin-1 acts as a modulator of mechanotransduction activity and presynaptic ribbon assembly. *J Cell Biol* 207: 375 – 391

Pepermans E, Michel V, Goodyear R, Bonnet C, Abdi S, Dupont T, Gherbi S, Holder M, Makrelouf M, Hardelin JP *et al* (2014) The CD2 isoform of protocadherin-15 is an essential component of the tip-link complex in mature auditory hair cells. *EMBO Mol Med* 6: 984 – 992

 © 2019 The Authors

Potter PK, Bowl MR, Jeyarajan P, Wisby L, Blease A, Goldsworthy ME, Simon MM, Greenaway S, Michel V, Barnard A *et al* (2016) Novel gene function revealed by mouse mutagenesis screens for models of age-related disease. *Nat Commun* 7: 12444

Prost J, Barbetta C, Joanny JF (2007) Dynamical control of the shape and size of stereocilia and microvilli. *Biophys J* 93: 1124 – 1133

Ranum PT, Goodwin AT, Yoshimura H, Kolbe DL, Walls WD, Koh JY, He DZZ, Smith RJH (2019) Insights into the biology of hearing and deafness revealed by single-cell RNA sequencing. *Cell Rep* 26: 3160 – 3171.e3163

Rzadzinska AK, Schneider ME, Davies C, Riordan GP, Kachar B (2004) An actin molecular treadmill and myosins maintain stereocilia functional architecture and self-renewal. *J Cell Biol* 164: 887 – 897

Sahly I, Dufour E, Schietroma C, Michel V, Bahloul A, Perfettini I, Pepermans E, Estivalet A, Carette D, Aghaie A *et al* (2012) Localization of Usher 1 proteins to the photoreceptor calyceal processes, which are absent from mice. *J Cell Biol* 199: 381 – 399

Schwander M, Kachar B, Muller U (2010) Review series: the cell biology of hearing. *J Cell Biol* 190: 9 – 20

Steiner AB, Kim T, Cabot V, Hudspeth AJ (2014) Dynamic gene expression by putative hair-cell progenitors during regeneration in the zebrafish lateral line. *Proc Natl Acad Sci USA* 111: E1393 – E1401

Sudlow C, Gallacher J, Allen N, Beral V, Burton P, Danesh J, Downey P, Elliott P, Green J, Landray M *et al* (2015) UK biobank: an open access resource for identifying the causes of a wide range of complex diseases of middle and old age. *PLoS Med* 12: e1001779

Valeria Z, Johnson SL, Christoph F, Marlies K, Holley MC, Jacopo M, Sergio M, Walter M (2013) Burst activity and ultrafast activation kinetics of CaV1.3 Ca2+ channels support presynaptic activity in adult gerbil hair cell ribbon synapses. *J Physiol* 591: 3811 – 3820

Velez-Ortega AC, Freeman MJ, Indzhykulian AA, Grossheim JM, Frolenkov GI (2017) Mechanotransduction current is essential for stability of the transducing stereocilia in mammalian auditory hair cells. *Elife* 6: e24661

Verpy E, Weil D, Leibovici M, Goodyear RJ, Hamard G, Houdon C, Lefevre GM, Hardelin JP, Richardson GP, Avan P *et al* (2008) Stereocilin-deficient mice reveal the origin of cochlear waveform distortions. *Nature* 456: 255 – 258

Xiong W, Grillet N, Elledge HM, Wagner TF, Zhao B, Johnson KR, Kazmierczak P, Muller U (2012) TMHS is an integral component of the mechanotransduction machinery of cochlear hair cells. *Cell* 151: 1283 – 1295

Xiong W, Wagner T, Yan L, Grillet N, Muller U (2014) Using injectoporation to deliver genes to mechanosensory hair cells. *Nat Protoc* 9: 2438 – 2449

Yang Y, Mohand-Said S, Danan A, Simonutti M, Fontaine V, Clerin E, Picaud S, Leveillard T, Sahel JA (2009) Functional cone rescue by RdCVF protein in a dominant model of retinitis pigmentosa. *Mol Ther* 17: 787 – 795

Zallocchi M, Meehan DT, Delimont D, Rutledge J, Gratton MA, Flannery J, Cosgrove D (2012) Role for a novel Usher protein complex in hair cell synaptic maturation. *PLoS ONE* 7: e30573

Zampini V, Ruttiger L, Johnson SL, Franz C, Furness DN, Waldhaus J, Xiong H, Hackney CM, Holley MC, Offenhauser N *et al* (2011) Eps8 regulates hair bundle length and functional maturation of mammalian auditory hair cells. *PLoS Biol* 9: e1001048

Zhao B, Wu Z, Grillet N, Yan L, Xiong W, Harkins-Perry S, Muller U (2014) TMIE is an essential component of the mechanotransduction machinery of cochlear hair cells. *Neuron* 84: 954 – 967

License: This is an open access article under the terms of the Creative Commons Attribution 4.0 License, which permits use, distribution and reproduction in any medium, provided the original work is properly cited.

Article 2

Functional defect at IHC ribbon synapses of Clrn2 mutant mice

Défauts synaptiques des cellules ciliées internes de souris mutantes *clarinette*

Thibault PEINEAU, Sandrine VITRY, Yohan BOULEAU, Aziz EL-AMRAOUI, Didier DULON

(Manuscrit en cours d'écriture)

Introduction

Le gène CLRN2 a été récemment découvert comme un nouveau gène impliqué dans une surdité. Chez l'homme, il a été identifié dans une famille iranienne consanguine comme une surdité génétique non syndromique neurosensorielle (Vona et al., 2020). Ce gène CLRN2 code pour une petite protéine à 4 segments transmembranaires de la "superfamille" des clarines (Figure 1). Cependant, au contraire du syndrome de Usher III lié au gène CLRN1, la surdité CLRN2 n'est pas associée à un défaut visuel. Des souris portant la mutation *clarinette* (c.12G > A induit par un agent mutagène l'ENU ou N-nitroso-N-éthylurée) sur le gène Clrn2 montrent aussi une surdité progressive sévère (Dunbar et al., 2019). Cette surdité est principalement liée à une désorganisation des stéréocils empêchant une bonne transduction mécano-électrique.

Chez la souris, la clarine-1 est essentielle à la fois pour la maintenance des stéréocils et l'organisation des canaux calciques à la zone active des cellules ciliées internes (Dulon et al., 2018). C'est pourquoi nous avons recherché chez les cellules ciliées internes de la souris *clarinette* un potentiel défaut de fonctionnement des canaux calciques et de l'exocytose synaptique.

Résultats

Comme observé dans de précédentes études (Dunbar et al., 2019), la mutation sur le gène *Clrn2* entraîne un défaut au niveau de la maintenance des stéréocils, qui est en partie la cause de l'apparition de la surdité progressive. La désorganisation des stéréocils, notamment de la 1ère rangée, produit une réduction drastique de l'activité mécano-électrique des cellules ciliées externes et internes (Figure 1).

Une injection précoce intra-cochléaire (P1-P2) d'un AAV portant le gène normal de la clarine-2 permet de prévenir le développement de la surdité progressive chez les souris mutantes *clarinette* (Figure 2). L'amplitude de l'onde P1-N1 est restauré de moitié mais les seuils auditifs sont quasiment identiques aux souris non-mutantes.

Chez les souris mutantes *clarinette*, les cellules ciliées internes (CCIs) présentent plusieurs défauts majeurs. Tout d'abord la taille des CCIs est significativement diminuée. Le potentiel d'activation des canaux calciques présente un décalage vers un potentiel de membrane plus négatif, et l'efficacité calcique de l'exocytose est largement diminuée (Figure 3).

Chez les souris mutantes *clarinette* injectées par le vecteur AAV portant le gène de la clarine-2, les CCIs conservent leurs propriétés d'exocytose synaptique normale (Figure 3).

Les CCIs des souris mutantes clarinette possèdent également des défauts sur les courants potassiques, notamment ceux à grande conductance et cinétique rapide (BK). Les courants BK sont largement diminués et leur potentiel d'activation présente un grand décalage vers les potentiels plus positif (Figure 4).

Conclusion

Notre étude démontre le rôle crucial de la clarine-2 dans la régulation du potentiel d'activation des canaux calciques et potassiques BK des CCIs. L'efficacité calcique de l'exocytose est également largement réduite. L'utilisation de vecteurs viraux AAV contenant le gène de la clarine-2 permet la restauration quasi-complète des défauts mécano-électriques et synaptiques chez les souris mutantes *clarinette*.

De précédentes études ont démontré le rôle de la clarine-1, codée par un gène paralogue, dans l'organisation et la régulation des canaux calciques Cav1.3 des CCIs (Dulon et al., 2018). Nos résultats suggèrent que la clarine-2 pourrait également avoir un rôle similaire en interagissant directement avec le domaine C-terminale régulatrice des canaux calciques (Scharinger et al., 2015) ou avec des sous-unités beta auxiliaires aux canaux calciques (Liang and Tavalin, 2007). De la même manière que clarine-1, la clarine-2 pourrait aussi interagir indirectement avec les canaux calciques via d'autres protéines régulatrices comme l'harmonine (Gregory et al., 2013).

Nos résultats suggèrent que la clarine-2 est indispensable pour le maintien de l'intégrité des canaux BK. Ces derniers étant très sensibles à la régulation du calcium et du potentiel de membrane pourraient être régulé indirectement par l'action de la clarine-2 au niveau des canaux calciques. Il est possible aussi que la clarine-2 interagisse directement sur les sous-unités gamma régulatrices des canaux BK (Lingle et al., 2019) qui entraînent un décalage positif très similaire à celui observé chez les souris mutantes c*larinette*.

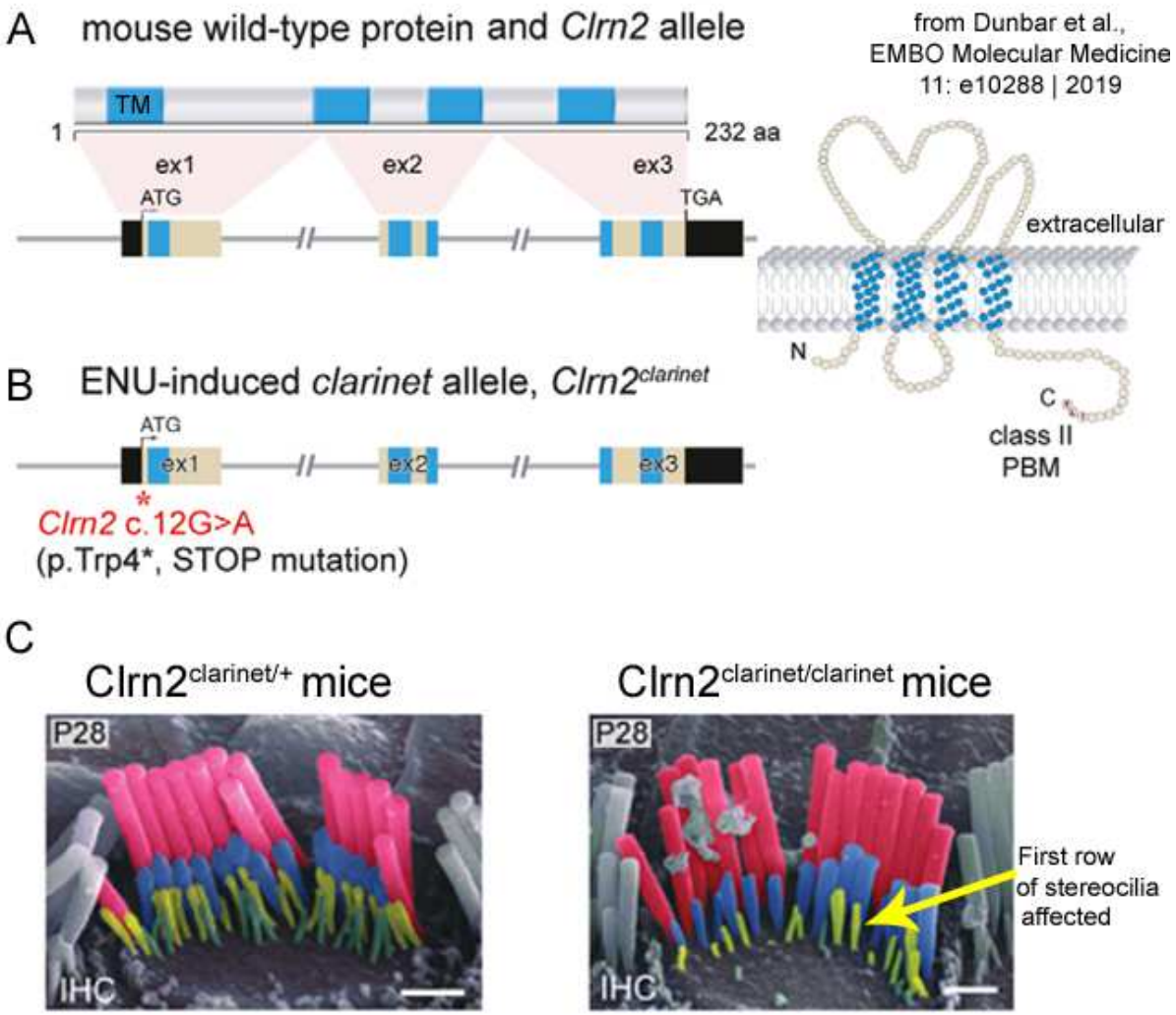
A mouse wild-type protein and Clrn2 allele
from Dunbar et al., EMBO Molecular Medicine 11: e10288 | 2019
TM
1
232 aa
ex1
ex2
ex3
ATG
TGA
extracellular
N
C
class II PBM
B ENU-induced clarinet allele, Clrn2clarinet
ATG
ex1
ex2
ex3
Clrn2 c.12G>A
(p.Trp4*, STOP mutation)
C
Clrn2clarinet/+ mice
Clrn2clarinet/clarinet mice
P28
IHC
First row of stereocilia affected

Figure 1

Figure 1. Sensory hair bundle defect in Clrn2$^{clarinet/clarinet}$ mice.

(**A**) The genomic structure of mouse Clrn2 (ENSMUST00000053250), and domains of the encoded tetraspan-like glycoprotein (232 amino acids). Black-filled boxes represent untranslated region of Clrn2. The positions of the transmembrane (TM) domains (blue) and the structure of Clrn2.

(**B**) The clarinet mutation, Clrn2^{clarinet} (c.12G > A) (red asterisk) leads to a premature stop codon at position 4 (p. Trp4*).

(**C**) Pseudo-colored scanning electron micrographs of individual IHC hair bundles from Clrn2$^{clarinet/+}$ and Clrn2$^{clarinet/clarinet}$ mice at P28. The two first rows of stereocilia of IHCs from P28 Clrn2$^{clarinet/clarinet}$ are disorganized, fewer in number and heterogeneous in height.

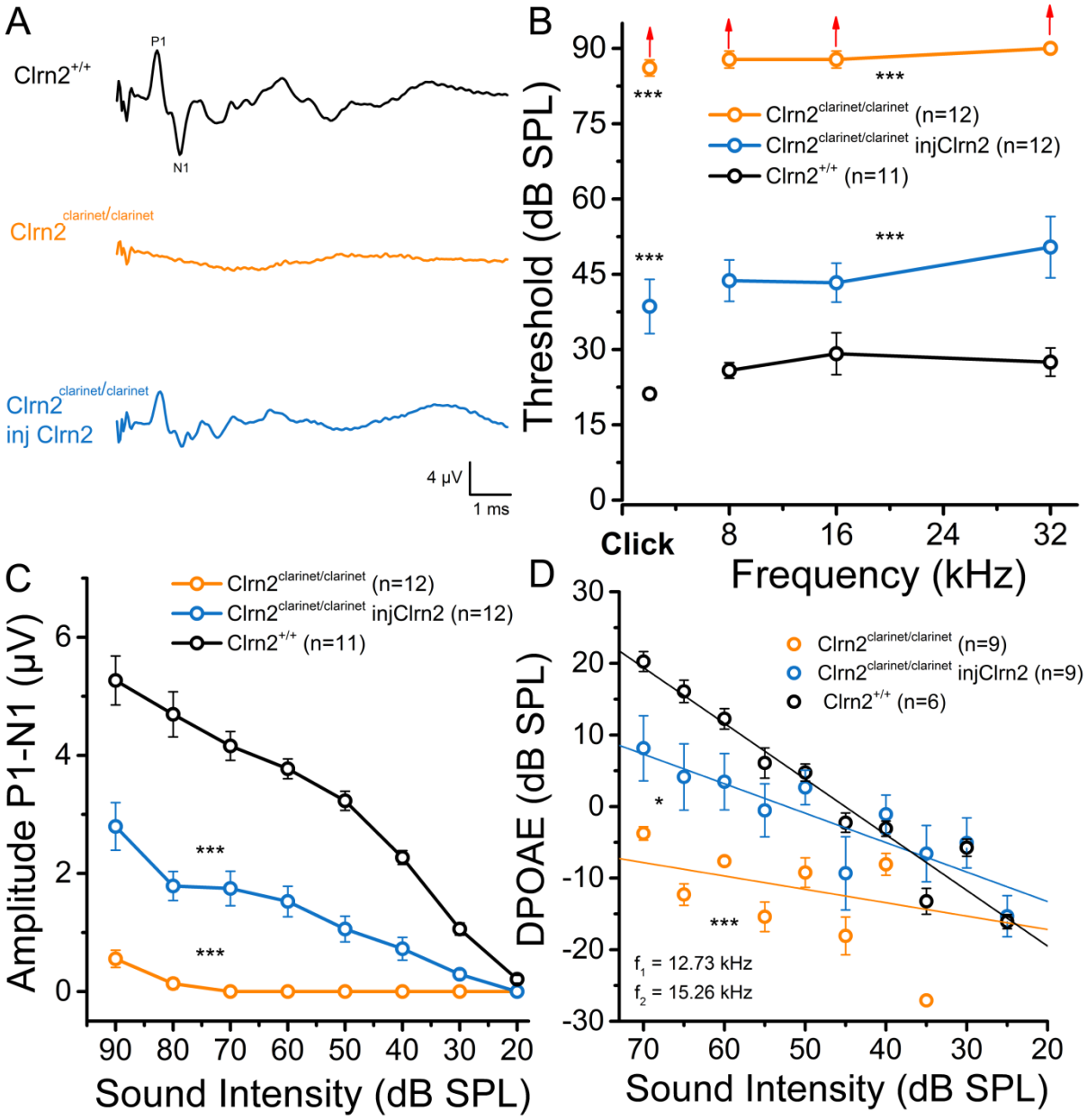
A
Clrn2+/+
P1
N1
Clrn2clarinet/clarinet
Clrn2clarinet/clarinet
inj Clrn2
4 µV
1 ms
B
Threshold (dB SPL)
Clrn2clarinet/clarinet (n=12)
Clrn2clarinet/clarinet injClrn2 (n=12)
Clrn2+/+ (n=11)
Click
Frequency (kHz)
C
Amplitude P1-N1 (µV)
Clrn2clarinet/clarinet (n=12)
Clrn2clarinet/clarinet injClrn2 (n=12)
Clrn2+/+ (n=11)
Sound Intensity (dB SPL)
D
DPOAE (dB SPL)
Clrn2clarinet/clarinet (n=9)
Clrn2clarinet/clarinet injClrn2 (n=9)
Clrn2+/+ (n=6)
f1 = 12.73 kHz
f2 = 15.26 kHz
Sound Intensity (dB SPL)

Figure 2.

Figure 2. Sensorineural hearing loss in Clrn2$^{clarinet/clarinet}$

(**A**) Examples of Click-ABR at 80 dB SPL.

(**B**) Click and frequencies ABR thresholds recorded from P28 Clrn2$^{+/+}$ mice (black; n=11), P28 Clrn2$^{clarinet/clarinet}$ mice (orange; n=12). Note a large increase in ABR thresholds in Clrn2$^{clarinet/clarinet}$ mice. P28 rescued Clrn2$^{clarinet/clarinet}$ mice (Blue; n=12) were obtained after intracochlear injection at P2ofan AAV containing Clrn2 gene (AAV_PHP.eB-CMV-Clrn2-IRES-GFP-WPRE) as previously described for Clrn1 (Dulon et al., 2018). Asterisks indicate significant difference with p<0.001 as compared to Clrn2$^{+/+}$mice (for tone ABRs: two-way ANOVA, post-hoc Tukey test; p=0.1E-7 and p=4.6E-46 respectively for Clrn2$^{clarinet/clarinet}$ and Clrn2$^{clarinet/clarinet}$ injected with AAV-Clrn2); (for click-ABRs: unpaired t-test; p=1.4E-26 and p=4.39059E-4).

(**C**) Click-Wave-I amplitude P1-N1 as a function of sound intensity in dB SPL.Clrn2$^{clarinet/clarinet}$ injected with AAV-Clrn2 displayed partially restored Wave-I. Asterisks indicate statistical difference compared to Clrn2$^{+/+}$ mice with p= 3.6E-11 and p= 6.37003E-5respectively for Clrn2$^{clarinet/clarinet}$ and Clrn2$^{clarinet/clarinet}$ injected with AAV-Clrn2 (two-way ANOVA).

(**D**) Distortion Products Otoacoustic Emissions (DPOAE in dB SPL) as a function of sound intensity (dB SPL). Note that in Clrn2$^{clarinet/clarinet}$ mice the DPOAEs are seriously affected and partially rescued in Clrn2$^{clarinet/clarinet}$ injected with AAV-Clrn2. These results suggest that the lack of Clrn2 affect the electro-mechanical activity (amplification) of the outer hair cells (OHCs), presumably by affecting their stereocilia organization (Dunbar et al., 2019). Asterisks indicate statistical difference compared to Clrn2$^{+/+}$ mice with p= 0.1E-7and p=0.03respectively for Clrn2$^{clarinet/clarinet}$ and Clrn2$^{clarinet/clarinet}$ injected with Clrn2 (two-way ANOVA between 70 to 45 dB SPL).

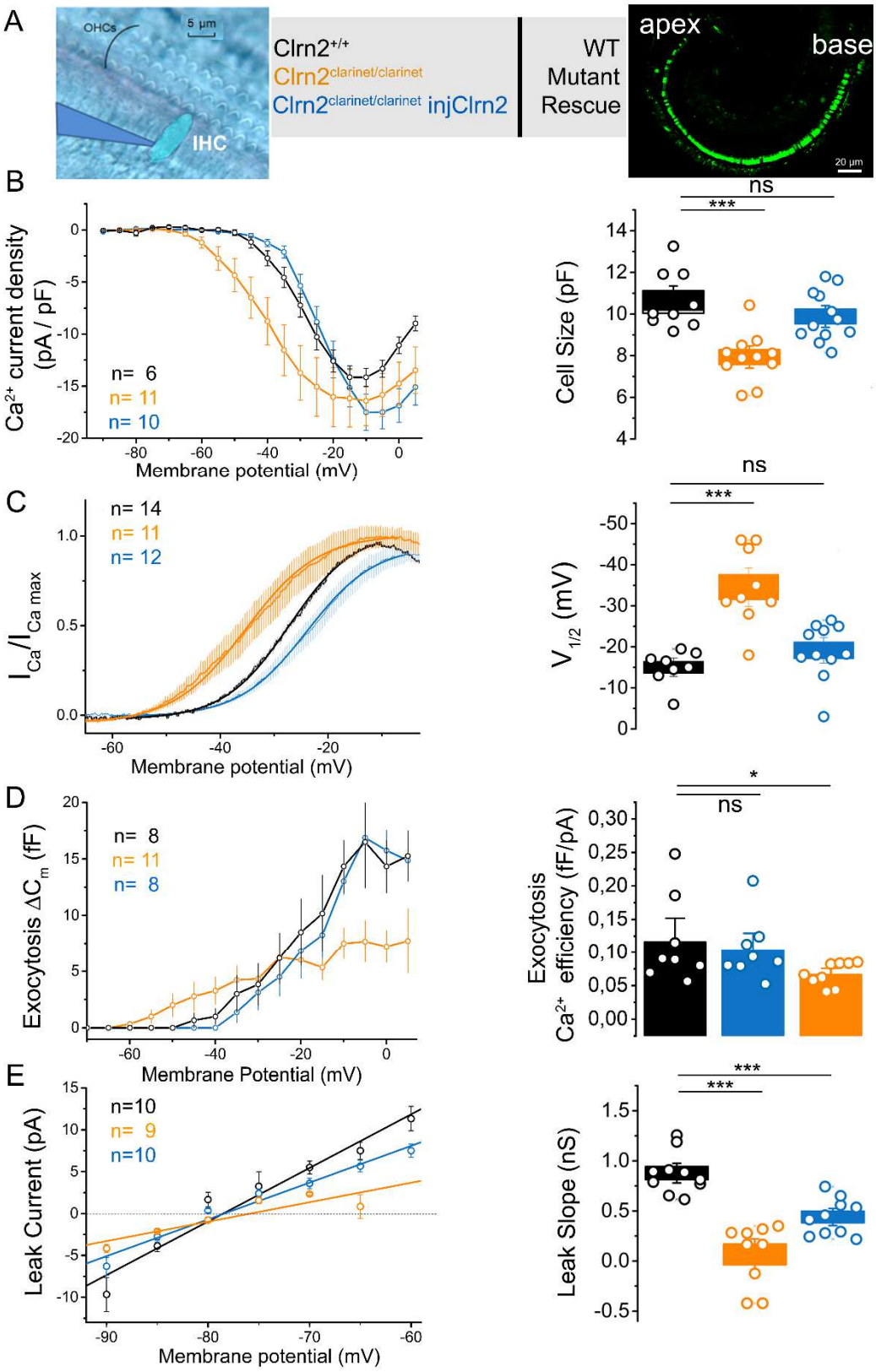
A
OHCs
5 µm
IHC
Clrn2+/+
Clrn2clarinet/clarinet
Clrn2clarinet/clarinet injClrn2
WT
Mutant
Rescue
apex
base
20 µm
B
Ca2+ current density (pA / pF)
n= 6
n= 11
n= 10
Membrane potential (mV)
Cell Size (pF)
ns
***
C
ICa/ICa max
n= 14
n= 11
n= 12
Membrane potential (mV)
V1/2 (mV)
ns
***
D
Exocytosis ΔCm (fF)
n= 8
n= 11
n= 8
Membrane Potential (mV)
Exocytosis Ca2+ efficiency (fF/pA)
*
ns
E
Leak Current (pA)
n=10
n= 9
n=10
Membrane potential (mV)
Leak Slope (nS)
***
***

Figure 3.

Figure 3. **Synaptic defect in Ca^{2+}-dependent exocytosis of P28 Clrn2$^{clarinet/clarinet}$ IHCs**

(**A**) Left image shows an ex-vivo organ of Corti explant from a P20 Clrn2$^{+/+}$ mice placed in the patch-clamp recording chamber containing artificial perilymph and observed under a FN1-Nikon microscope (X60 water immersion-objective). Right image shows, under confocal fluorescent microscopy, an AAV-GFP-Clrn2 transfected Clarin2$^{clarinet/clarinet}$ OC explant. The fluorescence due to the GFP cassette added in the AAV vector (AAV_PHP.eB-CMV-Clrn2-IRES-GFP-WPRE) indicated a good transfection of IHCs (> 90 %).

(**B**) Ca^{2+} current density of Clrn2$^{clarinet/clarinet}$ IHCs is similar to control Clrn2$^{+/+}$ IHCs (left graph) while Clarin2$^{clarinet/clarinet}$ IHCs were significantly smaller (resting cell surface membrane capacitance at -70 mV) than control IHCs (right graph). Asterisks indicate statistical difference with p=1.04E-4 and p=0.35 respectively forClrn2$^{clarinet/clarinet}$ and Clrn2$^{clarinet/clarinet}$ injected with AAV-Clrn2 (unpaired t-test).

(**C**) The voltage-activation curve of Ca^{2+} currents reveal a large negative shift of nearly 20 mV in Clrn2$^{clarinet/clarinet}$ IHCs. This shift is completely corrected in Clrn2$^{clarinet/clarinet}$ injected with AAV-Clrn2. Asterisks indicate statistical difference with p=2.37E-5 and p=0.45 respectively for Clrn2$^{clarinet/clarinet}$ and Clrn2$^{clarinet/clarinet}$ injected with Clrn2 (unpaired t-test).

(**D**) The voltage-dependent activation of exocytosis is also largely shifted to negative potentials in Clrn2$^{clarinet/clarinet}$ IHCs with a large decrease in amplitude. Exocytosis Ca^{2+} efficiency is also significantly decreased in Clrn2$^{clarinet/clarinet}$ IHCs (measured at I_{Ca} max for each cell). Asterisks indicate statistical difference with p=0.046 and p=0.67 respectively for Clrn2$^{clarinet/clarinet}$ and Clrn2$^{clarinet/clarinet}$ injected with AAV-Clrn2 (unpaired t-test).

(**E**) Leak currents measured between -90 and -60 mV (25 ms voltage-step) are significantly decreased in Clrn2$^{clarinet/clarinet}$ IHCs and partially recovered in Clrn2$^{clarinet/clarinet}$ injected with Clrn2 IHCs. Asterisks indicate statistical difference with p=1.2E-6 and p=0.8E-4respectively for Clrn2$^{clarinet/clarinet\ and}$ Clrn2$^{clarinet/clarinet}$ injected with Clrn2 (unpaired t-test). This resting leak current reflects the passive ionic current flowing through the mechanoelectrical channels (MET), suggesting their dysfunction in Clrn2 mutant IHCs.

Measurements of Ca^{2+} currents and membrane capacitance of IHCs were performed under whole-cell patch clamp conditions in P28 mice in the 20-40% normalized distance from the apex, an area coding for frequencies ranging from 8 to 16 kHz, by using an EPC10 amplifier controlled by Patchmaster pulse software (HEKA Elektronik, Germany). Patch pipettes were filled with a cesium-based intracellular solution containing (in mM): CsCl 145; MgCl2 1; HEPES 5; EGTA 1; TEA 20, ATP 2, GTP 0.3, pH 7.2, 300 mOsm. The organ of Corti was incubated in an extracellular perilymph-like solution containing NaCl 135; KCl 5.8; CaCl2 5; MgCl2 0.9; NaH2PO4 0.7; Glucose 5.6; Na pyruvate 2; HEPES 10, pH 7.4, 305 mOsm. This extracellular solution was complemented with 0.25 µM of apamin (Latoxan; cat # L8407) and 1 µM of XE-991 (Tocris Bioscience; cat # 2000) to block SK channels and KCNQ4 channels, respectively. The external Ca2+ concentration was increased from 1.3 to 5 mM to enhance the amplitude of Ca2+ currents to levels nearby body temperature. All experiments were performed at room temperature (22°C–24°C) as described in Peineau et al. (2021).

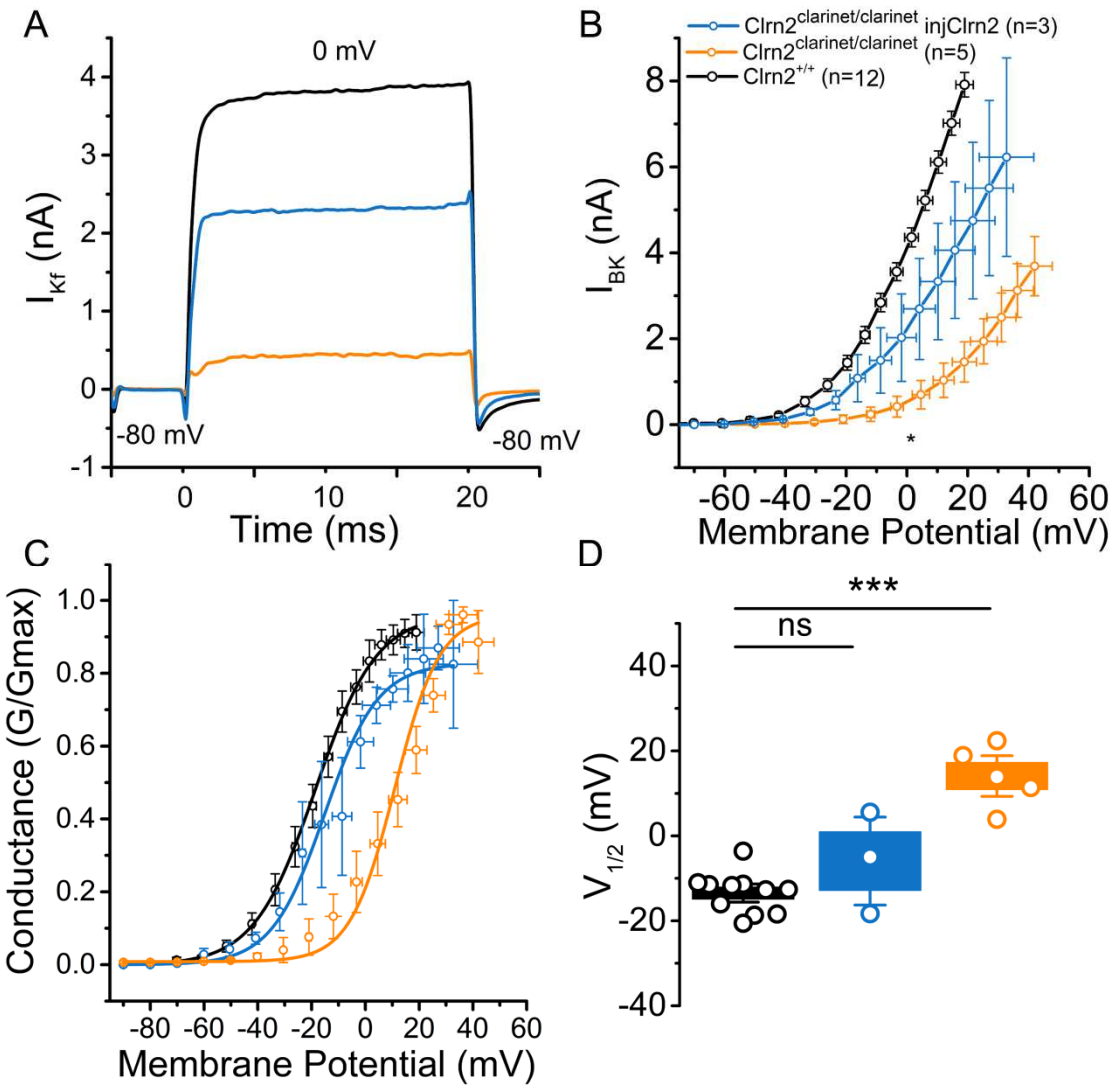
A
0 mV
-80 mV
-80 mV
I_{Kf} (nA)
Time (ms)
B
Clrn2clarinet/clarinet injClrn2 (n=3)
Clrn2clarinet/clarinet (n=5)
Clrn2+/+ (n=12)
I_{BK} (nA)
Membrane Potential (mV)
C
Conductance (G/Gmax)
Membrane Potential (mV)
D
***
ns
$V_{1/2}$ (mV)

Figure 4.

Figure 4. Defect in BK currents in Clrn2$^{clarinet/clarinet}$ IHCs

(**A**) Whole-cell patch-clamp recordings of BK currents in P28 IHCs from ex-vivo whole-mount preparation (Skinner et al., 2003). The figure shows comparative examples of BK currents when using a brief depolarization step of 20 ms from -80 to 0 mV in WT, mutant and rescued mice.

(**B**) Comparative BK current-voltage curves in Clrn2$^{+/+}$ (black), Clrn2$^{clarinet/clarinet}$ (orange) and Clrn2$^{clarinet/clarinet}$ injected with AAV-Clrn2 (blue). I_{BK} (termed also I_{Kf},f for fast, Kros et al., 1998) was measured 2.5 ms after the onset of the voltage-step stimulation allowing its separation from IK_s (non-BK slowly activating K channels). Note the large shift in the voltage-activation of BK channels in Clrn2 mutants.

Asterisk indicates statistical difference with p=0.038 and p=0.26 respectively for Clrn2$^{clarinet/clarinet}$ and Clrn2$^{clarinet/clarinet}$ injected with Clrn2 (unpaired t-test).

(**C**) Comparative BK conductance fitted with a Boltzmann function indicated a large shift in the half-max voltage activation from $V_{1/2}$ of -13,5 ± 1,43 mV in Clrn2$^{+/+}$ IHCs to14.1 ± 3.2 mV in Clrn2$^{clarinet/clarinet}$ IHCs and -5.9 ± 6.9 mV in rescued Clrn2$^{clarinet/clarinet}$ injected with AAV-Clrn2 IHCs.

(**D**) Comparative Box chart of the $V_{1/2}$ from graph in C. Asterisks indicate statistical difference with p=2.7E-6 and p=0.22 respectively for Clrn2$^{clarinet/clarinet}$ and rescued Clrn2$^{clarinet/clarinet}$ injected with AAV-Clrn2 (unpaired t-test).

Note that voltage error across series resistance (R_s = 5 ± 2 MΩ) and leak current were compensated for each IHC. Whole-cell patch clamp recordings were made in P28 mice in the 20-40% normalized distance from the apex, an area coding for frequencies ranging from 8 to 16 kHz, by using an EPC10 amplifier controlled by Patchmaster pulse software (HEKA Elektronik, Germany). Recording pipettes were filled with a KCl-based intracellular solution containing in mM: 158 KCl, 2 $MgCl_2$, 1.1 EGTA, 5 HEPES, and 3.05 KOH, pH 7.20. *All recordings were made at room temperature (22°C). All values are expressed as means ± SEM.*

Article 3

Targeted SNAP-25 deletion disrupts the function and structure of inner ear hair cell ribbon synapses

La délétion spécifique de la SNAP-25 dans les cellules ciliées internes perturbe les fonctions et la structure de la synapse à ruban.

(Manuscrit en préparation)

Introduction

La SNAP-25 est une protéine clé du complexe SNARE, un complexe essentiel dans l'exocytose des vésicules synaptiques du système nerveux central. En revanche, l'implication de cette protéine dans les synapses à rubans des cellules ciliées restent encore discutés. Le rôle de cette protéine dans les cellules ciliées n'a été exploré que sur des cultures organotypiques d'organe de Corti, dérivé d'embryons de souris "KO" pour SNAP-25, car l'absence de ce gène est léthale (Nouvian et al., 2011). Cette étude montre que l'exocytose synaptique des cellules ciliées internes immatures n'est pas affectée en absence de SNAP-25, suggérant que les protéines SNARE neuronales ne sont pas impliquées dans ces synapses à ruban. Pour essayer de lever cette ambiguïté, nous avons développé ici des modèles de souris où le gène de la SNAP-25 est supprimé spécifiquement dans les cellules ciliées. Ces modèles murins nous ont permis de démontrer l'importance de la SNAP-25 dans la fonction auditive et vestibulaire. La SNAP-25 est essentielle à l'exocytose rapide des cellules ciliées "matures" mais aussi à leur propre survie, probablement par la co-sécrétion de facteurs neurotrophiques essentiels tels que BDNF et NT3.

Résultats

Nous avons généré des souris dont le gène *Snap-25* est supprimé spécifiquement dans les cellules ciliées auditives et vestibulaires à différents du développement. Ces souris présentent à l'âge adulte une surdité profonde associée à des troubles vestibulaires importants. Ce phénotype est associé à un défaut de l'exocytose synaptique des synapses à ruban des cellules ciliées suivi d'une dégénérescence des synapses à rubans et des cellules ciliées elles-mêmes. Ce phénotype peut être prévenu par l'injection intra-cochléaire d'un vecteur AAV contenant le gène de la *Snap-25*.

Conclusion :

La protéine SNAP-25 est essentielle au fonctionnement des synapses à ruban, notamment dans l'exocytose rapide des vésicules synaptiques, de manière similaire à ce qui a été décrit dans les synapses neuronales (Oyler et al., 1989). Les mécanismes qui conduisent à une dégénérescence des synapses à rubans et des cellules ciliées elles-mêmes restent maintenant à élucider. Il faut noter que l'absence de SNAP-25 produit aussi une dégénérescence neuronale (Hoerder-Suabedissen et al., 2019).

Targeted SNAP-25 deletion disrupts the function and structure of inner ear hair cell ribbon synapses

Charlotte Calvet[1,2], Thibault Peineau[3], Andrea Lelli[1], Baptiste Plion[1], Ghizlène Lahlou[1,2,4], Julia Fanchette[1,5], Sylvie Nouaille[1], Jacques Boutet de Monvel[1], Amrit Estivalet[1], Philippe Jean[1], Vincent Michel[1], Martin Sachse[6], Nicolas Michalski[1], Paul Avan[7], Christine Petit[1], Didier Dulon[1,3], Saaid Safieddine[*1,2,8]

1 Institut de l'Audition, Institut Pasteur, INSERM, 75012 Paris, France

2 Sorbonne Université, Collège doctoral, 75005 Paris, France

3 Bordeaux NeuroCampus, Université de Bordeaux, 33076 Bordeaux, France

4 APHP, Sorbonne Université, Service d'ORL et de chirurgie cervico-faciale, 75013 Paris, France

5 APHP, Service d'ORL et de chirurgie cervico-faciale, Hôpital Bichat - Claude-Bernard, 75018 Paris, France

6 UTechS Ultrastructural Bio Imaging, Institut Pasteur, 75015 Paris, France

7 Laboratoire de Biophysique Sensorielle, Faculté de Médecine, Université d'Auvergne, Biophysique Médicale, Centre Jean Perrin, 63000 Clermont-Ferrand, France

8 Centre National de la Recherche Scientifique, France

Abstract

Hearing and balance are dependent on rapid, sustained otoferlin-dependent neurotransmitter release at the ribbon synapses of cochlear inner hair cells (IHCs). The function of SNARE proteins in this process remains unclear and controversial. We investigated the role in the inner ear of SNAP-25, a key molecule of the SNARE complex essential for synaptic vesicle exocytosis at brain synapses. To this end, we developed a conditional knockout mouse model in which *Snap-25* is inactivated specifically in hair cells at early postnatal stages. These mice displayed a strong reduction of the fast component of synaptic vesicle exocytosis in both cochlear IHCs and in vestibular hair cells. This synaptic deficit resulted in a loss of ribbons, followed by cochlear and vestibular hair cell degeneration, ultimately leading to profound deafness and severe balance disorders. The viral transfer of *Snap-25* in the mutant mice rescued their hearing by preventing the impairment of IHC exocytosis. These results show that SNAP-25 is required for fast synaptic vesicle fusion at hair cell ribbon synapses, demonstrating its essential role for normal hearing and balance functions.

42 **Introduction**

43 The auditory sensory inner hair cells (IHCs) encode sound into nerve impulses with
44 high temporal precision and sensitivity over a wide range of stimulus intensities [1–5].
45 The depolarization of IHCs in response to sound-evoked deflection of their hair bundle
46 results in rapid calcium influx through voltage-activated $Ca_V1.3$ Ca^{2+} channels located
47 in the active zone at the basal IHC pole [6–8], and the subsequent binding of Ca^{2+} ions
48 to otoferlin, the calcium sensor controlling the fusion of IHC synaptic vesicles [9–13].
49 Similar mechanisms of neurotransmitter release have been described in the vestibular
50 hair cells (VHCs, the sensory cells of the balance organs) [3], and in the immature
51 auditory outer hair cells (OHCs) [14]. A striking structural and functional feature of IHC
52 synapses is the presence of an electron-dense presynaptic organelle of submicron
53 diameter called a ribbon, marking the center of the synaptic active zone. Each ribbon
54 is surrounded by synaptic vesicles that are either attached or close to it. Despite their
55 structural differences, IHC ribbon synapses and conventional central nervous system
56 (CNS) synapses share several key mechanisms of regulated synaptic vesicle
57 exocytosis. IHC and CNS synapses are both equipped with the presynaptic scaffold
58 proteins, bassoon and RIM [15,16]. They also both contain several of the neuronal
59 SNARE (soluble N-ethylmaleimide sensitive factor attachment protein receptor)
60 proteins involved in synaptic vesicular trafficking and membrane fusion, including
61 syntaxin, SNAP-25 and VAMP [17,18]. The presence of these neuronal SNARE
62 transcripts in hair cells is well established [19], but the presence and the role of the
63 proteins they encode at the synapses of these cells remain unclear. Indeed, Ca^{2+}-
64 dependent exocytosis by IHCs is unaffected in organotypic cultures of organs of Corti
65 derived from embryonic *Snap-25*-null mice, suggesting that IHC ribbon synapses can
66 operate in the absence of neuronal SNAREs [20]. However, since *Snap-25*-null mice die

67 at birth [21], it has been impossible, to date, to investigate the consequences of *Snap-*
68 *25* deletion on the biophysical properties of mature IHC ribbon synapses, and to
69 uncover the possible functions of the protein in the inner ear. To resolve this issue, we
70 developed a hair cell-specific *Snap-25* knockout (*Snap-25* cKO) mouse model allowing
71 to study the role of SNAP-25 in auditory and vestibular hair cells at neonatal or mature
72 stages. We found that *Snap-25* inactivation in these mice before or after hearing onset
73 led to profound deafness, accompanied by severe balance disorders. This phenotype
74 was associated with a strongly defective exocytosis at the synapses of both cochlear
75 IHCs and VHCs, which was followed by ribbon degeneration and a progressive loss of
76 hair cells.
77
78
79
80
81
82
83
84
85
86
87
88
89
90
91

92 **Results**

93

94 **SNAP-25 expression in inner-ear hair cells**

95 To identify genes encoding proteins involved in synaptic function at the IHC synapses,
96 we adapted next generation single-cell mRNA amplification techniques to probe mRNA
97 content in samples containing ~20 cochlear IHCs. We sequenced these mouse IHC
98 samples at three different postnatal stages — P2, P7, and P16 — in addition to a
99 control P7 sample containing spiral ganglia and associated glial cells. We detected in
100 IHCs SNAP-25 mRNA and other members of the SNAP-25 gene family, including
101 SNAP-23, SNAP-29 and SNAP-47. Notably SNAP-25 mRNA was detected at levels
102 comparable to mRNA of the calcium channel $Ca_v1.3$, the SNARE protein VAMP2, and
103 ribeye, a major structural protein of the ribbon (Figure 1a). Using *in situ* hybridization
104 (see Methods), we were able to localize SNAP-25 mRNA to both IHCs and OHCs
105 (Figure 1b).

106

107 **Generation of mice with a hair cell-specific *Snap-25* knockout**

108 *Snap-25* deletion in mice is lethal at birth, as a result of respiratory failure due to the
109 lack of stimulus-evoked diaphragm contraction despite normal innervation. Previous
110 studies on hippocampal and cortical cultures derived from *Snap-25* KO mouse
111 embryos have revealed very low levels of neuronal survival, and a complete absence
112 of calcium evoked synaptic exocytosis in the few neurons that survive [21]. We
113 investigated the role of SNAP-25 in IHC ribbon synapse function, by using a hair cell-
114 specific Cre recombinase tool to generate *Snap-25*$^{flox/flox}$ mice with a selective
115 inactivation of *Snap-25* in the inner ear. In this mouse model, exon 4, which is common
116 to the two Snap-*25* isoforms, is flanked by two P-lox sites [22] (Fig. Suppl. 1). The

117 resulting mice were crossed with *PMyo15-hCre*$^{+/KI}$ mice, in which the expression of Cre
118 recombinase is restricted to cochlear and vestibular hair cells under the control of the
119 promoter of the myosin 15 gene [23].
120 The cell specificity of the inactivation was confirmed by crossing *PMyo15-hCre*$^{+/KI}$ mice
121 with the red fluorescent reporter mouse line *Rosa*-tdTomato. Consistent with the earlier
122 study by Caberlotto et al. [23], Cre expression in the cochlea was restricted to the hair
123 cells, and had a mosaic pattern with a baso-apical gradient on P1, which subsequently
124 became uniform along the entire cochlea by P6 (Fig. Suppl. 2). Thus, in the cochlea of
125 *Snap-25*$^{flox/flox}$*/PMyo15-hCre*$^{+/KI}$ mice, *Snap-25* inactivation occurs only in auditory hair
126 cells, from P1 onwards (Fig. Suppl. 2). A similar pattern was observed in the hair cells
127 of the vestibular epithelium (Fig. Suppl. 2). We thereafter refer to these mice as *Snap-*
128 *25* conditional knockout (*Snap-25* cKO) mice.
129

130 ***Snap-25* is essential for the maintenance of ribbon synapses and hair cells**

131 *Snap-25* cKO mice were viable and the displayed a normal Mendelian pattern of
132 inheritance. We analyzed the morphoanatomy of the organs of Corti of these mice at
133 various stages of development, using myosin 6 as a marker of auditory hair cells [24].
134 Overall, the organ of Corti displayed near normal morphology until P10 (Figure 2a). At
135 this stage, all the hair cells were still present. To determine the number and spatial
136 organization of ribbons in the IHCs of *Snap-25* cKO mice, organs of Corti were
137 microdissected on P10 and immunolabeled for myosin 6 and ribeye. We found that the
138 number of synaptic ribbons per IHC, in the mid-apical region of the cochlea, was
139 significantly smaller in *Snap-25* cKO mice (12.4 $\pm$ 2.8, n=20 cells from 4 mice) than in
140 wild-type mice (18.8 $\pm$ 2.7, n=15 cells from 3 mice) (unpaired t-test, p<0.0001)

141 (Figure 2b). We then performed transmission electron microscopy (TEM) on ultrathin
142 (70 nm) sections from P10 *Snap-25* cKO mice. Sections from the synaptic active zone
143 of IHCs of these mice displayed a normal ribbon structure decorated with synaptic
144 vesicles and facing the postsynaptic density of an auditory afferent dendrite (Figure
145 2b). However, from P10 onward, a progressive process of rapid hair cell degeneration
146 occurred (Figure 2a). Hair cell degeneration was also observed in the vestibular
147 sensory epithelium (Figure 4d). Auditory brainstem responses (ABRs) and vestibular
148 tests showed that, at adult stages, these mice suffered from profound deafness and a
149 severe balance defect (Figure 3a-3c).
150 Together, these results strongly support the idea that SNAP-25 is essential for the
151 maintenance of hair cells and their ribbon synapses.
152
153 ***Snap-25* deletion disrupts IHC exocytosis and causes hair cell loss**
154 We next investigated the kinetics of IHC synaptic exocytosis in *Snap-25* cKO mice
155 before (P8) and at (P12) hearing onset, using membrane capacitance measurements
156 performed in microdissected *ex vivo* explants of organs of Corti (Figure 4). On P8, the
157 level of exocytosis of the readily releasable pool of vesicles (RRP), recorded in
158 response to short depolarizations ranging from 5 to 30 ms, was significantly lower in
159 IHCs with *Snap-25* inactivation (Figure 4a; two-way ANOVA, $p<0.05$). At this stage,
160 IHCs from mutant mice were of normal size, as indicated by the value of their resting
161 membrane capacitance (8.27 ± 0.33 pF, $n=10$), which did not differ significantly from
162 the value measured in wild-type mice (9.03 ± 0.22 pF, $n=7$; unpaired-*t* test, non-
163 significant, $p=0.1$). In these P8 IHCs, the amplitude of the Ca^{2+} currents was marginally
164 smaller than that recorded in control IHCs (unpaired *t* test, $p=0.054$, Figure 4a). At this
165 stage, the *Snap-25* cKO IHCs had structurally normal hair bundles as imaged by

166 scanning electron microscopy (SEM) (Figure 4b), and their mechanoelectrical
167 transduction (MET) currents recorded by patch clamp (see Methods) displayed
168 amplitudes and kinetics similar to those of wild-type IHCs (Supplementary Fig 3). On
169 P12, exocytosis levels in *Snap-25* cKO IHCs had greatly decreased (two-way ANOVA,
170 $p<0.05$, Figure 4a). The resting membrane capacitance was reduced by almost a half,
171 from 10.89 ± 0.73 pF in wild-type IHCs (n=11) to 5.85 ± 0.62 pF in mutant IHCs (n=9)
172 (unpaired t test $p<0.05$). The amplitude of total IHC Ca^{2+} currents was also halved
173 (unpaired t test $p<0.05$), so that the total Ca^{2+} current to membrane capacitance ratio
174 (average Ca^{2+} current density measured in pA/pF) remained unchanged (unpaired t
175 test, p=0.24, Figure 4a). Similar decreases in exocytosis and Ca^{2+} current amplitude
176 were also recorded in vestibular hair cells from *Snap-25* cKO mice on P16 (Figure 4c).
177 These results strongly suggest that SNAP-25 is required for exocytosis at vestibular
178 and cochlear hair cell ribbon synapses.
179 Since *Snap-25* inactivation in neonatal inner ear hair cells resulted in a rapid
180 degeneration of IHCs starting at about the onset of hearing, (i.e. P12) for investigations
181 after the hearing onset, we delivered the Cre recombinase cDNA to the IHCs of *Snap-*
182 *25*$^{flox/flox}$ mice via *in vivo* cochlear injection on P14. We first analyzed the cellular
183 tropism and innocuity of AAV8-GFP-Cre in the mature organs of Corti of wild-type
184 mice. Following the injection of AAV8-GFP-Cre into the cochlea of P14 mice, the organ
185 of Corti was microdissected on P30 and immunostained for myosin 6 and GFP. We
186 found that AAV8-Cre-GFP transduced almost all the IHCs on this stage. In addition,
187 no significant effect could be detected on auditory brainstem response (ABR)
188 thresholds, which remained similar to those in non-injected P30 wild-type mice, except
189 at 15 kHz, for which a small increase, of about 5 dB, was noted (n=4; t test, p=0.036)
190 (Figure 5a, Fig. Suppl.4). By contrast, *Snap-25*$^{flox/flox}$ mice (n=14) subjected to Cre-

191 mediated *Snap-25* deletion on P14 displayed a progressive but significant increase in
192 ABR thresholds from P22 onward (Figure 5b). On P30, the increase in ABR thresholds
193 ranged from 20 to 40 dB, at all frequencies tested (5, 10, 15, 20, 32 and 40 kHz),
194 relative to non-injected *Snap-25*$^{flox/flox}$ mice (*n*=16) (unpaired *t* tests, *p*<0.001; <0.01;
195 <0.001; <0.01; <0.001; <0.001, respectively) (Figure 5b). The amplitude of ABR wave
196 I, which reflects the synchronous firing of the primary auditory neurons as a function of
197 sound intensity, when measured at 10 kHz and 80 dB SPL, was much smaller in mice
198 lacking SNAP-25 subjected to intracochlear Cre injection (0.040 µv ± 0.026 *n*=39 mice)
199 than in non-injected *Snap-25*$^{flox/flox}$ mice (0.083 µV ± 0.031 *n*=6 mice) (Mann Whitney,
200 p<0.001). Ten weeks after intracochlear Cre injection, the ABR thresholds exceeded
201 75 dB SPL at all frequencies tested, indicating severe hearing defect (t tests, p<0.05;
202 <0.01; <0.01; <0.001; <0.001; <0.01, respectively, *n*=7 injected *Snap-25*$^{flox/flox}$ mice,
203 *n*=6 wild-type mice) (Figure 5b). In contrast, distortion product otoacoustic emissions
204 (DPOAEs), which probe the functional integrity of OHCs, remained unaffected until
205 P50, the last time point tested (Mann Whitney, p>0.99, *n*=6 *Snap-25*$^{flox/flox}$ injected
206 mice, *n*=7 wild-type mice), suggesting that the inactivation of *Snap-25* after hearing
207 onset did not impair the cochlear amplifier function of the OHCs (Fig. Suppl. 5). The
208 observed increase in ABR thresholds accompanied by a decrease in wave I amplitude,
209 and normal DPOAEs, together indicate a defect of the afferent IHC ribbon synapses in
210 *Snap-25*$^{flox/flox}$ mice that had received AAV8-GFP-Cre injections. Indeed, recordings of
211 Ca^{2+}-evoked exocytosis in Cre-positive IHCs from AAV8-GFP-Cre-injected ears of
212 *Snap-25*$^{flox/flox}$ mice on P30 revealed a large decrease in the fast exocytotic release
213 component despite normal Ca^{2+} currents (Figure 5c). The Ca^{2+} efficiency of exocytosis
214 was also strongly reduced for depolarizations shorter than 40 ms (Figure 5c), indicating
215 an abnormal fusion of synaptic vesicles belonging to the RRP. The slow exocytosis

216 component of the Cre-positive IHCs, reflecting synaptic vesicle recruitment upon
217 stimulations longer than 50 ms, was however unaffected (Figure 5c), suggesting that
218 this slow component might make use of redundant SNAP-25 homologs, such as
219 SNAP-23, which is also present in IHCs (Figure 1a) [25,26]. The impairment of the RRP
220 response in IHCs lacking SNAP-25 was further confirmed in Ca^{2+} uncaging
221 experiments, which directly probe the function of the synaptic machinery independently
222 of voltage-triggered Ca^{2+} currents (Figure 5c). In IHCs from Cre-injected mice,
223 intracellular Ca^{2+} uncaging evoked maximal levels of exocytosis similar to those for
224 IHCs from control *Snap-25*$^{flox/flox}$ mice without Cre injection (1.18 ± 0.15 pF (*n*=13) and
225 1.16 ± 0.13 pF (*n*=13), respectively, p=0.49, unpaired *t* test), indicating that the total
226 number of competent synaptic vesicles for fusion was unaffected in IHCs lacking
227 SNAP-25. The maximal rate of exocytosis in IHCs from Cre-injected mice (32.5 ± 1.18
228 fF/ms (*n*=13) was also similar to that measured in control IHCs (32.7 ± 2.06 fF/ms
229 (*n*=13), p=0.36, unpaired *t* test). However, the onset of exocytosis in IHCs from Cre-
230 injected mice was significantly delayed (latencies of 22.2 ± 3.7 ms (*n*=13) versus 8.46
231 ± 1.30 ms (*n*=13), respectively, p<0.01, unpaired *t* test), indicating that the core of the
232 synaptic machinery was affected. These results suggest that *Snap-25* inactivation after
233 the onset of hearing leads to progressive deafness in mice due to RRP release deficits.
234 We then performed quantitative analyses of the number of ribbon synapses per IHC in
235 the *Snap-25*$^{flox/flox}$ AAV8-GFP-Cre-injected cochleas at mature stages. Two weeks after
236 Cre delivery (P28-P30), a stage at which synaptic exocytosis was probed, the organ
237 of Corti of the injected *Snap-25*$^{flox/flox}$ mice was microdissected and immunolabeled for
238 myosin 6, GFP and CtBP2 (Figure 6a). We found that the number of synapses per IHC
239 was significantly smaller in the Cre-positive cells (9.1 ± 4.9 *n*=20 cells from 7 mice)
240 than in wild-type IHCs (17.67 ± 1.5 *n*=21 cells from 6 mice; p<0.0001, *t* test). In

241 addition, throughout the spiral cochlea at this stage, we observed the presence of
242 patches of immunostained IHCs separated by zones without IHCs that had
243 considerably expanded by the age of three months (Figure 6b, 6c). Together, our
244 results suggest that the inactivation of *Snap-25* expression in IHCs causes a
245 degeneration of the ribbon synapses and, subsequently, of the IHCs, by impairing the
246 fast component of exocytosis in these cells. This hypothesis is consistent with the
247 notion that synaptic dysfunction contributes to pathogenic progression before the
248 occurrence of neurodegeneration [27–29].
249

250 **The virus-mediated transfer of *Snap-25* cDNA restores IHC exocytosis and**
251 **hearing in *Snap-25* cKO mice**

252 To verify that the defects described above were caused directly by the conditional
253 knockout of *Snap-25*, we performed gene rescue experiments with viral vector carrying
254 the *Snap*-25b splice variant shown to be the most effective in central synapses [25]. Viral
255 particles expressing *Snap*-25b driven by the CMV promoter were delivered to the
256 cochlea of *Snap-25* cKO mice on P2. Unlike untreated *Snap-25* cKO mice, the rescued
257 mice had recordable ABRs three weeks after *Snap-25b* cDNA transfer, with thresholds
258 ranging from wild-type levels to 30-40 dB above those levels (Figure 7a). The mean
259 amplitude of wave I in response to tone bursts was also partially rescued, reaching
260 about half that in control injected mice (n=9) at 10 kHz (n=7; t test, p<0.05) (Figure 7a).
261 Consistent with the ABR recordings, SEM and immunostaining analyses of the organs
262 of Corti, the non-rescued *Snap-25* cKO mice on P30 showed a complete loss of both
263 OHCs and IHCs (Figure 7b). By contrast, animals receiving AAV8-CMV-*Snap*-25
264 injections had well-preserved organs of Corti with a morphostructure similar to that of
265 wild-type hair cells on P30 (Figure 7b, 7c). Furthermore, whole-mount preparations of

266 the organ of Corti immunolabeled for myosin 6 and neurofilament to identify hair cells
267 and auditory afferent fibers, respectively, indicated that no IHC degeneration had
268 occurred at that stage in the rescued mice, and that afferent innervation was well
269 preserved throughout the entire cochlea (*n*=171 cells from 5 mice) (Figure 7c). The
270 number of synaptic ribbons per transduced IHC in *Snap-25* cKO mice (13.4 ± 3.2, *n*=25
271 cells from 3 mice) was significantly higher than that for IHCs from *Snap-25*$^{flox/flox}$ AAV8-
272 GFP-Cre-injected mice (9.1 ± 4.9; $p<0.001$, unpaired *t* test, Figures 6a, 8a), but
273 remained lower than that in wild-type IHCs (17.3 ± 2.6 *n*=25 cells from 3 mice;
274 $p<0.0001$, unpaired *t* test) (Figure 8a), potentially accounting for the partial recovery of
275 the ABR wave I amplitude in injected *Snap-25* cKO mice.
276 We then monitored Ca^{+}-evoked exocytosis in IHCs from *Snap-25* cKO mice 4 weeks
277 after the intracochlear delivery of AAV8-CMV-*Snap-25* on P2. We found that
278 exocytosis and Ca^{2+} currents in these *Snap-25* cKO injected mice (*n=7* and *n=6*,
279 respectively) had recovered to wild-type control levels (*n=11* and *n=14*, respectively)
280 (Figure 8b; two-way ANOVA for exocytosis, $p=0.10$ and unpaired *t* test for peak I_{Ca},
281 $p=0.34$). Ca^{2+} uncaging experiments further confirmed that RRP exocytosis kinetics in
282 transduced IHCs were also restored to wild-type levels with a similar onset latency (5.0
283 ± 0.5 ms (*n*=4) and 8.46 ± 1.3 ms, respectively, (*n*=10), $p=0.17$, unpaired *t* test; Figure
284 8b). The resting C_m size at -70 mV in rescued P30 IHCs also indicated a significant
285 rescue of cell size relative to the surviving IHCs from non-injected P12 *Snap-25* cKO
286 mice (9.08 ± 0.36 pF (*n*=15) vs. 5.85 ± 0.62 pF (*n*=9; $p < 0.05$, unpaired *t* test). Overall,
287 these data demonstrate that intracochlear AAV8-CMV-*Snap-25* transfer restores IHC
288 RRP exocytosis and hearing in *Snap-25* cKO mice.
289
290

291 **Discussion**

292 Since its discovery in 1989 [30], SNAP-25 has been widely implicated in neurotransmitter
293 release [31,32]**.** Its functional role has been confirmed by a large body of data obtained
294 from SNAP-25 null mutant models, tissue-specific genetic ablation or analyses of the
295 tissue-specific functions of SNAP-25 [21]. However, the role of SNAP-25 in IHC function
296 remained unresolved, and even questioned by the results obtained with organotypic
297 cultures of organ of Corti explants derived from *Snap-25* KO mouse embryos [20]. We
298 developed and characterized a *Snap-25* cKO mouse model in which the *Snap-25* gene
299 is selectively inactivated in auditory and vestibular HCs. We were able to show that up
300 to P8, the hearing organ exhibited near normal morphology, with no alterations to hair
301 cell mechanoelectrical transduction (MET) currents and normal ribbon synapse
302 structure, as demonstrated by electrophysiological recordings, hair cell
303 immunostaining and transmission electron microscopy. The normal ultrastructural
304 aspect of the IHC ribbon synapse is probably explained by the fact that the protein is
305 already produced in the hair cells at the time of the *Snap-25* gene inactivation.
306 However, during the second postnatal week of cochlear development, just before
307 hearing onset, both the auditory and vestibular hair cells of *Snap-25* cKO mice
308 presented a progressive dysfunction and degeneration of ribbon synapses, followed
309 by massive hair cell degeneration. This result suggests that SNAP-25 is essential for
310 the maintenance of both hair cells and ribbon synapses, a finding consistent with
311 several brain studies, demonstrating that the absence of SNAP-25 leads to synapse
312 disruption followed by neuronal death [21,33,34].

313 Our findings provide clear evidence for a crucial role of SNAP-25 in the second
314 postnatal week of cochlear development in mice, during which the auditory hair cells
315 are subjected to intense synaptic reorganization. The refinement of the afferent

316 neurites synapsing on the IHCs has been shown to be dependent on neurotrophic
317 factors [35–39]. In this context, it is interesting to note that, in addition to its role in synaptic
318 vesicle fusion, SNAP-25 has been shown to trigger the release of neurotrophic factors
319 from the organelles that transport them and fuse with membranes in callosal axons [40].
320 Consistent with these findings, neuronal loss has been observed both *in vivo* and *in*
321 *vitro* in the absence of several presynaptic proteins, including SNAP-25, munc18 and
322 syntaxin [21,41–45]. We suggest that SNAP-25 also plays a key role in neurotrophic
323 secretion by hair cells, which is required for the maintenance of hair cells and their
324 ribbon synapses [46–48].
325 One of the most notable findings of our study is the clarification of the role of SNAP-25
326 in mature IHC exocytosis. Inactivation of the *Snap-25* gene after hearing onset disrupts
327 the fast phase of IHC synaptic transmission, as demonstrated by our IHC membrane
328 capacitance measurements in response to cell depolarization or intracellular Ca^{2+}
329 uncaging. This finding is consistent with the complete absence of the RRP observed
330 following the stimulation by flash photolysis of caged Ca^{2+} in *Snap-25* KO embryonic
331 chromaffin cells [25]. Similarly, the rapid phase of secretion has also been reported to be
332 delayed in *Snap-25* KO embryonic chromaffin cells rescued with mutated SNAP-25 [49–
333 51]. In agreement with this observation, we also found an increase in latency for the
334 onset of exocytosis evoked by Ca^{2+} uncaging, indicating that the core of the synaptic
335 exocytosis machinery was affected by the absence of SNAP-25 in IHCs. Interestingly,
336 the impairment of IHC synaptic transmission followed by synapse and hair cell
337 degeneration is reminiscent of observations for the neuromuscular junction synapse
338 and *Drosophila melanogaster* photoreceptor neurons, and also consistent with the
339 growing evidence that synapse loss precedes cell degeneration [52–54]. We also verified
340 that the defects observed were, indeed, due to *Snap-25* conditional inactivation, by

341 demonstrating that the virus-mediated transfer of *Snap-25* cDNA to the inner ear of
342 *Snap-25* cKO mice successfully rescued IHC exocytosis, prevented degeneration of
343 the ribbon synapses and hair cells, and prevented the mutant mice from becoming
344 profoundly deaf. In light of these results, we can conclude that SNAP-25 is essential
345 for normal IHC exocytosis. In stark contrast, IHC exocytosis was found to be unaffected
346 in organotypic cultures derived from E18 *Snap-25* KO mouse embryos [20]. One of the
347 major limitations of these cultures was the very short time window for early *in vitro*
348 neonatal development of the organ of Corti. The absence of an exocytotic defect in this
349 study probably reflects the immaturity of the IHCs within organotypic explants.
350 Moreover, one cannot rule out possible redundancy and the compensatory regulation
351 of other genes at immature ribbon synapses. Toxin-resistant proteins from the SNAP-
352 25 family, such as SNAP-23, SNAP-29 or SNAP-47, may play a compensatory role in
353 the exocytosis observed in immature IHCs lacking SNAP-25. Both an absence of
354 SNAP-25 detection by immunolabeling and resistance of the protein to botulinum
355 toxins A and E, which normally block neurotransmitter release through proteolysis of
356 this SNARE, have been reported in hippocampal GABAergic synapses, and even in a
357 subset of glutamatergic terminals [55,56]. Finally, thanks to the SNARE-like role of the
358 FerA domain, otoferlin may also partially compensate for the lack of SNAP-25
359 in IHCs [57].
360 In conclusion, our results provide strong evidence that SNAP-25 acts as a crucial
361 t-SNARE protein involved in fast synaptic vesicle exocytosis at auditory and vestibular
362 hair cell ribbon active zones, with an action similar to that in central neuronal synapses.
363 In addition to its role in neurotransmission, SNAP-25 is also essential for ribbon
364 synapse maintenance and hair cell survival, probably through control over the
365 secretion of essential neurotrophic factors.

366

367 **Materials and methods**

368

369 ***Deep sequencing of inner hair cell mRNA***

370 IHC samples were collected in triplicate from excised organs of Corti (from P2, P7 and
371 P16 mice) placed under two nylon meshes and observed with an Olympus 40× water-
372 immersion objective (Tokyo, Japan). A patch pipette containing Hank's balanced salt
373 solution was used, with strong positive pressure, to separate IHCs from the
374 neighboring supporting cells. A second patch pipette with a small volume of Hank's
375 solution (~2 µL) was then used to collect 20 IHCs. Each sample consisted in 20 IHCs
376 collected from a different organ of Corti. The sampled IHCs were then processed for
377 reverse transcription to generate cDNA from mRNA, the PCR amplification of cDNAs,
378 and deep-sequencing with a protocol described in detail elsewhere [58,59]. Briefly,
379 sampled IHCs were placed in a tube containing the SuperScript III Reverse
380 Transcriptase reagents (Life Technologies) in accordance with the manufacturer's
381 instructions. The mRNA was then reverse-transcribed to generate cDNA, with a poly(T)
382 primer with an anchor sequence (UP1). A poly(A) tail was added to the 3' end of the
383 first-strand cDNAs, and the second-strand cDNAs were then synthesized with poly(T)
384 primers with another anchor sequence (UP2). The cDNAs were then uniformly
385 amplified by PCR with primers directed against the UP1 and UP2 anchor sequences.
386 The PCR products were purified, libraries were prepared and samples were deep-
387 sequenced with an Illumina Version 3 sequencer (100 bp paired-end reads, Eurofins,
388 Germany). For each transcript, the reads were mapped onto the mouse genome
389 (Genomatix, Munich, Germany) and normalized expression values were calculated as
390 follows: $f = 10^7 \times (\#reads_{region})/(\#reads_{mapped})$, where 10^7 is a normalization constant,

391 #reads$_{region}$ the number of reads (sum of base pairs) corresponding to the transcript,
392 and #reads$_{mapped}$ th e total number of mapped reads in the sample (sum of base pairs).
393 We did not normalize by the length of the sequenced mRNA because the vast majority
394 of sequenced reads were located at the 3' end of mRNAs, next to the poly(A) tail. We
395 considered only unambiguous unique hits for the analysis.
396
397 ***RNAscope***
398 For the RNAscope assays, cochleas from P7 wild-type C57BL/6J mice were extracted
399 in fresh cold phosphate-buffered saline and fixed by incubation with 4% PFA for 1 hour
400 at room temperature. The organs of Corti were then microdissected and dehydrated in
401 successive ethanol solutions of increasing concentration. They were then incubated
402 with hydrogen peroxide and protease (RNAscope ®), and the mouse SNAP-25-C1
403 probe (Cat No.516471) was added. The tissues were washed and incubated
404 successively with RNAscope Multiplex Fl V2 Amp1, Amp2 and Amp3 and horseradish
405 peroxidase, to amplify the signal. We then added the fluorescent Opal 570 probe
406 (1/1000 dilution). For immunohistochemical analysis, the tissue was incubated for 1
407 hour at room temperature in blocking solution (0.3% Triton + 1%BSA + 20% goat
408 serum), and then overnight at 4°C with the primary rabbit antibody directed against
409 otoferlin (1/200, produced in the laboratory), and for two hours with the donkey anti-
410 rabbit Alexa Fluor 488 (1/200, ab150073, Abcam)-labeled secondary antibody.
411
412 ***Hair cell-specific Snap-25 deletion***
413 The *Snap-25$^{flox/flox}$* mice were generated by homologous recombination (Institut
414 Clinique de la Souris, Illkirch, France). These mice were crossed with *PMyo15-hCre$^{+/KI}$*

415 mice to generate a hair cell specific *Snap-25* deletion[23]. The *Rosa*-tdTomato mice were
416 obtained from Jackson Laboratories.
417

418 ***Recombinant AAV constructs***

419 We used AAV8.CMV.HI.eGFP-Cre.WPRE.SV40 at titer of 2.88 x 10^{13} GC/mL and
420 AAV8-CMV-PI-SNAP-25 at titer of 1.72 x 10^{14} GC/mL. Both vectors were obtained
421 from Penn Vector Core. The coding sequence of the murine *Snap-25* cDNA
422 (UniProtKB ID P60879) was inserted into the p0101
423 (pAAV.CMV.PI.EGFP.WPRE.bGH) vector from Addgene. The recombinant vectors
424 were packaged in the AAV8 capsid and produced by the Penn Vector Core facility.
425

426 ***AAV delivery***

427 The protocols were approved by the Animal Care and Use Committee of the Institut
428 Pasteur. Isoflurane anesthesia was used on P1-P3 and P12-P15 mice. A left
429 postauricular incision was made, and the cochlear basal turn, stapedial artery and
430 facial nerve were used as landmarks to access the round window membrane or P1-P3
431 mice. For P12-P15 mice, the otic bulla was exposed and opened to access the round
432 window membrane. A micropipette (10 µm diameter) was used to inject 1 to 2 µL of
433 AAV8.CMV.HI.eGFP-Cre.WPRE.SV40 or AAV8-CMV-PI-SNAP-25b through the
434 round window membrane. The hole was then plugged with muscle and connective
435 tissue, and the skin was sealed with biological glue (3M Vetbond).
436

437 ***Auditory brainstem responses (ABR) recording***

438 The mice were anesthetized with ketamine (100 mg/kg) and xylazine (10 mg/kg) and
439 placed in an attenuated-sound box. Three electrodes were placed on the vertex, the

440 ipsilateral mastoid, and the lower back as the ground electrode. Pure-tone stimuli were
441 used at frequencies of 5, 10, 15, 20, 32, and 40 kHz. Sound intensities of 10 to 110
442 dB, in 10-dB steps, were tested. The hearing threshold was determined as the lowest
443 stimulus level resulting in a visual recognition of ABR waves. ABR analysis was
444 performed with Matlab software.
445 The amplitude of ABR wave I was measured (Matlab) for sounds of high intensity (70
446 to 90 dB), and the latency of this wave was determined as the time between the
447 stimulus and the peak amplitude of wave I.
448

449 ***Distortion product otoacoustic emission analysis***

450 Distortion product otoacoustic emissions (DPOAEs) were measured to evaluate OHC
451 function. Mice were anesthetized with ketamine and xylazine as previously described,
452 and body temperature was maintained close to 38°C with a heat pad. DPOAEs were
453 conducted with Otophylab (Echodia) and analyzed with RT-Lab software or with
454 CubeDis system, Mimosa Acoustics; ER10B microphone, Etymotic Research.
455 DPOAEs were generated in *Snap-25*$^{flox/flox}$ mice into which AAV8-GFP-Cre was
456 injected on P14 and *Snap-25*$^{flox/flox}$*/PMoy15hCre*$^{+/KI}$ mice into which AAV8-SNAP-25b
457 was injected on P2. The DPOAE at a frequency 2*f1-f2* was recorded in response to
458 two primary tones of similar energy levels, *f1* and *f2*, with *f2/f1* = 1.20. Frequency *f2*
459 was swept at 12 and 16 kHz or 10 and 15 kHz and responses were recorded after 60-
460 64 dB stimulation. The DPOAE threshold was plotted against frequency *f2*. The
461 DPOAE threshold was defined as the smallest primary level leading to a detectable
462 DPOAE.

463

464 ***Immunofluorescence***

465 Right and left inner ears were removed from the skulls of mutant (Cre-injected *Snap-*
466 *25*$^{flox/flox}$, *Snap-25*$^{flox/flox}$*/PMyo15-hCre*$^{+/KI}$) and control (non-injected *Snap-25*$^{flox/flox}$*,*
467 *Snap-25*$^{flox/flox}$*/PMyo15-hCre*$^{+/+}$ or C57BL6/J) mice. They were perfused with 4%
468 paraformaldehyde in PBS for 45 minutes at room temperature. Cochleas were
469 microdissected, rinsed with PBS and incubated for 1 hour at room temperature in PBS
470 supplemented with 20% normal horse serum and 0.3% Triton X-100.

471

472 The samples were then incubated overnight with various primary antibodies in PBS:
473 chicken anti-GFP (1:500; Abcam), rabbit anti-otoferlin (1:200, produced in the
474 laboratory), mouse anti-CTBP2 (1:100, Merck Millipore), guinea pig anti-ribeye (1:700
475 SYSY, GmbH), mouse anti-GluR2 (1:2000, Merck Millipore), and/or anti-myosin 6
476 (1:200, produced in the laboratory).

477

478 The samples were rinsed with PBS and incubated for 1 hour with various solutions of
479 secondary antibodies: ATTO-647–conjugated goat anti-rabbit IgG antibody (1:500
480 dilution; Sigma–Aldrich), ATTO-488–conjugated goat anti-chicken IgG antibody (1:500
481 dilution; Sigma–Aldrich), and ATTO-550–conjugated goat anti-mouse IgG antibody
482 (1:500 dilution; Sigma–Aldrich). Nuclei were labeled by incubation with 4',6-diamidino-
483 2-phenylindole (DAPI) (1:7500; Sigma–Aldrich) for 10 minutes. Samples were then
484 mounted in Fluorsave medium (Calbiochem, USA). Images were captured with a Zeiss
485 LSM-700 confocal microscope equipped with a Plan Apochromat 63x/1.4 N.A. oil
486 immersion lens (Carl Zeiss).

487

488 ***Patch-clamp recording and capacitance measurement***

489 Electrophysiological whole-cell patch-clamp recordings of hair cell mechanoelectrical
490 transduction currents were performed in cochlear explants from P8 mice, as
491 previously described [60].

492 All the recordings of IHC capacitance measurement were performed at the mid-apical
493 region of the cochlea 20–40% normalized distance from the apex, an area encoding
494 frequencies ranging from 8 to 16 kHz, with an EPC10 amplifier controlled by
495 Patchmaster software (HEKA Elektronik). For AAV8-GFP-Cre injections, only GFP-
496 expressing IHCs were recorded. IHCs were otherwise selected for recording at
497 random from the tissue preparation. Patch pipettes were pulled with a micropipette
498 puller (P-97 Flaming/Brown; Sutter Instrument) and fire-polished with an MF-830
499 microforge (Narishige) to obtain a resistance range of 2 to 4 MΩ. Patch pipettes were
500 filled with an intracellular cesium-based solution containing the following: 145 mM
501 CsCl, 1 mM $MgCl_2$, 5 mM HEPES, 1 mM EGTA, 20 mM tetraethylammonium
502 chloride, 2 mM ATP, and 0.3 mM GTP, pH 7.2, 300 mOsm. Changes in cell
503 membrane capacitance (ΔC_m) were used to monitor the fusion of synaptic vesicles
504 during exocytosis. ΔC_m was measured with the Lindau and Neher (1988) technique,
505 using the lock-in amplifier Patchmaster software (HEKA) and applying a 1 kHz
506 command sine wave (20 mV amplitude) at a holding potential of −80 mV before and
507 after the pulse experiment. As recording conditions can greatly influence capacitance
508 measurements, only IHC patch-clamp recordings with low series resistance, below
509 10 MΩ, and a maximum leak current of 25 pA (at V_h = −80 mV) were considered in
510 this study.

511

512 Electrophysiological experiments in vestibular type I hair cells (VHC-I) were performed
513 in intact whole-mount utricles at postnatal day 16 with internal and external solutions
514 similar to those described above for cochlear IHCs. In the utricle, type I vestibular hair
515 cell (VHC-I) were identified by contrast microscopy, on the basis of their large
516 surrounding calyceal afferent fiber, as previously described [10,61].
517

518 ***Voltage stimulation***

519 Two different protocols were used. First, readily releasable pool (RRP) exocytosis was
520 recorded by the depolarization of IHCs from −80 to −10 mV for increasing durations,
521 from 5 to 80 ms, in 5 ms increments. Second, the replenishment in vesicles of the
522 synaptic zone was probed by depolarizing IHCs during a train of 100 ms pulses from
523 −80 to −10 mV.
524

525 **Intracellular Ca^{2+} uncaging**

526 We triggered a rapid increase in intracellular Ca^{2+} concentration from the caged Ca^{2+}chelator DM-
527 Nitrophen (Interchim, catalog #317210), using a brief (100 ms) flash from a 365 nm UV light source
528 delivered by a Mic-LED-365 (350 mW; Prizmatix). The UV LED was connected directly to the epi-
529 illumination port at the rear of a Nikon FN1 upright microscope and illumination was focused through
530 the 60x objective (CFI Fluor 60x W NIR, WD = 2.0 mm, NA = 1). HCs were loaded with 145 mM CsCl,
531 5 mM HEPES, 20 mM TEA, 10 mM DM-Nitrophen, and 10 mM $CaCl_2$. Following patch rupture, we
532 systematically waited for 2 min at a holding potential of −70 mV to load and equilibrate the cells with the
533 intrapipette solution. Upon UV photolysis, $[Ca^{2+}]_i$, continuously measured with a C2 confocal system and
534 NIS-Elements imaging software (Nikon) coupled to the FN1 microscope, reached a peak of 20 ± 5 µM
535 within 15–20 ms [62].
536

537 ***Scanning electron microscopy***

538 Scanning electron microscopy was used to investigate the morphology of stereocilia
539 and cochlear hair cells after injection. Inner ears were fixed by incubation in 2.5%
540 glutaraldehyde in 0.1 M phosphate buffer (pH 7.3) for 2 hours at room temperature.
541 The organs of Corti were microdissected and the samples were incubated in an
542 alternating series of solutions of 1% osmium tetraoxide (O) and 0.1 M
543 thiocarbohydrazide (T) (sequence: OTOTO). The samples were then dehydrated by
544 incubation in a graduated series of ethanol solutions and dried to critical point with
545 hexamethyldisilazane (Sigma–Aldrich). Samples were analyzed with a Jeol
546 JSM6700F-type field emission scanning electron microscope operating at 5 kV.
547 Images were obtained with a charge-coupled camera (SIS Megaview3; Surface
548 Imaging Systems), acquired with analySIS (Soft Imaging System), and processed with
549 Photoshop CS6.

550

551 ***Transmission electron microscopy***

552 Cochleas were perfused with 4% paraformaldehyde and 2% glutaraldehyde in
553 Sorensen buffer at pH 7.4, and immersed in the fixative solution for 2 hours. They were
554 then postfixed by incubation overnight in 1% osmium tetraoxide in cacodylate buffer at
555 4°C. They were dehydrated in a graded series of acetone concentrations and
556 embedded in Spurr's low-viscosity epoxy resin (EMS, Hatfield, USA), which was then
557 hardened at 70°C. We cut 70 nm sections of the sensory epithelium (organ of Corti)
558 and collected them on 100-mesh parallel-bar copper grids. The grids were contrast-
559 stained with 4% uranyl acetate in dH_2O for 40 minutes and then with Reynold's lead
560 citrate for 3 minutes. The sections were viewed in a FEI *Tecnai* G2 *200kV* transmission
561 electron microscope.

562

563 ***Statistical analyses***

564 All statistical analyses were performed in GraphPad and the following tests were used,
565 as appropriate, depending on the data concerned: Mann-Whitney test, Student's *t* test,
566 one-way ANOVA, two-way ANOVA. Statistical significance is indicated in the figures
567 as follows: n.s., not significant; *$p < 0.05$; **$p < 0.01$; ***$p < 0.001$, ****$p<0.0001$. For
568 ABRs, DPOAEs, and ribbon counts, all values are given as means ± standard
569 deviation. For IHC and VHC patch-clamp recordings and Ca^{2+} imaging, values are
570 given as means ± SEM.

571

572

573

574

575

576

577

578

579

580

581

582

583

584

585 ***References***

586

587 1. Moser, T. & Beutner, D. Kinetics of exocytosis and endocytosis at the cochlear
588 inner hair cell afferent synapse of the mouse. *Proc. Natl. Acad. Sci. U. S. A.* **97**,
589 883–888 (2000).
590 2. Safieddine, S., El-Amraoui, A. & Petit, C. The Auditory Hair Cell Ribbon Synapse:
591 From Assembly to Function. *Annu. Rev. Neurosci.* **35**, 509–528 (2012).
592 3. Griesinger, C. B., Richards, C. D. & Ashmore, J. F. Fast vesicle replenishment
593 allows indefatigable signalling at the first auditory synapse. *Nature* vol. 435 212–5
594 (2005).
595 4. Parsons, T. D., Lenzi, D., Almers, W. & Roberts, W. M. Calcium-triggered
596 exocytosis and endocytosis in an isolated presynaptic cell: capacitance
597 measurements in saccular hair cells. *Neuron* vol. 13 875–83 (1994).
598 5. Rosenmund, C. & Stevens, C. F. Definition of the readily releasable pool of
599 vesicles at hippocampal synapses. *Neuron* vol. 16 1197–207 (1996).
600 6. Platzer, J. *et al.* Congenital deafness and sinoatrial node dysfunction in mice
601 lacking class D L-type Ca2+ channels. *Cell* **102**, 89–97 (2000).
602 7. Brandt, A., Striessnig, J. & Moser, T. CaV1.3 channels are essential for
603 development and presynaptic activity of cochlear inner hair cells. *J Neurosci* vol.
604 23 10832–40 (2003).
605 8. Zampini, V. *et al.* Elementary properties of CaV1.3 Ca(2+) channels expressed in
606 mouse cochlear inner hair cells. *J Physiol* vol. 588 187–99 (2010).
607 9. Roux, I. *et al.* Otoferlin, Defective in a Human Deafness Form, Is Essential for
608 Exocytosis at the Auditory Ribbon Synapse. *Cell* **127**, 277–289 (2006).
609 10. Dulon, D., Safieddine, S., Jones, S. M. & Petit, C. Otoferlin is critical for a highly

610 sensitive and linear calcium-dependent exocytosis at vestibular hair cell ribbon
611 synapses. *J. Neurosci. Off. J. Soc. Neurosci.* **29**, 10474–10487 (2009).
612 11. Beurg, M. *et al.* Control of Exocytosis by Synaptotagmins and Otoferlin in
613 Auditory Hair Cells. *J. Neurosci. Off. J. Soc. Neurosci.* **30**, 13281–13290 (2010).
614 12. Michalski, N. *et al.* Otoferlin acts as a Ca2+ sensor for vesicle fusion and vesicle
615 pool replenishment at auditory hair cell ribbon synapses. *eLife* **6**, (2017).
616 13. Vincent, P. F. Y. *et al.* Different CaV1.3 Channel Isoforms Control Distinct
617 Components of the Synaptic Vesicle Cycle in Auditory Inner Hair Cells. *J.*
618 *Neurosci. Off. J. Soc. Neurosci.* **37**, 2960–2975 (2017).
619 14. Beurg, M. *et al.* Calcium- and Otoferlin-Dependent Exocytosis by Immature Outer
620 Hair Cells. *J. Neurosci.* **28**, 1798–1803 (2008).
621 15. Frank, T. *et al.* Bassoon and the synaptic ribbon organize Ca2+ channels and
622 vesicles to add release sites and promote refilling. *Neuron* **68**, 724–738 (2010).
623 16. Jung, S. *et al.* Rab3-interacting molecules 2α and 2β promote the abundance of
624 voltage-gated CaV1.3 Ca2+ channels at hair cell active zones. *Proc. Natl. Acad.*
625 *Sci. U. S. A.* **112**, E3141-9 (2015).
626 17. Safieddine, S. & Wenthold, R. J. SNARE complex at the ribbon synapses of
627 cochlear hair cells: analysis of synaptic vesicle- and synaptic membrane-
628 associated proteins: SNARE complex of the ribbon-synapses of hair cells. *Eur. J.*
629 *Neurosci.* **11**, 803–812 (1999).
630 18. Nouvian, R., Beutner, D., Parsons, T. D. & Moser, T. Structure and Function of
631 the Hair Cell Ribbon Synapse. *J. Membr. Biol.* **209**, 153–165 (2006).
632 19. Scheffer, D. I., Shen, J., Corey, D. P. & Chen, Z.-Y. Gene Expression by Mouse
633 Inner Ear Hair Cells during Development. *J. Neurosci.* **35**, 6366–6380 (2015).
634 20. Nouvian, R. *et al.* Exocytosis at the hair cell ribbon synapse apparently operates

635 without neuronal SNARE proteins. *Nat. Neurosci.* **14**, 411–413 (2011).
636 21. Washbourne, P. *et al.* Genetic ablation of the t-SNARE SNAP-25 distinguishes
637 mechanisms of neuroexocytosis. *Nat. Neurosci.* **5**, 19–26 (2002).
638 22. Bark, I. C., Hahn, K. M., Ryabinin, A. E. & Wilson, M. C. Differential expression of
639 SNAP-25 protein isoforms during divergent vesicle fusion events of neural
640 development. *Proc. Natl. Acad. Sci. U. S. A.* **92**, 1510–1514 (1995).
641 23. Caberlotto, E. *et al.* Usher type 1G protein sans is a critical component of the tip-
642 link complex, a structure controlling actin polymerization in stereocilia. *Proc. Natl.*
643 *Acad. Sci.* **108**, 5825–5830 (2011).
644 24. Roux, I. *et al.* Myosin VI is required for the proper maturation and function of inner
645 hair cell ribbon synapses. *Hum. Mol. Genet.* **18**, 4615–4628 (2009).
646 25. Sørensen, J. B. *et al.* Differential Control of the Releasable Vesicle Pools by
647 SNAP-25 Splice Variants and SNAP-23. *Cell* **114**, 75–86 (2003).
648 26. Ramakrishnan, N. A., Drescher, M. J. & Drescher, D. G. The SNARE complex in
649 neuronal and sensory cells. *Mol. Cell. Neurosci.* **50**, 58–69 (2012).
650 27. Kujawa, S. G. & Liberman, M. C. Adding insult to injury: cochlear nerve
651 degeneration after 'temporary' noise-induced hearing loss. *J. Neurosci. Off. J.*
652 *Soc. Neurosci.* **29**, 14077–14085 (2009).
653 28. Lepeta, K. *et al.* Synaptopathies: synaptic dysfunction in neurological disorders -
654 A review from students to students. *J. Neurochem.* **138**, 785–805 (2016).
655 29. Taoufik, E., Kouroupi, G., Zygogianni, O. & Matsas, R. Synaptic dysfunction in
656 neurodegenerative and neurodevelopmental diseases: an overview of induced
657 pluripotent stem-cell-based disease models. *Open Biol.* **8**, (2018).
658 30. Oyler, G. A. *et al.* The identification of a novel synaptosomal-associated protein,
659 SNAP-25, differentially expressed by neuronal subpopulations. *J. Cell Biol.* **109**,

660 3039–3052 (1989).
661 31. Blasi, J. *et al.* Botulinum neurotoxin A selectively cleaves the synaptic protein
662 SNAP-25. *Nature* **365**, 160–163 (1993).
663 32. Schiavo, G. *et al.* Botulinum neurotoxins serotypes A and E cleave SNAP-25 at
664 distinct COOH-terminal peptide bonds. *FEBS Lett.* **335**, 99–103 (1993).
665 33. Molnár, Z. *et al.* Normal development of embryonic thalamocortical connectivity in
666 the absence of evoked synaptic activity. *J. Neurosci. Off. J. Soc. Neurosci.* **22**,
667 10313–10323 (2002).
668 34. Hoerder-Suabedissen, A. *et al.* Cell-Specific Loss of SNAP25 from Cortical
669 Projection Neurons Allows Normal Development but Causes Subsequent
670 Neurodegeneration. *Cereb. Cortex* **29**, 2148–2159 (2019).
671 35. Fritzsch, B., Silos-Santiago, I., Bianchi, L. M. & Farinas, I. Effects of neurotrophin
672 and neurotrophin receptor disruption on the afferent inner ear innervation. *Semin.*
673 *Cell Dev. Biol.* **8**, 277–284 (1997).
674 36. Bailey, E. M. & Green, S. H. Postnatal expression of neurotrophic factors
675 accessible to spiral ganglion neurons in the auditory system of adult hearing and
676 deafened rats. *J. Neurosci. Off. J. Soc. Neurosci.* **34**, 13110–13126 (2014).
677 37. Harasztosi, C. & Gummer, A. W. Different rates of endocytic activity and vesicle
678 transport from the apical and synaptic poles of the outer hair cell. *HNO* **67**, 449–
679 457 (2019).
680 38. Jh, S. & We, B. Synaptic and Golgi membrane recycling in cochlear hair cells. *J.*
681 *Neurocytol.* **15**, 311–328 (1986).
682 39. Sobkowicz, H. M., Rose, J. E., Scott, G. E. & Slapnick, S. M. Ribbon synapses in
683 the developing intact and cultured organ of Corti in the mouse. *J. Neurosci. Off. J.*
684 *Soc. Neurosci.* **2**, 942–957 (1982).

685 40. Shimojo, M. *et al.* SNAREs Controlling Vesicular Release of BDNF and
686 Development of Callosal Axons. *Cell Rep.* **11**, 1054–1066 (2015).
687 41. Delgado-Martínez, I., Nehring, R. B. & Sørensen, J. B. Differential Abilities of
688 SNAP-25 Homologs to Support Neuronal Function. *J. Neurosci.* **27**, 9380–9391
689 (2007).
690 42. Peng, L. *et al.* Cytotoxicity of botulinum neurotoxins reveals a direct role of
691 syntaxin 1 and SNAP-25 in neuron survival. *Nat. Commun.* **4**, 1472 (2013).
692 43. Verhage, M. *et al.* Synaptic assembly of the brain in the absence of
693 neurotransmitter secretion. *Science* vol. 287 864–9 (2000).
694 44. Vardar, G. *et al.* Distinct Functions of Syntaxin-1 in Neuronal Maintenance,
695 Synaptic Vesicle Docking, and Fusion in Mouse Neurons. *J. Neurosci. Off. J.*
696 *Soc. Neurosci.* **36**, 7911–7924 (2016).
697 45. Berliocchi, L. *et al.* Botulinum neurotoxin C initiates two different programs for
698 neurite degeneration and neuronal apoptosis. *J. Cell Biol.* **168**, 607–618 (2005).
699 46. Fritzsch, B., Tessarollo, L., Coppola, E. & Reichardt, L. F. Neurotrophins in the
700 ear: their roles in sensory neuron survival and fiber guidance. *Prog. Brain Res.*
701 **146**, 265–278 (2004).
702 47. Ramekers, D., Versnel, H., Grolman, W. & Klis, S. F. L. Neurotrophins and their
703 role in the cochlea. *Hear. Res.* **288**, 19–33 (2012).
704 48. Wan, G., Gómez-Casati, M. E., Gigliello, A. R., Liberman, M. C. & Corfas, G.
705 Neurotrophin-3 regulates ribbon synapse density in the cochlea and induces
706 synapse regeneration after acoustic trauma. *eLife* **3**, (2014).
707 49. Criado, M., Gil, A., Viniegra, S. & Gutiérrez, L. M. A single amino acid near the C
708 terminus of the synaptosomeassociated protein of 25 kDa (SNAP-25) is essential
709 for exocytosis in chromaffin cells. *Proc. Natl. Acad. Sci. U. S. A.* **96**, 7256–7261

710 (1999).

711 50. Wei, S. *et al.* Exocytotic mechanism studied by truncated and zero layer mutants
712 of the C-terminus of SNAP-25. *EMBO J.* **19**, 1279–1289 (2000).

713 51. Sørensen, J. B. *et al.* Sequential N- to C-terminal SNARE complex assembly
714 drives priming and fusion of secretory vesicles. *EMBO J.* **25**, 955–966 (2006).

715 52. Haberman, A. *et al.* The synaptic vesicle SNARE neuronal Synaptobrevin
716 promotes endolysosomal degradation and prevents neurodegeneration. *J. Cell*
717 *Biol.* **196**, 261–276 (2012).

718 53. Liu, Y. *et al.* Ubiquitin-Synaptobrevin Fusion Protein Causes Degeneration of
719 Presynaptic Motor Terminals in Mice. *J. Neurosci. Off. J. Soc. Neurosci.* **35**,
720 11514–11531 (2015).

721 54. Cardozo, P. L. *et al.* Synaptic Elimination in Neurological Disorders. *Curr.*
722 *Neuropharmacol.* **17**, 1071–1095 (2019).

723 55. Verderio, C. *et al.* SNAP-25 modulation of calcium dynamics underlies differences
724 in GABAergic and glutamatergic responsiveness to depolarization. *Neuron* **41**,
725 599–610 (2004).

726 56. Garbelli, R. *et al.* Heterogeneous expression of SNAP-25 in rat and human brain.
727 *J. Comp. Neurol.* **506**, 373–386 (2008).

728 57. Harsini, F. M. *et al.* FerA is a Membrane-Associating Four-Helix Bundle Domain
729 in the Ferlin Family of Membrane-Fusion Proteins. *Sci. Rep.* **8**, 10949 (2018).

730 58. Tang, F. *et al.* mRNA-Seq whole-transcriptome analysis of a single cell. *Nat.*
731 *Methods* **6**, 377–382 (2009).

732 59. Tang, F. *et al.* RNA-Seq analysis to capture the transcriptome landscape of a
733 single cell. *Nat. Protoc.* **5**, 516–535 (2010).

734 60. Michalski, N. *et al.* Harmonin-b, an actin-binding scaffold protein, is involved in

735 the adaptation of mechanoelectrical transduction by sensory hair cells. *Pflügers*
736 *Arch* vol. 459 115–130 (2009).
737 61. Vincent, P. F., Bouleau, Y., Safieddine, S., Petit, C. & Dulon, D. Exocytotic
738 machineries of vestibular type I and cochlear ribbon synapses display similar
739 intrinsic otoferlin-dependent Ca2+ sensitivity but a different coupling to Ca2+
740 channels. *J Neurosci* vol. 34 10853–69 (2014).
741 62. Vincent, P. F. Y., Bouleau, Y., Safieddine, S., Petit, C. & Dulon, D. Exocytotic
742 Machineries of Vestibular Type I and Cochlear Ribbon Synapses Display Similar
743 Intrinsic Otoferlin-Dependent Ca2+ Sensitivity But a Different Coupling to Ca2+
744 Channels. *J. Neurosci.* **34**, 10853–10869 (2014).
745
746
747
748
749
750
751
752
753
754
755
756
757

758

759

760

761 ## Figures and legends

762

763

764

765 **Figure 1. SNAP-25 mRNAs are localized to cochlear hair cells**

766

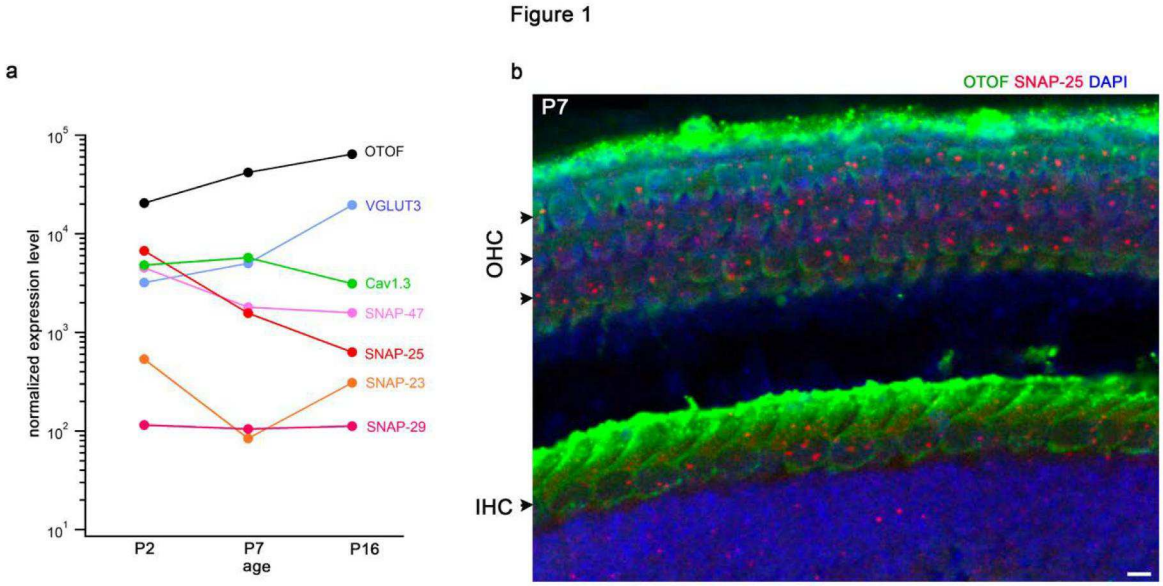

767

768 **(a)** Expression levels of mRNAs encoding proteins involved in synaptic transmission,

769 including $Ca_v1.3$, VGLUT3, otoferlin, SNAP-23, SNAP-29, SNAP-47, compared with

770 those of SNAP-25 mRNA in the IHCs of wild-type P2, P7, and P16 mice.

771 **(b)** P7 organ of Corti subjected to *In situ* hybridization (RNAscope technology) for

772 SNAP-25 mRNA (red), immunostained for otoferlin (green), and stained with DAPI

773 (blue). Scale bar = 10 µm.

774

Figure 2

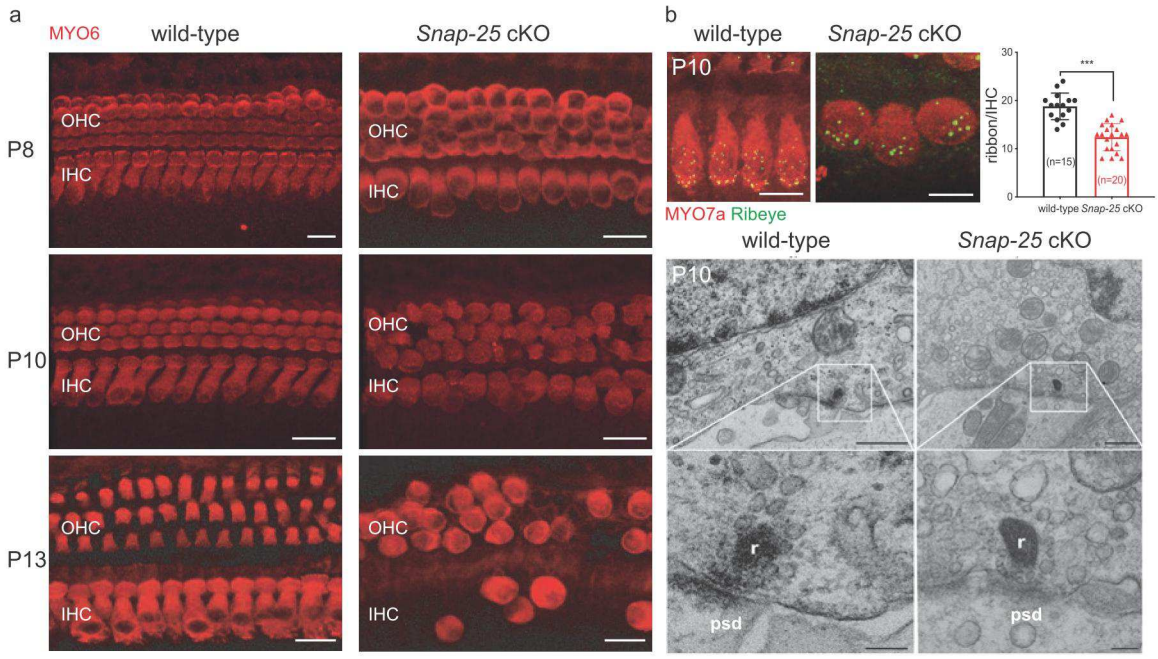

775

776 **Figure 2. Neonatal *Snap-25* deletion leads to ribbon degeneration and hair cell**
777 **loss**

778 **(a)** Organs of Corti obtained on P8, P10 and P13 from wild-type (left panel), and *Snap-*
779 *25* cKO (right panel) mice, and stained for myosin 6 (red). By P13, many hair cells
780 underwent a degeneration process. Scale bars=15 µm. **(b)** The upper panels show
781 organs of Corti from wild-type (left panel) and *Snap-25* cKO (middle panel) mice
782 immunostained for ribeye (green) and myosin 6 (red), and (right panel) a bar chart
783 summarizing IHC ribbon quantification. The lower panel shows 60 nm-thick
784 transmission electron microscopy sections of IHC ribbon synapses from P10 wild-type
785 (left) and *Snap-25* cKO (right) mice, with both synapses containing a ribbon (r)
786 decorated with synaptic vesicles facing a postsynaptic density (psd) of a primary
787 auditory dendrite. Uper and low Scale bars are 500 nm and 100 nm, repectively

788

789

790

Figure 3

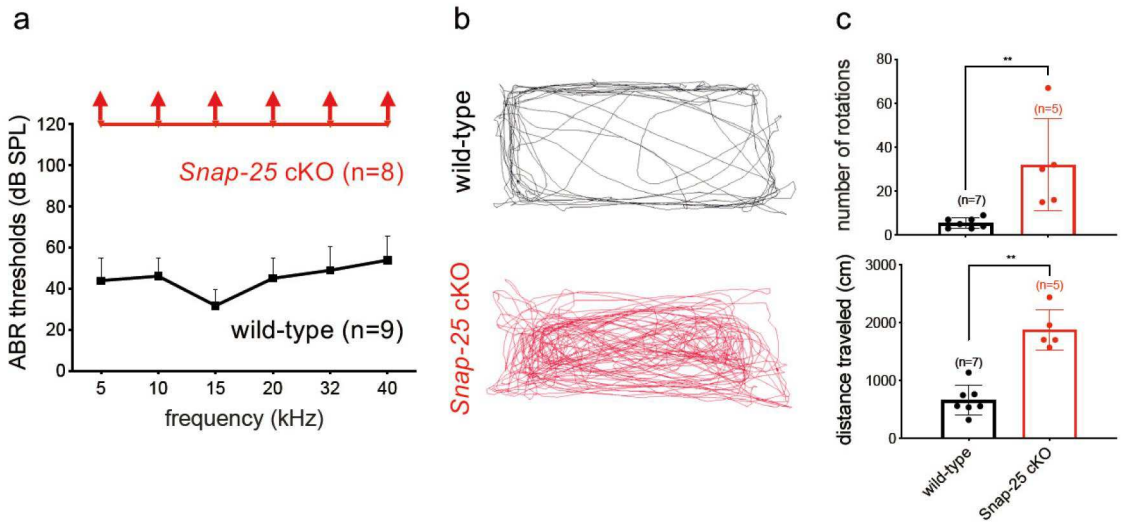

791

792 **Figure 3. Adult *Snap-25* cKO mice are profoundly deaf and have a severe balance**
793 **defect. (a)** Auditory brainstem responses recorded in *Snap-25* cKO mice (*n*=8) on P30
794 at the six frequencies tested (5, 10, 15, 20, 32 and 40 kHz), indicated profound
795 deafness relative to wild-type mice (*n*=9),
796 **(b)** Representative trace for open-field recordings over a period of 180 seconds for a
797 wild-type control and a P30 *Snap-25* cKO mouse, demonstrating that *Snap-25*
798 inactivation significantly increases circling behavior.
799 **(c)** Quantification of circling behavior and the distance covered, performed on P30.
800 The number of rotations and the distance traveled were significantly greater for
801 *Snap-25* cKO mice (*n*=5) than for wild-type mice (*n*=7), (unpaired *t* test, $p<0.01$, and
802 Mann-Whitney test, $p<0.01$, respectively).

803

804

805

806

Figure 4

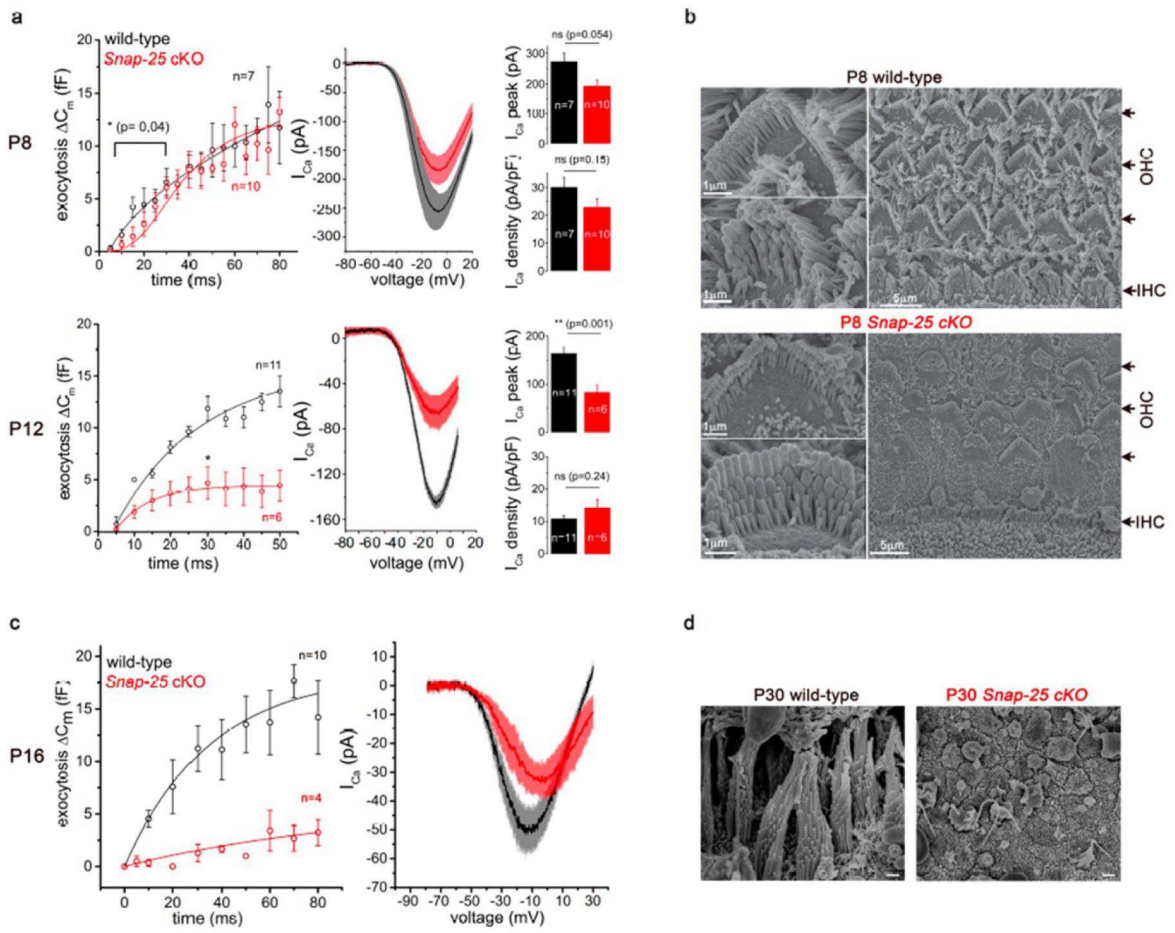

807

808 **Figure 4. *Snap-25* inactivation in prehearing mice disrupts Ca^{2+}-evoked**
809 **exocytosis in cochlear and vestibular hair cells**

810 (a) Comparative kinetics of IHC exocytosis in control wild-type and Snap-25 cKO mice
811 at P8 and P12 during voltage-steps of increasing duration from -80 mV to -10 mV. At
812 right Ca^{2+} currents were compared during a voltage-ramp protocol (1mV/ms from -90
813 to +30 mV) (**b**) Low- and high-magnification scanning electron micrographs of the
814 apical surface of the middle turn of P8 organs of Corti from a wild-type control (upper
815 panel) and a *Snap-25* cKO (lower panel) mouse. In both mice, the OHCs and IHCs
816 displayed the typical V- and U-shaped hair bundles, respectively. (**c**) Capacitance
817 measurements were performed on vestibular type I utricular hair cells (VHC) at P16 in
818 wild-type (black, *n*=10) and *Snap-25* cKO (red) (*n*=4) mice. The kinetics of exocytosis,

819 evoked with voltage-steps of increasing duration from -80 mV to -10 mV, was greatly
820 reduced in *Snap-25* cKO (two-way ANOVA, $p<0.01$). Note also a reduction of the
821 Ca^{2+} currents evoked during voltage-ramp stimulation. (**d**) High-magnification
822 scanning electron micrographs of wild-type (left panel) and *Snap-25* cKO (right panel)
823 P30utricles. The latter presents a disorganization and shortening of the hair bundles.
824 Scale bars= 1 µm
825
826
827

Figure 5

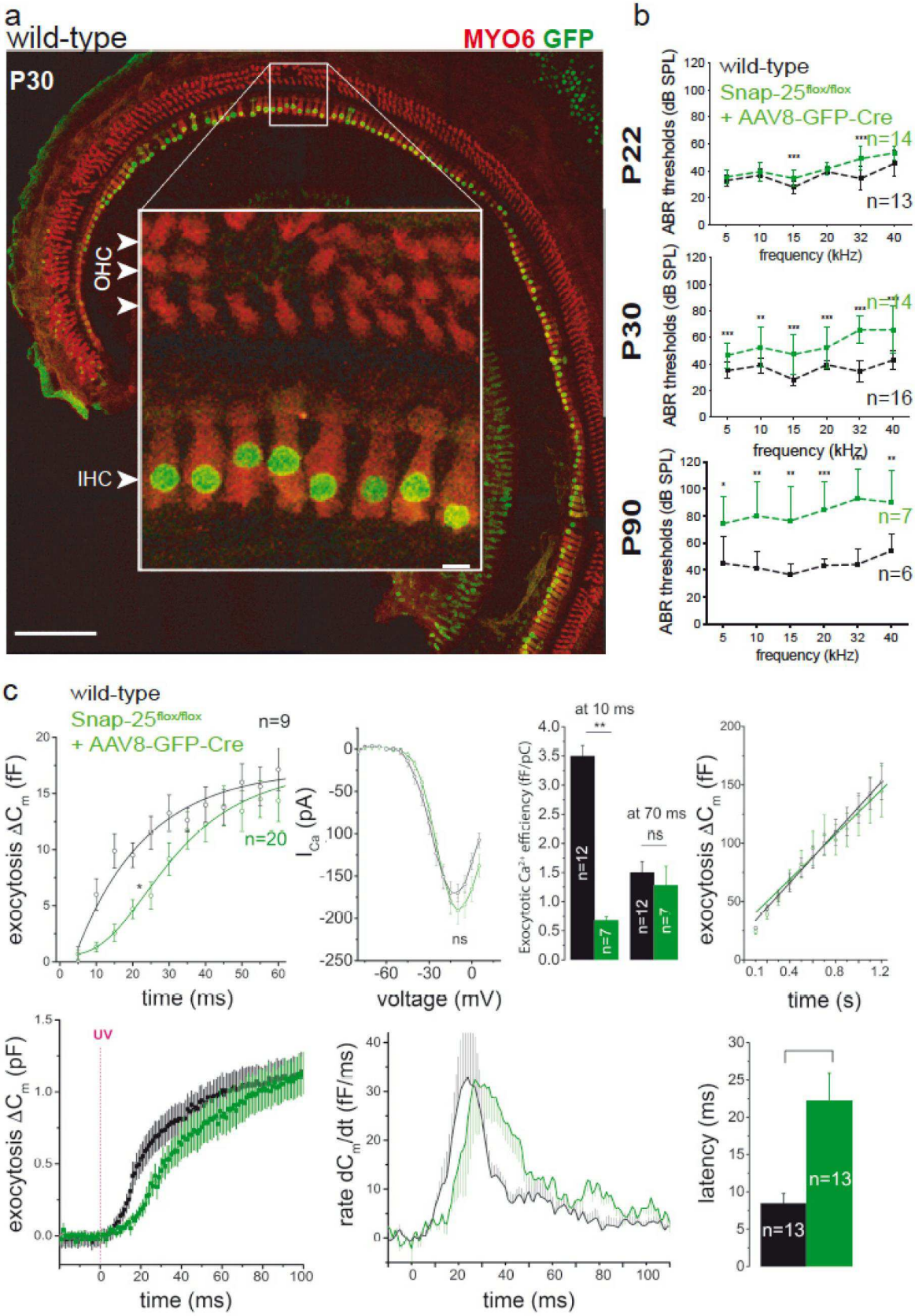
a
wild-type
MYO6 GFP
P30
OHC
IHC
b
P22
P30
P90
wild-type
Snap-25flox/flox
+ AAV8-GFP-Cre
n=14
n=13
n=14
n=16
n=7
n=6
ABR thresholds (dB SPL)
frequency (kHz)
c
wild-type
Snap-25flox/flox
+ AAV8-GFP-Cre
n=9
n=20
exocytosis ΔCm (fF)
time (ms)
ICa (pA)
voltage (mV)
ns
at 10 ms
at 70 ms
Exocytotic Ca2+ efficiency (fF/pC)
n=12
n=7
time (s)
UV
exocytosis ΔCm (pF)
rate dCm/dt (fF/ms)
latency (ms)

828

829 **Figure 5. *Snap-25* deletion in hearing mice disrupts RRP exocytosis and leads**
830 **to progressive hearing loss**

831 **(a)** Organ of Corti from the mid-to-apical turn of the cochlea of a P30 wild-type mouse
832 injected with AAV8-GFP-Cre on P14 and immunostained for myosin 6 (red) and GFP-
833 Cre (green). The inset shows a high magnification of the IHCs of the middle turn of the
834 cochlea. Scale bars = 10 µm inset and 100 µm in overview

835 **(b)** ABR recordings on P22 show a significant increase in the ABR thresholds in
836 injected *Snap-25*$^{flox/flox}$ mice (green, n=14) for measurements at 15 and 32 kHz relative
837 to wild-type mice (black, n=13) (t tests p<0.01 and p<0.001, respectively). This
838 difference extended to all frequencies tested on P30 and P90 (t tests, p<0.01 to
839 p<0.001).

840 **(c)** Electrophysiological parameters were assessed at P28-P30, after AAV8-GFP-Cre
841 injection on P14, in *Snap-25*$^{flox/flox}$ mice. The kinetics of exocytosis were significantly
842 reduced for brief depolarizing steps (-80 to -10 mV) lasting less than 30 ms (p<0.05;
843 two-way ANOVA). Calcium currents (I_{Ca}) were not significantly affected (peak
844 amplitude comparison, unpaired t test, p=0.19). Exocytotic Ca^{2+} efficiency measured
845 for a 10 ms voltage depolarization was significantly affected (unpaired t test, p<0.001),
846 whereas that for a 70 ms voltage depolarization was not (unpaired t test, p=0.38). Mean
847 cumulative ΔCm responses from GFP-positive (n=9) and control (n=5) IHCs elicited
848 with 100 ms repetitive voltage steps from -80 mV to -10 mV indicated that the slow
849 component of exocytosis was unaffected (two-way ANOVA p=0.39). Exocytosis
850 evoked by intracellular Ca^{2+}uncaging had a similar maximal ΔCm and maximal rate
851 (dC_m/dt), but a significantly longer latency (unpaired t test, p <0.01).

852

Figure 6

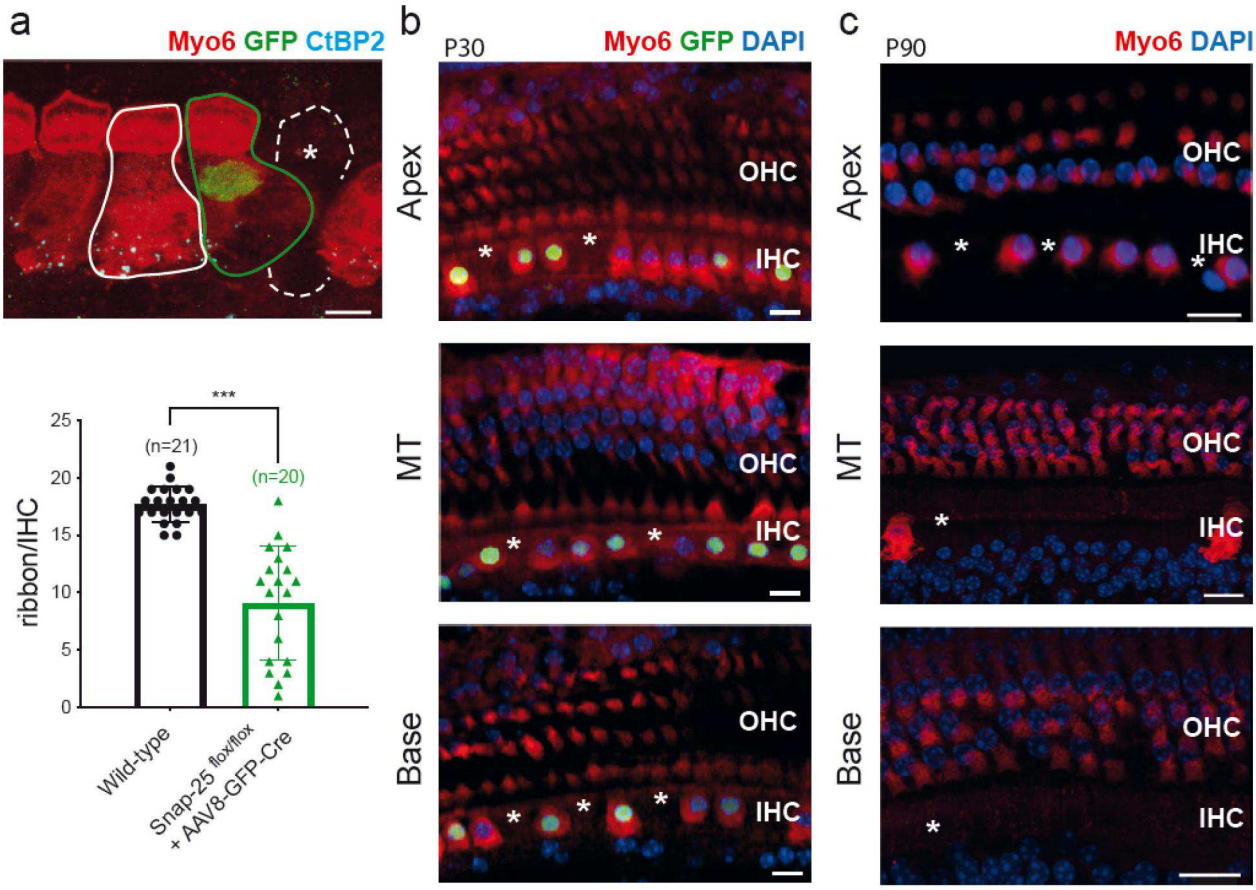

853

854

855 **Figure 6. *Snap-25* deletion after hearing onset reduces the number of ribbons**

856 **and leads to IHC degeneration**

857 **(a)** (upper panel) on P30, organs of Corti were immunostained for CtBP2 (cyan), GFP

858 (green), and myosin 6 (red) in *Snap-25*$^{flox/flox}$ mice injected with AAV8-GFP-Cre on P14.

859 The white, green, and dotted lines surround non-transduced, transduced (green

860 nucleus), and missing IHCs, respectively. Scale bar=10 µm. (lower panel) Bar chart

861 showing that the number of synaptic ribbons per IHC is significantly smaller in GFP-

862 positive cells transduced with AAV8-GFP-Cre (9.1 ± 4.9) (green, *n*=20 cells from 7

863 mice) than in wild-type IHCs (17.67 ± 1.5)(black, *n*=21 cells from 6 mice)(Mann-

864 Whitney test, $p<0.0001$).

865 **(b,c)** Maximum-intensity projections of confocal z-sections of P30 (b) and P90 (c)
866 organs of Corti from the apical, middle and basal turns of the cochlea in *Snap-25*$^{flox/flox}$
867 mice injected with AAV8-GFP-Cre on P14. The organs were immunostained for myosin
868 6 (red), and GFP-Cre (green) and were stained with DAPI (blue). The stars indicate
869 missing IHCs. Note the baso-apical progression of IHC degeneration, which worsens
870 with age. Scale bars = 15 µm.
871
872
873
874
875
876
877

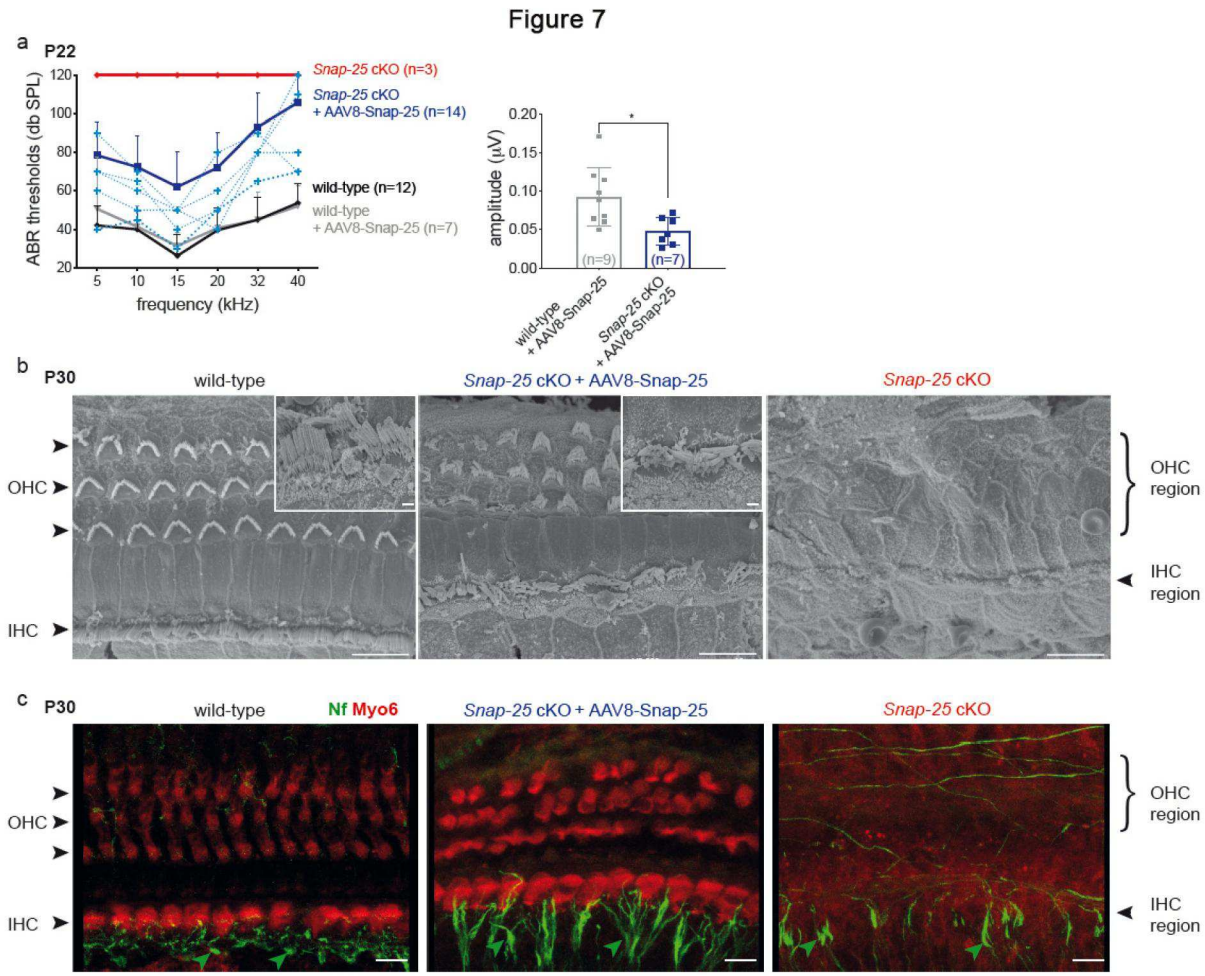

Figure 7. The AAV-mediated transfer of *Snap-25* cDNA to the cochlea of *Snap-25* cKO mice rescues hearing and prevents hair cell degeneration.

(a) ABRs were recorded between P20 and P25 for various frequencies (5, 10 ,15, 20, 32, 40 kHz) in *Snap-25* cKO non-injected mice (red, *n*=3), *Snap-25* cKO mice injected with AAV8-*Snap-25* on P2 (blue, *n*=14), wild-type non-injected mice (black, *n*=12) and wild-type mice injected with AAV8-*Snap-25* on P2 (gray, *n*=7). ABR recordings showed a significant improvement of hearing thresholds in the *Snap-25* cKO AAV8-*Snap-25*-injected mice. The five *Snap-25* cKO mice for which rescue was most effective are represented by blue dotted lines. Wave I amplitude (mV) was measured at 10 kHz for a sound intensity of 80dB SPL. The wave I amplitude in *Snap-25* cKO injected mice (blue, *n*=7) was half that in control injected mice (gray, *n*=9) (*t* test, $p < 0.05$).

890 (**b**) Low- and intermediate-magnification scanning electron micrographs of the apical
891 surface of the middle turn of P30 organs of Corti from a control wild-type mouse, a
892 *Snap-25* cKO mouse injected with the *Snap-25* cDNA on P2 and a *Snap-25* cKO non-
893 injected mouse. In the wild-type mouse, the OHCs and IHCs displayed the typical V-
894 and U-shaped hair bundles, respectively. In the injected *Snap-25* cKO mouse, both
895 OHCs and IHCs had hair bundles with a near wild-type shape, whereas all hair cells
896 were lost in the organ of Corti *Snap-25* cKO.
897 **(c)** Maximum-intensity projections of confocal z-sections from the cochlear middle turn
898 of a wild-type mouse, a *Snap-25* cKO mouse injected with the *Snap-25* cDNA at P2
899 and a *Snap-25* cKO non-injected mouse, immunostained for myosin 6 (red) and
900 neurofilament (green), to identify hair cells and auditory afferent fibers, respectively, at
901 P30. Note the complete loss of hair cells in the *Snap-25* cKO mice compared to the
902 AAV8-*Snap-25* rescued mice. Scale bar = 5 µm. Scale bars = 10 µm and 1 µm.
903
904
905
906
907

Figure 8

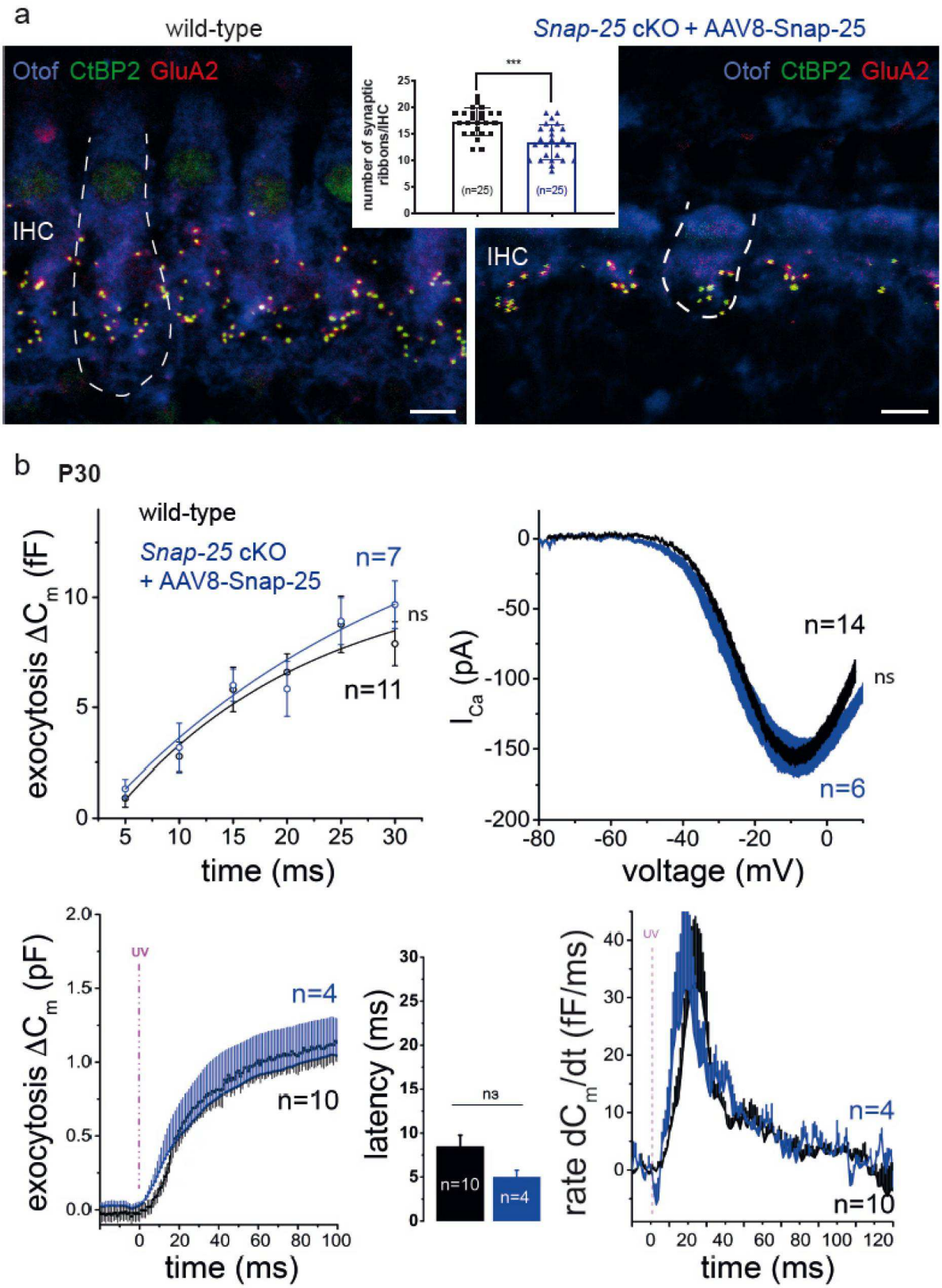
a
wild-type
Snap-25 cKO + AAV8-Snap-25
Otof CtBP2 GluA2
IHC
number of synaptic ribbons/IHC
***
(n=25)
(n=25)
b
P30
wild-type
Snap-25 cKO
+ AAV8-Snap-25
n=7
n=11
ns
exocytosis ΔCm (fF)
time (ms)
n=14
n=6
ICa (pA)
voltage (mV)
UV
n=4
n=10
exocytosis ΔCm (pF)
latency (ms)
rate dCm/dt (fF/ms)

908

909 **Figure 8. virus-mediated transfer of *Snap-25* cDNA to *Snap-25* cKO mice**
910 **prevents ribbon synapses and hair cells from degenerating, and rescues IHC**
911 **exocytosis**
912 **(a)** Maximum-intensity projections of confocal z-sections of IHCs from the cochlear
913 middle turn, immunostained for ribeye (green), GluA2 (red) and otoferlin (blue) at P30.
914 The micrographs were taken from a wild-type mouse (left panel) and a *Snap-25* cKO
915 mouse into which the *Snap-25* cDNA was injected (right panel). Scale bars = 5 µm.
916 Bar charts showing the number of synaptic ribbons per IHC in P30 wild-type (17.28 ±
917 2.57) and rescued *Snap-25* cKO mice (13.44 ± 3.24) (Mann-Whitney test, $p<0.0001$).
918 **(b)** Exocytosis and calcium currents recorded in IHCs from P30 *Snap-25* cKO mice
919 (injected with AAV8-Snap-25 on P2, blue) were similar to those from wild-type mice
920 (black, two-way ANOVA, $p=0.10$ and unpaired *t* test for I_{Ca} peak comparison $p=0.34$).
921 The exocytosis evoked by Ca^{2+} uncaging had a similar maximum amplitude (unpaired
922 *t* test $p=0.9$), maximum rate (unpaired *t* test $p=0.2$) and latency (unpaired *t* test, $p=0.17$)
923 to those of wild-type IHCs.
924
925
926
927
928
929
930
931
932
933

934

935 **Supplementary figures**

936

937

938

939

940 **Supplementary Fig.1**

941 **Engineering of *Snap-25* $^{flox/flox}$ mouse**. Schematic representation of the

942 recombinant *Snap-25* allele. A targeting vector was designed in which loxP sites

943 (red) were introduced upstream and downstream of *Snap-25* exon 4, and a neo

944 cassette flanked with FRT sites (purple) as selectable marker was introduced

945 downstream of exon 4.

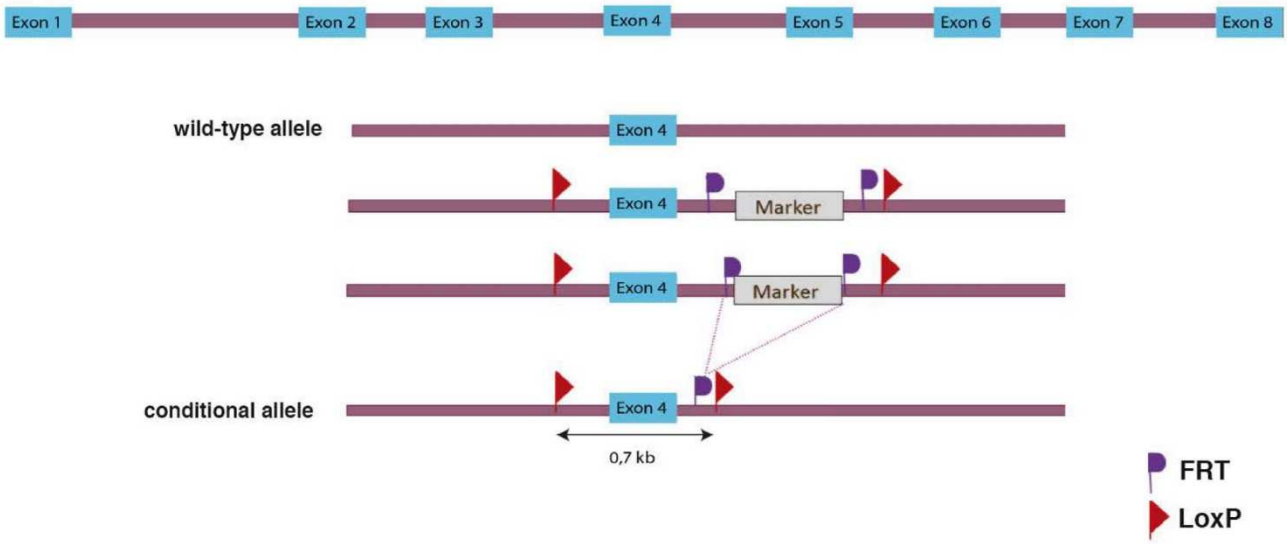

946

947

948

949

950

951 **Supplementary Fig.2**

952 **the *Myo15* promoter drives td-Tomato expression specifically in inner ear hair**

953 **cells.** Basal turns of Rosa-td-Tomato $^{+/KI}$ x Pmyo15-hCre $^{+/KI}$ mice organ of Corti and

954 vestibular end organs were microdissected at P1 (a,d), P5 (b,e) and P6 (c,f) and

955 immunostained for td-Tomato (red). Only the sensory hair cells expressed td-Tomato.

956

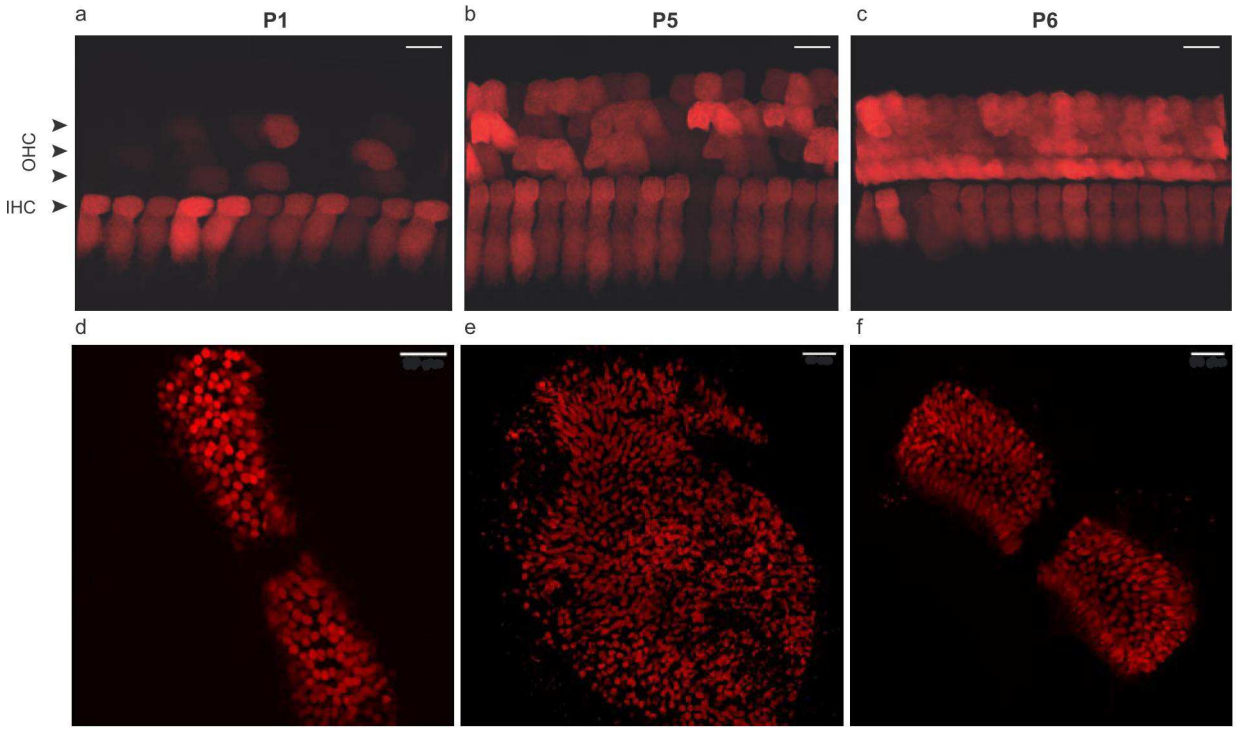

957 td-tomato

958

959

960

961

962

963

964

965

966 ***Supplementary Fig.3***

967 **The IHCs of *Snap-25* cKO mouse displayed normal mechanoelectrical**

968 **transduction (MET) currents.** (a) Bar charts show the peak amplitudes of the MET

969 currents (Imax) were similar in IHC of wild-type control mice (568,8 ± 25,8 pA, black,

970 n=7) and of *Snap-25* cKO mice (490,55 ± 35,6 pA, red, n=18) (unpaired t test, ns). (b)

971 Line graphs show the MET channel opening probability plotted as a function of hair

972 bundle displacement for IHCs of wild-type (black) and *Snap-25* cKO (red) mice. The

973 two curves are superimposed (two-way ANOVA, ns).

974

975 a

976

977

978

979

980

981

982

983

984

985

986

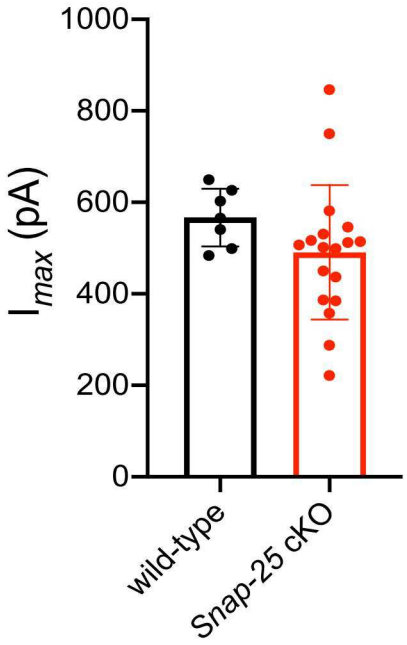

987

988

989

b

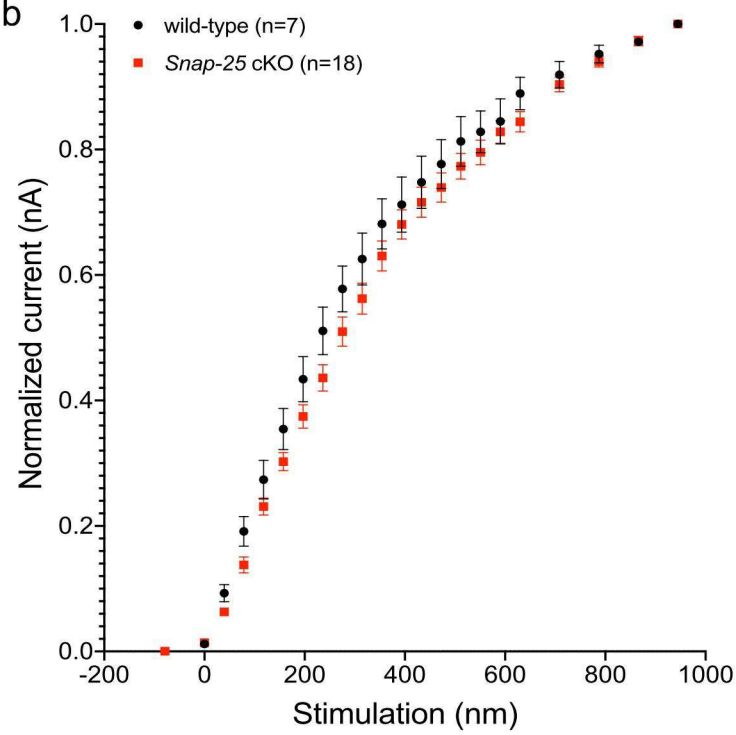

990
991
992
993
994
995
996
997 **Supplementary Fig.4**

998 **Surgery and cochlear delivery of AAV8-GFP-Cre at P14 in wild-type mice did**
999 **not affect significantly the hearing thresholds.** Auditory brainstem responses
1000 (ABR) were recorded at P20-P25 for different frequencies (5, 10 ,15, 20, 32, 40 kHz)
1001 in C57BL/6J mice after injection of AAV8-GFP-Cre at P14 (n=4 in red) compared to
1002 non-injected mice (n=8 in green). ABR thresholds were not altered after injection of
1003 AAV8-GFP-Cre in wild-type mice (unpaired t-tests ns except at 15kHz $p<0.05$).
1004

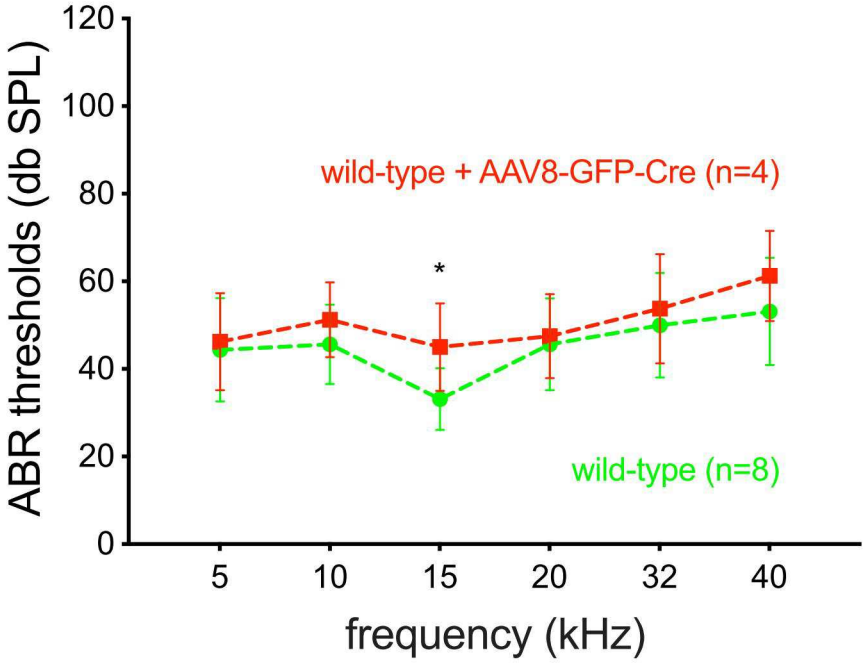

1005
1006
1007
1008
1009
1010
1011
1012
1013
1014

1015

1016

1017

1018

1019

1020

1021

1022 ***Supplementary Fig.5***

1023 **Surgery and cochlear viral delivery to P14 mice did not affect the function the**

1024 **outer hair cells.** Distortion product otoacoustic emissions (DPOAE) were recorded in

1025 adult P50 *Snap-25* $^{flox/flox}$ mice injected at P14 with AAV8-GFP-Cre (a, green curve,

1026 n=7) or in adult P28 *Snap-25 cKO* mice injected at P2 with AAV8-*Snap-25* (b, blue

1027 curve, n=3). DPOAE of the two injected groups were not significantly different when

1028 compared to the wild-type non-injected mice (black curves) (Mann Whitney test ns).

1029

1030

1031

1032

1033

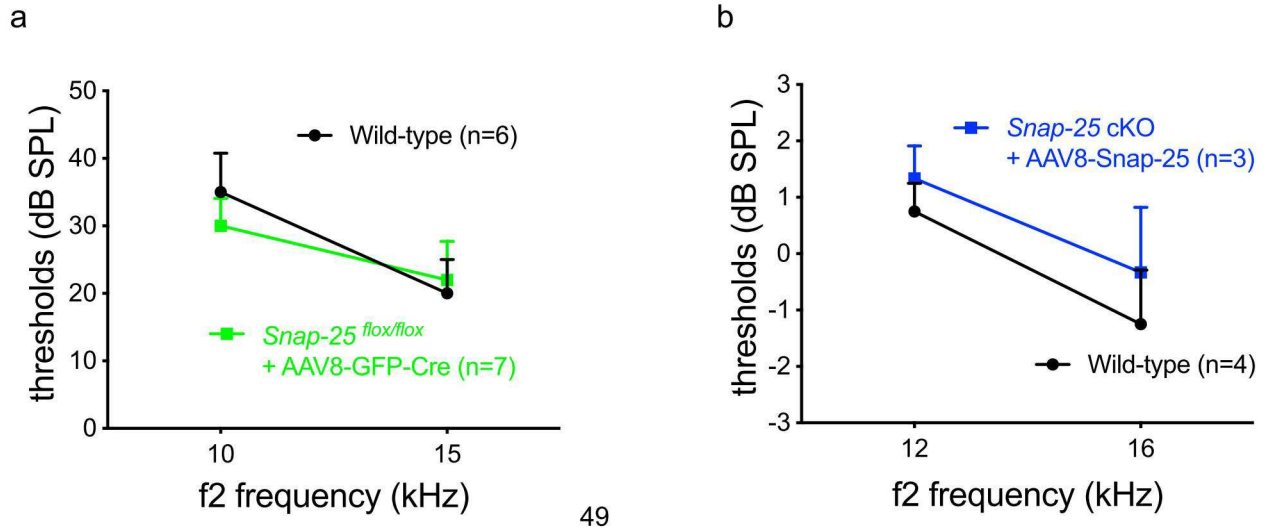

Article 4

Synaptic release potentiation at ageing auditory ribbon synapses

Potentialisation de l'exocytose synaptique lié à l'âge au niveau des synapses à ruban auditives

Publié dans

Frontiers in Aging Neuroscience

le 18 Octobre 2021

https://doi.org/10.3389/fnagi.2021.756449

Introduction

La perte d'audition lié à l'âge est couramment décrite comme une synaptopathie cochléaire qui résulte d'une dégradation progressive des synapses à ruban des cellules ciliées internes. Les changements structurels et fonctionnels de ces synapses avec l'âge ne sont pas encore entièrement établis. Nous avons étudié cette question sur la lignée de souris C57BL/6J qui présente une perte d'audition précoce lié à l'âge. Ces souris C57BL/6J présentent une mutation sur le gène de la cadherin-23 (Noben-Trauth et al., 2003). Nous confirmons chez ces souris une diminution progressive du nombre de synapses à ruban avec l'âge, bien avant que les cellules ciliées ou les neurones du ganglion spiralé commencent à dégénérer. Nous caractérisons pour la première fois au niveau cellulaire les changements fonctionnels des synapses restantes chez la souris âgée.

Résultats

Les Souris C57BL/6J développent une surdité progressive profonde liée à l'âge avec notamment une baisse de l'amplitude de l'onde P1-N1 suggérant une baisse du nombre des synapses afférentes associées aux cellules ciliées internes. De manière surprenante la hausse des seuils auditifs est associée à une réponse exacerbée des *startle reflex* aux faibles intensités sonores, suggérant une hyperacousie. L'origine de cette réponse pourrait provenir d'une potentialisation des synapses afférentes cochléaires restantes.

L'analyse en microscopie immuno-confocale nous montre une diminution drastique du nombre de synapses à ruban. Ce phénotype est associé à un rétrécissement important du corps cellulaire des cellules ciliées internes. Les rubans présynaptiques présentent une augmentation significative de leur volume, associée à une augmentation de la densité des récepteurs AMPARs postsynaptiques.

Par les techniques du patch-clamp et d'imagerie calcique sur explant d'organe de Corti ex-vivo, nous montrons une augmentation de la densité des courants calciques des cellules ciliées internes. Cette augmentation des réponses calciques est associée à une exocytose exacerbée, notamment l'exocytose soutenue. En parallèle ces cellules présentent une diminution importante de la taille des "patchs" de canaux BK ainsi qu'une modification de l'activation voltage-dépendant de ces canaux.

La diminution en taille des CCIs ainsi que l'augmentation de l'expression des protéines membranaires intracellulaires LC3B, marqueurs des vésicules autophagiques, suggèrent une activation de l'autophagie cellulaire avec l'âge dans les cellules ciliées de souris C57BL/6J. L'autophagie est un processus général cellulaire bien connu pour lutter contre la production excessive d'espèces réactives de l'oxygène (voir revue Chester et al. (2021)).

Conclusion

Notre étude démontre de nouveaux mécanismes fonctionnels et structurels de plasticité des synapses à ruban des cellules ciliées lié au vieillissement des souris C57BL/6J. Cette plasticité mène à une potentialisation de la synapse à ruban qui pourrait être à l'origine du phénomène paradoxal d'hyperacousie (hypersensibilité aux faibles intensités sonores) observée chez ces souris.

ARTICLE 4

frontiers in Aging Neuroscience

ORIGINAL RESEARCH
published: 18 October 2021
doi: 10.3389/fnagi.2021.756449

Synaptic Release Potentiation at Aging Auditory Ribbon Synapses

Thibault Peineau [1,2†], Séverin Belleudy [1†], Susanna Pietropaolo [3], Yohan Bouleau [1,2] and Didier Dulon [1,2]*

[1] Neurophysiologie de la Synapse Auditive, INSERM UMRS 1120, Bordeaux Neurocampus, Université de Bordeaux, Bordeaux, France, [2] Institut de l'Audition, Centre Institut Pasteur/Inserm, Paris, France, [3] INCIA, UMR 5287, CNRS, University of Bordeaux, Bat B2, Pessac, France

Age-related hidden hearing loss is often described as a cochlear synaptopathy that results from a progressive degeneration of the inner hair cell (IHC) ribbon synapses. The functional changes occurring at these synapses during aging are not fully understood. Here, we characterized this aging process in IHCs of C57BL/6J mice, a strain which is known to carry a cadherin-23 mutation and experiences early hearing loss with age. These mice, while displaying a large increase in auditory brainstem thresholds due to 50% loss of IHC synaptic ribbons at middle age (postnatal day 365), paradoxically showed enhanced acoustic startle reflex suggesting a hyperacusis-like response. The auditory defect was associated with a large shrinkage of the IHCs' cell body and a drastic enlargement of their remaining presynaptic ribbons which were facing enlarged postsynaptic AMPAR clusters. Presynaptic Ca^{2+} microdomains and the capacity of IHCs to sustain high rates of exocytosis were largely increased, while on the contrary the expression of the fast-repolarizing BK channels, known to negatively control transmitter release, was decreased. This age-related synaptic plasticity in IHCs suggested a functional potentiation of synaptic transmission at the surviving synapses, a process that could partially compensate the decrease in synapse number and underlie hyperacusis.

Keywords: auditory hair cells, synaptic ribbons, synaptopathy, hyperacusis, Ca^{2+} channels, exocytosis

OPEN ACCESS

Edited by:
Francesco Panza,
University of Bari Aldo Moro, Italy

Reviewed by:
Qiaojie Xiong,
Stony Brook University, United States
Jun Li,
Baylor College of Medicine,
United States

***Correspondence:**
Didier Dulon
didier.dulon@inserm.fr

† These authors have contributed equally to this work and share first authorship

***Received:** 10 August 2021*
***Accepted:** 21 September 2021*
***Published:** 18 October 2021*

Citation:
Peineau T, Belleudy S, Pietropaolo S, Bouleau Y and Dulon D (2021) Synaptic Release Potentiation at Aging Auditory Ribbon Synapses. Front. Aging Neurosci. 13:756449. doi: 10.3389/fnagi.2021.756449

INTRODUCTION

Age-related hearing loss (ARHL or presbycusis) is the most prevalent form of sensory disability in human populations and adversely affects the quality of life of many elderly individuals. Simultaneously with ARHL, chronic tinnitus and hyperacusis often develop due to abnormal neural activity in the central auditory system whose origin may arise from cochlear pathologies (for review see Knipper et al., 2013). The development of ARHL has been generally considered to be associated with primary degeneration of cochlear hair cells, with secondary deafferentation associating degeneration of spiral ganglion neurons and ribbon synapses. However, recent studies have resulted in a paradigm shift in the understanding of the early cause of ARHL (Kujawa and Liberman, 2015, 2019). During aging, hearing thresholds in the elderly often remain normal but speech intelligibility becomes hampered, especially in noisy environment. This pathology in the elderly is referred as hidden hearing loss and has been proposed to be caused in mice by an early loss of ribbon synapses contacting the inner hair cells (IHCs), well before any major loss of hair cells and spiral ganglion neurons (Stamataki et al., 2006). While glutamate excitotoxicity, resulting in nerve terminal swelling, has been proposed to play a role in the setting of noise-induced hearing

loss (Pujol and Puel, 1999; Hu et al., 2020), the molecular mechanisms underlying the degeneration of the cochlear ribbon synapses during aging remain to be elucidated. Oxidative damage due to an increase in ROS levels seems to play a crucial role in ARHL (Fu et al., 2018) but how the ribbon synapses are functionally affected remain unknown.

The C57BL/6J inbred strain of mice has been extensively used as model for ARHL (Johnson et al., 1997; Spongr et al., 1997; Hequembourg and Liberman, 2001; Bartolome et al., 2002; Henry, 2002). This mouse strain carries a cadherin-23 mutation (*Cdh23*^{753A}, also known as *Ahl*), which affects inner ear structures, characterized by progressive degeneration of ribbon synapses and spiral ganglion neurons, and results in age-related hearing loss. *Ahl* is a recessive single nucleotide mutation at 753 (G=>A) on the *Cdh23* gene on mouse chromosome 10 (Noben-Trauth et al., 2003). *Cdh23* encodes cadherin 23, a protein necessary for inner ear development and maintenance of the sensory hair cell structures, in particular the tip and lateral links of the stereocilia at the hair bundle (Siemens et al., 2004; Sollner et al., 2004; Lagziel et al., 2005; Michel et al., 2005; Kazmierczak et al., 2007), but growing anatomical evidence also suggests that synaptic rearrangements on sensory hair cells also contribute to auditory functional decline in C57BL/6J mice (Stamataki et al., 2006; Jiang et al., 2015; Zachary and Fuchs, 2015; Jeng et al., 2021). Surprisingly, aging C57BL/6J mice, although showing cochlear ribbon synapse degeneration and hearing loss, display increased acoustic startle reflex amplitudes (Ison and Allen, 2003; Ouagazzal et al., 2006; Ison et al., 2007) and a time increase in recovery from ABR short-term adaptation (Walton et al., 1995). Whether this exaggerated startle reflex can be explained by functional changes of cochlear hair cell ribbon synapses remain to be explored. Our present study will show that aged C57BL/6J mice, while losing nearly up to 50% of their IHC ribbon synapses, have IHCs with reduced BK channel clusters, larger remaining presynaptic ribbons (with increased Ca^{2+} microdomains and larger sustained exocytotic responses) facing postsynaptic afferent boutons with larger AMPAR clusters. All these features indicated that synaptic release potentiation occurs at auditory IHC ribbon synapses during aging. This age-related synaptic plasticity could be viewed as compensatory mechanisms of the decrease IHC synapse number and may explain the hyperacusis-like startle reflex observed in aged C57BL/6J mice.

RESULTS

Increased ABR Thresholds and Hyperacusis-Like Effect on ASR

As previously described (Zheng et al., 1999; Zhou et al., 2006), CBA/J mice, used here as a reference, showed no sign of rapid degradation of their hearing function with aging, as attested by constant click ABR thresholds near 15 dB SPL up to 1 year of age (**Figure 1A**). On the contrary, C57BL/6J mice, carrying the *Cdh23*^{753A} mutation, displayed an early progressive increase in ABR thresholds with aging (**Figure 1A**). Hearing thresholds started to increase significantly at postnatal day P180 to reach a mean 50 dB increase at P365 (click ABR thresholds above 65 dB SPL) as compared to young mature P30 mice. Distortion product otoacoustic emissions (DPOAEs) in P365 C57BL/6J mice were still present but significantly reduced, indicating that the electromechanical activity of the outer hair cells (OHCs) was also affected (**Figure 1D**). However, counting hair cells on surface preparations of organs of Corti from these P365 mice, in the mid-cochlea region (8–16 kHz), indicated only a moderate loss of OHCs and IHCs (statistically not significant; **Figure 2E**), in good agreement with the study of Zachary and Fuchs (Zachary and Fuchs, 2015). This moderate loss of OHCs suggested that the profound hearing loss occurring at P365 in C57BL/6J mice arose from additional factors than a simple alteration of the cochlear amplifier. We then compared the amplitude on the ABR wave-I as a function of sound intensity in young and old mice. The wave-I is known to result from the synchronous activity of the auditory nerve fibers and can provide an objective measure of ribbon synapses loss when measured at high sound intensity above 70 dB SPL. In P365 old mice, ABR wave-I amplitudes were largely reduced as compared to young mature P30 mice, even at high sound intensity when IHCs are directly stimulated and bypass the amplification process of the OHCs (**Figure 1B**). The large decrease in wave-I amplitude indicated a decreased number of auditory nerve fibers activated by sound and/or a decrease in their firing rate or synchrony. The latencies of the ABR wave-I were also significantly increased suggesting again that the IHC ribbon synapses are affected (**Figure 1C**).

Surprisingly, at lower sound intensities tested (between 20 and 35 dB above background noise level), the strength of the acoustic startle reflex (ASR) was found larger in old P365 C57BL/6J mice as compared to young P60, indicating hyperacusis reactivity (**Figure 1E**). The origin of this acoustic hypereactivity at low sound intensities could arise from central neural reorganization (Willott, 1996) and be consecutive to functional defect of the IHC ribbon synapses in aging C57BL/6J mice that we are going to characterize in this study. At loud sound intensities, 45 dB above background noise, the amplitudes of the ASR responses were however diminished in old mice, likely reflecting the increase in ABR thresholds due to a drastic decrease in the number of ribbon synapses per IHCs.

Drastic Loss of IHC Synaptic Ribbons With Aging

Confocal immunofluorescence imaging of the synaptic ribbons in IHCs from C57BL/6J mice, in the cochlear region encoding between 8 and 16 kHz, showed a progressive and large decrease in the number of synaptic ribbons with aging, from 16.3 ± 0.3 ribbons/IHC at P15 to 8.7 ± 0.5 ribbons/IHC at P365 (**Figures 2A–C**). This nearly 50% loss of synaptic ribbons in IHCs of C57BL/6J mice at P365 was in good agreement with previous studies (Zachary and Fuchs, 2015; Jeng et al., 2020). Counting the spiral ganglion neurons in the mid-frequency

Abbreviations: ABR, Auditory brainstem responses; AHRL, Age-related hearing loss; ASR, Acoustic startle reflex; AZ, active zone; dB(SPL), decibel Sound Pressure Level; DPOAE, Distorsion product otoacoustic emission; IHC, Inner Hair Cell; OHC, Outer Hair Cell; ROS, reactive oxygen species; RRP, readily releasable pool; SRP, secondarily releasable pool.

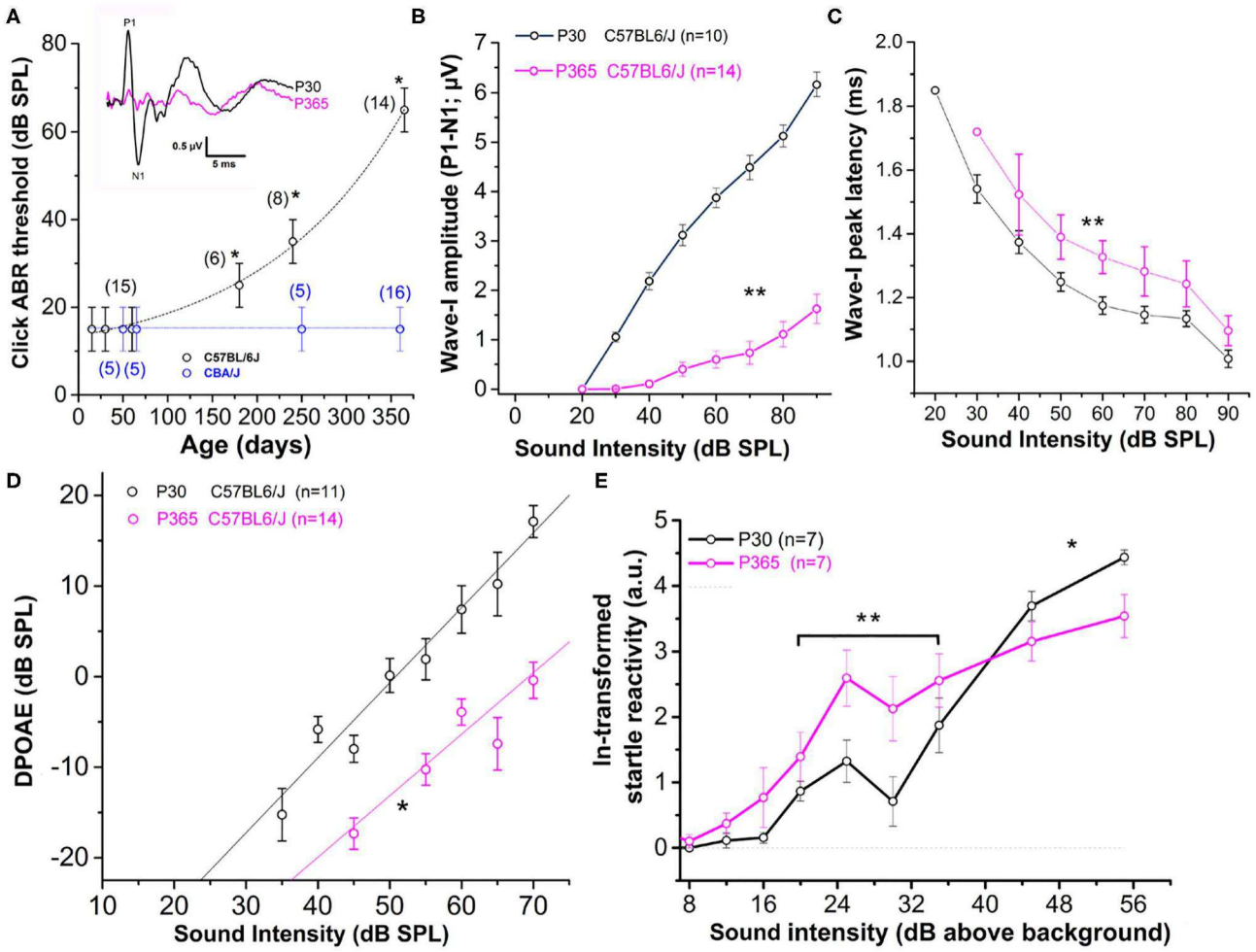

FIGURE 1 | Sensorineural hearing loss with Aging in C57BL/6J mice. **(A)** Click-ABR thresholds as a function of age in CBA/J mice (blue; $n = 5$–16) and C57BL/6J mice (black, $n = 6$–15). For each strain, asterisks indicate significant difference with $p < 0.05$ as compared to P30 mice (two-way ANOVA). Inset show comparative mean ABR waves at 70 dB SPL in P30 and P365 C57BL/6J mice. **(B)** Wave-I amplitude (P1–N1) as a function of sound intensity in young P30 (black) and old P365 (pink) C57BL/6J mice. Asterisks indicate significant difference with $p < 0.05$ (two-way ANOVA; $p = 0.001$). **(C)** Latency to reach peak amplitude of wave-I as a function of sound intensity. Significantly different with $p = 0.003$ between 80 and 50 dB SPL (two-way ANOVA; n is indicated in graph **B**). **(D)** Distortion products otoacoustic emissions (DPOAEs; $2f1$–$f2$ with $f1 = 12.73$ kHz and $f2 = 15.26$ kHz) as a function of sound intensity in young P30 (black) and old P360 (pink) C57BL/6J mice. Asterisk indicated significant difference with $p < 0.05$ (two-way ANOVA, $p = 0.01$). **(E)** Startle reactivity to acoustic stimulation. The intensity of startle reaction (in mV) was ln-transformed and obtained through two conditions of white-noise bursts of 20 and 40 ms. Note that below 35 dB above background the startle reaction is increased at P360 whereas at 45 and 55 dB above background the startle reaction is decreased compared to P30 mice. Asterisks indicated significant difference with $p < 0.05$ (two-way ANOVA, $p = 0.007$ between 20 and 35 dB and $p = 0.005$ between 45 and 55 dB).

region of the cochlea (8–16 kHz) showed a mean 20% loss of neurons in P365 mice as compared to P30 mice (**Figures 2D–F**). Remarkably, the age-related loss of neurons, averaging 20%, was much less pronounced than the loss of IHC synaptic ribbons (50%), suggesting that there was a large number of neurons surviving without dendritic/synaptic projection toward the organ of Corti as previously shown by Stamataki et al. (2006).

Enlarged Presynaptic Ribbons Associated With Larger Postsynaptic AMPAR Clusters

When analyzing the 3-D imaging reconstruction of the IHC synaptic ribbons from P365 C57BL/6J IHCs from high resolution confocal STED immunofluorescent sections, we found that these structures displayed a progressive increase in their mean size (volume) as compared to young P15 mice (**Figure 3A**). The mean volume of the synaptic ribbons increased nearly three-fold between P15 and P365 (**Figure 3B**). Interestingly, the increase in size of the ribbons started very early after P30, an age at which their number also started to decrease (**Figure 2B**) while hearing thresholds were still normal (**Figure 1A**).

We next investigated the changes occurring with aging in the spatial distribution of the synaptic ribbons at the basolateral membrane of the IHCs. It is worth recalling that larger presynaptic ribbons associated to low-spontaneous-rate afferent

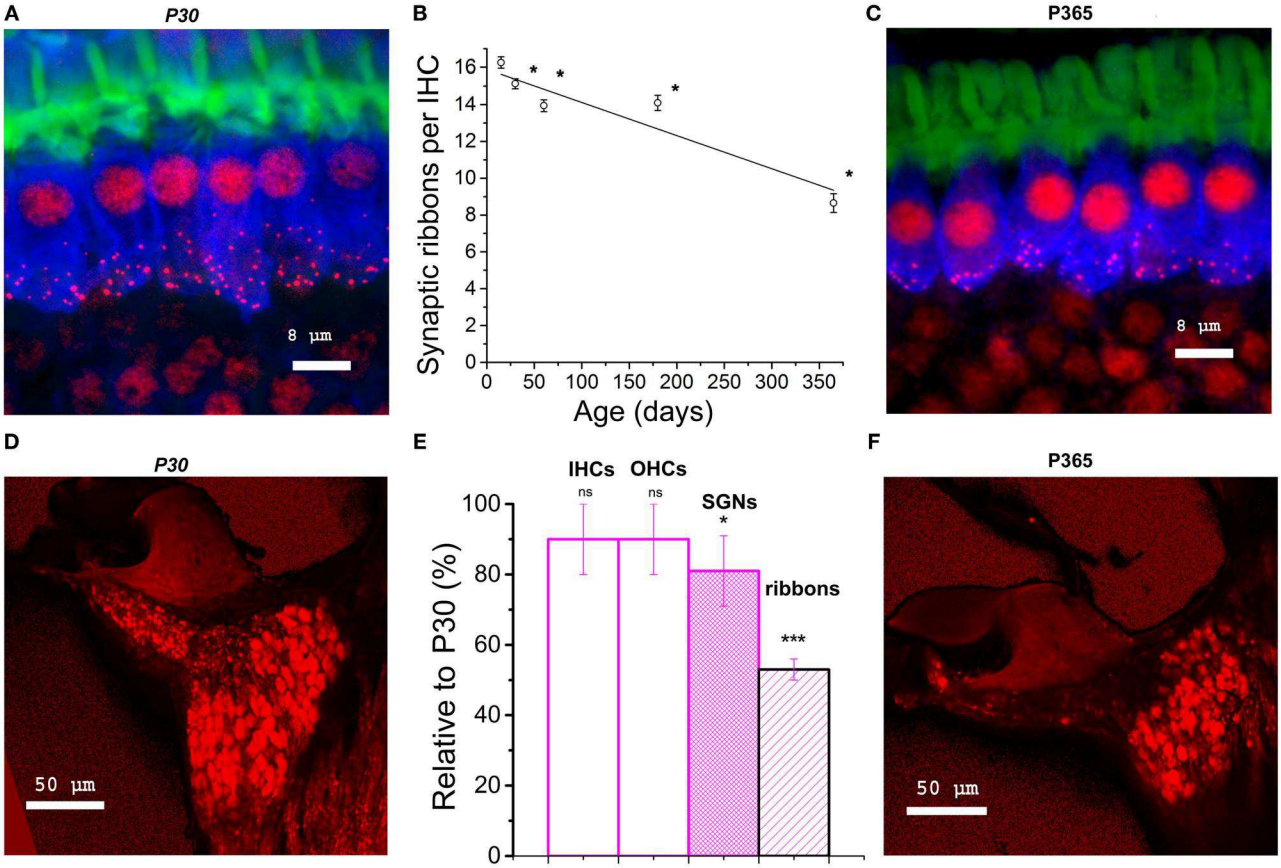

FIGURE 2 | Synaptic ribbon loss in aging IHCs and comparative density of spiral ganglion neurons. **(A–C)** Confocal immunofluorescence imaging of IHCs from P30 and P360 C57BL/6J mice. Image resulted from stack reconstructions of 22 slices of 0.3 µm thickness, showing F-actin (green, labeling the hair bundles), otoferlin (blue; a synaptic Ca^{2+} sensor labeling the entire IHC body) and synaptic ribbons (Ribeye/CtBP2, red dots). The white bars indicated 8 µm. **(B)** Plot of synaptic ribbon counts per IHC as a function of age in C57BL/6J mice (black) in the mid-frequency cochlear region (8–16 kHz). Asterisks indicate significant difference with $p < 0.05$ (comparison with P15 C57BL/6J mice, one-way ANOVA *post-hoc* Tukey test). 203, 306, 306, 306, and 295 ribbons were, respectively, analyzed at P15, P30, P60, P180, and P365 in 3–5 mice at each age. **(D–F)** Confocal immunofluorescence imaging of cochlear transversal sections from P30 and P360 mice (8–16 kHz area) where neurons and their afferent dendrites are labeled with dextran amines 3,000. **(E)** Analyzed in the mid-cochlea (8–16 kHz), comparative histogram of hair cells counts, SGNs and synaptic ribbons (three mice at each age relative to young mature P30 C57BL/6J mice). The asterisks indicated statistical difference with $p < 0.05$ (from left to right $p = 0.37$, 0.14, and 0.020 for SGNs and $p = 1.01E{-}14$ for ribbons, using unpaired *t*-test). Note the reduction in SGNs and the drastic decrease of the fluorescent labeling of the afferent nerve fibers projecting to the organ of Corti.

fibers are usually found at the modiolar side of the IHCs (i.e., the baso-lateral curved side of the IHCs directed toward the spiral ganglion neurons) while smaller ribbons associated with high-spontaneous-rate afferent fibers predominates at the pillar side (Liberman, 1982; Liberman et al., 2011). We found that, while a larger proportion of synaptic ribbons distributed at the modiolar side in young P30 IHCs (∼60%), the surviving ribbons in old P365 IHCs were evenly distributed at the pillar and modiolar side (**Figures 4A,B**). The loss of synaptic ribbons with aging was more pronounced at the modiolar side, i.e., at the side where most of the low-spontaneous (high threshold) fibers make contact to IHCs (**Figure 4C**). An increase in volume was noted both in pillar and modiolar ribbons (**Figure 4D**). Unlike young P30 IHCs, old P365 IHCs had modiolar and pillar ribbons with similar volume ($0.7 \pm 0.1\ \mu m^3$ and $0.57 \pm 0.07\ \mu m^3$, respectively; not significantly different, unpaired *t*-test p = 0.28, **Figure 4D**). Similar preferential loss of synaptic modiolar ribbons associated with an increase in ribbon volume was also reported after noise-induced hearing loss (Liberman and Kujawa, 2017; Hickman et al., 2020).

Postsynaptic afferent endings to ribbon IHCs express AMPA-type ionotropic glutamate [glutamate receptor A2 (GluA2)]-containing AMPA receptors (Matsubara et al., 1996; Hu et al., 2020). To determine whether the organization of postsynaptic AMPARs facing the IHCs ribbon was modified in old P365 mice we performed GluA2 immunostaining and confocal fluorescence imaging (**Figure 5**). As compared to young ribbon synapses, old synapses had larger ribbons associated with larger AMPAR clusters, suggesting that the changes occurring with aging are both at the pre and postsynaptic side in good agreement with the EM morphological analysis of Stamataki et al. (2006).

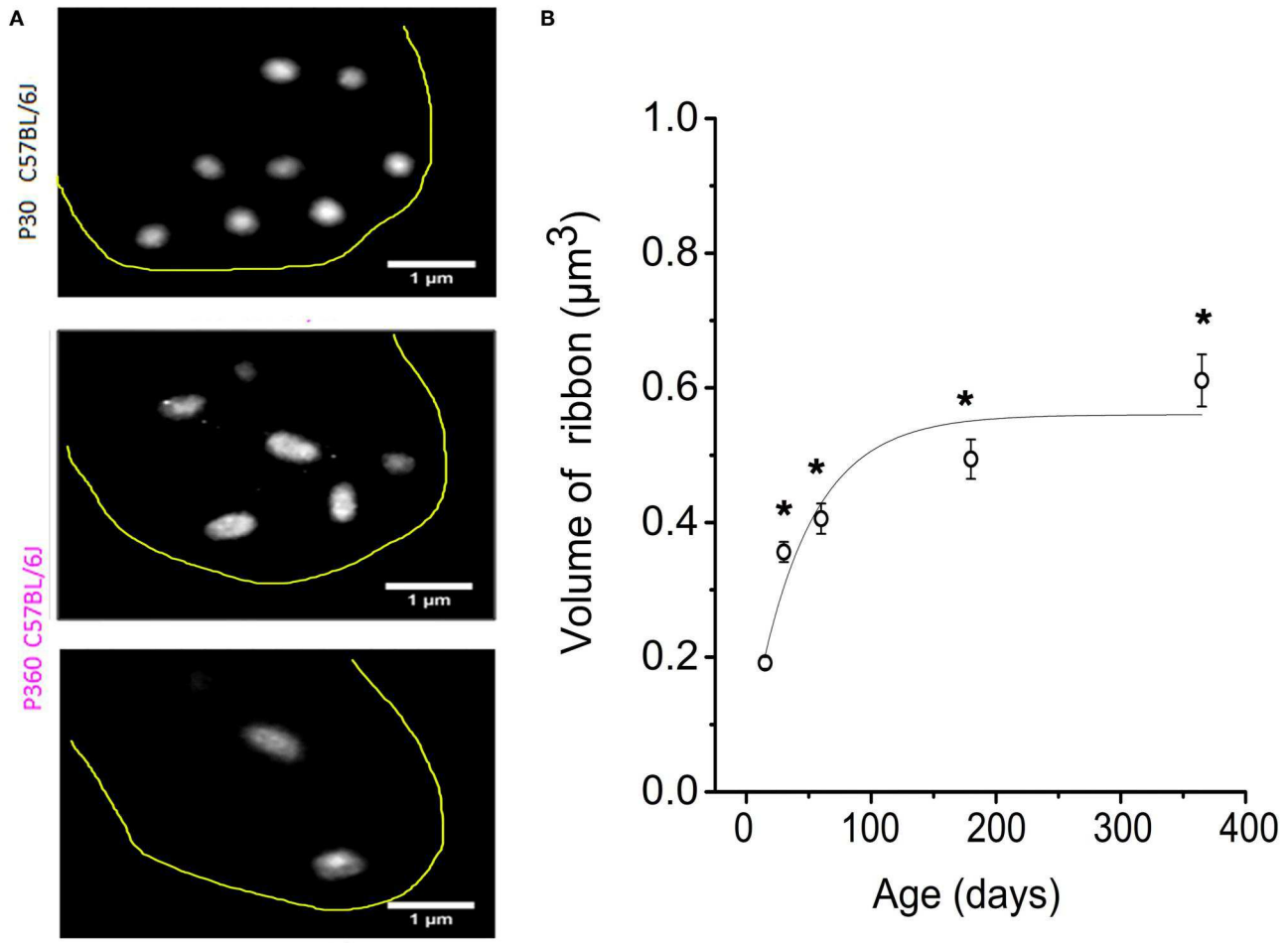

FIGURE 3 | IHC synaptic ribbons progressively increased in size with aging. **(A)** Example of high magnification confocal STED images (stack reconstruction of five 0.25 µm slices). The yellow line delineates the IHC contour. Ribbons were less numerous and larger in size in IHCs from P365 C57BL/6J mice. **(B)** The mean volume of the IHC synaptic ribbons was calculated in the mid-cochlear region (encoding 8–16 kHz), using the plugin 3D-Object counter of ImageJ, and was plotted as a function of age: P15 (203 ribbons–40 IHCs–3 mice), P30 (306 ribbons–98 IHCs–5 mice), P60 (306 ribbons–95 IHCs–3 mice), P180 (306 ribbons–67 IHCs–3 mice), P365 (295 ribbons–43 IHCs–3 mice). As indicated by the asterisks, when comparing with P15, the mean volume of the ribbons started significantly to increase significantly from P30 ($p < 0.05$; one-way ANOVA).

Drastic IHC Cell Size Reduction With Aging

To determine whether the loss of synaptic ribbons was associated with a cell size reduction in old P365 IHCs, we labeled the cytosol of IHCs with an antibody against myo-7a, an unconventional myosin essential for the hair bundle functional integrity and found in the apical sterocilia as well as the cytoplasm of the hair cells (Hasson et al., 1995). We found a drastic reduction of the basal infra-nuclear synaptic zone of the IHCs from an average of 15.7 ± 0.1 µm ($n = 34$) in P21 IHCs to 12.4 ± 0.3 µm ($n = 50$) in old P365 IHCs (unpaired-*t* test, $p = 1.1$ E−13, **Figures 6A–C**). The cell size reduction of old IHCs was confirmed by another method using whole-cell patch clamp measurement of the IHC resting membrane capacitance in organs of Corti preparation *ex-vivo* (**Figures 6D,E**). P365 IHCs displayed a significant smaller resting capacitance, measured at −70 mV, of 7.9 ± 0.4 pF ($n = 22$) as compared to P21 IHCs (10.8 ± 0.1 pF, $n = 44$, unpaired *t*-test, $p = 3.7$ E−10).

Higher Ca^{2+} Current Density and Exocytosis in Old IHCs

Although the loss of IHC ribbon synapses in C57BL/6J mice with aging is well-documented in the literature (Wan and Corfas, 2015), the functional changes of the remaining "old" IHC ribbon synapses has not yet been explored in detail at the cellular level. We investigated here the changes in the calcium-evoked exocytotic responses of aging IHCs from *ex-vivo* explants of the organ of Corti from aging C57BL/6J mice. We recall that Ca^{2+} is a key messenger for normal hearing since it tunes the transduction of the analogic sound signal into nerve impulses. This transduction occurs at the IHC synaptic active zone through the voltage-activation of $Ca_v1.3$ Ca^{2+} channels (Brandt et al., 2003; Vincent et al., 2017) and the action of the Ca^{2+} sensor otoferlin (Roux et al., 2006; Beurg et al., 2010; Michalski et al., 2017). Increase in the density of L-type Ca^{2+} channels have long been recognized as a characteristic of aging central neurons

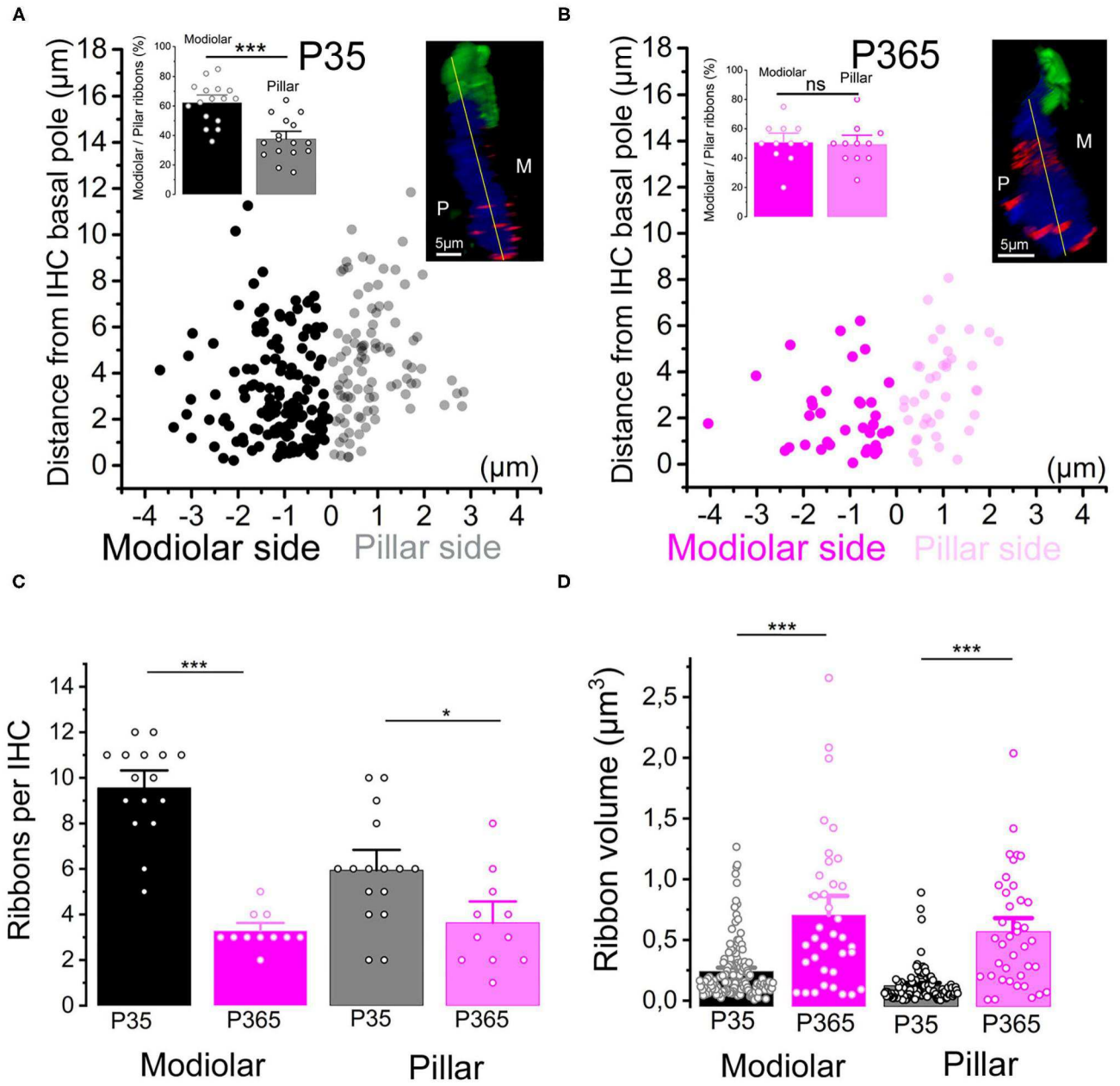

FIGURE 4 | Modiolar vs. pillar distribution of the synaptic ribbons with aging. **(A,B)** The distribution of IHC synaptic ribbons was splitted in two cell areas: P (pillar side) and M (Modiolar side). The two regions were determined using the K-means clustering method for each cell (see section Methods). The yellow lines in the inset confocal images was drawn to arbitrarily delineate the frontier between pillar and modiolar ribbons (green labeling F-actin, blue Otoferlin and red the synaptic ribbons). Note that in young P35 IHCs ($n = 16$), synaptic ribbons are preferentially localized in the modiolar region (62.3 ± 3.5% vs. 37.7 ± 3.5; unpaired t-test $p = 2.07$ E−5). In old P365 IHCs ($n = 11$), the remaining ribbons equally distributed in the modiolar and pillar side (50.7 ± 4.0% vs. 49.3 ± 4.0%, unpaired t-test; $p = 0.81$). **(C)** Synaptic ribbons were significantly loss both at the modiolar side and pillar side. However, the loss was much more pronounced in the IHCs' modiolar side (9.56 ± 0.5 ribbons ($n = 16$ IHCs) vs. 3.27 ± 0.24 ribbons ($n = 11$ IHCs); unpaired t-test $p = 5.57$ E−10) and pillar (5.9 ± 0.6 ribbons vs. 3.6 ± 0.6 ribbons, unpaired t-test $p = 0.016$). **(D)** The increase in volume affected both modiolar [P35 = 0.24 ± 0.02 μm^3 (153 ribbons) vs. P365 = 0.7 ± 0.1 μm^3 (36 ribbons) unpaired t-test, $p = 3.7$ E−11] and pillar [P35 = 0.12 ± 0.01 μm^3 (95 ribbons) vs. P365= 0.57 ± 0.07 μm^3 (40 ribbons), unpaired t-test $p = 7.5$ E−14] synaptic ribbons. This comparative analysis was performed in IHCs of the mid-cochlear region (encoding 8–16 kHz). Asterisks indicate statistical difference with $^*p < 0.05$ and $^{***}p < 0.001$.

(Campbell et al., 1996; Thibault and Landfield, 1996) but possible altered function in Ca^{2+} signaling has not been investigated in aging IHCs.

In the present study, whole cell patch-clamp recordings from old P365 IHCs showed a significantly increase in Ca^{2+} current density (Ca^{2+} current amplitude normalized to cell size) as

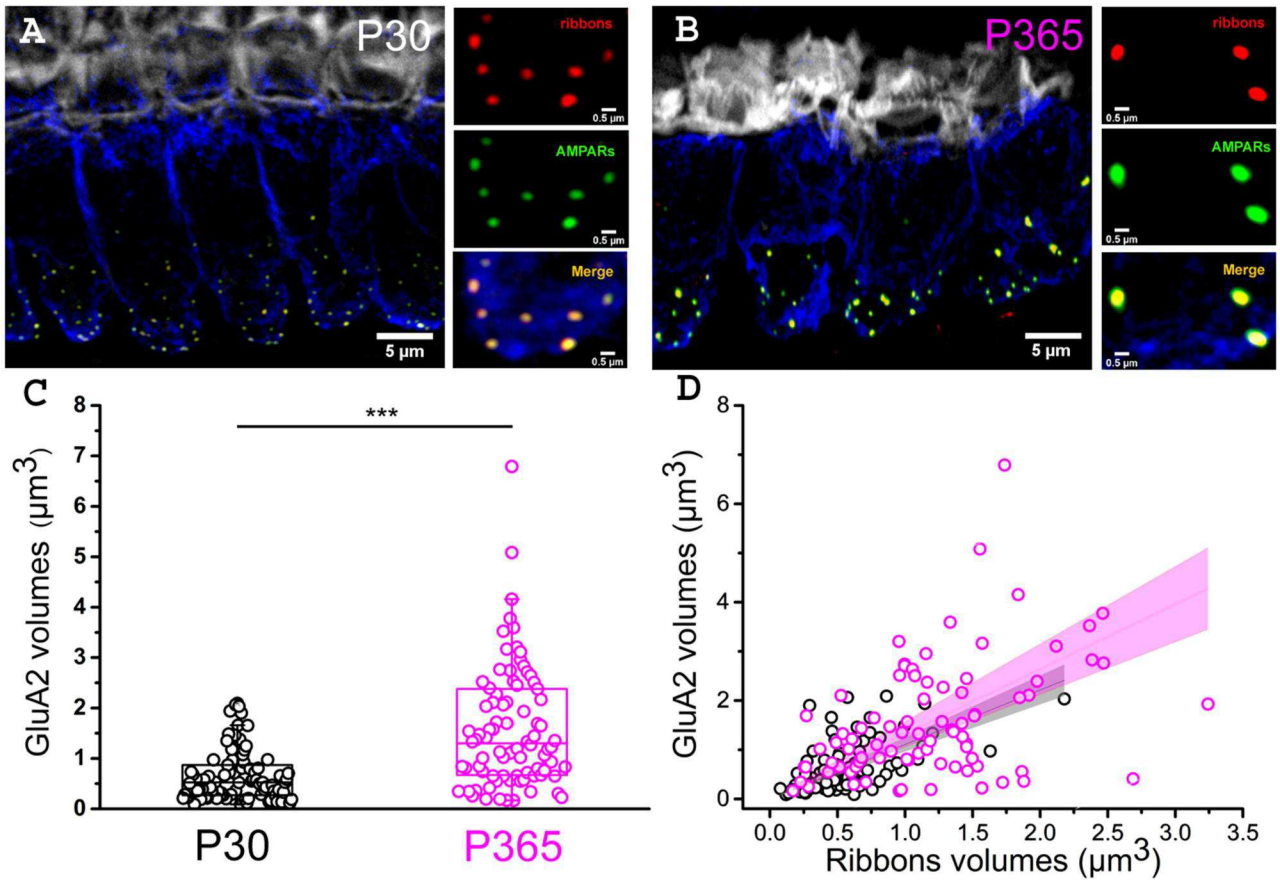

FIGURE 5 | Larger postsynaptic patches of GluA2 receptors in old IHCs. **(A,B)** Immuno-confocal imaging of IHCs (stack reconstructions of 22 slices of 0.3 µm thickness) showing otoferlin (blue), the synaptic ribbons (Ribeye/CtBP2, red dots) and the post-synaptic AMPA receptors (GluA2, green dots). Fluorescent-phaloidin (gray) labeled F-actin in the strereocilia. The white bars indicate 5 µm in **(A,B)**, then 0.5 µm in the 3 small panels. **(C)** Comparative distribution of the volume of postsynaptic patches of AMPA GluA2 receptors. Note that the GluA2 receptor volume significantly increased with aging in C57Bl/6J mice ($p < 0.001$; unpaired-*t* test); ($n = 86$ synapses; from three mice at P30 (16 IHCs) and P365 (29 IHCs); mid-cochlear region encoding 8–16 kHz). **(D)** Comparative volume distribution of postsynaptic GluA2 and corresponding postsynaptic ribbon in P30 and P365 IHCs. Note a good linear correlation between GluA2 and ribbon volumes (Pearson's coefficient $r = 0.93$ and 0.86, respectively, for P30 and P360).

compared to young mature P30 IHCs, rising from a mean peak value of 15.8 ± 1.75 pA/pF to 20.1 ± 1.9 pA/pF at −10 mV (**Figure 7A**; unpaired *t*-test, $p < 0.05$). The voltage-activation curve of the Ca^{2+} currents in old P365 IHCs remained similar to the young mature P30 IHCs, with a mean half-voltage activation ($V_{1/2}$) of −29.3 ± 1.1 and −26.7 ± 2.8 mV, respectively (unpaired *t*-test, $p = 0.06$).

Patch-clamp measurement of membrane capacitance upon depolarizing voltage-steps from −80 to −10 mV with increasing time duration allowed to compare the kinetics of vesicle exocytosis in young and old IHCs. For brief stimulations below 25 ms, a time-frame addressing the release of the Readily Releasable Pool (RRP) of vesicles, the exocytosis response (normalized to cell size) was similar in P30 and P365 IHCs (**Figures 7B,C**). However, longer depolarization above 25 ms revealed a more sustained exocytotic response in old IHCs, suggesting the mobilization of a more efficient secondarily releasable pool (SRP), i.e., a more efficient vesicle recruitment in these cells (**Figures 7B,D**). To investigate whether this increased SRP exocytosis was due to higher Ca^{2+} microdomains at the ribbon active zones, we used the high affinity Ca^{2+}-indicator Rhod-2 (K_d = 570 nM) which is known to allow a good monitoring of low Ca^{2+} concentrations ranging from 20 nM to 20 µM (Del Nido et al., 1998). We choose to use Rhod-2 rather than a low affinity Ca^{2+} dye such as OGB-5N with a Kd at 20 µM (Vincent et al., 2014) because we wanted here to primarily probe the amplitude of the Ca^{2+} microdomains, where the changes in Ca^{2+} concentrations are due to Ca^{2+} diffusion and are lower than at the nanodomain range near the Ca^{2+} channels. Ca^{2+} microdomains allow vesicle replenishment, a process occurring at the µm scale away from the ribbon and their associated Ca^{2+} channels (Spassova et al., 2004; Johnson et al., 2005; Graydon et al., 2011). We found that, upon 5 consecutive long 100 ms voltage-step stimulations (from −80 to −10 mV), IHCs displayed brighter transient Ca^{2+} hot spots (measured in 1 μm^2 areas) at their basal synaptic area in P365 mice as

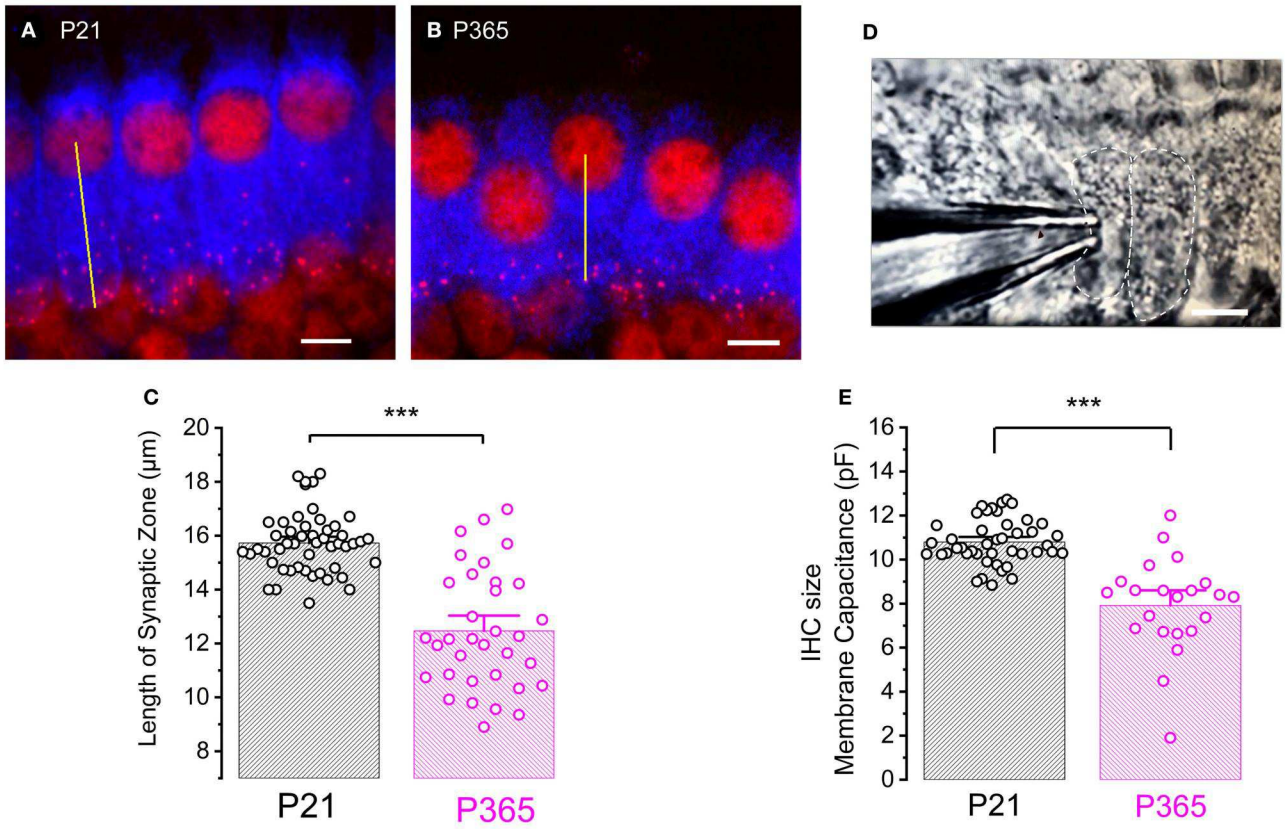

FIGURE 6 | Cell size reduction of IHCs with aging. **(A,B)** Immuno-confocal imaging of IHCs labeled for myo-7a (blue) and CtBP2 (labeling the ribbons, red) in P21 **(A)** and P365 **(B)** mice (reconstructed stack images of 22 slices of 0.3 µm thick). The length of the infra-nuclear synaptic zone was measured from the center of the nucleus to the bottom of the cell as indicated by the yellow line. The scale bar indicated 5 µm. **(C)** Comparative histogram of the length of the infra-nuclear synaptic zone. Asterisks indicated statistical significance with $p < 0.0001$, unpaired *t*-test, $n = 50$ IHCs for P21 and 34 IHCs for P365. Measurements were made from IHCs of the mid-cochlear region (8–16 kHz). **(D)** Photomicrograph showing a row of IHCs in an *ex-vivo* organ of Corti explant and a patch-clamp recording electrode allowing measurements of capacitive and ionic currents. **(E)** Comparative mean IHC resting membrane capacitance, measured at −70 mV, in whole-cell patch-clamp configuration. Asterisks indicated values with significant difference with $p < 0.0001$, unpaired-*t* test, $n = 44$ IHCs for P21 and $n = 22$ for P365.

compared to young P30 IHCs (**Figures 8A,B**). This indicated the expression of synaptic Ca^{2+} microdomains with larger amplitude in old P365 IHCs, a response likely due to a larger Ca^{2+} channel density at their ribbon active zones (**Figure 7A**). Simultaneously, in the same cells, the application of the 5 consecutive 100 ms stimulations, generated a facilitated vesicular recruitment in old P365 IHCs (**Figure 8D**). Also, as a consequence of increased Ca^{2+} microdomains in old IHCs, the simultaneous recording of Ca^{2+} currents showed an enhanced time-inactivation, indicative of an increased Ca^{2+}-dependent inactivation due to higher intracellular Ca^{2+} concentration (**Figure 8C**).

Aging Promoted Autophagy in IHCs Through the Recruitment of LC3B

The size reduction of the old IHCs (**Figure 6**) suggested that the degenerative process of the ribbon synapses was associated with a concomitant reduction of the cell surface membrane of IHCs during aging, suggesting a largely augmented uptake of plasma membrane through endocytosis. Like other type of cells, such as neurons or retinal cells, auditory hair cells utilize autophagic pathways to maintain cell homeostasis during excessive ROS production (Fu et al., 2018; Defourny et al., 2019). Autophagy is a degradation process where cytoplasmic and plasma membrane components are engulfed by vesicles called autophagosomes. To determine whether this process could explain the IHC size reduction with aging, we investigated the recruitment of LC3B, a structural protein of autophagosomal membranes. We assessed and compared the autophagosome numbers and surface area in young P30 and old P365 IHCs by quantifying LC3B puncta numbers/cell by using confocal immunofluoresence. We found that the number and overall surface area of LC3-positive structures in IHCs largely increased with aging (**Figure 9**), indicating an increased autophagosome formation. Similar investigations in P365 CBA/J mice, a strain which does not display early age-related hearing loss (**Figure 1**), showed a weak expression of LC3B in IHCs (**Figure 9**).

Clustering and Voltage-Dependent Activation of BK Channels Are Affected in Aging IHCs

There is increasing evidence that oxydative damage due to an increase in ROS levels plays a crucial role in age-related

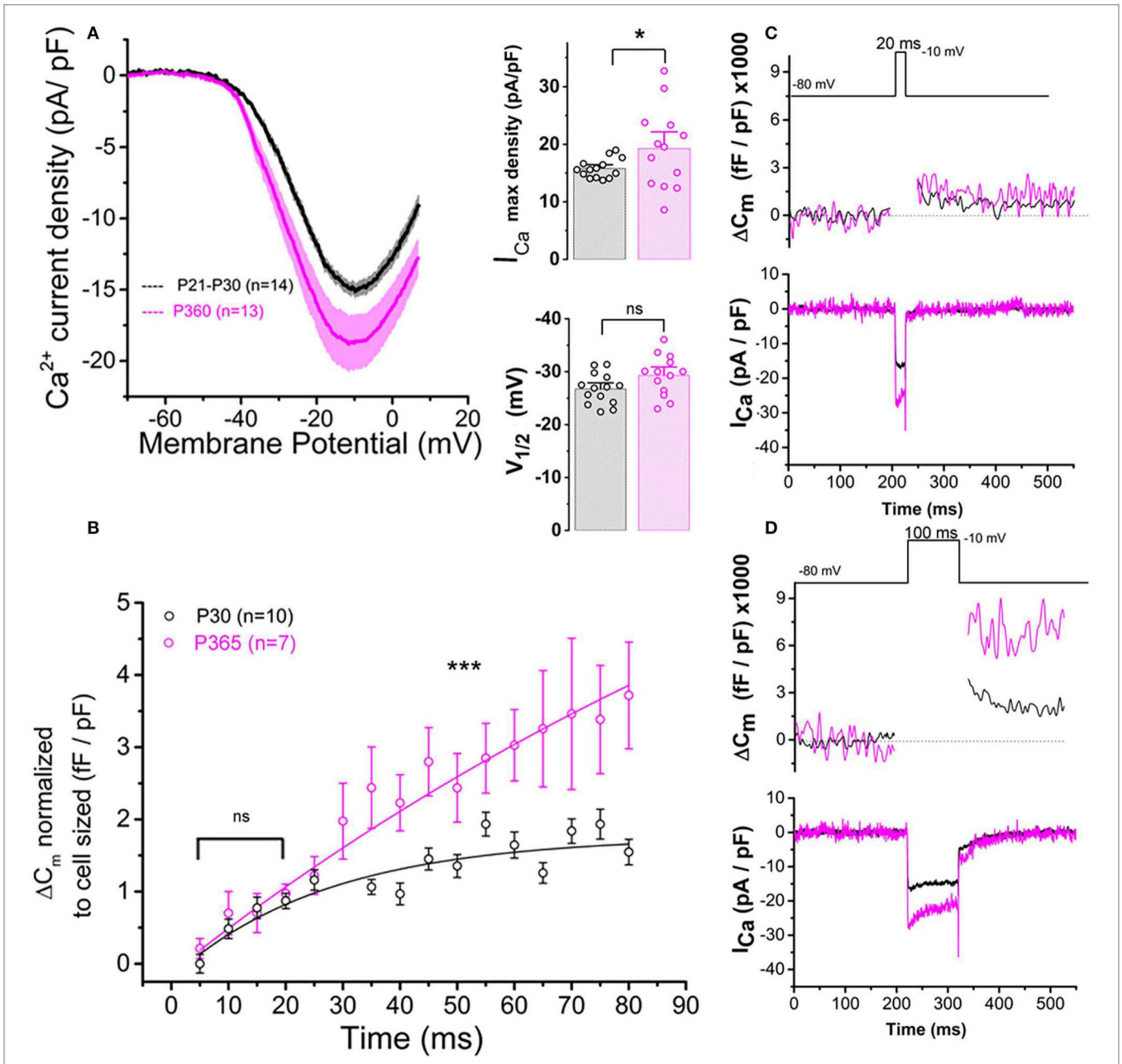

FIGURE 7 | Ca^{2+} currents and exocytosis are exacerbated in IHCs from aged C57BL6/J mice. **(A)** Ca^{2+} current density of old P365 IHCs (pink) was larger as compared to young mature P21 IHCs (black). IHCs were subjected to a voltage ramp stimulation from −90 to +30 mV in 120 ms, giving a slope change in voltage of 1 mV/ms. Comparative I_{Ca} maximum density measured at −10 mV indicated a significant increase in P360 IHCs (unpaired two-sample *t*-test, $p = 0.03$) while the half-max voltage activation ($V_{1/2}$) of the Ca^{2+} currents remained unchanged (unpaired *t*-test, $p = 0.06$). **(B)** Kinetics of exocytosis were evoked by a voltage-steps from −80 to −10 mV with increasing duration from 5 to 80 ms. Note that brief stimulations below 25 ms, a time-frame addressing the release of the Readily Releasable Pool of vesicles, the exocytotic response (normalized to cell size) was similar in P30 and P360 IHCs ($p = 0.2$; two-way ANOVA). Longer stimulations, above 30 ms, which probed the activation of the secondarily releasable pool of vesicles, showed a significant increase in exocytosis (two-way ANOVA; $p = 2.3$ E−8), indicating that old IHCs were more likely to sustain high rates of vesicular release. **(C,D)** Representative examples of ΔC_m and I_{Ca} recordings from P30 and P365 IHCs during a 20 ms and a 100 ms voltage-step stimulation from −80 to −10 mV. The number of IHCs, indicated in graph, were obtained from five mice at P365 and six mice at P30. Asterisks indicate statistical difference with $^*p < 0.05$ and $^{***}p < 0.001$.

degeneration of the synaptic ribbon synapses (Fu et al., 2018; Rousset et al., 2020). BK ($K_{Ca1.1}$) channels are known to be highly sensitive to oxydative stress and their activity is a good indicator of intracellular ROS production (Sahoo et al., 2014; Hermann et al., 2015). Interestingly, a decrease in BK channel expression in IHCs has been associated to noise-related ROS and peroxysome

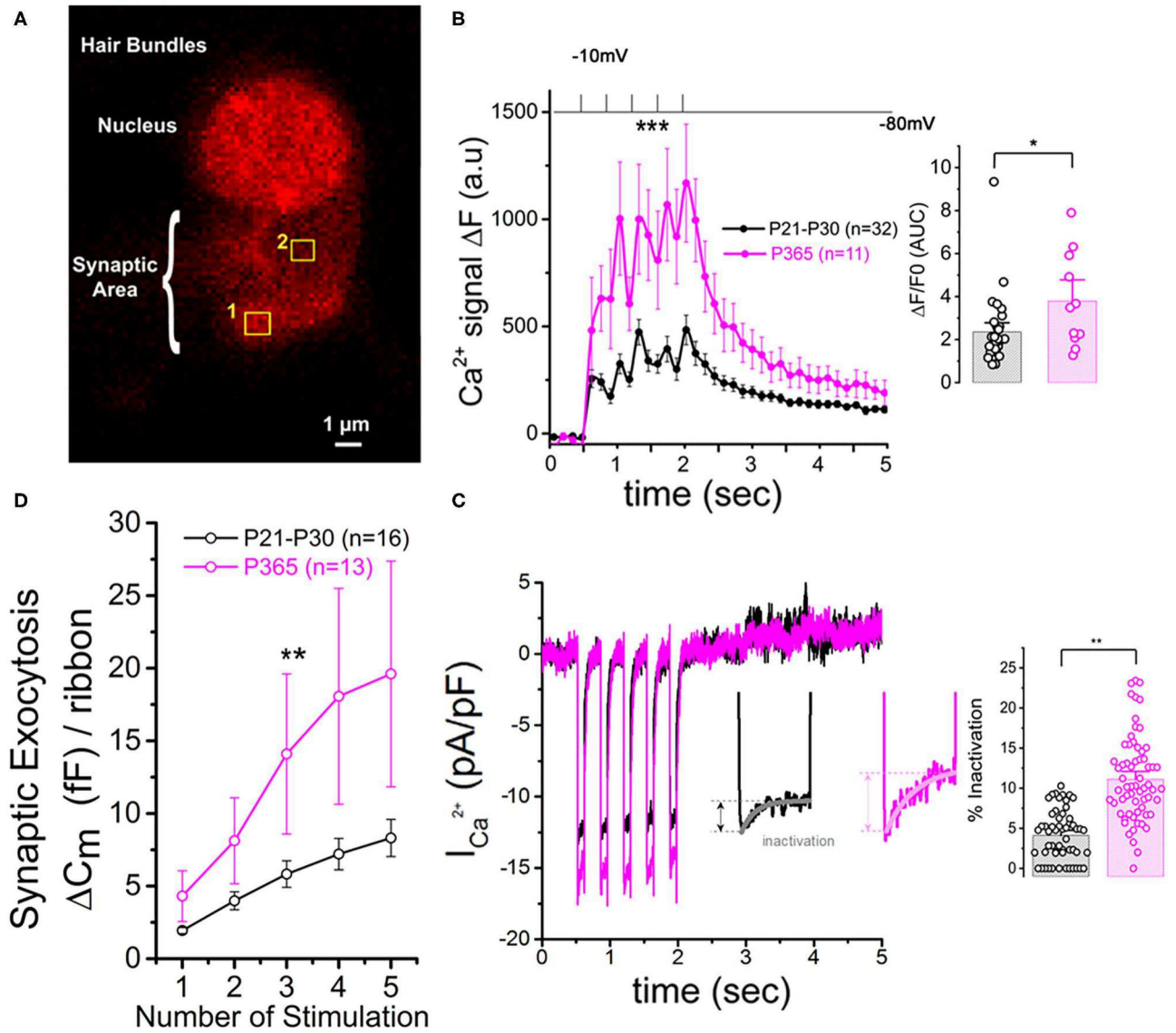

FIGURE 8 | Larger synaptic Ca^{2+} signaling and increased sustained exocytosis in aged IHCs. **(A)** Example of confocal Ca^{2+} imaging, using the intracellular fluorescent Ca^{2+} indicator Rhod2, in an IHC. The cell was voltage-clamped at −80 mV and stimulated by 5 (100 ms) consecutive voltage-step to −10 mV. The photograph shows two examples of square zones (1 μm^2) below the cell nucleus where voltage-induced calcium increase was measured. **(B)** Comparative mean amplitude of transient fluorescent hot spots showed higher Ca^{2+} responses at the presynaptic active zones of old P365 IHCs (pink) as compared to young mature P30 IHCs (black). Hair cells were depolarized by 5 five consecutive 100 ms depolarizing steps from −80 to −10 mV. The values n in the graph indicated the number of active zones analyzed for young (six IHCs from six mice) and old mice (five IHCs from five mice), respectively. The peak of the 5 calcium responses ($\Delta F = F–F_0$ with F_0 as the fluorescent base line value averaged 0.5 s before stimulation) were significantly larger in old IHCs [two-way ANOVA ($p = 8.8$ E−5)]. The histogram compared the overall fluorescent response $\Delta F/F_0$ occurring during the 5 stimulations (0.5–2.5 s). The integral of the Ca^{2+} response (Area Under the Curve, AUC) was significantly larger in old P365 IHCs (unpaired *t*-test, $p = 0.03$). **(C)** Comparative mean of calcium current recorded at the same time during the five stimulations shown in **(B)**. Note that the inactivating part of the calcium current is increased in P365 IHCs. Asterisk indicate statistical analysis with unpaired *t*-test. **(D)** The concomitant exocytosis was also measured during the five stimulations shown in **(B)**, Exocytosis was normalized for each IHC to their ribbon number or cell size; both normalizations giving similar results. The exocytotic responses were larger in old P365 IHCs. The asterisks indicated statistically significant difference with $p < 0.05$ (two-way ANOVA; $p = 0.0015$).

pathology (Delmaghani et al., 2015) but never yet described in IHCs during age-relate hearing loss. It is worth recalling that BK channels allows fast repolarization of IHCs and are essential for phase-locking of the auditory afferent neurons (Kros et al., 1998; Skinner et al., 2003; Oliver et al., 2006; Kurt et al., 2012). We here investigated, using immunofluorescent confocal microscopy, the comparative level expression of BK channels in IHCs from young (P30) and old P365 C57BL/6J mice. In young mature IHCs, BK channels are known to be organized in a dozen of clusters at the neck of the IHCs below the cuticular plate (Pyott et al., 2004; Hafidi et al., 2005). We used 3-D reconstructions from stacks of confocal images of immunostained organs of Corti (mid-cochlear

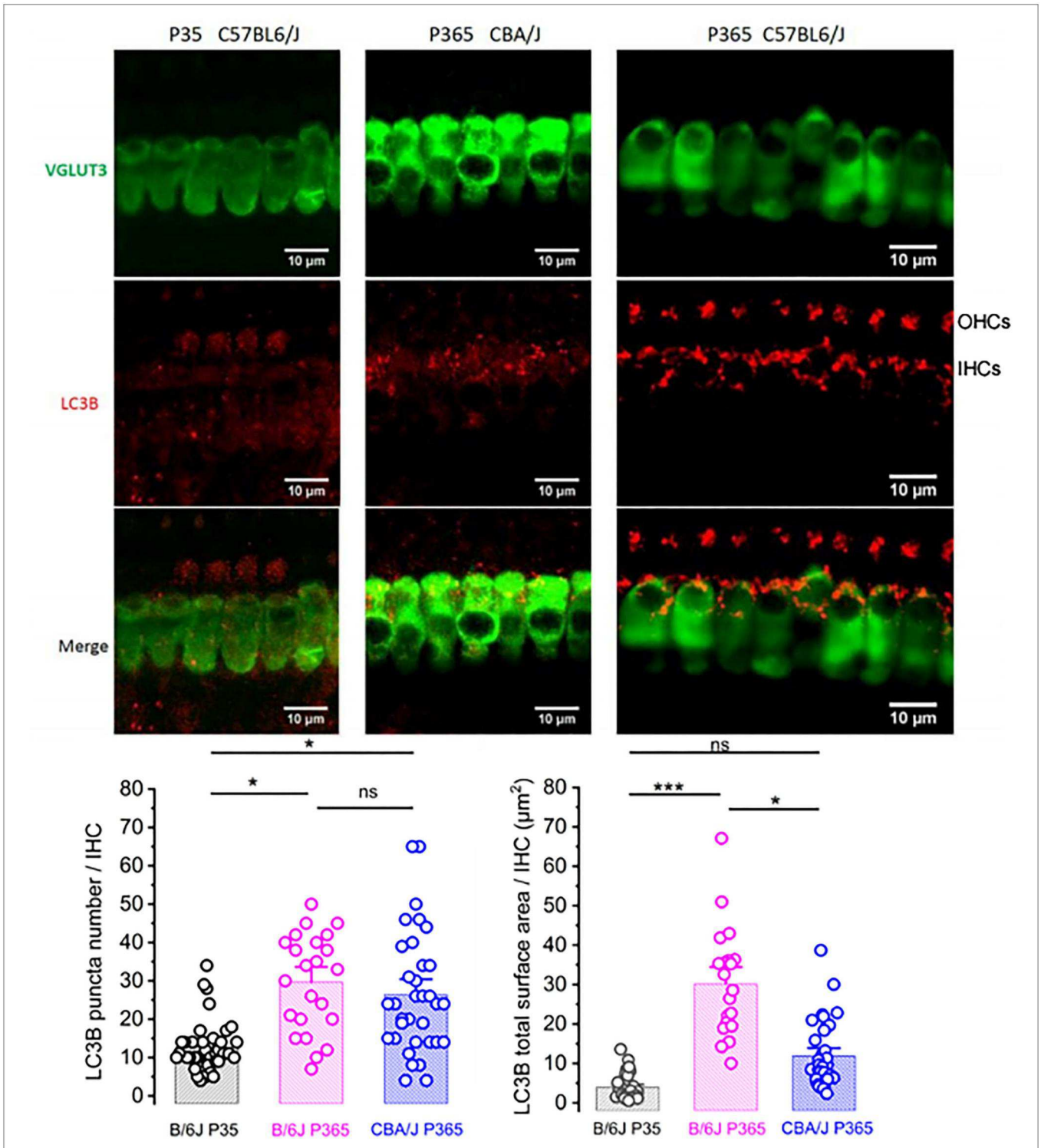

FIGURE 9 | LC3-positive structures are prominent in aging IHCs. Representative confocal immunofluorescence images showing LC3B staining in IHCs from young P30 C57BL/6J (left), old P365 CBA/J (middle), and old P365 C57BL/6J (right) mice. The histograms below show the quantification of the LC3B puncta average number and average mean surface area per IHC. Images were obtained from processing confocal stack images (22 of 0.3 µm thickness) using ImageJ quantification tool (3D-object counter). Quantification was performed from 23 to 38 IHCs for each condition in the mid-cochlea (encoding region 8–16 kHz; 3 mice). Asterisks indicate statistical significance $p < 0.05$ (unpaired *t*-test).

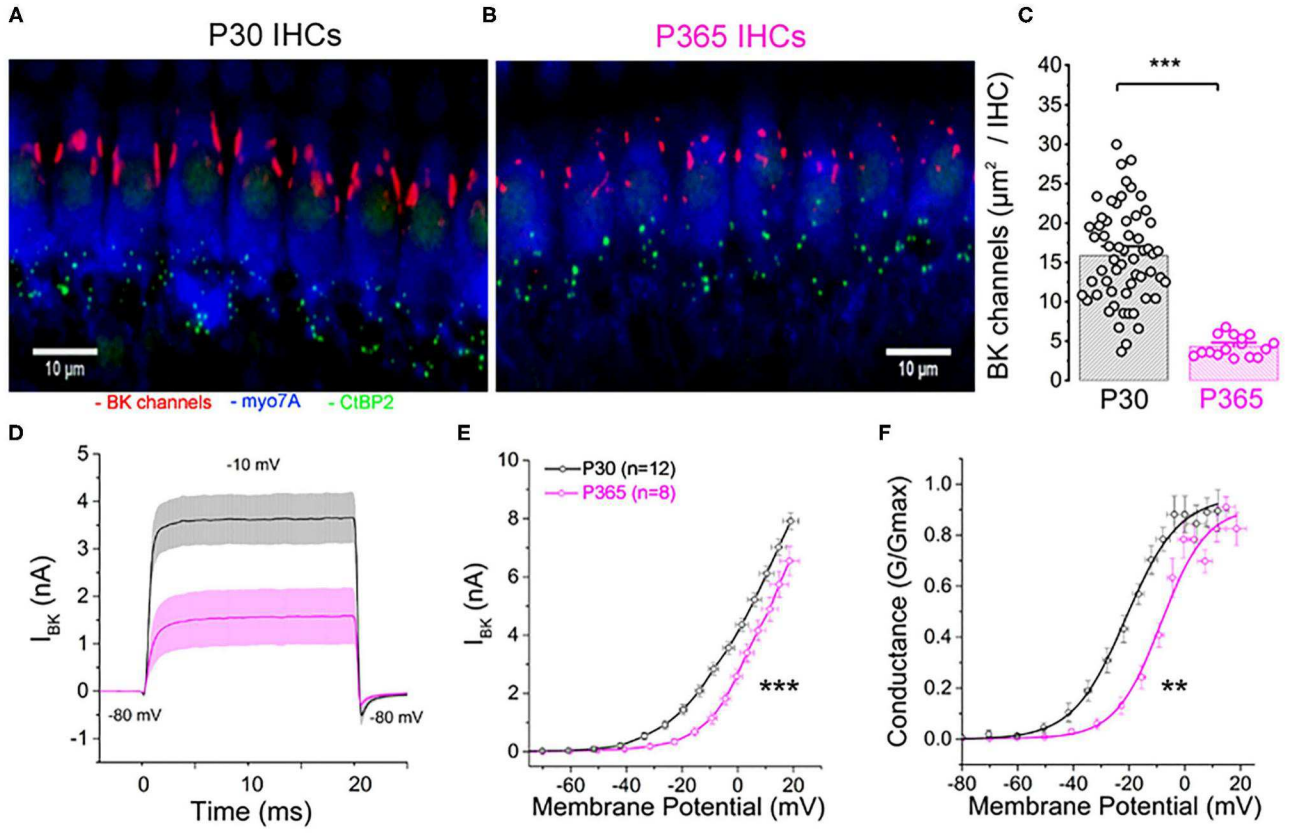

FIGURE 10 | Immunofluorescent confocal imaging of BK channels in aging IHCs. **(A)** Numerous large BK channel clusters (red) are localized extrasynaptically below the cuticular plate of IHCs in young mature P30 C57BL6/J mice. **(B)** Note the strong reduction in size of the BK channels clusters in IHCs of old P365 C57BL6/J mice. **(C)** Histogram comparing the total surface area covered by the BK channel clusters per IHC in the mid-turn cochlea (region encoding 8–16 kHz). The total number of IHCs analyzed was 58 and 16 from P30 ($n = 3$) and P365 ($n = 3$) mice, respectively. Asterisks indicate statistical significance with $p < 0.05$ ($p = 1.12$ E−7; unpaired *t*-test). **(D)** Comparative fast outward potassium currents (IKf), carried by BK channels, recorded from P30 (black, $n = 12$) and P360 (pink, $n = 8$) IHCs when using a brief depolarization step of 20 ms from −80 to −10 mV. **(E)** Comparative BK current–voltage curves ($n = 12$ and 8 IHCs, respectively, in P30 and P360 mice, from three mice at each age). Significantly different two-way ANOVA, $p = 2.7$ E−8. IKf was measured 2.5 ms after the onset of the voltage-step stimulation. **(F)** Comparative BK conductance fitted with a Boltzman function indicated a V1/2 of −20.5 ± 5.7 mV in P30 IHCs and of −13.7 ± 1.4 mV in P365 IHCs, respectively (unpaired *t*-test, $p = 0.009$). Note that voltage error across series resistance (Rs = 5 ± 2 MΩ) and leak current were compensated for each IHC. All values are expressed as means ± SEM.

frequency region 8–16 kHz) to determine the mean total surface area of the BK clusters per IHCs (**Figures 10A–C**). The results indicated that the membrane surface covered by BK channel clusters was reduced almost three-fold in P365 IHCs as compared to P30 IHCs.

To further characterize the changes in BK channel function with aging, we performed whole cell patch-clamp recordings in IHCs from P30 and P365 mice. Since BK currents in IHCs have the peculiar property to be extremely fast activating currents (also termed IK_f; Kros et al., 1998), these currents were recorded during brief 20 ms depolarizing steps and measured 2.5 ms after their onset (**Figures 10D–F**). BK currents in IHCs from young mature have also the particularity to activate at extremely negative membrane potential (near −60 mV) (Lingle et al., 2019). While the whole-cell conductance of BK channels from P365 IHCs was not significantly different from P30 IHCs (0.26 ± 0.04 nS and 0.23 ±.0.03 nS, respectively), their voltage-dependant activation showed a large positive shift of 7 mV (**Figure 10F**). Interestingly, the decrease in size of the BK patches and the positive voltage-activation shift in old IHCs somewhat resembled the phenotype observed in mice KO for LRRC52, a γ BK regulatory subunits (Lang et al., 2019; Lingle et al., 2019), suggesting that the BK complex formed with this γ subunit could be one the target of the degenerative oxydative process in aging C57BL56/J mice IHCs.

DISCUSSION

Larger Synaptic Ribbons Associated With Increased Ca^{2+} Signals

Ribbons are presynaptic organelles tethering glutamate-filled vesicles at the hair cell active zone (AZ, **Figure 11**). These intracellular structures, composed of the protein RIBEYE, are

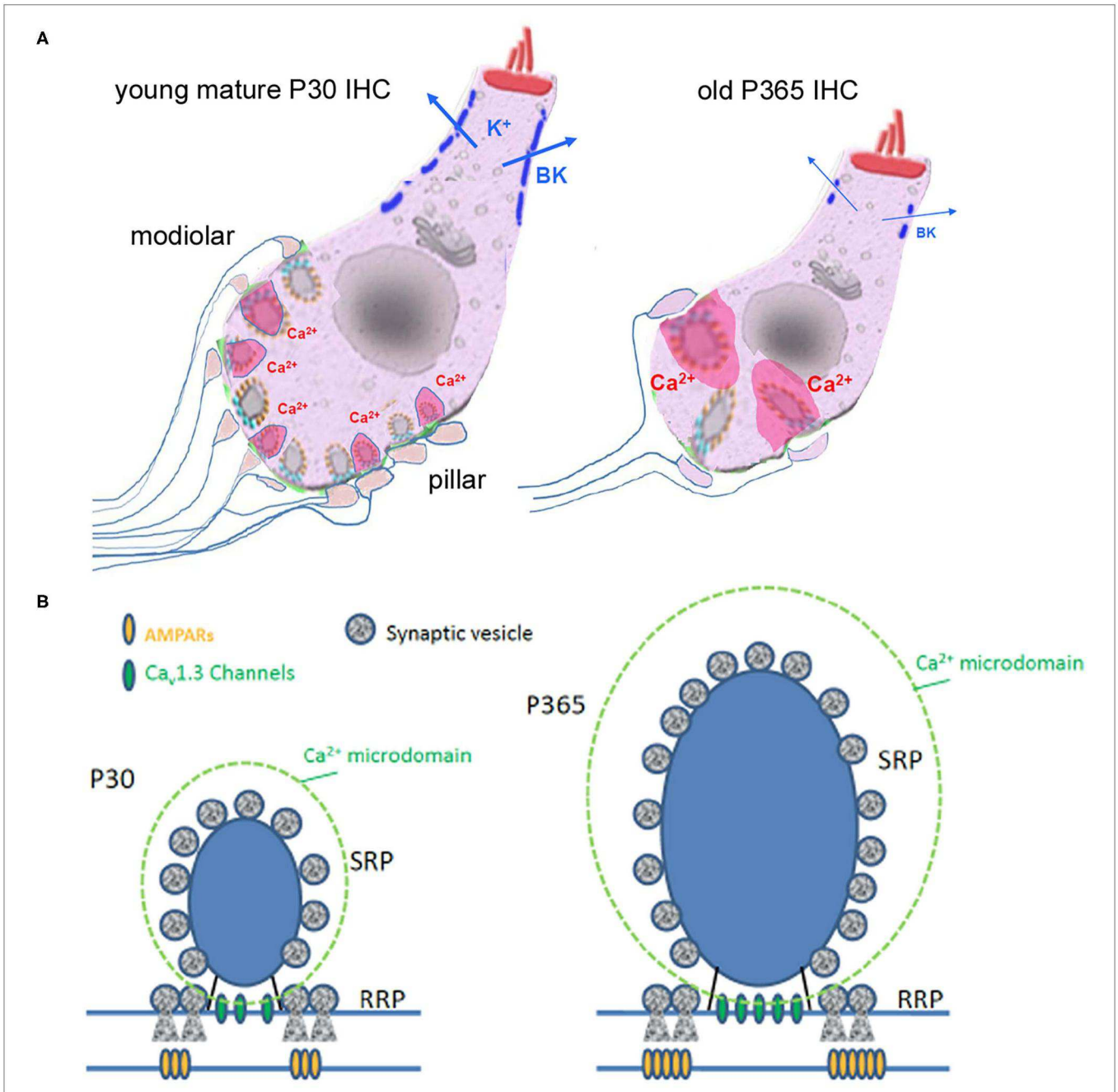

FIGURE 11 | Synaptic IHC degeneration was associated with a strong potentiation of the remaining ribbon synapses in aging C57BL/6J mice. **(A)** Age-related hearing loss in P360 mice was associated with IHC shrinkage (cell size reduction), an important loss of afferent ribbon synapses (>50%), a drastic enlargement of the surviving synaptic ribbons (both at pillar and modiolar side), an increase in Ca^{2+} signaling (larger Ca^{2+} microdomain amplitude as indicated by the larger pink domains around the ribbons) and a large decrease in the fast-repolarizing BK channel clusters (blue bars). **(B)** Hypothetical view of a young and old IHC ribbon synapse.

anchored by the scaffold protein bassoon to the AZ plasma membrane, adjacent to Ca^{2+} $Ca_V1.3$ channels (Brandt et al., 2003; Graydon et al., 2011; Jing et al., 2013; Vincent et al., 2017). Ribbons are essential for high rate of transmitter release and for high temporal precision of neuronal encoding of sound at the auditory afferent nerve fibers (Becker et al., 2018; Jean et al., 2018). Each auditory IHC have 10 to 20 synaptic ribbons depending of their cochlear frequency location (Meyer et al., 2009). Ribbons are heterogeneous in size and each ribbon makes a single synaptic contact with one afferent nerve fiber. Remarkably, fibers associated to large ribbons display low spontaneous rate and high-threshold have the tendency to be distributed at the modiolar side of IHCs (Liberman et al., 2011). Nerve fibers associated

with smaller ribbons display high spontaneous rate and low-threshold activation, are mainly located toward the pillar side of IHCs. Interestingly, we found here that old C57BL6/J IHCs preferentially loose modiolar ribbons (known to be associated with high threshold low spontaneous fibers), therefore mimicking what is happening during noise-induced hearing loss (Fernandez et al., 2015; Liberman and Kujawa, 2017; Hickman et al., 2020). Heterogeneity in the voltage-dependence of Ca^{2+} channels and release site coupling has been recently proposed to contribute to the firing fiber specificity, with modiolar ribbons being activated at more negative potentials (Ozcete and Moser, 2021). In our study, we did not find evidence for a voltage-shift in the voltage-dependence of Ca^{2+} channels with aging but we did observe an increase in the density of Ca^{2+} currents. The increase in Ca^{2+} entry was further confirmed by the stronger time-inactivation of the Ca^{2+} currents (Grant and Fuchs, 2008; Vincent et al., 2017).

One of the most striking observations was that the IHC synaptic ribbons underwent a nearly three-fold increase in size with aging, confirming a certain degree of plasticity of these synaptic structures. The enlargement of the presynaptic ribbons was in good agreement with a previous ultrastructural study in aging C57BL/6J mice by Stamataki et al. (2006) and the recent study of Jeng et al. (2020). Interestingly, the size of the young mature IHC synaptic ribbons is known to correlate positively with the AZ Ca^{2+} microdomain amplitude, as well as the number and gating of the $Ca_v1.3$ Ca^{2+} channels (Frank et al., 2009; Neef et al., 2018). Also, hair cells of transgenic zebrafish with enlarged ribbons display larger ribbon-localized Ca^{2+} currents (Sheets et al., 2017). In agreement with these previous studies, we found here, in IHCs from aging C57BL/6J mice, that the remaining larger ribbons were associated with larger Ca^{2+} microdomain amplitude, and larger density of calcium currents, reinforcing the idea that Ca^{2+} ions regulate the size of the synaptic ribbons. In this context, It is worth recalling that mitochondrial-Ca^{2+} uptake has been proposed to lower cellular NAD^+/NADH redox and regulates ribbon size, possibly by acting through the NAD^+ binding site of the B domain of RIBEYE (Wong et al., 2019). *In vitro* work has shown that NAD^+ and NADH can promote interactions between ribeye domains (Magupalli et al., 2008) and the size of the ribbons would be then sensitive to the subcellular synaptic NAD^+/NADH redox level (Wong et al., 2019), suggesting that the increase in size of the IHCs ribbons from aged C57BL/6J mice also results from NAD^+/NADH homeostasis disruption.

Increased Capacity for Sustained IHC Synaptic Exocytosis: Implication for the Discharge Pattern of the Auditory Nerve Firing

As a consequence of larger Ca^{2+} microdomains, we found that IHCs from old C57BL/6J mice had larger and more sustained exocytotic responses. These larger release responses could also well be explained by a higher synaptic vesicle density at the active zone of the IHC ribbon synapses as suggested by the EM study of Stamataki et al. (2006). Surprisingly, the recent study of Jeng et al. (2020), which did not perform Ca^{2+} imaging, concluded that the size and kinetics of Ca^{2+}-dependent exocytosis in IHCs were unaffected in aging mice but this study did not normalize the IHC exocytotic responses to their cell size or to their ribbon synapse number, and therefore may have overlooked the differential phenotype.

What would be the consequences on the discharge pattern of the remaining afferent fibers of a more sustained release capacity in old ribbon synapses? Fast adaptation in the discharge rate of the afferent auditory nerve fibers is thought to be one of their essential property for emphasizing the timing information of sound stimuli. This adaption takes the form of a fast increase in spike rate at stimulus onset that rapidly declines in a double exponential decay to a lower steady-state rate after a few tens of milliseconds (Taberner and Liberman, 2005). The origin of this fast adaptation has been proposed to arise first from H^+ release block of Ca^{2+} channels and second to rapid depletion of synaptic vesicle release (Vincent et al., 2017). We predict that the increased capacity to sustain SRP exocytosis in old IHCs with larger ribbons would have the tendency to decrease the level of firing adaptation of the auditory fibers and therefore explain the altered recovery from short-term adaptation in old C57BL/6J mice (Walton et al., 1995).

Furthermore, we confirmed here the hyperacusis-like effect of the startle responses in old C57BL/6J mice (Ison et al., 2007). This increased response at low sound intensity could be explained by a release potentiation at the IHC ribbon synapses due to the presynaptic higher Ca^{2+} channel density associated with a larger ribbon coupled with a larger vesicular SRP, and increased expression of post-synaptic AMPARs. All these features would make the auditory ribbon synapses hypersensitive and underlie the hyperacusis-like reflex in old C57BL/6J mice.

IHC Shrinkage and Disruption of BK Channel Clusters

Another novel observation of our study was the drastic reduction in cell size of IHCs from aging C57BL/6J mice. Interestingly, tuberous sclerosis rapamycin-sensitive complex 1 (mTORC1) has been shown to be overactivated and promote oxidative damages to synapse ribbon loss in aging C57BL/6 mice (Fu et al., 2018). We found that aged P365 IHCs had an increase expression of the autophagy marker LC3B. The activation of the mTOR pathway with aging could therefore trigger the cell size reduction of IHCs, by activating the autophagy pathway, as proposed in many other cell types (Fingar et al., 2002; Fumarola et al., 2005). In addition, our study described another novel remarkable feature of aging IHCs, a drastic disruption of the BK channel clusters, suggesting that these potassium channels are also a good indicator of the redox state and autophagy in IHCs. The expression and distribution of BK channels could be regulated through the rapamycin insensitive mTOR complex 2 (mTORC2) as shown in the kidney glomerulus podocytes (Wang et al., 2019). Interestingly, the disruption of the BK channel clusters in aging IHCs was associated with a large positive

shift in their voltage-activation curve, suggesting that the fast-repolarizing property mediated by BK channels which likely contributes to decrease transmitter release (Skinner et al., 2003), would be largely hampered during sound stimuli in aging mice, an additional factor that may also contribute to hyperacusis.

A Role of Cadherin-23 in Ribbon Synapse Maintenance and Function?

In the CNS, cadherins are considered as essential Ca^{2+}-binding transmembrane cell adhesion molecules that regulate synapse formation and function (Bamji, 2005). In the murine retina, cadherin-23 is highly abundant at the ribbon synapse of rod photoreceptor cells (Bolz et al., 2002). The presence of cadherin-23 at IHC ribbon synapses remain unknown. The results observed by our study and others in C57BL/6J mice suggest that this molecule plays a crucial role in hair cell ribbon synapse maintenance and function. It is possible that the *Cdh23*^{753A} mutation weakens the mechanical organization of the hair cell synaptic contacts leading with aging to their progressive disorganization. The exacerbated release of glutamate in aging ribbon synapses could then lead to excitotoxicity and progressive synapse degeneration.

CONCLUSIONS

In conclusion, our study unraveled several novel functional and structural features of aging in IHC ribbon synapses from C57BL/6J mice (**Figure 11**): (1) a large reduction in IHC cell size, (2) a drastic enlargement of the presynaptic ribbons and postsynaptic AMPAR clusters, (3) an increased presynaptic Ca^{2+} signaling associated with a stronger sustained exocytotic response, and (4) a disruption of BK channel clusters and a drastic shift in their voltage-dependence decreasing their potential negative feedback on neurotransmission. Overall, these results suggested that aging IHCs ribbon synapses can undergo important structural and functional plasticity that led to synaptic potentiation that could explain the paradoxical hyperacusis-like exaggeration of the acoustic startle reflex observed in C57BL/6J mice.

MATERIALS AND METHODS

Mice

Inbred C57BL/6J mice of either sex (Souris JAX™ C57BL/6J, Jackson Laboratory) which are homozygous for the recessive cadherin-23 mutation *Cdh23*^{753A} (also known as Ah1) were used in the present study. Hearing thresholds and IHC ribbon counts in mice of either sex were performed at postnatal ages: P15, P30, P60, P180, and P365. CBA/J mice of either sex (from Charles River) were also tested as controls at P50, P250, and P365. Animal care and all procedures were approved by the institutional care and use committee of the University of Bordeaux and the French Ministry of Agriculture (agreement C33-063-075).

Assessment of Hearing Thresholds (ABRs)

To record ABRs (Auditory Brainstem Responses, which represent the sound-evoked synchronous firing of the auditory cochlear nerve fibers and the activation of the subsequent central auditory relays), mice were anesthetized with intraperitoneal injection of xylazine (6 mg/ml, Rompun Bayer) and ketamine (80 mg/ml, Virbac) mixture diluted in physiological saline. The mouse was placed in a closed acoustic chamber and its body temperature was kept constant at 37°C during ABRs recording. For sound stimulus generation and data acquisition, we used a TDT RZ6/BioSigRZ system (Tucker-Davis Technologies). Click-based ABR signals were averaged after the presentation of a series of 512 stimulations. Thresholds were defined as the lowest stimulus for recognizable wave-I and II. The amplitude of ABR wave-I was estimated by measuring the voltage difference between the positive (P1) and negative (N1) peak of wave-I. Sound intensities of 10–90 dB SPL in 10 dB step, were tested.

Distortion product otoacoustic emissions (DPOAEs), which originate from the electromechanical activity of the outer hair cells (OHCs), were tested by using two simultaneous continuous pure tones with frequency ratio of 1.2 ($f1 = 12.73$ kHz and $f2 = 15.26$ kHz). DPOAEs were collected with the TDT RZ6/BioSigRZ system designed to measure the level of the "cubic difference tone" $2f1–f2$.

Acoustic Startle Reflex Measurements

Testing was conducted in four acoustic startle chambers for mice (SR-LAB, San Diego Instruments, San Diego, CA). Each chamber consisted of a nonrestrictive cylindrical enclosure attached horizontally on a mobile platform, which was in turn resting on a solid base inside a sound-attenuated isolation cubicle. A high-frequency loudspeaker mounted directly above the animal enclosure inside each cubicle produced a continuous background noise of 65 dBA and various acoustic stimuli in the form of white noise. Mechanical vibrations caused by the startle response of the mouse were converted into analog signals by a piezoelectric accelerometer attached to the platform. A total of 130 readings were taken at 0.5-ms intervals (i.e., spanning across 65 ms), starting at the onset of the startle stimulus. The average amplitude over the 65 ms was used to determine the stimulus reactivity. The sensitivity of the stabilimeter was routinely calibrated to ensure consistency between chambers and across sessions.

Acoustic startle reflex was assessed during a session lasting for ∼30 min, in which the mice were presented with a series of discrete pulse-alone trials of different intensities and durations. Ten pulse intensities were used: 69, 73, 77, 81, 85, 90, 95, 100, 110, and 120 dBA lasting for either 20 or 40 ms (background noise level: 65 dBA). A session began when the animals were placed into the Plexiglas enclosure. The mice were acclimatized to the apparatus for 2 min before the first trial began. The first six trials consisted of six pulse-alone trials of 120 dBA, comprising three trials of each duration. These trials served to stabilize the animals' startle response, and were analyzed separately. Subsequently, the animals were presented with five blocks of discrete test trials. Each block consisted of 20 pulse alone trials, one for each intensity and duration. All trials were presented in a pseudorandom order with an inter-trials interval of 14 s.

Tissue Preparation and Immunocytochemistry

Mice were deeply anesthetized with isofluorane (Vetflurane, Virbac). The ramps of the cochlear apparatus were dissected and prepared as previously described by Vincent et al. (2014). Inner ears (cochleae) were fixed by incubation in 4% paraformaldehyde in phosphate-buffered saline (PBS), pH 7.4, at 4°C overnight and washed with cold phosphate buffered saline (PBS). They were then incubated for 2 days in PBS solution containing 10% EDTA pH 7.4 at 4°C. The middle part of the organ of Corti (area encoding between 8 and 16 kHz) was then dissected and the tectorial membrane removed. The tissue was first incubated with PBS containing 30% normal horse serum and triton X100 0.5 % for 1 h at room temperature. Synaptic ribbons were labeled with anti-CtBP2 (1/200 Goat polyclonal, Santa Cruz, USA; cat # SC-5966 or 1/200 Mouse IgG1 monoclonal antibody BD Biosciences, cat # 612044). Otoferlin was labeled with a mouse monoclonal antibody (1/200 AbCam, cat # ab53233). Autophagy was detected by labeling LC3B protein with anti-Rabbit monoclonal antibody [1/200 LC3B(D11) XP, Cell Signaling Technology, cat # 3868]. BK channels were labeled with a Rabbit polyclonal antibody (1/200, Alomone, Israel, cat #APC-021). Explants of Organ of Corti were incubated overnight at 4°C with primary antibodies. The following fluorescent secondary antibodies 1/500 were then used: anti-Goat Donkey polyclonal Fluoprobes 547H (Interchim, cat# FP-SB2110), anti-Mouse Donkey polyclonal Fluoprobes 647H (Interchim, cat# FP-SC4110), anti-Mouse Donkey polyclonal Alexa Fluor 488 (AbCam, cat# ab150109), anti-Mouse Goat polyclonal Alexa Fluor 546 (Molecular Probes, cat# A-11003), anti-Mouse Goat polyclonal Alexa Fluor 488 (Molecular Probes, cat# A-10680), anti-Rabbit Donkey polyclonal Fluoprobes 594 (Interchim, cat# FP-SD5110). Actin-F was also used to visualize hair cells (1/100, Phalloidin Fluoprobe 405, Interchim, Montlucon, France; cat # FP-CA9870). For Image Acquisition, organ of Corti samples were analyzed using a confocal laser scanning microscope Leica SP8 with a 63X oil immersion objective (NA = 1.4) and white light laser (470–670 nm) (Bordeaux Imaging Center). Phalloidin was imaged by using a diode laser at 405 nm also mounted on the microscope. For complete 3D-stack reconstruction of IHCs, 25–30 images (0.3 μm thickness) were acquired as previously described (Vincent et al., 2014). Ribbon volumes were calculated using the 3D-Objects Counter Plugin of ImageJ. Image resolution was 0.038 μm/pixel. As previously described by Hickman et al. (2020) and Jeng et al. (2020), the *x,y,z* coordinates of ribbons in each z-stack were transformed into a coordinate system based on the modiolar-pillar polarity of the IHCs. We determined the pillar vs. modiolar distribution of the synaptic ribbons by using a *k*-means clustering method in the *z*-stack position of each ribbon, with arbitrarily choosing the number of clusters as 2 (OriginPro 9.1software, OriginLab, Northampton, USA). From these two clusters, we determine arbitrarily the border between the modiolar and pillar side in each IHC by taking the half-distance between the two nearest ribbon of each cluster.

High Resolution Imaging of Synaptic Ribbons With Confocal STED Microscopy

For high-resolution imaging of IHC ribbons, we used a Leica DMI6000 TCS SP8 STED microscope with 93X glycerol immersion objective (NA 1.3) (Bordeaux Imaging Center). Mouse sensory organs were fixed and incubated with primary anti CtBP2 (1/100) antibodies in conditions similar to those described above for confocal microscopy. Secondary antibodies Goat anti- IgG1 Mouse polyclonal Alexa Fluor 647 (Jackson, cat# 115-605-205) were used to label CtBP2 primary antibodies. The pulsed STED depletion laser (pulsed laser IR, Spectra Physics Mai Tai) was set at 775 nm. Stack images were acquired with the following parameters: scan rate 200 Hz, 775 nm depletion laser power between 8 and 15%, scans frames accumulated per *X–Y* section 8 times, *z*-step size 0.25 μm, number of plans between 8 and 10, pixel size 20 nm giving an *X–Y* image size of 21 × 5 μm (1,024 × 256 pixels).

Counting Spiral Ganglion Neurons

The afferent nerve fibers of the auditory nerve were fluorescently labeled using a retrograde track tracing technique with dextran amines (Fritzsch et al., 2016). Cochleae were extracted from temporal bone of freshly euthanized mice and rapidly immerged intact into ice-cold artificial perilymph (NaCl 135; KCl 5.8; $CaCl_2$ 1.3; $MgCl_2$ 0.9; NaH_2PO_4 0.7; Glucose 5.6; Na pyruvate 2; HEPES 10, pH 7.4, 305 mOsm). A small crystal of tetramethyl rhodamine dextran amines 3000 (Life technologies, NY) was placed for 15–20 min at the edge of the auditory nerve coming out at the internal auditory canal of the intact cochlea and rinsed with artificial perilymph. The intracochlear sensory tissues were then fixed by gentle perfusion of a 4% PFA solution for 30 min and rinsed with PBS. They were then decalcified for 2 days in PBS solution containing 10% EDTA pH 7.4 at 4°C. The cochleae were then sliced with a razor blade along the longitudinal cochlear axes and the slices were then mounted on a glass-slide for fluorescent confocal microscopy observation. The quantification of the spiral ganglion neurons per surface area of the neural ganglion were made in the middle part of the cochlea in a region encoding 8–16 kHz, by using the 3D object counter application of ImageJ software.

Ca^{2+} Currents and Whole-Cell Membrane Capacitance Measurement in IHCs

Measurements of resting membrane capacitance of IHCs were performed at P30 and P365 mice in the 20–40% normalized distance from the apex, an area coding for frequencies ranging from 8 to 16 kHz, by using an EPC10 amplifier controlled by Patchmaster pulse software (HEKA Elektronik, Germany), as previously described in detail (Vincent et al., 2014, 2015). The organ of Corti was incubated in an extracellular perilymph-like solution containing NaCl 135; KCl 5.8; $CaCl_2$ 5; $MgCl_2$ 0.9; NaH_2PO_4 0.7; Glucose 5.6; Na pyruvate 2; HEPES 10, pH 7.4, 305 mOsm. This extracellular solution was complemented with 0.25 μM of apamin (Latoxan; cat # L8407) and 1 μM of XE-991 (Tocris Bioscience; cat # 2000) to block SK channels and KCNQ4 channels, respectively. The external Ca^{2+} concentration was

increased from 1.3 to 5 mM to enhance the amplitude of Ca^{2+} currents to levels nearby body temperature. All experiments were performed at room temperature (22–24°C).

Patch pipettes were pulled with a micropipette Puller P-97 Flaming/Brown (Sutter Instrument, Novato, CA, USA) and fire-polished with a Micro forge MF-830 (Narishige, Japan) to obtain a resistance range from 3 to 5 MΩ. Patch pipettes were filled with a cesium-based intracellular solution containing (in mM): CsCl 145; $MgCl_2$ 1; HEPES 5; EGTA 1; TEA 20, ATP 2, GTP 0.3, pH 7.2, 300 mOsm. Measurements of the resting membrane capacitance (cell size) of IHCs were obtained in whole-cell voltage-clamp configuration at −70 mV and after 2 min equilibrium of the internal patch-pipette recording solution with the IHC cytosol.

BK Currents

Whole-cell recordings of BK currents were recorded in P30 and P365 IHCs from *ex-vivo* whole-mount preparation (Skinner et al., 2003) as described above for Ca^{2+} currents. Recording pipettes were filled with a KCl-based intracellular solution containing in mM: 158 KCl, 2 $MgCl_2$, 1.1 EGTA, 5 HEPES, and 3.05 KOH, pH 7.20.

Intracellular Ca^{2+} Imaging

Fluorescent Ca^{2+} signals were measured with a C2 confocal system and NIS-element imaging software (Nikon) coupled to the FN1 upright microscope as previously described (Vincent et al., 2014, 2017). For Ca^{2+} imaging in IHCs, in which membrane capacitance and Ca^{2+} currents were simultaneously recorded, patch pipettes were filled with the same cesium-base solution described above supplemented with 50 μM of the red fluorescent indicator Rhod2 (R14220, Invitrogen™, Thermofisher Scientific). The Ca^{2+} dye was excited with a 543 nm Helium Neon Laser system (Melles Griot 05-LGR-193-381) coupled to a Nikon C2-confocal FN1- upright microscope and emission fluorescence at 552–617 nm was recorded at 18 images/s (resolution 0.4 μm/pixel). Using the Nikon imaging system NIS-Elements, IHC active zones were first individually identified by their fluorescent transient responses, following a 100 ms stimulation (from −80 to −10 mV) and then the focal plane (with pinhole 1.1 μm) was adjusted in the z dimension to give the brightest value for each active zone. Then, after a 1 min rest, each active zone was stimulated by a train of five consecutive 100 ms stimulation, each separated by 250 ms. Fluorescence emission in each active zone was subsequently measured with ImageJ software by drawing a region of interest of 1 μm^2 at the synaptic zone (**Figure 8A**). Emission fluorescent signals were analyzed and normalized by the ratio $\Delta F/F_0$ ratio, where F_0 was the fluorescence level before stimulation.

Statistical Analysis

Results were analyzed with OriginPro 9.1software (OriginLab, Northampton, USA). Data were tested for normal distribution using the Shapiro–Wilk normality test, and parametric or nonparametric tests were applied accordingly. For statistical analyses with two data sets, two-tailed unpaired *t*-tests or two-sided Mann–Whitney tests were used. For comparisons of more than two data sets, one-way ANOVA or two-way ANOVA followed by Tukey multiple comparison test were used when data was normally distributed. If a data set was not normally distributed Kruskal–Wallis tests followed by Dunn multiple comparison tests, respectively, was used. When more than two data sets were compared and significant differences were found, reported *p*-values correspond to the *post-hoc* multiple comparison test. Values of $p < 0.05$ were considered significant. Results are expressed as mean ± SEM.

DATA AVAILABILITY STATEMENT

The raw data supporting the conclusions of this article will be made available by the authors, without undue reservation.

ETHICS STATEMENT

The animal study was reviewed and approved by Ethic Committee University of Bordeaux CEEA50.

AUTHOR CONTRIBUTIONS

DD designed research and wrote the paper. SB, TP, YB, and DD performed research and analyzed the data. SP performed the Acoustic Startle Experiments. All authors contributed to the article and approved the submitted version.

FUNDING

This work was supported by a grant from the Fondation Pour l'Audition to DD (Starting Grant FPA IDA09 2019-2024, CLINICAL TRANSLA–010703E), and from the French Society of Audioprosthesis professionals, Entendre SAS (Saint Cyr l'Ecole 78210 France). Part of the content of the manuscript has previously appeared as a preprint online at bioRxiv https://doi.org/10.1101/2020.05.15.097550.

REFERENCES

Bamji, S. X. (2005). Cadherins: actin with the cytoskeleton to form synapses. *Neuron* 47, 175–8. doi: 10.1016/j.neuron.2005.06.024

Bartolome, M. V., del, C. E., Lopez, L. M., Carricondo, F., Poch-Broto, J., and Gil-Loyzaga, P. (2002). Effects of aging on C57BL/6J mice: an electrophysiological and morphological study. *Adv. Otorhinolaryngol.* 59, 106–111. doi: 10.1159/000059247

Becker, L., Schnee, M. E., Niwa, M., Sun, W., Maxeiner, S., Talaei, S., et al. (2018). The presynaptic ribbon maintains vesicle populations at the hair cell afferent fiber synapse. *Elife* 7:e30241. doi: 10.7554/eLife.30241

Beurg, M., Michalski, N., Safieddine, S., Bouleau, Y., Schneggenburger, R., Chapman, E. R., et al. (2010). Control of exocytosis by synaptotagmins and otoferlin in auditory hair cells. *J. Neurosci.* 30, 13281–13290. doi: 10.1523/JNEUROSCI.2528-10.2010

Bolz, H., Reiners, J., Wolfrum, U., and Gal, A. (2002). "The role of cadherins in Ca^{2+}-mediated cell adhesion and inherited photoreceptor degeneration," in

Photoreceptors and Calcium, Vol. 514, Advances in Experimental Medicine and Biology, eds. W. Baehr and K. Palczewski (Boston, MA: Springer), 399–410.

Brandt, A., Striessnig, J., and Moser, T. (2003). CaV1.3 channels are essential for development and presynaptic activity of cochlear inner hair cells. *J. Neurosci.* 23, 10832–10840. doi: 10.1523/JNEUROSCI.23-34-10832.2003

Campbell, L. W., Hao, S. Y., Thibault, O., Blalock, E. M., and Landfield, P. W. (1996). Aging changes in voltage-gated calcium currents in hippocampal CA1 neurons. *J. Neurosci.* 16, 6286–6295. doi: 10.1523/JNEUROSCI.16-19-06286.1996

Defourny, J., Aghaie, A., Perfettini, I., Avan, P., Delmaghani, S., and Petit, C. (2019). Pejvakin-mediated pexophagy protects auditory hair cells against noise-induced damage. *Proc. Natl. Acad. Sci. U. S. A.* 116, 8010–8017. doi: 10.1073/pnas.1821844116

Del Nido, P. J., Glynn, P., Buenaventura, P., Salama, G., and Koretsky, A. P. (1998). Fluorescence measurement of calcium transients in perfused rabbit heart using rhod 2. *Am. J. Physiol.* 274, H728–H741. doi: 10.1152/ajpheart.1998.274.2.H728

Delmaghani, S., Defourny, J., Aghaie, A., Beurg, M., Dulon, D., Thelen, N., et al. (2015). Hypervulnerability to sound exposure through impaired adaptive proliferation of peroxisomes. *Cell* 163, 894–906. doi: 10.1016/j.cell.2015.10.023

Fernandez, K. A., Jeffers, P. W., Lall, K., Liberman, M. C., and Kujawa, S. G. (2015). Aging after noise exposure: acceleration of cochlear synaptopathy in "recovered" ears. *J. Neurosci.* 35, 7509–7520. doi: 10.1523/JNEUROSCI.5138-14.2015

Fingar, D. C., Salama, S., Tsou, C., Harlow, E., and Blenis, J. (2002). Mammalian cell size is controlled by mTOR and its downstream targets S6K1 and 4EBP1/eIF4E. *Genes Dev.* 16, 1472–1487. doi: 10.1101/gad.995802

Frank, T., Khimich, D., Neef, A., and Moser, T. (2009). Mechanisms contributing to synaptic Ca2+ signals and their heterogeneity in hair cells. *Proc. Natl. Acad. Sci. U. S. A.* 106, 4483–4488. doi: 10.1073/pnas.0813213106

Fritzsch, B., Duncan, J. S., Kersigo, J., Gray, B., and Elliott, K. L. (2016). Neuroanatomical tracing techniques in the ear: history, state of the art, and future developments. *Methods Mol. Biol.* 1427, 243–262. doi: 10.1007/978-1-4939-3615-1_14

Fu, X., Sun, X., Zhang, L., Jin, Y., Chai, R., Yang, L., et al. (2018). Tuberous sclerosis complex-mediated mTORC1 overactivation promotes age-related hearing loss. *J. Clin. Invest.* 128, 4938–4955. doi: 10.1172/JCI98058

Fumarola, C., La Monica, S., Alfieri, R. R., Borra, E., and Guidotti, G. G. (2005). Cell size reduction induced by inhibition of the mTOR/S6K-signaling pathway protects Jurkat cells from apoptosis. *Cell Death Differ.* 12, 1344–1357. doi: 10.1038/sj.cdd.4401660

Grant, L., and Fuchs, P. (2008). Calcium- and calmodulin-dependent inactivation of calcium channels in inner hair cells of the rat cochlea. *J. Neurophysiol.* 99, 2183–2193. doi: 10.1152/jn.01174.2007

Graydon, C. W., Cho, S., Li, G. L., Kachar, B., and von Gersdorff, H. (2011). Sharp Ca(2)(+) nanodomains beneath the ribbon promote highly synchronous multivesicular release at hair cell synapses. *J. Neurosci.* 31, 16637–16650. doi: 10.1523/JNEUROSCI.1866-11.2011

Hafidi, A., Beurg, M., and Dulon, D. (2005). Localization and developmental expression of BK channels in mammalian cochlear hair cells. *Neuroscience* 130, 475–484. doi: 10.1016/j.neuroscience.2004.09.038

Hasson, T., Heintzelman, M. B., Santos-Sacchi, J., Corey, D. P., and Mooseker, M. S. (1995). Expression in cochlea and retina of myosin VIIa, the gene product defective in Usher syndrome type 1B. *Proc. Natl. Acad. Sci. U. S. A.* 92, 9815–9819. doi: 10.1073/pnas.92.21.9815

Henry, K. R. (2002). Sex- and age-related elevation of cochlear nerve envelope response (CNER) and auditory brainstem response (ABR) thresholds in C57BL/6 mice. *Hear. Res.* 170, 107–115. doi: 10.1016/S0378-5955(02)00391-X

Hequembourg, S., and Liberman, M. C. (2001). Spiral ligament pathology: a major aspect of age-related cochlear degeneration in C57BL/6 mice. *J. Assoc. Res. Otolaryngol.* 2, 118–129. doi: 10.1007/s101620010075

Hermann, A., Sitdikova, G. F., and Weiger, T. M. (2015). Oxidative stress and maxi calcium-activated potassium (BK) channels. *Biomolecules* 5, 1870–1911. doi: 10.3390/biom5031870

Hickman, T. T., Hashimoto, K., Liberman, L. D., and Liberman, M. C. (2020). Synaptic migration and reorganization after noise exposure suggests regeneration in a mature mammalian cochlea. *Sci. Rep.* 10:19945. doi: 10.1038/s41598-020-76553-w

Hu, N., Rutherford, M. A., and Green, S. H. (2020). Protection of cochlear synapses from noise-induced excitotoxic trauma by blockade of Ca(2+)-permeable AMPA receptors. *Proc. Natl. Acad. Sci. U. S. A.* 117, 3828–3838. doi: 10.1073/pnas.1914247117

Ison, J. R., and Allen, P. D. (2003). Low-frequency tone pips elicit exaggerated startle reflexes in C57BL/6J mice with hearing loss. *J. Assoc. Res. Otolaryngol.* 4, 495–504. doi: 10.1007/s10162-002-3046-2

Ison, J. R., Allen, P. D., and O'Neill, W. E. (2007). Age-related hearing loss in C57BL/6J mice has both frequency-specific and non-frequency-specific components that produce a hyperacusis-like exaggeration of the acoustic startle reflex. *J. Assoc. Res. Otolaryngol.* 8, 539–550. doi: 10.1007/s10162-007-0098-3

Jean, P., Lopez de la Morena, D., Michanski, S., Jaime Tobon, L. M., Chakrabarti, R., Picher, M. M., et al. (2018). The synaptic ribbon is critical for sound encoding at high rates and with temporal precision. *Elife* 7:e29275. doi: 10.7554/eLife.29275

Jeng, J. Y., Carlton, A. J., Johnson, S. L., Brown, S. D. M., Holley, M. C., Bowl, M. R., et al. (2021). Biophysical and morphological changes in inner hair cells and their efferent innervation in the ageing mouse cochlea. *J. Physiol.* 599, 269–287. doi: 10.1113/JP280256

Jeng, J. Y., Ceriani, F., Olt, J., Brown, S. D. M., Holley, M. C., Bowl, M. R., et al. (2020). Pathophysiological changes in inner hair cell ribbon synapses in the ageing mammalian cochlea. *J. Physiol.* 598, 4339–4355. doi: 10.1113/JP280018

Jiang, X. W., Li, X. R., and Zhang, Y. P. (2015). Changes of ribbon synapses number of cochlear hair cells in C57BL/6J mice with age(Delta). *Int. J. Clin. Exp. Med.* 8, 19058–19064.

Jing, Z., Rutherford, M. A., Takago, H., Frank, T., Fejtova, A., Khimich, D., et al. (2013). Disruption of the presynaptic cytomatrix protein bassoon degrades ribbon anchorage, multiquantal release, and sound encoding at the hair cell afferent synapse. *J. Neurosci.* 33, 4456–4467. doi: 10.1523/JNEUROSCI.3491-12.2013

Johnson, K. R., Erway, L. C., Cook, S. A., Willott, J. F., and Zheng, Q. Y. (1997). A major gene affecting age-related hearing loss in C57BL/6J mice. *Hear. Res.* 114, 83–92. doi: 10.1016/S0378-5955(97)00155-X

Johnson, S. L., Marcotti, W., and Kros, C. J. (2005). Increase in efficiency and reduction in Ca2+ dependence of exocytosis during development of mouse inner hair cells. *J. Physiol.* 563(Pt 1), 177–191. doi: 10.1113/jphysiol.2004.074740

Kazmierczak, P., Sakaguchi, H., Tokita, J., Wilson-Kubalek, E. M., Milligan, R. A., Muller, U., et al. (2007). Cadherin 23 and protocadherin 15 interact to form tip-link filaments in sensory hair cells. *Nature* 449, 87–91. doi: 10.1038/nature06091

Knipper, M., Van Dijk, P., Nunes, I., Ruttiger, L., and Zimmermann, U. (2013). Advances in the neurobiology of hearing disorders: recent developments regarding the basis of tinnitus and hyperacusis. *Prog. Neurobiol.* 111, 17–33. doi: 10.1016/j.pneurobio.2013.08.002

Kros, C. J., Ruppersberg, J. P., and Rusch, A. (1998). Expression of a potassium current in inner hair cells during development of hearing in mice. *Nature* 394, 281–284. doi: 10.1038/28401

Kujawa, S. G., and Liberman, M. C. (2015). Synaptopathy in the noise-exposed and aging cochlea: primary neural degeneration in acquired sensorineural hearing loss. *Hear. Res.* 330(Pt B), 191–199. doi: 10.1016/j.heares.2015.02.009

Kujawa, S. G., and Liberman, M. C. (2019). Translating animal models to human therapeutics in noise-induced and age-related hearing loss. *Hear. Res.* 377, 44–52. doi: 10.1016/j.heares.2019.03.003

Kurt, S., Sausbier, M., Ruttiger, L., Brandt, N., Moeller, C. K., Kindler, J., et al. (2012). Critical role for cochlear hair cell BK channels for coding the temporal structure and dynamic range of auditory information for central auditory processing. *FASEB J.* 26, 3834–3843. doi: 10.1096/fj.11-200535

Lagziel, A., Ahmed, Z. M., Schultz, J. M., Morell, R. J., Belyantseva, I. A., and Friedman, T. B. (2005). Spatiotemporal pattern and isoforms of cadherin 23 in wild type and waltzer mice during inner ear hair cell development. *Dev. Biol.* 280, 295–306. doi: 10.1016/j.ydbio.2005.01.015

Lang, I., Jung, M., Niemeyer, B. A., Ruth, P., and Engel, J. (2019). Expression of the LRRC52 gamma subunit (gamma2) may provide Ca(2+)-independent activation of BK currents in mouse inner hair cells. *FASEB J.* 33, 11721–11734. doi: 10.1096/fj.201900701RR

Liberman, L. D., Wang, H., and Liberman, M. C. (2011). Opposing gradients of ribbon size and AMPA receptor expression underlie sensitivity differences among cochlear-nerve/hair-cell synapses. *J. Neurosci.* 31, 801–808. doi: 10.1523/JNEUROSCI.3389-10.2011

Liberman, M. C. (1982). Single-neuron labeling in the cat auditory nerve. *Science* 216, 1239–1241. doi: 10.1126/science.7079757

Liberman, M. C., and Kujawa, S. G. (2017). Cochlear synaptopathy in acquired sensorineural hearing loss: manifestations and mechanisms. *Hear. Res.* 349, 138–147. doi: 10.1016/j.heares.2017.01.003

Lingle, C. J., Martinez-Espinosa, P. L., Yang-Hood, A., Boero, L. E., Payne, S., Persic, D., et al. (2019). LRRC52 regulates BK channel function and localization in mouse cochlear inner hair cells. *Proc. Natl. Acad. Sci. U. S. A.* 116, 18397–18403. doi: 10.1073/pnas.1907065116

Magupalli, V. G., Schwarz, K., Alpadi, K., Natarajan, S., Seigel, G. M., and Schmitz, F. (2008). Multiple RIBEYE-RIBEYE interactions create a dynamic scaffold for the formation of synaptic ribbons. *J. Neurosci.* 28, 7954–7967. doi: 10.1523/JNEUROSCI.1964-08.2008

Matsubara, A., Laake, J. H., Davanger, S., Usami, S., and Ottersen, O. P. (1996). Organization of AMPA receptor subunits at a glutamate synapse: a quantitative immunogold analysis of hair cell synapses in the rat organ of Corti. *J. Neurosci.* 16, 4457–4467. doi: 10.1523/JNEUROSCI.16-14-04457.1996

Meyer, A. C., Frank, T., Khimich, D., Hoch, G., Riedel, D., Chapochnikov, N. M., et al. (2009). Tuning of synapse number, structure and function in the cochlea. *Nat. Neurosci.* 12, 444–453. doi: 10.1038/nn.2293

Michalski, N., Goutman, J. D., Auclair, S. M., Boutet de Monvel, J., Tertrais, M., Emptoz, A., et al. (2017). Otoferlin acts as a Ca(2+) sensor for vesicle fusion and vesicle pool replenishment at auditory hair cell ribbon synapses. *Elife* 6:e31013. doi: 10.7554/eLife.31013.024

Michel, V., Goodyear, R. J., Weil, D., Marcotti, W., Perfettini, I., Wolfrum, U., et al. (2005). Cadherin 23 is a component of the transient lateral links in the developing hair bundles of cochlear sensory cells. *Dev. Biol.* 280, 281–294. doi: 10.1016/j.ydbio.2005.01.014

Neef, J., Urban, N. T., Ohn, T. L., Frank, T., Jean, P., Hell, S. W., et al. (2018). Quantitative optical nanophysiology of Ca(2+) signaling at inner hair cell active zones. *Nat. Commun.* 9:290. doi: 10.1038/s41467-017-02612-y

Noben-Trauth, K., Zheng, Q. Y., and Johnson, K. R. (2003). Association of cadherin 23 with polygenic inheritance and genetic modification of sensorineural hearing loss. *Nat. Genet.* 35, 21–23. doi: 10.1038/ng1226

Oliver, D., Taberner, A. M., Thurm, H., Sausbier, M., Arntz, C., Ruth, P., et al. (2006). The role of BKCa channels in electrical signal encoding in the mammalian auditory periphery. *J. Neurosci.* 26, 6181–6189. doi: 10.1523/JNEUROSCI.1047-06.2006

Ouagazzal, A. M., Reiss, D., and Romand, R. (2006). Effects of age-related hearing loss on startle reflex and prepulse inhibition in mice on pure and mixed C57BL and 129 genetic background. *Behav. Brain Res.* 172, 307–315. doi: 10.1016/j.bbr.2006.05.018

Ozcete, O. D., and Moser, T. (2021). A sensory cell diversifies its output by varying Ca(2+) influx-release coupling among active zones. *EMBO J.* 40:e106010. doi: 10.15252/embj.2020106010

Pujol, R., and Puel, J. L. (1999). Excitotoxicity, synaptic repair, and functional recovery in the mammalian cochlea: a review of recent findings. *Ann. N. Y. Acad. Sci.* 884, 249–254. doi: 10.1111/j.1749-6632.1999.tb08646.x

Pyott, S. J., Glowatzki, E., Trimmer, J. S., and Aldrich, R. W. (2004). Extrasynaptic localization of inactivating calcium-activated potassium channels in mouse inner hair cells. *J. Neurosci.* 24, 9469–9474. doi: 10.1523/JNEUROSCI.3162-04.2004

Rousset, F., Nacher-Soler, G., Coelho, M., Ilmjarv, S., Kokje, V. B. C., Marteyn, A., et al. (2020). Redox activation of excitatory pathways in auditory neurons as mechanism of age-related hearing loss. *Redox Biol.* 30:101434. doi: 10.1016/j.redox.2020.101434

Roux, I., Safieddine, S., Nouvian, R., Grati, M., Simmler, M. C., Bahloul, A., et al. (2006). Otoferlin, defective in a human deafness form, is essential for exocytosis at the auditory ribbon synapse. *Cell* 127, 277–289. doi: 10.1016/j.cell.2006.08.040

Sahoo, N., Hoshi, T., and Heinemann, S. H. (2014). Oxidative modulation of voltage-gated potassium channels. *Antioxid. Redox Signal.* 21, 933–952. doi: 10.1089/ars.2013.5614

Sheets, L., He, X. J., Olt, J., Schreck, M., Petralia, R. S., Wang, Y. X., et al. (2017). Enlargement of ribbons in zebrafish hair cells increases calcium currents but disrupts afferent spontaneous activity and timing of stimulus onset. *J. Neurosci.* 37, 6299–6313. doi: 10.1523/JNEUROSCI.2878-16.2017

Siemens, J., Lillo, C., Dumont, R. A., Reynolds, A., Williams, D. S., Gillespie, P. G., et al. (2004). Cadherin 23 is a component of the tip link in hair-cell stereocilia. *Nature* 428, 950–955. doi: 10.1038/nature02483

Skinner, L. J., Enee, V., Beurg, M., Jung, H. H., Ryan, A. F., Hafidi, A., et al. (2003). Contribution of BK Ca2+-activated K+ channels to auditory neurotransmission in the Guinea pig cochlea. *J. Neurophysiol.* 90, 320–332. doi: 10.1152/jn.01155.2002

Sollner, C., Rauch, G. J., Siemens, J., Geisler, R., Schuster, S. C., Muller, U., et al. (2004). Mutations in cadherin 23 affect tip links in zebrafish sensory hair cells. *Nature* 428, 955–959. doi: 10.1038/nature02484

Spassova, M. A., Soboloff, J., He, L. P., Hewavitharana, T., Xu, W., Venkatachalam, K., et al. (2004). Calcium entry mediated by SOCs and TRP channels: variations and enigma. *Biochim. Biophys. Acta* 1742, 9–20. doi: 10.1016/j.bbamcr.2004.09.001

Spongr, V. P., Flood, D. G., Frisina, R. D., and Salvi, R. J. (1997). Quantitative measures of hair cell loss in CBA and C57BL/6 mice throughout their life spans. *J. Acoust. Soc. Am.* 101, 3546–3553. doi: 10.1121/1.418315

Stamataki, S., Francis, H. W., Lehar, M., May, B. J., and Ryugo, D. K. (2006). Synaptic alterations at inner hair cells precede spiral ganglion cell loss in aging C57BL/6J mice. *Hear. Res.* 221, 104–118. doi: 10.1016/j.heares.2006.07.014

Taberner, A. M., and Liberman, M. C. (2005). Response properties of single auditory nerve fibers in the mouse. *J. Neurophysiol.* 93, 557–569. doi: 10.1152/jn.00574.2004

Thibault, O., and Landfield, P. W. (1996). Increase in single L-type calcium channels in hippocampal neurons during aging. *Science.* 272, 1017–1020. doi: 10.1126/science.272.5264.1017

Vincent, P. F., Bouleau, Y., Charpentier, G., Emptoz, A., Safieddine, S., Petit, C., et al. (2017). Different CaV1.3 channel isoforms control distinct components of the synaptic vesicle cycle in auditory inner hair cells. *J. Neurosci.* 37, 2960–2975. doi: 10.1523/JNEUROSCI.2374-16.2017

Vincent, P. F., Bouleau, Y., Petit, C., and Dulon, D. (2015). A synaptic F-actin network controls otoferlin-dependent exocytosis in auditory inner hair cells. *Elife* 4:10988. doi: 10.7554/eLife.10988.008

Vincent, P. F., Bouleau, Y., Safieddine, S., Petit, C., and Dulon, D. (2014). Exocytotic machineries of vestibular type I and cochlear ribbon synapses display similar intrinsic otoferlin-dependent Ca2+ sensitivity but a different coupling to Ca2+ channels. *J. Neurosci.* 34, 10853–10869. doi: 10.1523/JNEUROSCI.0947-14.2014

Walton, J. P., Frisina, R. D., and Meierhans, L. R. (1995). Sensorineural hearing loss alters recovery from short-term adaptation in the C57BL/6 mouse. *Hear. Res.* 88, 19–26. doi: 10.1016/0378-5955(95)00093-J

Wan, G., and Corfas, G. (2015). No longer falling on deaf ears: mechanisms of degeneration and regeneration of cochlear ribbon synapses. *Hear. Res.* 329, 1–10. doi: 10.1016/j.heares.2015.04.008

Wang, Y., Tao, J., Wang, M., Yang, L., Ning, F., Xin, H., et al. (2019). Mechanism of regulation of big-conductance Ca(2+)-activated K(+) channels by mTOR complex 2 in podocytes. *Front. Physiol.* 10:167. doi: 10.3389/fphys.2019.00167

Willott, J. F. (1996). Anatomic and physiologic aging: a behavioral neuroscience perspective. *J. Am. Acad. Audiol.* 7, 141–151.

Wong, H. C., Zhang, Q., Beirl, A. J., Petralia, R. S., Wang, Y. X., and Kindt, K. (2019). Synaptic mitochondria regulate hair-cell synapse size and function. *Elife* 8:e48914. doi: 10.7554/eLife.48914.sa2

Zachary, S. P., and Fuchs, P. A. (2015). Re-emergent inhibition of cochlear inner hair cells in a mouse model of hearing loss. *J. Neurosci.* 35, 9701–9706. doi: 10.1523/JNEUROSCI.0879-15.2015

Zheng, Q. Y., Johnson, K. R., and Erway, L. C. (1999). Assessment of hearing in 80 inbred strains of mice by ABR threshold analyses. *Hear. Res.* 130, 94–107. doi: 10.1016/S0378-5955(99)00003-9

Zhou, X., Jen, P. H., Seburn, K. L., Frankel, W. N., and Zheng, Q. Y. (2006). Auditory brainstem responses in 10 inbred strains of mice. *Brain Res.* 1091, 16–26. doi: 10.1016/j.brainres.2006.01.107

Conflict of Interest: The authors declare that the research was conducted in the absence of any commercial or financial relationships that could be construed as a potential conflict of interest.

Publisher's Note: All claims expressed in this article are solely those of the authors and do not necessarily represent those of their affiliated organizations, or those of the publisher, the editors and the reviewers. Any product that may be evaluated in this article, or claim that may be made by its manufacturer, is not guaranteed or endorsed by the publisher.

Copyright © 2021 Peineau, Belleudy, Pietropaolo, Bouleau and Dulon. This is an open-access article distributed under the terms of the Creative Commons Attribution License (CC BY). The use, distribution or reproduction in other forums is permitted, provided the original author(s) and the copyright owner(s) are credited and that the original publication in this journal is cited, in accordance with accepted academic practice. No use, distribution or reproduction is permitted which does not comply with these terms.

DISCUSSION

Dans mon travail de thèse j'ai abordé trois aspects du fonctionnement des synapses à ruban des CCIs :

1) Le rôle de la clarine-2 dans la régulation voltage-dépendante des canaux $Ca_V1.3$, les canaux calciques essentiels au déclenchement de la libération des vésicules synaptiques (ou exocytose). Individuellement ces canaux $Ca_V1.3$ sont organisés en configuration nanodomaine (quelques nm) avec les vésicules synaptiques dans la ZA. La réponse synchrone de ces nanodomaines calciques, en fonction du voltage, forme un microdomaine calcique plus large à l'échelle du ruban (quelques centaines de nm) pour un recrutement actif des vésicules.

2) Le rôle des SNAREs, dont la SNAP-25 en particulier, en tant que protéines d'attachement ou d'encrage des vésicules synaptiques à la membrane plasmique des ZA. Ces protéines sont essentielles au bon fonctionnement des synapses centrales neuronales mais leur rôle dans les CCIs restait encore controversé.

3) Leurs changements fonctionnels lors du processus de vieillissement chez la souris C57BL/6J, en particulier la modification des microdomaines calciques présynaptiques et leur impact sur l'exocytose.

I. Rôle de la clarine-2 dans la maintenance morpho-fonctionnelle des stéréocils

On sait qu'un déficit en clarine-1 provoque une surdité profonde progressive du à une désorganisation des stéréocils (Geng et al., 2009; Geng et al., 2012; Dulon et al., 2018). Nous montrons ici que la clarine-2 encodée par un gène paralogue de la clarine-1 joue aussi un rôle important dans la maintenance des stéréocils. En effet, l'étude des souris mutantes *clarinette* où l'expression de la clarine-2 est altérée permet de mettre en évidence le développement d'une surdité profonde progressive (Dunbar et al., 2019). La morphogénèse des stéréocils n'est pas affectée, en revanche on observe une réduction progressive de la taille des deux premières rangées de stéréocils à partir de P8 dans les CCEs et de P16 dans les CCIs. Cette réduction progressive des stéréocils est également observée dès P6-7 dans les souris mutantes ayant un défaut génétique au niveau des acteurs importants de la mécano-transduction comme TMC1/TMC2, TMIE ou LHFPL5 (Kawashima et al., 2011; Xiong et al.,

2012; Zhao et al., 2014). Ce phénotype est aussi retrouvé lors d'un traitement pharmacologique *in vivo* de souris « wild-type » par un bloqueur perméable des canaux de MET, le FM1-43 (Velez-Ortega et al., 2017), suggérant que l'activité des MET est essentielle pour la stabilité des stéréocils. A partir de P6 en chez la souris *clarinette*, le bout apical des stéréocils se déforme pour passer d'une forme conique dû à la tension des « tip-links » a une forme sphérique et aplatie, suggérant une perte de tension ou rupture des « tip-links ». De plus, dans ces souris mutantes, la protéine harmonine-b, une protéine essentielle à l'attachement des « tip-links » à l'actine et au bon fonctionnement de la mécano-transduction (Michalski et al., 2009) se retrouve délocalisée à l'apex des stéréocils au lieu du point d'encrage du « tip-link ». Cette délocalisation de l'harmonine-b se retrouve également dans les souris mutantes pour les dimères composant le « tip-links » : cadhérine-23 et protocadhérine-15 (Lefevre et al., 2008). La persistance d'un faible courant de MET chez les souris clarinette suggère que la clarin-2 n'est pas directement associée au fonctionnement du complexe des canaux de MET mais qu'elle intervient dans la maintenance de la tension des « tip-links ».

II. Rôle de la clarine-2 au niveau des synapses à ruban

La clarine-1, en plus de son rôle dans la morphogénèse des stéréocils, joue également un rôle important dans l'exocytose des vésicules glutamatergiques dans les synapses à ruban des CCIs (Dulon et al., 2018). En effet dans un modèle de souris n'exprimant pas clarine-1, on observe un défaut de l'efficacité calcique de l'exocytose. Ce défaut fonctionnel s'explique par une désorganisation structurelle de la synapse. Le regroupement des canaux calciques $Ca_V1.3$ au niveau des ZA est anormalement faible par rapport à la normale. La clarine-1 semble faire le lien entre les canaux calciques $Ca_V1.3$, via notamment la sous-unité $Ca_V\beta_2$ des canaux, et l'architecture de la synapse à ruban via la protéine d'échafaudage harmonine-b qui contacte directement le réseau de filaments d'actine (voir figure 25).

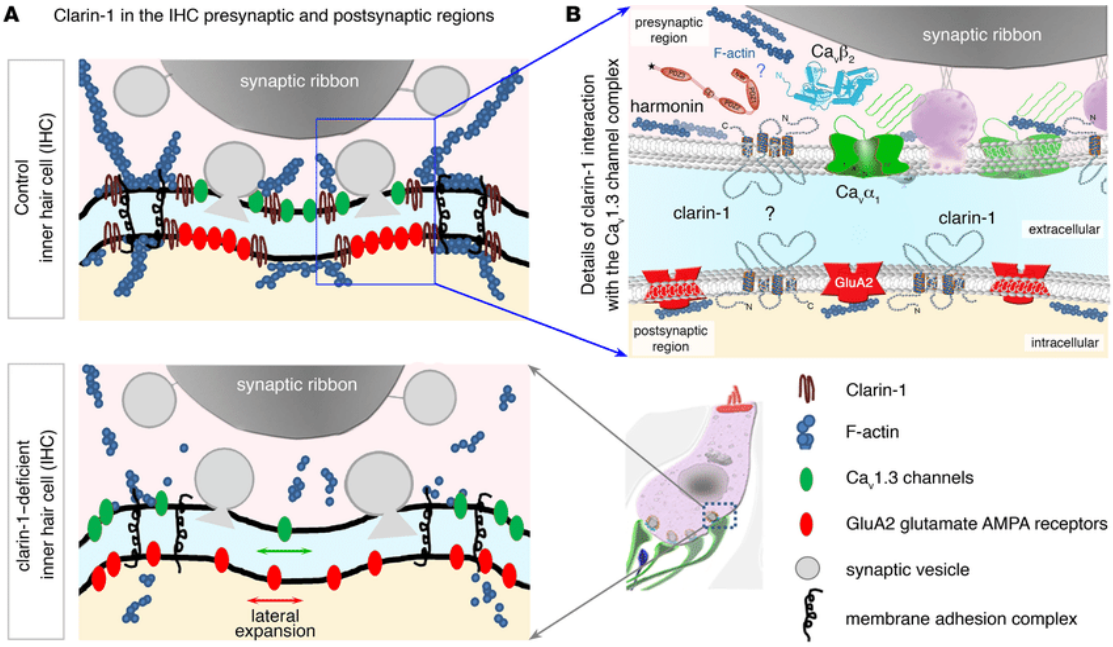

Figure 25. La clarine-1 est essentielle à l'organisation morpho-fonctionnelle des zones actives des CCIs : d'après Dulon et al. (2018). En absence de clarin-1, l'agrégation des canaux $Ca_V1.3$ dans la ZA présynaptique et des récepteurs AMPA postsynaptiques sont altérées. On suppose une désorganisation similaire en absence de clarine-2.

L'étude des paramètres électrophysiologiques des CCIs de souris mutantes clarine-2 nous a permis de retrouver des défauts synaptiques fonctionnels ressemblant à ceux observés chez les souris KO clarin-1. Nous observons aussi une réduction de l'efficacité calcique de l'exocytose. Cette réduction suggère comme pour la clarine-1, une désorganisation des canaux calciques $Ca_V1.3$ au niveau des ZA des CCIs. La réduction de l'efficacité calcique n'est cependant pas associée à une augmentation de la densité du courant calcique comme pour les CCIs de souris KO clarine-1. De manière remarquable, la courbe d'activation voltage-dépendante des canaux calciques des CCIs des souris clarinette présente un décalage négatif important de 20 mV. Ces résultats suggèrent que la clarine-2 est un facteur important de la régulation fonctionnelle du complexe Cav1.3.

III. Perspectives sur le rôle de la clarine-2

Nous ne savons pas si les canaux $Ca_V1.3$ des CCIs de souris clarinette présentent une désorganisation spatiale similaire à celle observée chez les souris mutante KO clarin-1 (voir Figure 23). Pour cela des investigations par imagerie confocale immunofluorescente devront être réalisées. Comme pour la clarin-1 (Dulon et al., 2018), la colocalisation du marquage immunofluorescent des canaux calciques avec le ruban synaptique, la principale structure des ZA, permettra de déterminer le niveau de regroupement et d'organisation des canaux calciques à ces ZA.

L'identification *in vitro* des interactions protéiques de la clarine-2 avec les différents composant du complexe Cav1.3 permettra également de mieux comprendre le lien entre la clarine-2, les canaux calciques $Ca_V1.3$ et l'architecture des synapses à ruban. Comme pour la clarine-1, l'harmonine-b et la sous-unité régulatrice $Ca_V\beta_2$ semblent être des candidats potentiels. L'harmonine-b est une protéine à plusieurs domaines PDZ qui interagit avec le réseau de filaments d'actine et le domaine C-terminal des canaux calciques $Ca_V1.3$ (Gregory et al., 2013). L'harmonine-b contrôle l'expression des canaux calciques à la surface des membranes plasmiques via l'activation de la voie de dégradation dépendante de l'ubiquitine.

Enfin, nous nous proposons également d'étudier des souris double mutantes sur les gènes clarine-1 et clarine-2. Elles permettront d'évaluer les interactions et les compensations éventuelles de ces deux protéines. La fonction vestibulaire sera également explorée.

IV. La SNAP-25 est essentielle pour la fusion rapide des vésicules synaptiques et la survie des synapses à ruban

Le rôle de la SNAP-25, protéine du complexe SNAREs, est bien caractérisée dans les synapses neuronales. Elle est située dans la membrane plasmique des neurones et permet l'amarrage des vésicules synaptiques pour faciliter leur fusion rapide (Oyler et al., 1989; Bark et al., 1995; Washbourne et al., 2002; Sorensen et al., 2006).

Malgré la présence d'ARNm codant pour la SNAP-25 dans les cellules ciliées (Scheffer et al., 2015), son importance dans l'exocytose des synapses à ruban restait à démontrer. Une s étude précédente utilisant des neurotoxines pouvant cliver les principales SNAREs (synaptobrévine, syntaxine et SNAP-25) a démontré qu'elles n'altéraient pas l'exocytose des CCIs (Nouvian et al., 2011). L'absence d'effet des neurotoxines peut aussi bien s'expliquer par l'inaccessibilité de ces molécules aux sites de clivage des protéines SNAREs des CCIs ou par l'expression de protéines SNAREs résistantes dans les CCIs. Par ailleurs, cette même étude précédente montrait une exocytose normale des CCIs chez la souris « knock-out » pour le gène codant pour SNAP-25. Cependant, comme ce modèle murin KO-SNAP-25 n'est pas viable, l'étude de l'exocytose des CCIs sur ce modèle s'est faite sur des cultures d'organe de Corti dérivées d'embryons de souriceaux à E18 ; c'est-à-dire à un stade très immature.

Puisque la délétion totale du gène codant pour la SNAP-25 est léthale chez le souriceau, nous avons développé un modèle de souris de « knock-out » conditionnel SNAP-25 avec une délétion spécifique dans les cellules ciliées. La délétion du gène codant pour la SNAP-25 est dépendante de l'action de la Cre-recombinase exprimée sous l'action du promoteur de la myosine-15. Nos résultats montrent que la SNAP-25 est essentielle au maintien de l'intégrité des synapses à ruban mais aussi à la survie des cellules ciliées elles-mêmes. Il est à noter que l'absence de la SNAP-25 dans les neurones conduit également à leur dégénérescence progressive (Molnar et al., 2002; Hoerder-Suabedissen et al., 2019) suggérant qu'elle joue un rôle important dans la sécrétion de facteurs neurotrophiques permettant la maintenance des synapses et la survie des l neurones (Shimojo et al., 2015). Ce mécanisme qui pourrait aussi expliquer la dégénérescence des rubans et cellules ciliées chez les souris KO conditionnel-SNAP25 par un défaut de sécrétion de facteur trophique tels que NT-3 ou BDNF (Fritzsch et al., 2004).

Notre étude montre par ailleurs que la SNAP-25 est essentielle à la phase rapide de l'exocytose des CCIs et des cellules vestibulaires (voir Figure 26). Ce défaut d'exocytose rapide est également observé *in vitro* dans des cellules neuronales embryonnaires présentant une SNAP-25 muté (Criado et al., 1999).

Nous notons que le défaut sur l'exocytose des CCIs n'est pas total comme pour le KO-otoferline, en particulier l'exocytose lente du SRP subsiste. La présence d'autres protéines de la famille des SNAP comme la SNAP-23, SNAP-29 ou encore la SNAP-47 pourraient compenser en partie la SNAP-25 (Kadkova et al., 2019).

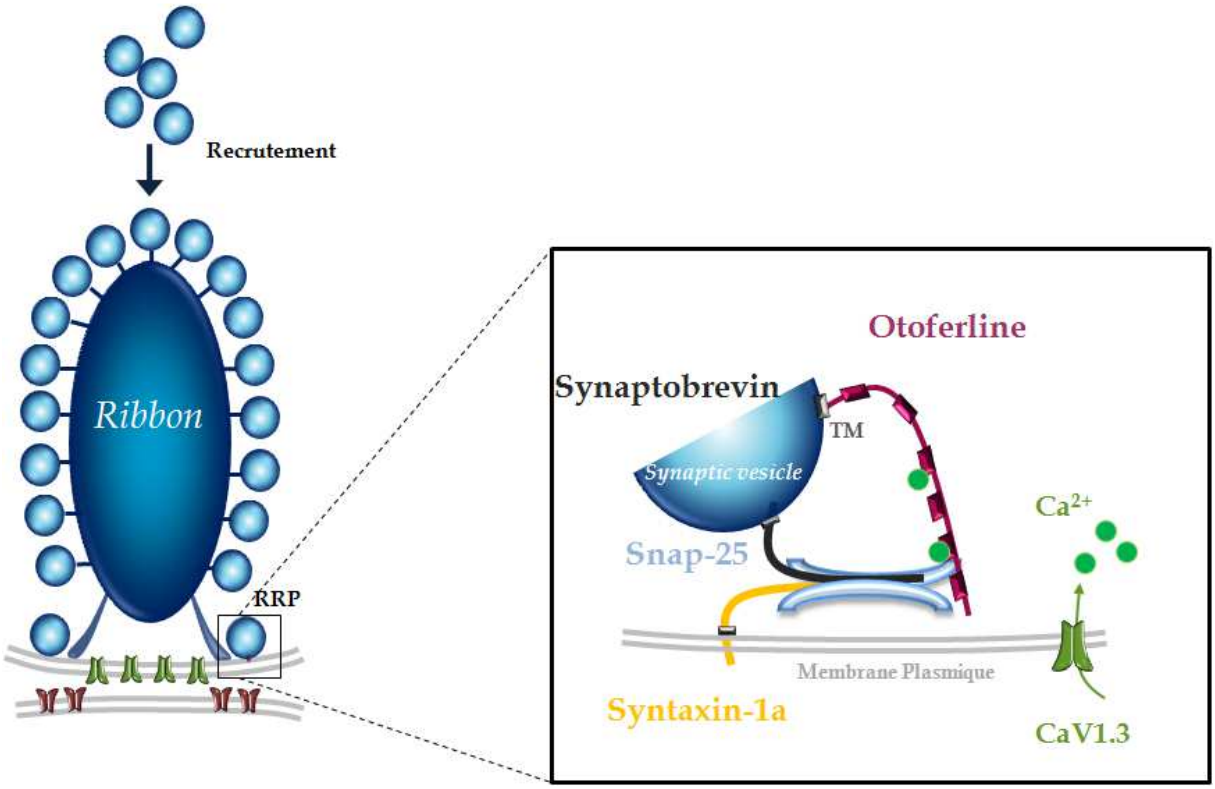

Figure 26. Représentation schématique des différentes protéines impliquées dans la fusion des vésicules glutamatergiques dans les synapses à ruban des cellules ciliées inspirée de M. Tertrais et al. 2018. Notre étude démontre que la SNAP-25 est un élément essentiel de l'exocytose rapide, probablement en interagissant avec le senseur calcique l'otoferline. L'implication de la synaptobrévine, protéine v-SNAREs associée aux vésicules, et de la syntaxin-1a associée à la membrane plasmique sont encore à démontrer.

V. Les changements structurels et fonctionnels des synapses à ruban des CCI lors du vieillissement

Les souris C57BL/6J portent une mutation sur le gène codant pour la cadhérine-23 et développent une surdité précoce importante liée à l'âge. Cette surdité se manifeste par une perte de plus de 50% des synapses à ruban afférentes contactant les CCIs. Nous observons une dégénérescence préférentielle des rubans du côté modiolaire des CCIs, cad ceux qui font face généralement aux fibres postsynaptiques à haut seuil d'activation et ayant une activité spontanée faible. La perte de ces synapses à haut-seuil est également observée lors d'un trauma acoustique (Fernandez et al., 2015; Liberman and Kujawa, 2017; Hickman et al., 2020). Ces résultats suggèrent que ces synapses à haut seuil sont plus sensibles au stress oxydatif provoqué par le vieillissement cellulaire ou le trauma acoustique.

Nous observons que les rubans synaptiques ont tendance à grossir avec l'âge pour en moyenne tripler de taille à un an. Ces observations sont en accord avec une étude précédente montrant la croissance en taille des rubans dans plusieurs lignées de souris avec l'âge (Stamataki et al., 2006; Jeng et al., 2020). Cette croissance des rubans synaptiques est également associée à une augmentation de la densité postsynaptiques des fibres afférentes du ganglion spiral. Nous montrons chez les souris C57BL/6J âgées, que la densité du courant calcique des CCIs augmente et qu'elle est associée à une augmentation de la taille des microdomaines calciques au ruban. L'augmentation des microdomaines calciques présynaptiques avec l'âge est associée à une augmentation de l'exocytose soutenue des vésicules du SRP (voir figure 25). Bien qu'il n'y ait pas d'enregistrements de l'activité des fibres postsynaptiques effectués chez la souris âgées, nos résultats suggèrent que la capacité augmentée de l'exocytose soutenue des CCIs âgées pourrait réduire l'amplitude de l'adaptation soutenue des fibres afférentes.

L'ensemble de nos résultats suggèrent une potentialisation des synapses à ruban avec l'âge. Cette potentialisation des synapses des CCIs pourrait expliquer les *startle reflexes* exacerbées (hyperacousie) des souris C57BL/6J âgées (Ison et al., 2007)

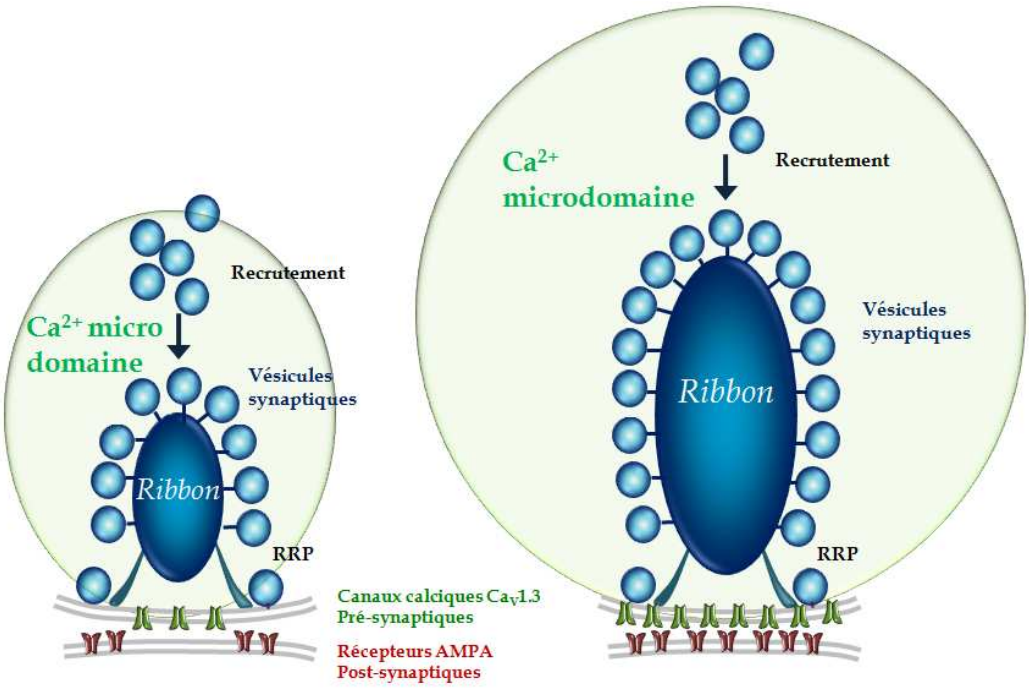

Figure 27. Evolution de la synapse à ruban des CCIs des souris C57BL/6J avec l'âge : d'après Peineau et al. (2021). En plus d'une perte de plus de 50 % des rubans à 1 an, on observe une augmentation du volume des rubans restants, un agrandissement du microdomaine calcique au ruban et des patches postsynaptiques de récepteurs AMPA.

VI. Stress oxydatif et vieillissement des CCIs

Le vieillissement cellulaire en général se manifeste par une augmentation du stress oxydatif reflétant un déséquilibre entre la production importante des ROS par les mitochondries et la baisse de production des antioxydants. En plus de la production des ROS par les mitochondries, s'ajoute aussi la production de ROS par une famille de protéines appelée les NOX pour NAD(P)H oxydases que l'on retrouve dans la membrane plasmique. Les mitochondries et les NOX en produisant des ROS vont aussi produire en grande quantité des coenzymes NADH et NAPDH sous leur forme oxydé (NAD^+ et $NADP^+$).

Il a été démontré que le domaine ribeye-B des rubans est sensible à la fixation du NADH permettant l'arrêt de sa polymérisation. Cependant la présence de la forme oxydé NAD^+, à l'inverse, favorise les interactions entre les domaines ribeye et participe à l'augmentation de la taille des rubans (Magupalli et al., 2008; Wong et al., 2019). Ces

résultats suggèrent que l'augmentation de la taille des rubans avec l'âge chez les souris C57BL/6J résultent d'un déséquilibre de l'homéostasie de NAD^+/NADH.

L'augmentation de ce stress oxydatif est aussi visible au niveau des canaux potassiques. Il a été démontré que le stress oxydatif modifiait considérablement l'activité des canaux BK en produisant un décalage-positif de leur courbe d'activation voltage-dépendante ce qui a pour conséquence l'allongement de la durée de repolarisation des potentiels d'actions (Sahoo et al., 2014; Hermann et al., 2015). Les canaux BK semblent être de bons indicateurs du stress oxydatif. Dans les CCI de souris KO-Pejvakin, une protéine senseur des ROS qui recrute la machinerie autophagique et le peroxysome, dont la mutation est à l'origine de la surdité DFNB59, on observe aussi une modification d'expression des courants BK (Delmaghani et al., 2006; Defourny et al., 2019). Notre observation du décalage de la courbe d'activation des courant BK des CCIs âgées ainsi que leur baisse de regroupement sous la plaque cuticulaire, confirment un déséquilibre oxydatif.

L'autophagie est un processus de régulation induit par le stress oxydatif. Il consiste à engloutir via de grandes vésicules (Autophagosome) et à décomposer de grandes structures intracellulaires endommagées grâce à la fusion de l'autophagosome avec un lysosome ou un peroxysome. Dans les souris âgées C57BL/6J on note l'augmentation de l'expression d'un marqueur membranaire de ces autophagosomes appelé LC3B suggérant une augmentation de l'autophagie avec l'âge. Ce processus est régulé par le complexe mTOR, son inhibition active la voie autophagique. C'est principalement un mécanisme de défense permettant de recycler les protéines endommagées mais sa suractivation est néfaste pour les cellules, pouvant même les entraîner dans l'apoptose cellulaire. Une mutation du complexe mTOR chez la souris entraînant sa suractivation entraîne une perte auditive précoce liée à l'âge (Fu et al., 2018).

VII. Perspectives

Pour contrer naturellement le stress oxydatif, les cellules disposent de molécules antioxydantes non enzymatique ou enzymatique comme la SOD (superoxyde dismutase) par exemple, une enzyme qui protège les cellules de la présence de superoxyde (McFadden et al., 1999). Ces antioxydants empêchent la formation ou diminuent la présence de ROS et permettent *in fine* de réduire le stress oxydatif.

Certains antioxydants se révèlent efficaces comme traitement thérapeutique après un trauma acoustique ou en prévention de molécules médicamenteuses ototoxiques. Cependant ils n'ont pas encore montré leur efficacité dans le traitement de la surdité liée l'âge chez l'Homme. Cependant chez la souris l'utilisation de facteurs antioxydants comme la rapamycine ou le N-acétylcystéine permettent de prévenir contre le vieillissement cellulaire et la perte d'audition liée à l'âge (Zhang et al., 2014; Ding et al., 2016; Fu et al., 2018).

Dans des expériences futures, l'utilisation de facteurs antioxydants pourraient nous donner des indications sur la réversibilité ou non des changements structurels et fonctionnels observés dans les synapses à ruban. De plus, le développement d'un protocole de traitement préventif des pertes d'audition liée à l'âge chez la souris pourrait ouvrir la voie à un traitement adaptable à l'Homme.

Le ciblage des NOX pour réduire la production de ROS est aussi envisageable en prévention des pertes auditives liée au vieillissement. Un modèle de souris présentant une mutation sur une sous-unité du complexe NOX ($p22^{PHOX}$) suggèrent que la réduction de l'activité du complexe NOX, entraînant une baisse de production des ROS, permet de préserver la morphologie cochléaire au cours du temps (Rousset et al., 2020). Des investigations futures au niveau cellulaire et moléculaire sur ces souris $p22^{PHOX}$ nous permettront de mieux comprendre les mécanismes de dégradation de l'audition avec l'âge.

RÉFÉRENCES BIBLIOGRAPHIQUES

Adato, A., Vreugde, S., Joensuu, T., Avidan, N., Hamalainen, R., Belenkiy, O., et al. (2002). USH3A transcripts encode clarin-1, a four-transmembrane-domain protein with a possible role in sensory synapses. *Eur J Hum Genet* 10(6)**,** 339-350. doi: 10.1038/sj.ejhg.5200831

Arikkath, J., and Campbell, K.P. (2003). Auxiliary subunits: essential components of the voltage-gated calcium channel complex. *Curr Opin Neurobiol* 13(3)**,** 298-307. doi: 10.1016/s0959-4388(03)00066-7

Bach, M., and Meigen, T. (1999). Do's and don'ts in Fourier analysis of steady-state potentials. *Documenta Ophthalmologica* 99(1)**,** 69-82. doi: 10.1023/A:1002648202420

Bark, I.C., Hahn, K.M., Ryabinin, A.E., and Wilson, M.C. (1995). Differential expression of SNAP-25 protein isoforms during divergent vesicle fusion events of neural development. *Proc Natl Acad Sci U S A* 92(5)**,** 1510-1514. doi: 10.1073/pnas.92.5.1510

Becker, L., Schnee, M.E., Niwa, M., Sun, W., Maxeiner, S., Talaei, S., et al. (2018). The presynaptic ribbon maintains vesicle populations at the hair cell afferent fiber synapse. *Elife* 7. doi: 10.7554/eLife.30241

Bekesy, G. (1952). Direct observation of the vibrations of the cochlear partition under a microscope. *Acta Otolaryngol* 42(3)**,** 197-201. doi: 10.3109/00016485209120346

Belyantseva, I.A., Boger, E.T., Naz, S., Frolenkov, G.I., Sellers, J.R., Ahmed, Z.M., et al. (2005). Myosin-XVa is required for tip localization of whirlin and differential elongation of hair-cell stereocilia. *Nat Cell Biol* 7(2)**,** 148-156. doi: 10.1038/ncb1219

Beurg, M., Evans, M.G., Hackney, C.M., and Fettiplace, R. (2006). A large-conductance calcium-selective mechanotransducer channel in mammalian cochlear hair cells. *J Neurosci* 26(43)**,** 10992-11000. doi: 10.1523/JNEUROSCI.2188-06.2006

Beurg, M., Hafidi, A., Skinner, L.J., Ruel, J., Nouvian, R., Henaff, M., et al. (2005). Ryanodine receptors and BK channels act as a presynaptic depressor of neurotransmission in cochlear inner hair cells. *Eur J Neurosci* 22(5)**,** 1109-1119. doi: 10.1111/j.1460-9568.2005.04310.x

Beurg, M., Michalski, N., Safieddine, S., Bouleau, Y., Schneggenburger, R., Chapman, E.R., et al. (2010). Control of exocytosis by synaptotagmins and otoferlin in auditory hair cells. *J Neurosci* 30(40)**,** 13281-13290. doi: 10.1523/JNEUROSCI.2528-10.2010

Blanchet, C., Erostegui, C., Sugasawa, M., and Dulon, D. (1996). Acetylcholine-induced potassium current of guinea pig outer hair cells: its dependence on a calcium influx through nicotinic-like receptors. *J Neurosci* 16(8)**,** 2574-2584.

Bock, G., Gebhart, M., Scharinger, A., Jangsangthong, W., Busquet, P., Poggiani, C., et al. (2011). Functional properties of a newly identified C-terminal splice variant of Cav1.3 L-type Ca2+ channels. *J Biol Chem* 286(49)**,** 42736-42748. doi: 10.1074/jbc.M111.269951

Bonnet, C., and El-Amraoui, A. (2012). Usher syndrome (sensorineural deafness and retinitis pigmentosa): pathogenesis, molecular diagnosis and therapeutic approaches. *Curr Opin Neurol* 25(1)**,** 42-49. doi: 10.1097/WCO.0b013e32834ef8b2

Brandt, A., Striessnig, J., and Moser, T. (2003). CaV1.3 channels are essential for development and presynaptic activity of cochlear inner hair cells. *J Neurosci* 23(34)**,** 10832-10840.

Chapochnikov, N.M., Takago, H., Huang, C.H., Pangrsic, T., Khimich, D., Neef, J., et al. (2014). Uniquantal release through a dynamic fusion pore is a candidate mechanism of hair cell exocytosis. *Neuron* 83(6)**,** 1389-1403. doi: 10.1016/j.neuron.2014.08.003

Chester, J., Johnston, E., Walker, D., Jones, M., Ionescu, C.M., Wagle, S.R., et al. (2021). A Review on Recent Advancement on Age-Related Hearing Loss: The Applications of

Nanotechnology, Drug Pharmacology, and Biotechnology. *Pharmaceutics* 13(7). doi: 10.3390/pharmaceutics13071041
Chinnery, P.F. (2015). Mitochondrial disease in adults: what's old and what's new? *EMBO Mol Med* 7(12)**,** 1503-1512. doi: 10.15252/emmm.201505079
Corey, D.P., Garcia-Anoveros, J., Holt, J.R., Kwan, K.Y., Lin, S.Y., Vollrath, M.A., et al. (2004). TRPA1 is a candidate for the mechanosensitive transduction channel of vertebrate hair cells. *Nature* 432(7018)**,** 723-730. doi: 10.1038/nature03066
Crawford, A.C., Evans, M.G., and Fettiplace, R. (1991). The actions of calcium on the mechano-electrical transducer current of turtle hair cells. *J Physiol* 434**,** 369-398. doi: 10.1113/jphysiol.1991.sp018475
Criado, M., Gil, A., Viniegra, S., and Gutierrez, L.M. (1999). A single amino acid near the C terminus of the synaptosomeassociated protein of 25 kDa (SNAP-25) is essential for exocytosis in chromaffin cells. *Proc Natl Acad Sci U S A* 96(13)**,** 7256-7261. doi: 10.1073/pnas.96.13.7256
Cui, G., Meyer, A.C., Calin-Jageman, I., Neef, J., Haeseleer, F., Moser, T., et al. (2007). Ca2+-binding proteins tune Ca2+-feedback to Cav1.3 channels in mouse auditory hair cells. *J Physiol* 585(Pt 3)**,** 791-803. doi: 10.1113/jphysiol.2007.142307
Defourny, J., Aghaie, A., Perfettini, I., Avan, P., Delmaghani, S., and Petit, C. (2019). Pejvakin-mediated pexophagy protects auditory hair cells against noise-induced damage. *Proc Natl Acad Sci U S A* 116(16)**,** 8010-8017. doi: 10.1073/pnas.1821844116
Delmaghani, S., del Castillo, F.J., Michel, V., Leibovici, M., Aghaie, A., Ron, U., et al. (2006). Mutations in the gene encoding pejvakin, a newly identified protein of the afferent auditory pathway, cause DFNB59 auditory neuropathy. *Nat Genet* 38(7)**,** 770-778. doi: 10.1038/ng1829
DeVries, S.H. (2001). Exocytosed protons feedback to suppress the Ca2+ current in mammalian cone photoreceptors. *Neuron* 32(6)**,** 1107-1117. doi: 10.1016/s0896-6273(01)00535-9
Dick, O., Hack, I., Altrock, W.D., Garner, C.C., Gundelfinger, E.D., and Brandstatter, J.H. (2001). Localization of the presynaptic cytomatrix protein Piccolo at ribbon and conventional synapses in the rat retina: comparison with Bassoon. *J Comp Neurol* 439(2)**,** 224-234. doi: 10.1002/cne.1344
Ding, D., Jiang, H., Chen, G.D., Longo-Guess, C., Muthaiah, V.P., Tian, C., et al. (2016). N-acetyl-cysteine prevents age-related hearing loss and the progressive loss of inner hair cells in gamma-glutamyl transferase 1 deficient mice. *Aging (Albany NY)* 8(4)**,** 730-750. doi: 10.18632/aging.100927
Dulon, D., Blanchet, C., and Laffon, E. (1994). Photo-released intracellular Ca2+ evokes reversible mechanical responses in supporting cells of the guinea-pig organ of Corti. *Biochem Biophys Res Commun* 201(3)**,** 1263-1269. doi: 10.1006/bbrc.1994.1841
Dulon, D., and Lenoir, M. (1996). Cholinergic responses in developing outer hair cells of the rat cochlea. *Eur J Neurosci* 8(9)**,** 1945-1952. doi: 10.1111/j.1460-9568.1996.tb01338.x
Dulon, D., Mosnier, I., Bouccara, D. (2012). *Ototoxicité médicamenteuse, EMC - Oto-rhino-laryngologie, http://dx.doi.org/10.1016/S0246-0351(12)39238-6.*
Dulon, D., Papal, S., Patni, P., Cortese, M., Vincent, P.F., Tertrais, M., et al. (2018). Clarin-1 gene transfer rescues auditory synaptopathy in model of Usher syndrome. *J Clin Invest* 128(8)**,** 3382-3401. doi: 10.1172/JCI94351
Dulon, D., and Schacht, J. (1992). Motility of cochlear outer hair cells. *Am J Otol* 13(2)**,** 108-112.

Dulon, D., Zajic, G., and Schacht, J. (1990). Increasing intracellular free calcium induces circumferential contractions in isolated cochlear outer hair cells. *J Neurosci* 10(4)**,** 1388-1397.

Dunbar, L.A., Patni, P., Aguilar, C., Mburu, P., Corns, L., Wells, H.R., et al. (2019). Clarin-2 is essential for hearing by maintaining stereocilia integrity and function. *EMBO Mol Med* 11(9)**,** e10288. doi: 10.15252/emmm.201910288

Elgoyhen, A.B., Johnson, D.S., Boulter, J., Vetter, D.E., and Heinemann, S. (1994). Alpha 9: an acetylcholine receptor with novel pharmacological properties expressed in rat cochlear hair cells. *Cell* 79(4)**,** 705-715. doi: 10.1016/0092-8674(94)90555-x

Elgoyhen, A.B., and Katz, E. (2012). The efferent medial olivocochlear-hair cell synapse. *J Physiol Paris* 106(1-2)**,** 47-56. doi: 10.1016/j.jphysparis.2011.06.001

Elgoyhen, A.B., Vetter, D.E., Katz, E., Rothlin, C.V., Heinemann, S.F., and Boulter, J. (2001). alpha10: a determinant of nicotinic cholinergic receptor function in mammalian vestibular and cochlear mechanosensory hair cells. *Proc Natl Acad Sci U S A* 98(6)**,** 3501-3506. doi: 10.1073/pnas.051622798

Engel, J., Braig, C., Ruttiger, L., Kuhn, S., Zimmermann, U., Blin, N., et al. (2006). Two classes of outer hair cells along the tonotopic axis of the cochlea. *Neuroscience* 143(3)**,** 837-849. doi: 10.1016/j.neuroscience.2006.08.060

Eybalin, M., Charachon, G., and Renard, N. (1993). Dopaminergic lateral efferent innervation of the guinea-pig cochlea: immunoelectron microscopy of catecholamine-synthesizing enzymes and effect of 6-hydroxydopamine. *Neuroscience* 54(1)**,** 133-142. doi: 10.1016/0306-4522(93)90389-w

Ezan, J., and Montcouquiol, M. (2014). [The multiple links between cilia and planar cell polarity]. *Med Sci (Paris)* 30(11)**,** 1004-1010. doi: 10.1051/medsci/20143011015

Fernandez, K.A., Jeffers, P.W., Lall, K., Liberman, M.C., and Kujawa, S.G. (2015). Aging after noise exposure: acceleration of cochlear synaptopathy in "recovered" ears. *J Neurosci* 35(19)**,** 7509-7520. doi: 10.1523/JNEUROSCI.5138-14.2015

Ferrary, E., Couloigner, V., Sterkers, O. (2007). Physiologie des liquides labyrinthiques. *EMC - Oto-rhino-laryngologie* 22(3)**,** 1-7. doi: http://dx.doi.org/10.1016/S0246-0351(07)41887-6

Fettiplace, R. (2017). Hair Cell Transduction, Tuning, and Synaptic Transmission in the Mammalian Cochlea. *Compr Physiol* 7(4)**,** 1197-1227. doi: 10.1002/cphy.c160049

Fettiplace, R., and Kim, K.X. (2014). The physiology of mechanoelectrical transduction channels in hearing. *Physiol Rev* 94(3)**,** 951-986. doi: 10.1152/physrev.00038.2013

Frank, T., Rutherford, M.A., Strenzke, N., Neef, A., Pangrsic, T., Khimich, D., et al. (2010). Bassoon and the synaptic ribbon organize Ca(2)+ channels and vesicles to add release sites and promote refilling. *Neuron* 68(4)**,** 724-738. doi: 10.1016/j.neuron.2010.10.027

Fritzsch, B., Tessarollo, L., Coppola, E., and Reichardt, L.F. (2004). Neurotrophins in the ear: their roles in sensory neuron survival and fiber guidance. *Prog Brain Res* 146**,** 265-278. doi: 10.1016/S0079-6123(03)46017-2

Fu, X., Sun, X., Zhang, L., Jin, Y., Chai, R., Yang, L., et al. (2018). Tuberous sclerosis complex-mediated mTORC1 overactivation promotes age-related hearing loss. *J Clin Invest* 128(11)**,** 4938-4955. doi: 10.1172/JCI98058

Fuchs, P.A., and Glowatzki, E. (2015). Synaptic studies inform the functional diversity of cochlear afferents. *Hear Res* 330(Pt A)**,** 18-25. doi: 10.1016/j.heares.2015.09.007

Fulop, T., Larbi, A., Khalil, A., Cohen, A.A., and Witkowski, J.M. (2019). Are We Ill Because We Age? *Front Physiol* 10**,** 1508. doi: 10.3389/fphys.2019.01508

Geleoc, G.S., Lennan, G.W., Richardson, G.P., and Kros, C.J. (1997). A quantitative comparison of mechanoelectrical transduction in vestibular and auditory hair cells of neonatal mice. *Proc Biol Sci* 264(1381)**,** 611-621. doi: 10.1098/rspb.1997.0087

Geng, R., Geller, S.F., Hayashi, T., Ray, C.A., Reh, T.A., Bermingham-McDonogh, O., et al. (2009). Usher syndrome IIIA gene clarin-1 is essential for hair cell function and associated neural activation. *Hum Mol Genet* 18(15)**,** 2748-2760. doi: 10.1093/hmg/ddp210

Geng, R., Melki, S., Chen, D.H., Tian, G., Furness, D.N., Oshima-Takago, T., et al. (2012). The mechanosensory structure of the hair cell requires clarin-1, a protein encoded by Usher syndrome III causative gene. *J Neurosci* 32(28)**,** 9485-9498. doi: 10.1523/JNEUROSCI.0311-12.2012

Glowatzki, E., Cheng, N., Hiel, H., Yi, E., Tanaka, K., Ellis-Davies, G.C., et al. (2006). The glutamate-aspartate transporter GLAST mediates glutamate uptake at inner hair cell afferent synapses in the mammalian cochlea. *J Neurosci* 26(29)**,** 7659-7664. doi: 10.1523/JNEUROSCI.1545-06.2006

Glowatzki, E., and Fuchs, P.A. (2002). Transmitter release at the hair cell ribbon synapse. *Nat Neurosci* 5(2)**,** 147-154. doi: 10.1038/nn796

Glueckert, R., Pfaller, K., Kinnefors, A., Schrott-Fischer, A., and Rask-Andersen, H. (2005). High resolution scanning electron microscopy of the human organ of Corti. A study using freshly fixed surgical specimens. *Hear Res* 199(1-2)**,** 40-56. doi: 10.1016/j.heares.2004.05.006

Goodyear RJ, Eatock, R.A., Fay, R.R., and Popper, A.N. (2006). *The development of hair cells in the inner ear in : Vertebrate hair cells.* Springer.

Grati, M., and Kachar, B. (2011). Myosin VIIa and sans localization at stereocilia upper tip-link density implicates these Usher syndrome proteins in mechanotransduction. *Proc Natl Acad Sci U S A* 108(28)**,** 11476-11481. doi: 10.1073/pnas.1104161108

Graydon, C.W., Cho, S., Li, G.L., Kachar, B., and von Gersdorff, H. (2011). Sharp Ca(2)(+) nanodomains beneath the ribbon promote highly synchronous multivesicular release at hair cell synapses. *J Neurosci* 31(46)**,** 16637-16650. doi: 10.1523/JNEUROSCI.1866-11.2011

Graydon, C.W., Zhang, J., Oesch, N.W., Sousa, A.A., Leapman, R.D., and Diamond, J.S. (2014). Passive diffusion as a mechanism underlying ribbon synapse vesicle release and resupply. *J Neurosci* 34(27)**,** 8948-8962. doi: 10.1523/JNEUROSCI.1022-14.2014

Gregory, F.D., Pangrsic, T., Calin-Jageman, I.E., Moser, T., and Lee, A. (2013). Harmonin enhances voltage-dependent facilitation of Cav1.3 channels and synchronous exocytosis in mouse inner hair cells. *J Physiol* 591(13)**,** 3253-3269. doi: 10.1113/jphysiol.2013.254367

Hafidi, A., Beurg, M., and Dulon, D. (2005). Localization and developmental expression of BK channels in mammalian cochlear hair cells. *Neuroscience* 130(2)**,** 475-484. doi: 10.1016/j.neuroscience.2004.09.038

Harman, D. (1956). Aging: a theory based on free radical and radiation chemistry. *J Gerontol* 11(3)**,** 298-300. doi: 10.1093/geronj/11.3.298

Hermann, A., Sitdikova, G.F., and Weiger, T.M. (2015). Oxidative Stress and Maxi Calcium-Activated Potassium (BK) Channels. *Biomolecules* 5(3)**,** 1870-1911. doi: 10.3390/biom5031870

Hertzog, M., Milanesi, F., Hazelwood, L., Disanza, A., Liu, H., Perlade, E., et al. (2010). Molecular basis for the dual function of Eps8 on actin dynamics: bundling and capping. *PLoS Biol* 8(6)**,** e1000387. doi: 10.1371/journal.pbio.1000387

Hickman, T.T., Hashimoto, K., Liberman, L.D., and Liberman, M.C. (2020). Synaptic migration and reorganization after noise exposure suggests regeneration in a mature mammalian cochlea. *Sci Rep* 10(1)**,** 19945. doi: 10.1038/s41598-020-76553-w

Hoerder-Suabedissen, A., Korrell, K.V., Hayashi, S., Jeans, A., Ramirez, D.M.O., Grant, E., et al. (2019). Cell-Specific Loss of SNAP25 from Cortical Projection Neurons Allows

Normal Development but Causes Subsequent Neurodegeneration. *Cereb Cortex* 29(5)**,** 2148-2159. doi: 10.1093/cercor/bhy127
Hofer, N.T., Pinggera, A., Nikonishyna, Y.V., Tuluc, P., Fritz, E.M., Obermair, G.J., et al. (2021). Stabilization of negative activation voltages of Cav1.3 L-Type Ca(2+)-channels by alternative splicing. *Channels (Austin)* 15(1)**,** 38-52. doi: 10.1080/19336950.2020.1859260
Holley, M.C., Kalinec, F., and Kachar, B. (1992). Structure of the cortical cytoskeleton in mammalian outer hair cells. *J Cell Sci* 102 (Pt 3)**,** 569-580.
Hudspeth, A.J., and Corey, D.P. (1977). Sensitivity, polarity, and conductance change in the response of vertebrate hair cells to controlled mechanical stimuli. *Proc Natl Acad Sci U S A* 74(6)**,** 2407-2411. doi: 10.1073/pnas.74.6.2407
Imtiaz, A., Maqsood, A., Rehman, A.U., Morell, R.J., Holt, J.R., Friedman, T.B., et al. (2016). Recessive mutations of TMC1 associated with moderate to severe hearing loss. *Neurogenetics* 17(2)**,** 115-123. doi: 10.1007/s10048-016-0477-1
Ison, J.R., Allen, P.D., and O'Neill, W.E. (2007). Age-related hearing loss in C57BL/6J mice has both frequency-specific and non-frequency-specific components that produce a hyperacusis-like exaggeration of the acoustic startle reflex. *J Assoc Res Otolaryngol* 8(4)**,** 539-550. doi: 10.1007/s10162-007-0098-3
Jean, P., Anttonen, T., Michanski, S., de Diego, A.M.G., Steyer, A.M., Neef, A., et al. (2020). Macromolecular and electrical coupling between inner hair cells in the rodent cochlea. *Nat Commun* 11(1)**,** 3208. doi: 10.1038/s41467-020-17003-z
Jean, P., Lopez de la Morena, D., Michanski, S., Jaime Tobon, L.M., Chakrabarti, R., Picher, M.M., et al. (2018). The synaptic ribbon is critical for sound encoding at high rates and with temporal precision. *Elife* 7. doi: 10.7554/eLife.29275
Jeng, J.Y., Johnson, S.L., Carlton, A.J., De Tomasi, L., Goodyear, R.J., De Faveri, F., et al. (2020). Age-related changes in the biophysical and morphological characteristics of mouse cochlear outer hair cells. *J Physiol* 598(18)**,** 3891-3910. doi: 10.1113/JP279795
Jing, Z., Rutherford, M.A., Takago, H., Frank, T., Fejtova, A., Khimich, D., et al. (2013). Disruption of the presynaptic cytomatrix protein bassoon degrades ribbon anchorage, multiquantal release, and sound encoding at the hair cell afferent synapse. *J Neurosci* 33(10)**,** 4456-4467. doi: 10.1523/JNEUROSCI.3491-12.2013
Jung, S.Y., Kim, S.S., and Yeo, S.G. (2020). Impact of Endoplasmic Reticulum Stress in Otorhinolaryngologic Diseases. *Int J Mol Sci* 21(11). doi: 10.3390/ijms21114121
Kadkova, A., Radecke, J., and Sorensen, J.B. (2019). The SNAP-25 Protein Family. *Neuroscience* 420**,** 50-71. doi: 10.1016/j.neuroscience.2018.09.020
Kanigur Sultuybek, G., Soydas, T., and Yenmis, G. (2019). NF-kappaB as the mediator of metformin's effect on ageing and ageing-related diseases. *Clin Exp Pharmacol Physiol* 46(5)**,** 413-422. doi: 10.1111/1440-1681.13073
Karet, F.E., Finberg, K.E., Nelson, R.D., Nayir, A., Mocan, H., Sanjad, S.A., et al. (1999). Mutations in the gene encoding B1 subunit of H+-ATPase cause renal tubular acidosis with sensorineural deafness. *Nat Genet* 21(1)**,** 84-90. doi: 10.1038/5022
Katsumi, S., Sahin, M.I., Lewis, R.M., Iyer, J.S., Landegger, L.D., and Stankovic, K.M. (2019). Intracochlear Perfusion of Tumor Necrosis Factor-Alpha Induces Sensorineural Hearing Loss and Synaptic Degeneration in Guinea Pigs. *Front Neurol* 10**,** 1353. doi: 10.3389/fneur.2019.01353
Katz, E., Elgoyhen, A.B., Gomez-Casati, M.E., Knipper, M., Vetter, D.E., Fuchs, P.A., et al. (2004). Developmental regulation of nicotinic synapses on cochlear inner hair cells. *J Neurosci* 24(36)**,** 7814-7820. doi: 10.1523/JNEUROSCI.2102-04.2004

Kawashima, Y., Geleoc, G.S., Kurima, K., Labay, V., Lelli, A., Asai, Y., et al. (2011). Mechanotransduction in mouse inner ear hair cells requires transmembrane channel-like genes. *J Clin Invest* 121(12)**,** 4796-4809. doi: 10.1172/JCI60405

Kazmierczak, P., Sakaguchi, H., Tokita, J., Wilson-Kubalek, E.M., Milligan, R.A., Muller, U., et al. (2007). Cadherin 23 and protocadherin 15 interact to form tip-link filaments in sensory hair cells. *Nature* 449(7158)**,** 87-91. doi: 10.1038/nature06091

Keithley, E.M. (2020). Pathology and mechanisms of cochlear aging. *J Neurosci Res* 98(9)**,** 1674-1684. doi: 10.1002/jnr.24439

Kemp DT. Stimulated acoustic emissions from within the human auditory system. J Acoust Soc Am. 1978 Nov;64(5):1386-91. doi: 10.1121/1.382104. PMID: 744838.

Khan, S., and Chang, R. (2013). Anatomy of the vestibular system: a review. *NeuroRehabilitation* 32(3)**,** 437-443. doi: 10.3233/NRE-130866

Khimich, D., Nouvian, R., Pujol, R., Tom Dieck, S., Egner, A., Gundelfinger, E.D., et al. (2005). Hair cell synaptic ribbons are essential for synchronous auditory signalling. *Nature* 434(7035)**,** 889-894. doi: 10.1038/nature03418

Kim, K.X., Beurg, M., Hackney, C.M., Furness, D.N., Mahendrasingam, S., and Fettiplace, R. (2013). The role of transmembrane channel-like proteins in the operation of hair cell mechanotransducer channels. *J Gen Physiol* 142(5)**,** 493-505. doi: 10.1085/jgp.201311068

Kirk, M.E., Meredith, F.L., Benke, T.A., and Rennie, K.J. (2017). AMPA receptor-mediated rapid EPSCs in vestibular calyx afferents. *J Neurophysiol* 117(6)**,** 2312-2323. doi: 10.1152/jn.00394.2016

Kitajiri, S., Sakamoto, T., Belyantseva, I.A., Goodyear, R.J., Stepanyan, R., Fujiwara, I., et al. (2010). Actin-bundling protein TRIOBP forms resilient rootlets of hair cell stereocilia essential for hearing. *Cell* 141(5)**,** 786-798. doi: 10.1016/j.cell.2010.03.049

Koffler, T., Ushakov, K., and Avraham, K.B. (2015). Genetics of Hearing Loss: Syndromic. *Otolaryngol Clin North Am* 48(6)**,** 1041-1061. doi: 10.1016/j.otc.2015.07.007

Kurima, K., Ebrahim, S., Pan, B., Sedlacek, M., Sengupta, P., Millis, B.A., et al. (2015). TMC1 and TMC2 Localize at the Site of Mechanotransduction in Mammalian Inner Ear Hair Cell Stereocilia. *Cell Rep* 12(10)**,** 1606-1617. doi: 10.1016/j.celrep.2015.07.058

Kuzmenkina, E., Novikova, E., Jangsangthong, W., Matthes, J., and Herzig, S. (2019). Single-Channel Resolution of the Interaction between C-Terminal CaV1.3 Isoforms and Calmodulin. *Biophys J* 116(5)**,** 836-846. doi: 10.1016/j.bpj.2019.01.025

Kwan, K.Y., Allchorne, A.J., Vollrath, M.A., Christensen, A.P., Zhang, D.S., Woolf, C.J., et al. (2006). TRPA1 contributes to cold, mechanical, and chemical nociception but is not essential for hair-cell transduction. *Neuron* 50(2)**,** 277-289. doi: 10.1016/j.neuron.2006.03.042

Lefevre, G., Michel, V., Weil, D., Lepelletier, L., Bizard, E., Wolfrum, U., et al. (2008). A core cochlear phenotype in USH1 mouse mutants implicates fibrous links of the hair bundle in its cohesion, orientation and differential growth. *Development* 135(8)**,** 1427-1437. doi: 10.1242/dev.012922

Li–dong, Z., Jun, L., Yin–yan, H., Jian–he, S., and Shi–ming, Y. (2008). Supporting Cells–a New Area in Cochlear Physiology Study. *Journal of Otology* 3(1)**,** 9-17. doi: 10.1016/s1672-2930(08)50002-x

Liang, H., DeMaria, C.D., Erickson, M.G., Mori, M.X., Alseikhan, B.A., and Yue, D.T. (2003). Unified mechanisms of Ca2+ regulation across the Ca2+ channel family. *Neuron* 39(6)**,** 951-960. doi: 10.1016/s0896-6273(03)00560-9

Liang, Y., and Tavalin, S.J. (2007). Auxiliary beta subunits differentially determine pka utilization of distinct regulatory sites on Cav1.3 L type Ca2+ channels. *Channels (Austin)* 1(2)**,** 102-112. doi: 10.4161/chan.4284

Liberman, M.C. (1978). Auditory-nerve response from cats raised in a low-noise chamber. *J Acoust Soc Am* 63(2)**,** 442-455. doi: 10.1121/1.381736

Liberman, M.C. (1982a). The cochlear frequency map for the cat: labeling auditory-nerve fibers of known characteristic frequency. *J Acoust Soc Am* 72(5)**,** 1441-1449. doi: 10.1121/1.388677

Liberman, M.C. (1982b). Single-neuron labeling in the cat auditory nerve. *Science* 216(4551)**,** 1239-1241. doi: 10.1126/science.7079757

Liberman, M.C., and Kujawa, S.G. (2017). Cochlear synaptopathy in acquired sensorineural hearing loss: Manifestations and mechanisms. *Hear Res* 349**,** 138-147. doi: 10.1016/j.heares.2017.01.003

Lingappan, K. (2018). NF-kappaB in Oxidative Stress. *Curr Opin Toxicol* 7**,** 81-86. doi: 10.1016/j.cotox.2017.11.002

Lingle, C.J., Martinez-Espinosa, P.L., Yang-Hood, A., Boero, L.E., Payne, S., Persic, D., et al. (2019). LRRC52 regulates BK channel function and localization in mouse cochlear inner hair cells. *Proc Natl Acad Sci U S A* 116(37)**,** 18397-18403. doi: 10.1073/pnas.1907065116

Liu, C., Glowatzki, E., and Fuchs, P.A. (2015). Unmyelinated type II afferent neurons report cochlear damage. *Proc Natl Acad Sci U S A* 112(47)**,** 14723-14727. doi: 10.1073/pnas.1515228112

Magupalli, V.G., Schwarz, K., Alpadi, K., Natarajan, S., Seigel, G.M., and Schmitz, F. (2008). Multiple RIBEYE-RIBEYE interactions create a dynamic scaffold for the formation of synaptic ribbons. *J Neurosci* 28(32)**,** 7954-7967. doi: 10.1523/JNEUROSCI.1964-08.2008

Mahendrasingam, S., and Furness, D.N. (2019). Ultrastructural localization of the likely mechanoelectrical transduction channel protein, transmembrane-like channel 1 (TMC1) during development of cochlear hair cells. *Sci Rep* 9(1)**,** 1274. doi: 10.1038/s41598-018-37563-x

Manor, U., Disanza, A., Grati, M., Andrade, L., Lin, H., Di Fiore, P.P., et al. (2011). Regulation of stereocilia length by myosin XVa and whirlin depends on the actin-regulatory protein Eps8. *Curr Biol* 21(2)**,** 167-172. doi: 10.1016/j.cub.2010.12.046

Marcotti, W., Johnson, S.L., Holley, M.C., and Kros, C.J. (2003). Developmental changes in the expression of potassium currents of embryonic, neonatal and mature mouse inner hair cells. *J Physiol* 548(Pt 2)**,** 383-400. doi: 10.1113/jphysiol.2002.034801

Matsumoto, N., and Kalinec, F. (2005). Prestin-dependent and prestin-independent motility of guinea pig outer hair cells. *Hear Res* 208(1-2)**,** 1-13. doi: 10.1016/j.heares.2005.03.030

McFadden, S.L., Ding, D., Burkard, R.F., Jiang, H., Reaume, A.G., Flood, D.G., et al. (1999). Cu/Zn SOD deficiency potentiates hearing loss and cochlear pathology in aged 129,CD-1 mice. *J Comp Neurol* 413(1)**,** 101-112.

McGrath, J., Roy, P., and Perrin, B.J. (2017). Stereocilia morphogenesis and maintenance through regulation of actin stability. *Seminars in Cell & Developmental Biology* 65**,** 88-95. doi: https://doi.org/10.1016/j.semcdb.2016.08.017

Menardo, J., Tang, Y., Ladrech, S., Lenoir, M., Casas, F., Michel, C., et al. (2012). Oxidative stress, inflammation, and autophagic stress as the key mechanisms of premature age-related hearing loss in SAMP8 mouse Cochlea. *Antioxid Redox Signal* 16(3)**,** 263-274. doi: 10.1089/ars.2011.4037

Meyer, A.C., Frank, T., Khimich, D., Hoch, G., Riedel, D., Chapochnikov, N.M., et al. (2009). Tuning of synapse number, structure and function in the cochlea. *Nat Neurosci* 12(4)**,** 444-453. doi: 10.1038/nn.2293

Meyer, A.C., and Moser, T. (2010). Structure and function of cochlear afferent innervation. *Curr Opin Otolaryngol Head Neck Surg* 18(5)**,** 441-446. doi: 10.1097/MOO.0b013e32833e0586

Michalski, N., Goutman, J.D., Auclair, S.M., Boutet de Monvel, J., Tertrais, M., Emptoz, A., et al. (2017). Otoferlin acts as a Ca(2+) sensor for vesicle fusion and vesicle pool replenishment at auditory hair cell ribbon synapses. *Elife* 6. doi: 10.7554/eLife.31013

Michalski, N., Michel, V., Caberlotto, E., Lefevre, G.M., van Aken, A.F., Tinevez, J.Y., et al. (2009). Harmonin-b, an actin-binding scaffold protein, is involved in the adaptation of mechanoelectrical transduction by sensory hair cells. *Pflugers Arch* 459(1)**,** 115-130. doi: 10.1007/s00424-009-0711-x

Molnar, Z., Lopez-Bendito, G., Small, J., Partridge, L.D., Blakemore, C., and Wilson, M.C. (2002). Normal development of embryonic thalamocortical connectivity in the absence of evoked synaptic activity. *J Neurosci* 22(23)**,** 10313-10323.

Montcouquiol, M., Rachel, R.A., Lanford, P.J., Copeland, N.G., Jenkins, N.A., and Kelley, M.W. (2003). Identification of Vangl2 and Scrb1 as planar polarity genes in mammals. *Nature* 423(6936)**,** 173-177. doi: 10.1038/nature01618

Morrill, S., and He, D.Z.Z. (2017). Apoptosis in inner ear sensory hair cells. *J Otol* 12(4)**,** 151-164. doi: 10.1016/j.joto.2017.08.001

Moser, T., Grabner, C.P., and Schmitz, F. (2020). Sensory Processing at Ribbon Synapses in the Retina and the Cochlea. *Physiol Rev* 100(1)**,** 103-144. doi: 10.1152/physrev.00026.2018

Nadol, J.B., Jr. (1988). Comparative anatomy of the cochlea and auditory nerve in mammals. *Hear Res* 34(3)**,** 253-266. doi: 10.1016/0378-5955(88)90006-8

Neef, J., Gehrt, A., Bulankina, A.V., Meyer, A.C., Riedel, D., Gregg, R.G., et al. (2009). The Ca2+ channel subunit beta2 regulates Ca2+ channel abundance and function in inner hair cells and is required for hearing. *J Neurosci* 29(34)**,** 10730-10740. doi: 10.1523/JNEUROSCI.1577-09.2009

Nicolson, T. (2015). Ribbon synapses in zebrafish hair cells. *Hear Res* 330(Pt B)**,** 170-177. doi: 10.1016/j.heares.2015.04.003

Noben-Trauth, K., Zheng, Q.Y., and Johnson, K.R. (2003). Association of cadherin 23 with polygenic inheritance and genetic modification of sensorineural hearing loss. *Nat Genet* 35(1)**,** 21-23. doi: 10.1038/ng1226

Nouvian, R., Eybalin, M., and Puel, J.L. (2015). Cochlear efferents in developing adult and pathological conditions. *Cell Tissue Res* 361(1)**,** 301-309. doi: 10.1007/s00441-015-2158-z

Nouvian, R., Neef, J., Bulankina, A.V., Reisinger, E., Pangrsic, T., Frank, T., et al. (2011). Exocytosis at the hair cell ribbon synapse apparently operates without neuronal SNARE proteins. *Nat Neurosci* 14(4)**,** 411-413. doi: 10.1038/nn.2774

Oliver, D., Taberner, A.M., Thurm, H., Sausbier, M., Arntz, C., Ruth, P., et al. (2006). The role of BKCa channels in electrical signal encoding in the mammalian auditory periphery. *J Neurosci* 26(23)**,** 6181-6189. doi: 10.1523/JNEUROSCI.1047-06.2006

Oyler, G.A., Higgins, G.A., Hart, R.A., Battenberg, E., Billingsley, M., Bloom, F.E., et al. (1989). The identification of a novel synaptosomal-associated protein, SNAP-25, differentially expressed by neuronal subpopulations. *J Cell Biol* 109(6 Pt 1)**,** 3039-3052. doi: 10.1083/jcb.109.6.3039

Paffenholz, R., Bergstrom, R.A., Pasutto, F., Wabnitz, P., Munroe, R.J., Jagla, W., et al. (2004). Vestibular defects in head-tilt mice result from mutations in Nox3, encoding an NADPH oxidase. *Genes Dev* 18(5)**,** 486-491. doi: 10.1101/gad.1172504

Pan, B., Geleoc, G.S., Asai, Y., Horwitz, G.C., Kurima, K., Ishikawa, K., et al. (2013). TMC1 and TMC2 are components of the mechanotransduction channel in hair cells of the mammalian inner ear. *Neuron* 79(3)**,** 504-515. doi: 10.1016/j.neuron.2013.06.019

Pangrsic, T., Reisinger, E., and Moser, T. (2012). Otoferlin: a multi-C2 domain protein essential for hearing. *Trends Neurosci* 35(11)**,** 671-680. doi: 10.1016/j.tins.2012.08.002

Peineau, T., Belleudy, S., Pietropaolo, S., Bouleau, Y., and Dulon, D. (2021). Synaptic Release Potentiation at Aging Auditory Ribbon Synapses. *Frontiers in Aging Neuroscience* 13(670). doi: 10.3389/fnagi.2021.756449

Pickles, J. (2013). *An Introduction to the Physiology of Hearing: Fourth Edition.* Brill.

Pickles, J.O., Comis, S.D., and Osborne, M.P. (1984). Cross-links between stereocilia in the guinea pig organ of Corti, and their possible relation to sensory transduction. *Hear Res* 15(2)**,** 103-112. doi: 10.1016/0378-5955(84)90041-8

Pienkowski, M. (2015). Music is Good for Your Brain, but Don't Blast it. *Front Young Minds* 3:8. doi: 10.3389/frym.2015.00008

Platzer, J., Engel, J., Schrott-Fischer, A., Stephan, K., Bova, S., Chen, H., et al. (2000). Congenital deafness and sinoatrial node dysfunction in mice lacking class D L-type Ca2+ channels. *Cell* 102(1)**,** 89-97. doi: 10.1016/s0092-8674(00)00013-1

Puel, J.L. (1995). Chemical synaptic transmission in the cochlea. *Prog Neurobiol* 47(6)**,** 449-476. doi: 10.1016/0301-0082(95)00028-3

Pujol, R., and Puel, J.L. (1999). Excitotoxicity, synaptic repair, and functional recovery in the mammalian cochlea: a review of recent findings. *Ann N Y Acad Sci* 884**,** 249-254. doi: 10.1111/j.1749-6632.1999.tb08646.x

Pyott, S.J., and Duncan, R.K. (2016). BK Channels in the Vertebrate Inner Ear. *Int Rev Neurobiol* 128**,** 369-399. doi: 10.1016/bs.irn.2016.03.016

Rastogi, R., Geng, X., Li, F., and Ding, Y. (2016). NOX Activation by Subunit Interaction and Underlying Mechanisms in Disease. *Front Cell Neurosci* 10**,** 301. doi: 10.3389/fncel.2016.00301

Richardson, G.P., Lukashkin, A.N., and Russell, I.J. (2008). The tectorial membrane: one slice of a complex cochlear sandwich. *Curr Opin Otolaryngol Head Neck Surg* 16(5)**,** 458-464. doi: 10.1097/MOO.0b013e32830e20c4

Richardson, G.P., Russell, I.J., Duance, V.C., and Bailey, A.J. (1987). Polypeptide composition of the mammalian tectorial membrane. *Hear Res* 25(1)**,** 45-60. doi: 10.1016/0378-5955(87)90078-5

Rousset, F., Nacher-Soler, G., Coelho, M., Ilmjarv, S., Kokje, V.B.C., Marteyn, A., et al. (2020). Redox activation of excitatory pathways in auditory neurons as mechanism of age-related hearing loss. *Redox Biol* 30**,** 101434. doi: 10.1016/j.redox.2020.101434

Roux, I., Safieddine, S., Nouvian, R., Grati, M., Simmler, M.C., Bahloul, A., et al. (2006). Otoferlin, defective in a human deafness form, is essential for exocytosis at the auditory ribbon synapse. *Cell* 127(2)**,** 277-289. doi: 10.1016/j.cell.2006.08.040

Ruel, J., Emery, S., Nouvian, R., Bersot, T., Amilhon, B., Van Rybroek, J.M., et al. (2008). Impairment of SLC17A8 encoding vesicular glutamate transporter-3, VGLUT3, underlies nonsyndromic deafness DFNA25 and inner hair cell dysfunction in null mice. *Am J Hum Genet* 83(2)**,** 278-292. doi: 10.1016/j.ajhg.2008.07.008

Ruel, J., Wang, J., Rebillard, G., Eybalin, M., Lloyd, R., Pujol, R., et al. (2007). Physiology, pharmacology and plasticity at the inner hair cell synaptic complex. *Hear Res* 227(1-2)**,** 19-27. doi: 10.1016/j.heares.2006.08.017

Ruttiger, L., Sausbier, M., Zimmermann, U., Winter, H., Braig, C., Engel, J., et al. (2004). Deletion of the Ca2+-activated potassium (BK) alpha-subunit but not the BKbeta1-subunit leads to progressive hearing loss. *Proc Natl Acad Sci U S A* 101(35)**,** 12922-12927. doi: 10.1073/pnas.0402660101

Sadeghi, S.G., Pyott, S.J., Yu, Z., and Glowatzki, E. (2014). Glutamatergic signaling at the vestibular hair cell calyx synapse. *J Neurosci* 34(44)**,** 14536-14550. doi: 10.1523/JNEUROSCI.0369-13.2014

Safieddine, S., and Wenthold, R.J. (1999). SNARE complex at the ribbon synapses of cochlear hair cells: analysis of synaptic vesicle- and synaptic membrane-associated proteins. *Eur J Neurosci* 11(3)**,** 803-812. doi: 10.1046/j.1460-9568.1999.00487.x

Sahoo, N., Hoshi, T., and Heinemann, S.H. (2014). Oxidative modulation of voltage-gated potassium channels. *Antioxid Redox Signal* 21(6)**,** 933-952. doi: 10.1089/ars.2013.5614

Sanada, F., Taniyama, Y., Muratsu, J., Otsu, R., Shimizu, H., Rakugi, H., et al. (2018). Source of Chronic Inflammation in Aging. *Front Cardiovasc Med* 5**,** 12. doi: 10.3389/fcvm.2018.00012

Scharinger, A., Eckrich, S., Vandael, D.H., Schonig, K., Koschak, A., Hecker, D., et al. (2015). Cell-type-specific tuning of Cav1.3 Ca(2+)-channels by a C-terminal automodulatory domain. *Front Cell Neurosci* 9**,** 309. doi: 10.3389/fncel.2015.00309

Schmitz, F., Konigstorfer, A., and Sudhof, T.C. (2000). RIBEYE, a component of synaptic ribbons: a protein's journey through evolution provides insight into synaptic ribbon function. *Neuron* 28(3)**,** 857-872. doi: 10.1016/s0896-6273(00)00159-8

Seal, R.P., Akil, O., Yi, E., Weber, C.M., Grant, L., Yoo, J., et al. (2008). Sensorineural deafness and seizures in mice lacking vesicular glutamate transporter 3. *Neuron* 57(2)**,** 263-275. doi: 10.1016/j.neuron.2007.11.032

Sebe, J.Y., Cho, S., Sheets, L., Rutherford, M.A., von Gersdorff, H., and Raible, D.W. (2017). Ca(2+)-Permeable AMPARs Mediate Glutamatergic Transmission and Excitotoxic Damage at the Hair Cell Ribbon Synapse. *J Neurosci* 37(25)**,** 6162-6175. doi: 10.1523/JNEUROSCI.3644-16.2017

Shen, C., Rathore, S.S., Yu, H., Gulbranson, D.R., Hua, R., Zhang, C., et al. (2015). The trans-SNARE-regulating function of Munc18-1 is essential to synaptic exocytosis. *Nat Commun* 6**,** 8852. doi: 10.1038/ncomms9852

Shimojo, M., Courchet, J., Pieraut, S., Torabi-Rander, N., Sando, R., 3rd, Polleux, F., et al. (2015). SNAREs Controlling Vesicular Release of BDNF and Development of Callosal Axons. *Cell Rep* 11(7)**,** 1054-1066. doi: 10.1016/j.celrep.2015.04.032

Shin, J.B., Longo-Guess, C.M., Gagnon, L.H., Saylor, K.W., Dumont, R.A., Spinelli, K.J., et al. (2010). The R109H variant of fascin-2, a developmentally regulated actin crosslinker in hair-cell stereocilia, underlies early-onset hearing loss of DBA/2J mice. *J Neurosci* 30(29)**,** 9683-9694. doi: 10.1523/JNEUROSCI.1541-10.2010

Sidi, S., Friedrich, R.W., and Nicolson, T. (2003). NompC TRP channel required for vertebrate sensory hair cell mechanotransduction. *Science* 301(5629)**,** 96-99. doi: 10.1126/science.1084370

Sies, H., Berndt, C., and Jones, D.P. (2017). Oxidative Stress. *Annu Rev Biochem* 86**,** 715-748. doi: 10.1146/annurev-biochem-061516-045037

Singh, A., Gebhart, M., Fritsch, R., Sinnegger-Brauns, M.J., Poggiani, C., Hoda, J.C., et al. (2008). Modulation of voltage- and Ca2+-dependent gating of CaV1.3 L-type calcium channels by alternative splicing of a C-terminal regulatory domain. *J Biol Chem* 283(30)**,** 20733-20744. doi: 10.1074/jbc.M802254200

Skinner, L.J., Enee, V., Beurg, M., Jung, H.H., Ryan, A.F., Hafidi, A., et al. (2003). Contribution of BK Ca2+-activated K+ channels to auditory neurotransmission in the Guinea pig cochlea. *J Neurophysiol* 90(1)**,** 320-332. doi: 10.1152/jn.01155.2002

Snellman, J., Mehta, B., Babai, N., Bartoletti, T.M., Akmentin, W., Francis, A., et al. (2011). Acute destruction of the synaptic ribbon reveals a role for the ribbon in vesicle priming. *Nat Neurosci* 14(9)**,** 1135-1141. doi: 10.1038/nn.2870

Someya, S., and Prolla, T.A. (2010). Mitochondrial oxidative damage and apoptosis in age-related hearing loss. *Mech Ageing Dev* 131(7-8)**,** 480-486. doi: 10.1016/j.mad.2010.04.006

Someya, S., Xu, J., Kondo, K., Ding, D., Salvi, R.J., Yamasoba, T., et al. (2009). Age-related hearing loss in C57BL/6J mice is mediated by Bak-dependent mitochondrial apoptosis. *Proc Natl Acad Sci U S A* 106(46)**,** 19432-19437. doi: 10.1073/pnas.0908786106

Sorensen, J.B., Wiederhold, K., Muller, E.M., Milosevic, I., Nagy, G., de Groot, B.L., et al. (2006). Sequential N- to C-terminal SNARE complex assembly drives priming and fusion of secretory vesicles. *EMBO J* 25(5)**,** 955-966. doi: 10.1038/sj.emboj.7601003

Spiwoks-Becker, I., Maus, C., tom Dieck, S., Fejtova, A., Engel, L., Wolloscheck, T., et al. (2008). Active zone proteins are dynamically associated with synaptic ribbons in rat pinealocytes. *Cell Tissue Res* 333(2)**,** 185-195. doi: 10.1007/s00441-008-0627-3

Stamataki, S., Francis, H.W., Lehar, M., May, B.J., and Ryugo, D.K. (2006). Synaptic alterations at inner hair cells precede spiral ganglion cell loss in aging C57BL/6J mice. *Hear Res* 221(1-2)**,** 104-118. doi: 10.1016/j.heares.2006.07.014

Taberner, A.M., and Liberman, M.C. (2005). Response properties of single auditory nerve fibers in the mouse. *J Neurophysiol* 93(1)**,** 557-569. doi: 10.1152/jn.00574.2004

Tertrais, M., Bouleau, Y., Emptoz, A., Belleudy, S., Sutton, R.B., Petit, C., et al. (2019). Viral Transfer of Mini-Otoferlins Partially Restores the Fast Component of Exocytosis and Uncovers Ultrafast Endocytosis in Auditory Hair Cells of Otoferlin Knock-Out Mice. *J Neurosci* 39(18)**,** 3394-3411. doi: 10.1523/JNEUROSCI.1550-18.2018

Tertrais, M. (2018). Exploration du rôle des différents domaines C2 de l'otoferline et des isoformes des canaux calciques CaV1.3 dans la transmission synaptique des cellules ciliées auditives. PhD Thesis.

Velez-Ortega, A.C., Freeman, M.J., Indzhykulian, A.A., Grossheim, J.M., and Frolenkov, G.I. (2017). Mechanotransduction current is essential for stability of the transducing stereocilia in mammalian auditory hair cells. *Elife* 6. doi: 10.7554/eLife.24661

Vina, J. (2019). The free radical theory of frailty: Mechanisms and opportunities for interventions to promote successful aging. *Free Radic Biol Med* 134**,** 690-694. doi: 10.1016/j.freeradbiomed.2019.01.045

Vincent, P.F., Bouleau, Y., Charpentier, G., Emptoz, A., Safieddine, S., Petit, C., et al. (2017). Different CaV1.3 Channel Isoforms Control Distinct Components of the Synaptic Vesicle Cycle in Auditory Inner Hair Cells. *J Neurosci* 37(11)**,** 2960-2975. doi: 10.1523/JNEUROSCI.2374-16.2017

Vincent, P.F.Y., Cho, S., Tertrais, M., Bouleau, Y., von Gersdorff, H., and Dulon, D. (2018). Clustered Ca(2+) Channels Are Blocked by Synaptic Vesicle Proton Release at Mammalian Auditory Ribbon Synapses. *Cell Rep* 25(12)**,** 3451-3464 e3453. doi: 10.1016/j.celrep.2018.11.072

Vona, B., Rad, A., and Reisinger, E. (2020). The Many Faces of DFNB9: Relating OTOF Variants to Hearing Impairment. *Genes (Basel)* 11(12). doi: 10.3390/genes11121411

Vona B, Mazaheri N, Lin SJ, Dunbar LA, Maroofian R, Azaiez H, Booth KT, Vitry S, Rad A, Rüschendorf F, Varshney P, Fowler B, Beetz C, Alagramam KN, Murphy D, Shariati G, Sedaghat A, Houlden H, Petree C, VijayKumar S, Smith RJH, Haaf T, El-Amraoui

A, Bowl MR, Varshney GK, Galehdari H. A biallelic variant in CLRN2 causes non-syndromic hearing loss in humans. Hum Genet. 2021 Jun;140(6):915-931. doi: 10.1007/s00439-020-02254-z. Epub 2021 Jan 26. PMID: 33496845; PMCID: PMC8099798.

Wan, G., Corfas, G., and Stone, J.S. (2013). Inner ear supporting cells: rethinking the silent majority. *Semin Cell Dev Biol* 24(5)**,** 448-459. doi: 10.1016/j.semcdb.2013.03.009

Washbourne, P., Thompson, P.M., Carta, M., Costa, E.T., Mathews, J.R., Lopez-Bendito, G., et al. (2002). Genetic ablation of the t-SNARE SNAP-25 distinguishes mechanisms of neuroexocytosis. *Nat Neurosci* 5(1)**,** 19-26. doi: 10.1038/nn783

Wei, A.D., Gutman, G.A., Aldrich, R., Chandy, K.G., Grissmer, S., and Wulff, H. (2005). International Union of Pharmacology. LII. Nomenclature and molecular relationships of calcium-activated potassium channels. *Pharmacol Rev* 57(4)**,** 463-472. doi: 10.1124/pr.57.4.9

Wersinger, E., McLean, W.J., Fuchs, P.A., and Pyott, S.J. (2010). BK channels mediate cholinergic inhibition of high frequency cochlear hair cells. *PLoS One* 5(11)**,** e13836. doi: 10.1371/journal.pone.0013836

Wichmann, C., and Moser, T. (2015). Relating structure and function of inner hair cell ribbon synapses. *Cell Tissue Res* 361(1)**,** 95-114. doi: 10.1007/s00441-014-2102-7

Wong, C.O., Chen, K., Lin, Y.Q., Chao, Y., Duraine, L., Lu, Z., et al. (2014). A TRPV channel in Drosophila motor neurons regulates presynaptic resting Ca2+ levels, synapse growth, and synaptic transmission. *Neuron* 84(4)**,** 764-777. doi: 10.1016/j.neuron.2014.09.030

Wong, H.C., Zhang, Q., Beirl, A.J., Petralia, R.S., Wang, Y.X., and Kindt, K. (2019). Synaptic mitochondria regulate hair-cell synapse size and function. *Elife* 8. doi: 10.7554/eLife.48914

Wu, J., Ye, J., Kong, W., Zhang, S., and Zheng, Y. (2020). Programmed cell death pathways in hearing loss: A review of apoptosis, autophagy and programmed necrosis. *Cell Prolif* 53(11)**,** e12915. doi: 10.1111/cpr.12915

Xiong, W., Grillet, N., Elledge, H.M., Wagner, T.F., Zhao, B., Johnson, K.R., et al. (2012). TMHS is an integral component of the mechanotransduction machinery of cochlear hair cells. *Cell* 151(6)**,** 1283-1295. doi: 10.1016/j.cell.2012.10.041

Yang, P.S., Alseikhan, B.A., Hiel, H., Grant, L., Mori, M.X., Yang, W., et al. (2006). Switching of Ca2+-dependent inactivation of Ca(v)1.3 channels by calcium binding proteins of auditory hair cells. *J Neurosci* 26(42)**,** 10677-10689. doi: 10.1523/JNEUROSCI.3236-06.2006

Yasunaga, S., Grati, M., Cohen-Salmon, M., El-Amraoui, A., Mustapha, M., Salem, N., et al. (1999). A mutation in OTOF, encoding otoferlin, a FER-1-like protein, causes DFNB9, a nonsyndromic form of deafness. *Nat Genet* 21(4)**,** 363-369. doi: 10.1038/7693

Ye, B., Fan, C., Shen, Y., Wang, Q., Hu, H., and Xiang, M. (2018). The Antioxidative Role of Autophagy in Hearing Loss. *Front Neurosci* 12**,** 1010. doi: 10.3389/fnins.2018.01010

Zhang, Y., Bokov, A., Gelfond, J., Soto, V., Ikeno, Y., Hubbard, G., et al. (2014). Rapamycin extends life and health in C57BL/6 mice. *J Gerontol A Biol Sci Med Sci* 69(2)**,** 119-130. doi: 10.1093/gerona/glt056

Zhao, B., Wu, Z., Grillet, N., Yan, L., Xiong, W., Harkins-Perry, S., et al. (2014). TMIE is an essential component of the mechanotransduction machinery of cochlear hair cells. *Neuron* 84(5)**,** 954-967. doi: 10.1016/j.neuron.2014.10.041

Zhao, W., Gao, X., Qiu, S., Gao, B., Gao, S., Zhang, X., et al. (2019). A subunit of V-ATPases, ATP6V1B2, underlies the pathology of intellectual disability. *EBioMedicine* 45**,** 408-421. doi: 10.1016/j.ebiom.2019.06.035

Zheng, J., Shen, W., He, D.Z., Long, K.B., Madison, L.D., and Dallos, P. (2000a). Prestin is the motor protein of cochlear outer hair cells. *Nature* 405(6783)**,** 149-155. doi: 10.1038/35012009

Zheng, L., Sekerkova, G., Vranich, K., Tilney, L.G., Mugnaini, E., and Bartles, J.R. (2000b). The deaf jerker mouse has a mutation in the gene encoding the espin actin-bundling proteins of hair cell stereocilia and lacks espins. *Cell* 102(3)**,** 377-385. doi: 10.1016/s0092-8674(00)00042-8

Zheng, W., and Holt, J.R. (2021). The Mechanosensory Transduction Machinery in Inner Ear Hair Cells. *Annu Rev Biophys* 50**,** 31-51. doi: 10.1146/annurev-biophys-062420-081842

Zhou, W., and Jones, S.W. (1996). The effects of external pH on calcium channel currents in bullfrog sympathetic neurons. *Biophys J* 70(3)**,** 1326-1334. doi: 10.1016/S0006-3495(96)79689-3

Synaptopathies des cellules ciliées auditives associées à un dysfonctionnement de l'exocytose Ca^{2+}-dépendante

Les signaux acoustiques sont encodés en impulsions électriques nerveuses au niveau des synapses à ruban des cellules ciliées internes (CCI) de la cochlée. L'exocytose des vésicules synaptiques glutamatergiques des CCIs est déclenchée par l'activation des canaux calciques voltage-dépendent $Ca_V1.3$ et requiert un senseur calcique particulier : l'otoferline. Ces canaux calciques $Ca_V1.3$ s'organisent de façon spatialement resserrée autour des rubans synaptiques en formant un complexe avec l'harmonine et la clarin-1 associées à l'actine-F. Dans la première partie de notre étude, nous avons étudié le rôle possible du nouvellement identifié paralogue de la clarine-1, la clarine-2, dans les synapses à ruban des CCI. Nous démontrons que la clarine-2 est impliquée dans la régulation du potentiel d'activation des canaux calciques des CCIs et en conséquence de l'exocytose synaptique. Dans une deuxième partie de notre travail nous avons étudié le rôle de la SNAP-25 dans l'exocytose des CCI. La SNAP-25 est une protéine essentielle du complexe SNARE qui permet l'amarrage des vésicules synaptiques à la membrane et leur fusion dans les synapses neuronales centrales mais dont le rôle au niveau des CCI est encore largement débattu. En utilisant des souris dont la SNAP-25 est sélectivement supprimée dans les cellules ciliées, nous montrons que la SNAP-25 est essentielle à la fonction auditive et vestibulaire, du fait d'une perte de l'exocytose rapide des cellules ciliées, suivi par une dégénérescence progressive des synapses et des cellules ciliées elles-mêmes. Dans une troisième partie, nous avons étudié la dégénérescence des synapses à ruban des CCI au cours du vieillissement. Nous observons chez les souris C57BL/6J âgées que les synapses à rubans des CCIs restantes, qui n'ont pas encore dégénérées, présentent des rubans agrandis, une augmentation des microdomaines calciques autour des rubans et une plus grande capacité à soutenir l'exocytose suggérant une potentialisation de ces synapses. Cette potentialisation des synapses à ruban âgées pourrait en partie expliquer l'hyperacousie paradoxalement observée dans la presbyacousie.

Mots-clés : Surdité, Cellules ciliées auditives, Exocytose calcium-dépendante.

Auditory hair cells synaptopathies due to Ca^{2+}-dependent exocytosis disruption

Acoustic signals are encoded into electrical nerve impulses at the ribbon synapses of the cochlear inner hair cells (IHC). Exocytosis of the synaptic glutamatergic vesicles at these ribbon synapses is triggered by the activation of the voltage-dependent calcium channels $Ca_V1.3$ and required a specific calcium sensor: otoferlin. In the first part of my thesis, we studied the role of clarin-2, a newly identified tetraspan protein paralog of clarin-1, in these synapses. We know from previous studies that clarin-1, by forming a complex associating $Ca_V1.3$ channels, harmonin-b and actin-F, is essential for a compact spatial organization of the Ca1.3 channels at the active zone of the IHC ribbons. We show that clarin-2 is essential for a normal voltage-dependent activation of the IHC calcium channels and is likely part of the clarin-1 complex at the ribbon synapses. In the second part of my thesis, we studied the role of SNAP-25, a protein of the SNARE complex implicated in the docking, priming and fusion of the synaptic vesicles at neuronal central synapses but whose implication at the ribbon hair cell synapses remain still under debate. We show that mutant mice specifically deleted for SNAP-25 in hair cells are profoundly deaf and have a severe vestibular deficit. Electrophysiological patch-clamp recordings in IHCs and utricular hair cells indicated a severe defect in fast exocytosis. This synaptic functional defect was associated with a progressive degeneration of the ribbon synapses and the hair cells themselves, suggesting that SNAP-25 is also essential for the release of important neurotrophic factors. In the third part of my thesis, we investigated the functional changes of the aging ribbon synapses in C57BL/6J mice. We found that the aging synaptic IHC ribbons, while progressively degenerating, become larger with enlarged Ca^{2+} microdomains to produce a more sustained exocytosis of synaptic vesicles. The expression and the voltage dependence of the fast BK channels, essential for fast IHC repolarization, were also severely affected with aging. All these results suggested that the IHC ribbon synapses become potentiated with aging, a process that may partly explain the paradoxical hyperacusis phenomenon in presbyacusis.

Keywords : Hearing loss, Auditory hair cells, Calcium-dependent exocytosis.